



**HAL**  
open science

# Soft X-ray Radiolysis of Water and Biomolecules : Insights from Experiments and Simulations

Aashini Rajpal

► **To cite this version:**

Aashini Rajpal. Soft X-ray Radiolysis of Water and Biomolecules : Insights from Experiments and Simulations. Theoretical and/or physical chemistry. Université Paris-Saclay, 2023. English. NNT : 2023UPASF058 . tel-04672714

**HAL Id: tel-04672714**

**<https://theses.hal.science/tel-04672714>**

Submitted on 19 Aug 2024

**HAL** is a multi-disciplinary open access archive for the deposit and dissemination of scientific research documents, whether they are published or not. The documents may come from teaching and research institutions in France or abroad, or from public or private research centers.

L'archive ouverte pluridisciplinaire **HAL**, est destinée au dépôt et à la diffusion de documents scientifiques de niveau recherche, publiés ou non, émanant des établissements d'enseignement et de recherche français ou étrangers, des laboratoires publics ou privés.

# Soft X-ray Radiolysis of Water and Biomolecules: Insights from Experiments and Simulations

*Radiolyse par les rayons X-mous de l'eau et des biomolécules :  
expériences et simulations*

## Thèse de doctorat de l'université Paris-Saclay

École doctorale n° 571 : Sciences chimiques : molécules,  
matériaux, instrumentations et biosystèmes (2MIB)  
Spécialité de doctorat : Chimie  
Graduate School : Chimie. Référent : Faculté des Sciences d'Orsay

Thèse préparée dans l'unité de recherche **NIMBE**  
(Université Paris-Saclay, CEA, CNRS), sous la direction  
de **Jean-Philippe RENAULT**, Directeur de recherche CEA, CEA Saclay, le co-  
encadrement de **Marie-Anne HERVE DU PENHOAT**, Maître de conférences, IMPMC,  
Sorbonne Université et le co-encadrement de **Christophe NICOLAS**, Scientifique de  
ligne, Synchrotron SOLEIL

Thèse soutenue à Paris-Saclay, le 9 octobre 2023, par

**Aashini RAJPAL**

## Composition du Jury

Membres du jury avec voix délibérative

<b>Aurélien de la LANDE</b> Directeur de Recherche, ICP, Université Paris-Saclay	Président
<b>Marie DAVIDKOVA</b> Chercheuse Senior (eq. HDR), Nuclear Physics Institute CAS, Prague, Czech Republic	Rapporteuse & Examinatrice
<b>Patrick ROUSSEAU</b> MCF HDR, CIMAP, Université de Caen Normandie	Rapporteur & Examineur
<b>Sylwia PTASINSKA</b> Professeure, Université de Notre Dame, Notre Dame, Indiana, United States of America	Examinatrice
<b>Géraldine FERAUD</b> MCF, LERMA, Sorbonne Université	Examinatrice

**Titre :** Radiolyse par les rayons X-mous de l'eau et des biomolécules: expériences et simulations.

**Mots clés :** Radiolyse, superoxyde, irradiation, rayons X-mous, synchrotron

**Résumé :** La thèse vise à comprendre l'interaction des rayons X mous ( $< 2$  keV) avec l'eau et des dipeptides en solution aqueuse. Les rayons X mous sont des rayonnements faiblement pénétrants mais qui génèrent des dépôts d'énergie denses, ils interagissent principalement par ionisation en couche interne (si l'énergie du photon est supérieure au seuil K de l'atome cible), suivie par un effet Auger pour les éléments de faible Z, conduisant ainsi à la formation de molécules multiples ionisées. Pour les effets indirects des radiations, des échantillons d'eau liquide ont été irradiés au dessus du seuil K de l'oxygène (532 eV), ce qui entraîne la formation de molécules d'eau doublement ionisées ( $H_2O^{2+}$ ) dans le milieu. La dissociation de  $H_2O^{2+}$  et les réactions consécutives de ses produits de dissociation au sein des traces d'ionisation conduisent à la production d'espèces superoxydes ( $HO_2^\circ$ ). La formation de  $HO_2^\circ$  n'avait pas encore été étudiée dans la gamme d'énergie des rayons X mous, en raison de leur faible pénétration dans les

milieux condensés ainsi que des faibles rendements radicalaires dans cette gamme d'énergie. Dans cette thèse, nous proposons un moyen de détecter les faibles rendements en radicaux formés lors de l'irradiation par des rayons X mous. Nous présentons le développement d'une technique de détection en ligne très sensible, c'est-à-dire une cellule microfluidique ayant une fenêtre en nitrure de silicium de 150 nm d'épaisseur couplée à une cellule de détection UV en ligne. Cette technique de détection de pointe a permis d'obtenir une sensibilité jusqu'à une concentration de  $10^{-8}$  mol  $L^{-1}$ , grâce à une correction en temps réel de la ligne de base. Pour les effets directs, les événements ultrarapides (étape physique) se produisant lors de l'interaction des rayons X mous avec un dipeptide aqueux ont été étudiés à l'aide de la spectroscopie de photoélectrons X (XPS) résonnante et non résonnante. Ces études ont été étayées par des simulations de dynamique moléculaire *ab initio* (AIMD).

**Title :** Soft X-ray Radiolysis of Water and Biomolecules: Insights from Experiments and Simulations.

**Keywords :** Radiolysis, superoxide, irradiation, soft X-rays, synchrotron

**Abstract :** The thesis aims to achieve an understanding of the interaction of low penetrating densely energy-depositing soft X-rays ( $< 2$  keV) with water and water-dipeptide systems. Soft X-rays dominantly interact via core-shell ionization (given the photon energy is above the absorption edge of the target atom), followed by Auger decay for elements with low Z, leading to multiply ionized molecules. For indirect effects, the interaction of soft X-rays with water was studied, by performing irradiations above the O K-edge (532 eV) that results in a doubly ionized water molecule ( $H_2O^{2+}$ ). The dissociation of  $H_2O^{2+}$  and the consecutive reactions of its dissociation product in the ionization tracks, leads to the production of superoxide species ( $HO_2^\circ$ ). This  $HO_2^\circ$  formation was not yet studied in the soft X-ray energy range, because of the low

penetration of soft X-rays in condensed media and low radical yields in this energy range. Via this thesis, we provide a way to detect low radical yields formed upon irradiation with soft X-rays. We present the development of a highly sensitive in-line detection technique, i.e. a microfluidic cell having a 150 nm thick silicon nitride window coupled to an in-line UV detection cell. This state-of-the-art detection technique allowed a sensitivity down to the concentration of  $10^{-8}$  mol  $L^{-1}$ , thanks to a real-time baseline correction. For the direct effects, the ultrafast events (physical stage) occurring upon the interaction of soft X-rays with aqueous dipeptide were studied using resonant and non-resonant X-ray photoelectron spectroscopy. These studies were supported by *ab-initio* molecular dynamics (AIMD) simulations.



## ACKNOWLEDGMENTS

---

First and foremost, I extend my heartfelt thanks to all the esteemed Jury members - **Patrick ROUSSEAU, Marie DAVIDKOVA, Sylvia PTASINSKA, Aurélien de la LANDE** and **Géraldine FERAUD** for generously agreeing to serve as jury members of my thesis defense. Your willingness to invest time in reading my manuscript and evaluating my work is deeply appreciated. I would like to thank them for an engaging discussion during my defense and their words of appreciation that followed. It means a great deal to me, and I wish to stand by their expectation in my future work as well.

My sincere thanks to my supervisor, **Jean-Philippe RENAULT**, and co-supervisors, **Marie-Anne Hervé du PENHOAT** and **Christophe NICOLAS**. Their constant support and motivation made this thesis possible. The results obtained and the development made during my thesis would not have been possible without their guidance or the scientific rigour that each of them possesses and has instilled in me. I am grateful for their responsiveness to my queries, even at untimely hours. I thank them for helping me find my strengths and for helping me to work on my weaknesses. I am at a loss for words to thank them for making this PhD a smooth journey for me. Thank you for the words of encouragement and advice that will help me become a better version of myself.

I would like to convey my humble gratitude to the **2MIB doctoral school** and **University Paris Saclay** for accepting my application to carry out this thesis and allowing me to defend it. None of this work would have been possible without the funding received from ANR (**HighEneCh project**), the computational time granted at **MeSU supercomputer** (Sorbonne University) and at the French national computing centers (**CINES, IDRIS**), as well as the beamtimes allocated at various beamlines of **SOLEIL synchrotron**.

My heart is overwhelmed as I write here, thinking of the people I met during my doctoral journey and the things I learned from each of them. Although bridging the initial language barrier to integrate into the laboratory was a challenging task, it was achieved through mutual efforts. These three years have been a memorable experience, and I owe it to every member of the lab - both permanent and non-permanent. It is through your collective support that I have experienced significant growth, both scientifically and professionally. It has been a pleasure working with such an interdisciplinary and talented group of people.

Therefore, I extend my thanks to my team **IRAMIS/NIMBE/LIONS** at sites 546, 462 and 125 at **CEA Saclay**. I also want to acknowledge **Joseph, Fadwa, Vagisha, Manon, Dora, Marion, Laura, Florent, Emeline, Zahraa and Charaf** for their constant support and encouragement during my PhD. I also thank them for helping me with the administration and logistics. Additionally, my thanks go to my teams at the partner laboratories, **BIBIP/IMPMC (Sorbonne University)** and **PLEIADES beamline (Synchrotron SOLEIL)**, for providing a nice environment to work in.

Special appreciation goes to **Corinne Chevallard** for familiarizing me with microfluidics and **Lucie HUART** (IMPMC, Sorbonne University), whose groundwork on this project during her PhD thesis laid the foundation for our subsequent accomplishments. It was a pleasure to work and to learn from them.

I extend my gratitude towards all the beamline scientists of **PLEIADES beamline (Aleksander MILOSAVLJEVIC, John BOZEK and Emmauel ROBERT)**, **METROLOGIE beamline (Pascal MERCERE and Dasilva PAULO)** and **TEMPO beamline (Lenart DUDY)** as well as the Chemistry, Biology and Surface laboratories of SOLEIL synchrotron, for their support during the intense beamtime sessions.

Thanks to **Marine FOURNIER** (LCPMR, Sorbonne University) for being part of one of the beamtimes at TEMPO beamline and providing a helping hand during an intense beamtime. I wish you all the very best and success for your PhD project. I would also like to thank **Jean-Jacques GALLET, Fabrice BOURNEL and Francois ROCHET** from LCPMR (Sorbonne University) for their support during the TEMPO beamtime and for familiarizing me with the NAP-XPS setup.

I would like to thank **Mark LEVENSTEIN** (LIONS, CEA Saclay) for providing me with an opportunity to participate in one of his beamtimes at SWING beamline (SOLEIL synchrotron) to perform SAXS/WAXS experiments using a microfluidic device.

Special thanks to **Hugo MARROUX** from LYDIE, CEA Saclay (and **my supervisors** for facilitating the connection), for providing his valuable insights for the XFEL proposal submitted to the European XFEL in Hamburg.

Many thanks to **Jocelyne LEROY** (LICSEN, CEA Saclay) for making the solid-state XPS measurements. Special thanks to **Benoit GERVAIS** (CIMAP, Caen) for his consistent guidance as a member of my comité de suivi and for performing the Monte Carlo simulations that

proved to be crucial to my experimental results. I would also like to thank **Alexandre GIULIANI** (DESIRS beamline, SOLEIL Synchrotron) for granting the use of the mass spectrometer. Many thanks to **Marie-Francoise POLITIS** for her valuable insights into the theoretical counterpart of my PhD thesis.

I am truly blessed and humbled to have had such an incredible network of individuals who believed in me.

Along my doctoral journey, I not only acquired scientific knowledge but also practiced the ethics and integrity that accompany scientific research. The personnel and professional networks established during these years will enrich both the quality of my social life and scientific career. This accomplishment would not have been possible without the guidance I received over the years from **my professors** (from master's, bachelor's and high school). I also want to acknowledge **my friends (Neil, Gokul, Kunj, Gmji** and all my classmates from my master and my hometown) for their assistance in the formatting of the manuscript, handling the administrative work and most importantly, standing by my side throughout.

Last but not least, this work would have not been possible without the encouragement and the belief my **parents, my grandparents** and **my brother** showed in me over the years. Their strategy for me to adopt a 'CAN DO attitude' has paid off.





# CONTENTS

---

Abstract - French and English .....	i
Acknowledgments .....	iii
<b>Chapter 1: Introduction</b> .....	<b>1</b>
1.1. Context .....	2
1.2. Specificity of soft X-rays .....	5
1.2.1. Core-shell dynamics .....	5
1.2.2. Soft X-ray, a difficult radiation to work with .....	8
1.2.3. Soft X-rays: the right tool to investigate Direct and Indirect Effects? .....	10
1.3. The current understanding of interaction of soft X-ray photons with solvent .....	10
1.3.1. Expected radiolytic effect of soft X-rays: Multiple ionization of water .....	12
1.3.2. Superoxide radical production from multiple ionization .....	13
1.3.3. Theoretical studies to understand multiple ionization and HO <sub>2</sub> <sup>°</sup> production ... .....	16
1.4. Spectroscopy- A good tool to study the interaction of photons with solute .....	17
1.4.1. Soft X-ray spectroscopic techniques .....	18
1.4.2. Studies of biomolecules using soft X-ray spectroscopic techniques .....	23
1.5. Research Objectives .....	25
References .....	26
<b>Chapter 2: Materials and Methods</b> .....	<b>40</b>
2.1. Chemical products .....	47
<b>2.2. Gamma irradiation</b> .....	<b>48</b>
2.2.1. Gamma dosimetry .....	49
2.3. Synchrotron Soft X-ray irradiation .....	51
2.3.1. Synchrotron light source .....	51
2.3.2. SOLEIL Beamlines .....	53
2.4. Experimental set and analysis techniques .....	56
2.4.1. In-air beam extraction at METROLOGIE beamline: IRAD setup .....	56
2.4.2. Microfluidic cell design and set-up .....	58
2.4.3. Optical Interferometry .....	61
2.4.4 UV-visible spectrophotometry .....	62

2.4.5. XPS analysis .....	65
2.5. Theoretical methods .....	73
2.5.1. General concepts .....	73
2.5.2. Modelling the doubly ionized species .....	83
References .....	93
<b>Chapter 3: Experimental approach for HO<sub>2</sub><sup>°</sup> detection .....</b>	<b>103</b>
3.1. Optimizing the chemical detection system with reference $\gamma$ source .....	105
3.1.1. Optimizing the conditions for the chemical detection system .....	106
3.1.2. Optimizing concentration of the probe and enzymes .....	110
3.1.3. Irradiation using reference gamma source .....	112
3.2. Irradiation using soft X-rays .....	114
3.2.1. Microfluidic cell: A solution for poor penetrating soft X-rays .....	114
3.2.2. In-line UV analysis: A solution for low radical yield .....	123
3.2.3. Dose calculation .....	128
3.2.4. Uncertainty calculation .....	134
3.2.5. Superoxide detection upon irradiation with soft X-rays .....	136
3.3. Conclusion .....	144
References .....	145
<b>Chapter 4: Modeling of HO<sub>2</sub> using Ab-initio approach .....</b>	<b>151</b>
4.1. System of interest .....	152
4.2. Double ionization and early state dynamics of H <sub>2</sub> O <sup>2+</sup> : protocol A (TD DFT + CPMD approach) .....	154
4.2.1. 30 fs Ehrenfest MD followed by CPMD .....	155
4.2.2. Protocol B: full CPMD and choice of a suitable pre-dissociated water molecule geometry .....	163
4.3. Dynamics of pre-dissociated H <sub>2</sub> O <sup>2+</sup> : protocol B (CPMD approach) .....	167
4.4. Conclusion .....	174
References .....	175
<b>Chapter 5: Spectroscopic studies of biomolecules in aqueous environment .....</b>	<b>178</b>
5.1. Choice of the aqueous biomolecules .....	179
5.2. Understanding the effect of core ionizations .....	181
5.3. Valence band characterization .....	89
5.4. Identifying the involved orbitals: DOS calculations using AIMD .....	190
5.5. Enhancing specific electronic transitions: Resonant Auger study .....	196
5.5.1. Enhancement at the Carbon edge .....	197
5.5.2. Enhancement at the Nitrogen edge .....	204
5.6. Electronic structures of Gly and Gly-Gly .....	208
5.7. Conclusion .....	211
References .....	212
<b>Chapter 6: Conclusion and perspective .....</b>	<b>216</b>
6.1. Conclusion .....	217

6.2. Perspective .....	220
References .....	231
<b>Appendices</b> .....	<b>233</b>
Appendix I: Experimental approach for HO <sub>2</sub> <sup>°</sup> detection .....	234
Appendix II: Modeling of H <sub>2</sub> O <sup>2+</sup> using Ab-initio approach .....	240
Appendix III: Spectroscopic studies of biomolecules in aqueous.....	252
Appendix IV: TDDFT of solvated formamide .....	254
Appendix V. List of conferences .....	259
Appendix VI. List of Publications .....	260
References appendices.....	261
<b>List of figures</b> .....	<b>263</b>
<b>List of tables</b> .....	<b>270</b>
<b>List of abbreviations</b> .....	<b>271</b>
<b>Résumé étendu en français</b> .....	<b>273</b>

## CONTENTS CHAPTER 1

---

Chapter 1: Introduction.....	1
<b>1.1. Context</b> .....	<b>2</b>
<b>1.2. Specificity of soft X-rays</b> .....	<b>5</b>
1.2.1. Core-shell dynamics .....	5
1.2.2. Soft X-ray, a difficult radiation to work with.....	8
1.2.3. Soft X-rays: the right tool to investigate Direct and Indirect Effects? .....	10
<b>1.3. The current understanding of the interaction of soft X-ray photons with solvent</b> .....	<b>10</b>
1.3.1. Expected radiolytic effect of soft X-rays: Multiple ionization of water .....	12
1.3.2. Superoxide radical production from multiple ionization .....	13
1.3.3. Theoretical studies to understand multiple ionization and HO <sub>2</sub> <sup>°</sup> production .....	16
<b>1.4. Spectroscopy- A good tool to study the interaction of photons with solute</b> .....	<b>17</b>
1.4.1. Soft X-ray spectroscopic techniques .....	18
1.4.1.1. X-ray Photoelectron Spectroscopy .....	19
1.4.1.1.i. Principle .....	19
1.4.1.1.ii. Understanding the XPS spectrum.....	21
1.4.1.2. X-ray absorption spectroscopy .....	23
1.4.2. Studies of biomolecules using soft X-ray spectroscopic techniques .....	23
<b>1.5. Research Objectives</b> .....	<b>25</b>
<b>References</b> .....	<b>26</b>

# Chapter 1: Introduction

## 1.1. Context

The thesis centers on unraveling the intricate interaction of water and biomolecules with soft X-ray radiation. Radiations are present everywhere in our environment, with varying levels of exposure from both natural and human-made sources.<sup>1</sup> It is the emission of energy in the form of electromagnetic waves or moving subatomic particles. Natural sources of radiation include cosmic radiation from outer space and radioactive materials in the Earth's crust and atmosphere. Meanwhile, human-made sources include nuclear power plants, medical diagnostic and therapeutic procedures, and even consumer products.<sup>2</sup> The study of radiation's interaction with matter has captivated scientists since the era of Marie Curie, Henri Becquerel and Wilhelm Röntgen, playing a vital role in advancing our understanding of the natural world, spanning from physics to medicine.<sup>3,4,5</sup>

Outside multi-photon interactions, depending upon their energy, electromagnetic radiation can be classified into either ionizing radiation (towards higher energy in the electromagnetic spectrum) or non-ionizing radiation (towards lower energy in the electromagnetic spectrum), see figure 1.1. Non-ionizing radiations are not energetic enough to remove electrons from atoms or molecules. Their interaction with matter may result in molecular reorganization following electronic excitation, processes described as photochemistry in the case of non-ionizing photons. Ionizing radiations, on the other hand, can detach electrons from atoms or molecules, producing positively charged ions and negatively charged electrons. The ionizing radiations can be further characterized as photons (X-rays or Gamma rays), neutrons and charged particles (protons, alpha, beta or heavy ions), resulting in very different interactions (see figure 1.1).

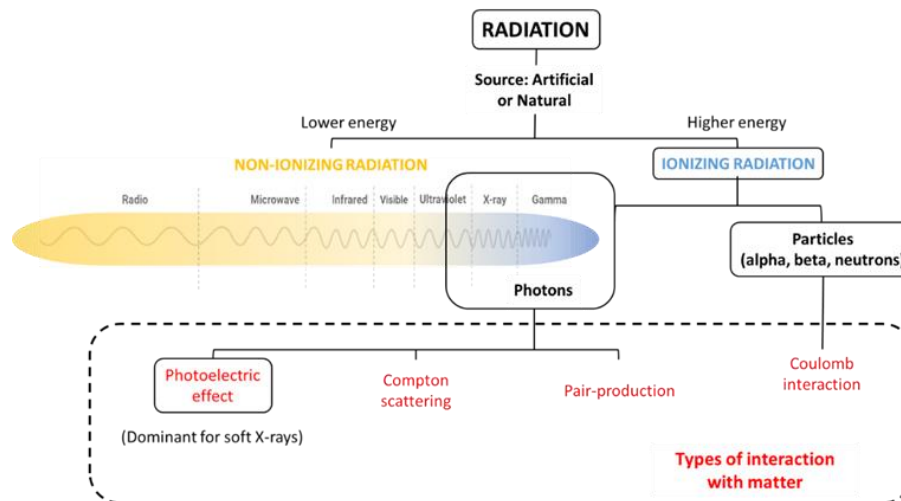


**Figure 1.1:** Classification of radiations based on their energy and type. The different interactions of the ionizing radiation with the matter are also shown.

Charged particles interact via Coulomb interactions<sup>6</sup> and the photons, on the other hand, interact with the matter mainly via three different processes, namely, photoelectric effect, Compton scattering and pair production.<sup>7</sup> However, the dominant interaction pathway depends on the energy of the incoming photon as well as on the atomic number 'Z' of the target (see figure 1.2).<sup>8</sup> In the case of photons, if the photons produce electrons that have enough energy to be ionizing on their own, the whole process will be described as radiolysis. If the electrons do not have sufficient energy, this will be described as photolysis, and discussed along with other photochemical processes.

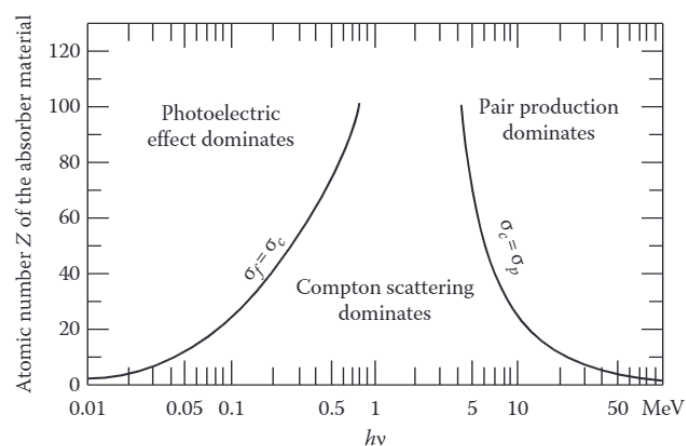


**Figure 1.2:** The relative importance of different interaction processes of electromagnetic ionizing radiation with matter, as a function of incident photon energy and atomic number 'Z' of the target. The two black curves denote the Z values and the photon energies, for which the relative importance of the neighboring effects is equal. The figure is taken from reference.<sup>9</sup>

Researchers have been studying the effect of ionizing radiation on living organisms for decades, and a substantial amount of knowledge has been attained about how ionizing radiation damage living cells and tissues.<sup>10,11,12</sup> These damages are classified as either direct or indirect effects.<sup>13,14</sup> The direct effect refers to the direct ionisation of the biomolecules (solute) resulting in radiation damage (see figure 1.3), whereas an indirect effect refers to the event connected to the ionization of the solvent water molecules. When the solvent water molecules are ionized, they can dissociate to produce reactive oxygen species, ROS, (radicals, and neutral species ( $^{\circ}\text{OH}$ ,  $\text{HO}_2^{\circ}$ ,  $\text{H}_2\text{O}_2$  etc.)) that are highly reactive and can result in an indirect damage, when the ROS interact with the solute (see figure 1.3).

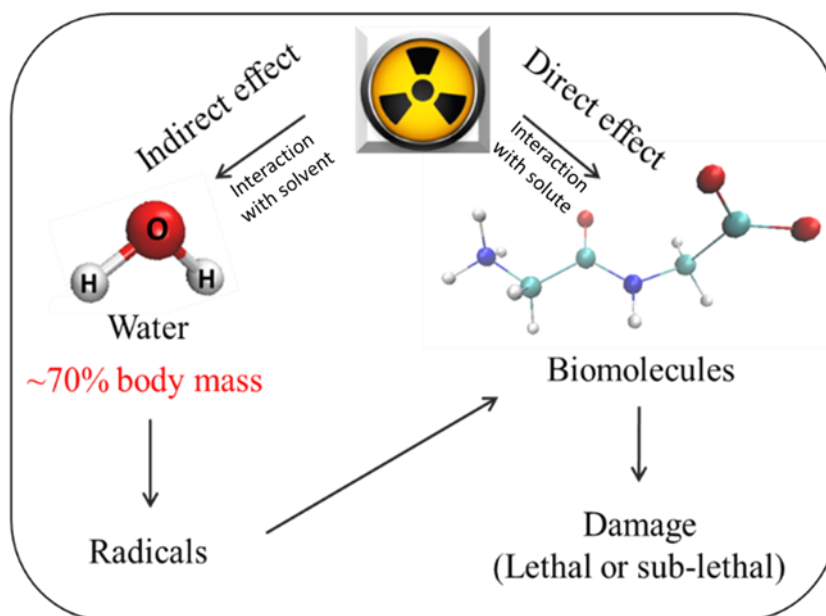


**Figure 1.3:** Interaction of ionizing radiation with living system, causing damage *via* either direct or indirect effects. Another type of damage (not shown here) to the biomolecules that occurs due to the transfer of the electrons and holes from the tightly bound solvation shell<sup>15</sup> is the quasi-direct effect.<sup>16,17</sup>

The indirect damages can lead to modifications in the cells, specially to the DNA.<sup>18,14</sup> These modifications include cleavage of the chemical bonds in the DNA (single or double strand breaks), etc.. These indirect damages can occur within few  $\mu\text{s}$  (where the chemical and biological effects may overlap) and can last up to years, as elaborated in the section 1.3.<sup>19</sup>

There is also an intermediate situation where the damage to the biomolecules occurs because of the charge transfers from the tightly bound solvent water molecules, in the first hydration sphere. The damage is then termed as a quasi-direct effect.<sup>20,21</sup>

Irrespective of the direct, quasi-direct or indirect effects, these damages can be self-repairable (eg. DNA single-strand breaks) or fatal (unrepaired or mis-repaired DNA double-strand breaks)<sup>22</sup> leading to cancer.<sup>23</sup>

The extent of damage caused by ionizing radiation can vary to a large extent depending on the dose delivered to the sample/molecule, i.e. the amount of energy absorbed per unit of mass ( $1 \text{ Gy} = 1 \text{ J/kg}$ ).<sup>24</sup> However, there are other factors that can largely affect the extent of these damages, including the rate at which the dose is delivered to the sample, i.e. the dose rate ( $\text{Gy/s}$ )<sup>25</sup> and the linear energy transfer, LET,<sup>26</sup> which is the amount of energy that an ionizing radiation transfers to the material traversed per unit of path length. Depending upon the LET of the radiation, they can either result in sparsely ionized tracks (Low LET) or densely ionized tracks (High LET). The studies in the soft X-ray energy range have shown that the soft X-rays behave like particles with high LET.<sup>27</sup>

## 1.2. Specificity of soft X-rays

### 1.2.1. Core-shell dynamics

The low energy X-rays, known as the soft X-rays (0.2 keV – 2 keV), are low penetrating ionizing radiations that are almost at the frontier, not much described, between photolysis and radiolysis. They interact dominantly via *core-shell ionization* of the atom leading to the emission of a photoelectron, given that the energy of the photons is above the ionization K-edge of the atom (K-edge ionization energies for Oxygen, Carbon and Nitrogen are around  $532.0 \pm 0.4 \text{ eV}$ ,  $283.8 \pm 0.4 \text{ eV}$  and  $401.6 \pm 4 \text{ eV}$ , respectively<sup>28</sup> and depend on the environment of the probed atom). This process is a part of the *photoelectric effect* (discovered by Hertz in 1887,<sup>29</sup> and later explained by Einstein in 1905<sup>30</sup>) that results in an unstable core-hole creation that is stabilized either via a radiative decay (emission of electromagnetic radiation) or via a non-radiative decay (Auger decay,  $\sim 4 \text{ fs}$  in case of water<sup>31</sup>), see figure 1.4.<sup>32</sup> For elements with low atomic number ( $Z$ ), the Auger decay is the dominant stabilization pathway.<sup>33</sup> During an Auger decay, the energy released during the filling of the core-hole by a valence electron leads to the emission of another electron from the atom. This results in a doubly ionized species



(two hole final electronic state: 2h). The emitted secondary electrons (photo and Auger electrons) in this process may have sufficient energy to create single ionizations of the neighbouring species in the nanometric range, resulting in dense ionization tracks. It is for this reason that the soft X-rays have been shown to behave like particles with high LET.<sup>27,34</sup> The combination of core-ionization with high LET secondary electrons trigger a radiolysis that may be drastically different from what is known with photons of higher energy.

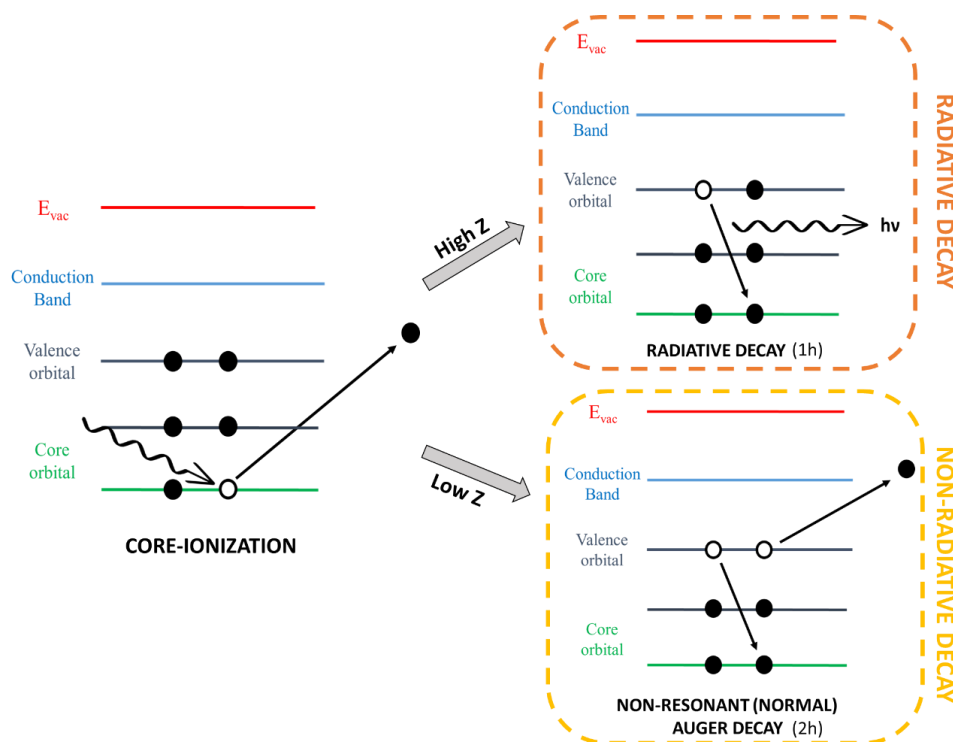


**Figure 1.4:** The absorption of the soft X-ray photons resulting in inner-shell ionization. The unstable system then stabilizes via either a radiative, resulting in 1 hole electronic final state (1h), or non-radiative normal Auger decay, resulting in two hole electronic final state (2h). The preferable pathway depends on the atomic number ( $Z$ ) of the target element.

Below a given ionization threshold, the photon energy is not enough to directly eject the core electron from the molecule like during the core-ionization process. However, a core-excitation can occur if the incident soft X-ray photons have an energy that matches the energy difference between the 1s electronic level of a given atom in the molecule and an unoccupied excited state of the same neutral molecule.<sup>35</sup> The excited molecule is thus unstable and can decay via different de-excitation pathways, shown in the figure 1.5.<sup>31,35,36</sup>

If the core-hole is filled by the electron that was excited earlier, followed by the removal of an electron from the valence orbitals, it is referred to as the participator resonant Auger decay.

It results in a final electronic state with one hole (1h) in the valence orbital (see figure 1.5).<sup>36</sup> This final state is identical to that obtained during valence ionization (1h), where a direct ejection of a valence electron takes place.<sup>36</sup>

However, if the core-hole vacancy is filled by another electron from the outer shell and the excited core-electron doesn't participate in the decay process, it is referred to as the spectator resonant Auger de-excitation. The obtained final electronic state has two holes and an excited electron (called the spectator electron), i.e. 2h1e. Moreover, the resonant electrons emitted (participator or spectator), contrary to normal Auger electrons with their kinetic energies independent of the photon energy, see their kinetic energies disperse linearly with the photon energy.<sup>37</sup>

In liquids specifically, there exists another prominent decay pathway, i.e. the ultrafast delocalization of the spectator electron in the medium.<sup>31</sup> The final state in this case is similar to the normal Auger decay (see figure 1.4).

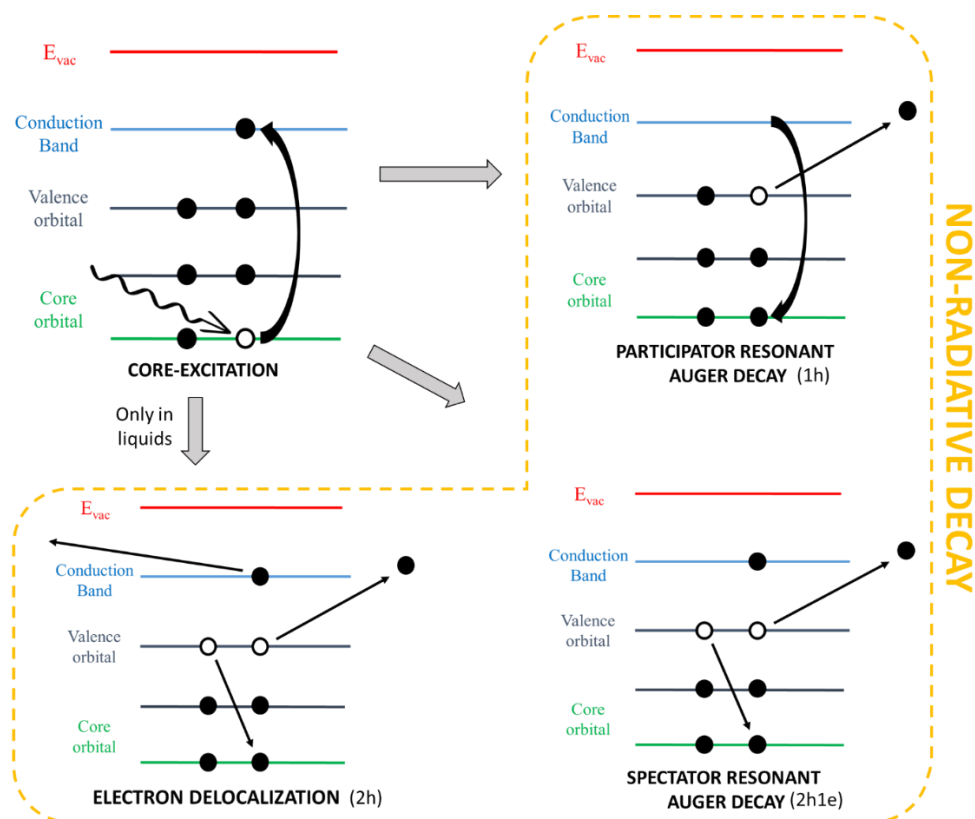


**Figure 1.5:** Various non-radiative de-excitation pathways as a result of core-excitation of the atom. The well-known pathways include the participator and spectators Auger decay. Another decay pathway that can occur in the case of liquids is the electron delocalization. For each of the de-excitation pathways, the resulting final state is mentioned.

All these relaxation pathways (after excitation or ionization) occur locally, i.e. within the originally excited or ionized molecule. However, there are certain non-local relaxation pathways that occur,<sup>38</sup> and especially in the aqueous phase (see figure 1.6). One of these is the Intermolecular Coulombic Decay (ICD), wherein the core-hole is filled by the electron from the valence shell. The energy released during this step is transferred to a neighboring molecule, which results in the ejection of its valence electron. There are other non-local relaxation pathways like electron-transfer mediated decay (ETMD) involving two or three molecules, where the core-hole vacancy is filled by the valence electron from the neighboring molecule. It is then followed by the release of another valence electron from the same neighboring species or another species adjacent to it.<sup>39</sup> It should be noted that in the case of non-local relaxation pathways, the charge is localized on different molecules.

The secondary electrons emitted from all these relaxation pathways are capable of propagating the damage in the biomolecules.

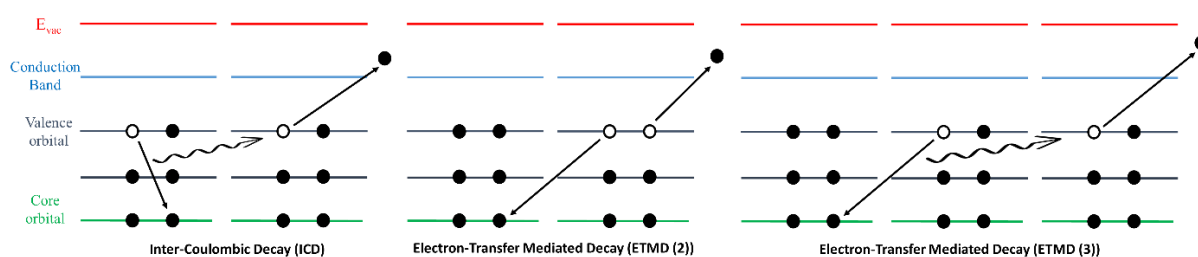


**Figure 1.6:** Non-local relaxation pathway after the core-hole creation: Inter-Coulombic Decay (ICD) in the left involving two molecules in the relaxation process. The relaxation using electron transfer mediated decay (ETMD) is shown in center and on the right, involving two and three different molecules during the decay, respectively.

### 1.2.2. Soft X-ray, a difficult radiation to work with

The soft X-ray studies in the condensed phase remain limited, primarily due to the low penetration depth of soft X-rays in the condensed medium.<sup>40</sup> The transmission of an X-ray beam in a homogeneous sample of a thickness ( $x$ ) can be expressed using the equation 1.1.

$$T = \frac{I}{I_0} = e^{-\mu x} \quad 1.1$$

$$T = e^{-\left(\frac{\mu}{\rho}\right)\rho x} \quad 1.2$$

Where  $I_0$  is the incoming photon intensity,  $I$  is the reduced intensity due to the attenuation of the photons through the sample.  $\mu$  ( $\text{cm}^{-1}$ ) is the linear attenuation coefficient that is the inverse of the attenuation length. The expression can also be written as shown in equation 1.2, where  $\mu/\rho$  is the mass attenuation coefficient and  $\rho$  ( $\text{g}/\text{cm}^3$ ) is the volumetric mass density of the sample. The mass attenuation coefficients are tabulated in the literature<sup>41</sup> for different atoms as a function of photon energy and these values can be used to calculate the mass attenuation coefficient of a compound.

The attenuation length (and thereby the mass attenuation coefficient) depends on the incident photon energy (see figure 1.7).

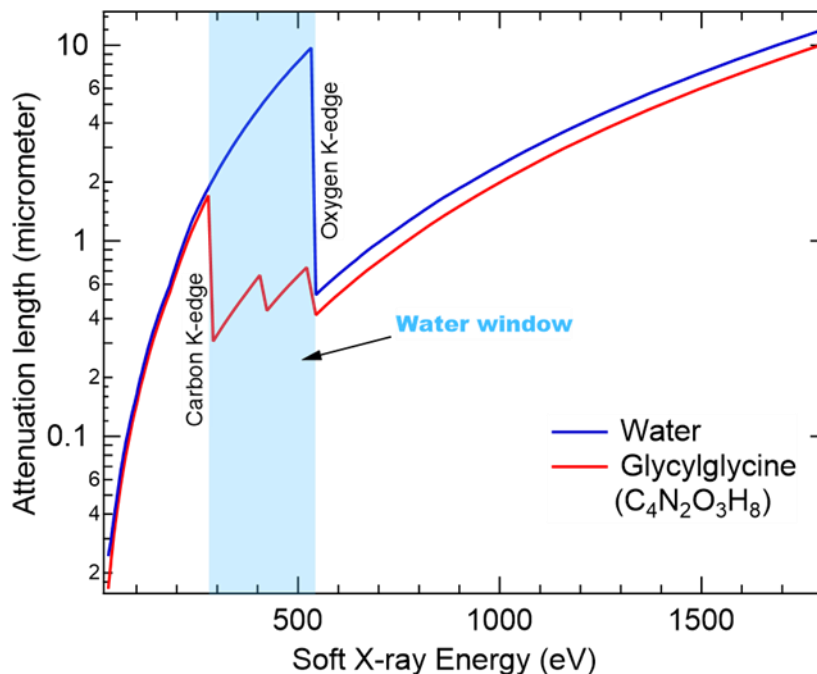


**Figure 1.7:** Attenuation length of soft X-rays in water and protein, depicting the absorption K edge of the atoms. The water window is the region between the carbon and oxygen absorption K-edges. The attenuation length were calculated using CXRO<sup>42</sup> for water and for the simplest dipeptide, Glycylglycine with the composition  $\text{C}_4\text{N}_2\text{O}_3\text{H}_8$  and density of  $1.58 \text{ g}/\text{cm}^3$ .<sup>43</sup>

Another challenge arises concerning the X-ray source. Since the discovery of X-rays, continuous effort have been made to improve the sources of X-ray. Initially, the X-ray tubes emitting characteristic X-rays (Al-K, C-K etc.) restricted the studies due to their low flux,<sup>44</sup> especially in the lower energy range of soft X-rays. However, the field of X-rays witnessed

significant advancements with the development of the second (early 1970s) and third generation (early 1990s) synchrotron light sources, and the X-ray free electron laser (XFEL) light source (early 2000s).<sup>45</sup> These technological advancements have made it possible to generate tunable X-rays with high flux, brightness, and exceptional resolving power.<sup>46</sup> Thanks to these, the field of X-ray microscopy and X-ray spectroscopy has gained a lot of attention. Laser plasma soft X-ray source is another advancing source, allowing to perform radiobiology experiments.<sup>47</sup>

### 1.2.3. Soft X rays: the right tool to investigate Direct and Indirect Effects?

Owing to the energy range of soft X-rays (0.2 – 2 keV), it is possible to decipher radiation damage caused by both effects, direct and indirect.<sup>48</sup> Almost 96 % of the biological system is made up of light atoms including carbon, nitrogen, and oxygen,<sup>49</sup> all the elements that can be specifically ionized by soft X-rays. This is because by tuning the incoming photon energies above the photoionization threshold of an atom, soft X-rays can predominantly interact with the desired atom via inner-shell ionization. For instance, if the photon energy is above the oxygen atom, the interaction majorly occurs with the water molecules, which results in the indirect effects.

Indeed, the soft X-ray energy range also offers a significant contrast between water and biomolecules, in the region between the carbon and oxygen absorption K-edges, called the 'water window'. Soft X-rays are absorbed around 10 times more in biomolecules than in pure water (see figure 1.7),<sup>50</sup> and for this reason, it is usually considered as if water is transparent to soft X-rays in the water window.<sup>51</sup> This energy range is, therefore, well-suited for studying the direct effects as well.<sup>47</sup>

### 1.3. The current understanding of the interaction of soft X-ray photons with the solvent

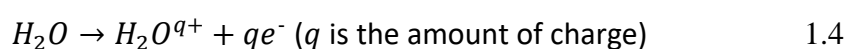
Soft X-ray indirect effects occur at the frontier of the water photolysis and water radiolysis (see figure 1.8). Concerning the photolysis of water, the irradiation of water using ultraviolet radiation (energy range below the soft X-rays), can result in an excited or singly ionized water molecule that converts to a limited number of radicals ( $^{\circ}\text{OH}$ ,  $e_{\text{aq}}^{-}$ , etc.). It has been widely studied.<sup>52,53,54,55,56,57</sup>

Water radiolysis is much more complex and can trigger a number of chemical events prior to any indirect biological damage.<sup>58,59</sup> Water radiolysis has also been studied using high energy photons (X-rays, gamma rays) and charged particles, followed by dissociation of the ionized molecules.<sup>60,61,62</sup>

It can be divided into three stages based on the timescale at which these events occur. These stages are shown for different incoming photon energies in figure 1.8. These stages have been extensively studied experimentally and theoretically for conventional radiations such as gamma rays and swift highly charged ions.<sup>63,64,62,65</sup>

The first stage is the physical stage that can last up to few femtoseconds (fs). At this stage, the interaction of photons with the water molecules leads to either their excitation or ionization (see equations 1.3 and 1.4). The second stage, the physico-chemical stage, which typically lasts for a few picoseconds (ps), accounts for the dissociation of the excited or ionized molecules and their fast recombination with neighbor molecules. The third stage, i.e. the chemical stage (up to few  $\mu$ s), accounts for the diffusion and reaction of all the species. In cells, these stages are followed by the biochemical reactions that can lead to the biological damage. Here, the resulting species from the above defined stages can react with the biomolecules (which can occur within seconds and can last for days).<sup>66</sup>

Some products ( $e_{aq}^-$ ,  $HO^\circ$ ,  $H_2O_2$ ) and reactions (equations 1.5 to 1.9) are common between the two processes (photolysis and radiolysis) and are shown in the figure 1.8.



However, the knowledge on water radiolysis/photolysis by soft X-ray photons remains scarce, as will be discussed in section 1.3.1 and as depicted in the figure 1.8.

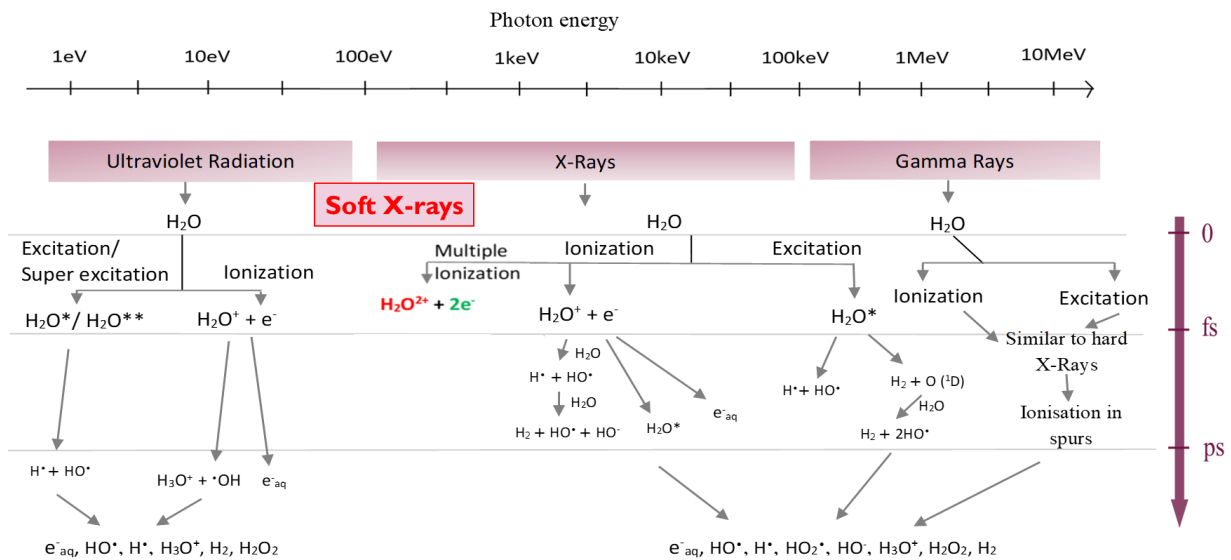


**Figure 1.8:** Interaction of photons with water: different stages involved in water radiolysis and photolysis based on the time scale of the events (adapted from Le Caër S., 2011<sup>67</sup>), resulting in species responsible for indirect radiation damage. The knowledge of dissociation of the multiply ionized water molecule using soft X-rays is scarce.

A process quite pronounced in soft X-rays and also, known to occur in the high LET projectiles, is the occurrence of multiple ionization.<sup>60</sup> In the case of 1 MeV/u carbon ions, for instance, the multiply ionized molecules account to approximately 28% of total ionization and the doubly ionized molecules represent 18% of the total ionization.<sup>68</sup> Despite a number of studies on water radiolysis, very little is known about the fate of multiply ionized  $H_2O$  molecules.

### 1.3.1. Expected radiolytic effect of soft X-rays: Multiple ionization of water

In the physical stage, the soft X-rays interact with matter dominantly via the photoelectric effect, as discussed in the section 1.2.1. In the case of irradiation of water molecules, if the incident photon energy surpasses the oxygen K-edge threshold, inner shell ionization becomes dominant. This results in an Auger decay, leading to doubly ionized water molecules along with two secondary electrons (photo and Auger electrons) (see figure 1.4). The dissociation of singly ionized water molecules in the soft X-ray energy range has been studied through  $^{\circ}OH$  yields measurements.<sup>27,40,69</sup> As mentioned, the dissociation of the doubly ionized water molecule is still not very well understood, especially in the presence of the photo and Auger

electron ionization tracks. The emitted electrons are known to have sufficient energy to create singly ionized water molecules along the ionization tracks that have nanometric scales (1 nm to 10 nm) around the multiply ionized water molecule. This results in multiple secondary electrons within the ionization track.

For the later stages (physicochemical and chemical), water radiolysis with soft X-rays has been experimentally studied in the past for Fricke dosimetry,<sup>70,71,69</sup> where the authors present the oxidation yield of the ferrous ions, using synchrotron light source. The findings have reported a decrease in the oxidation yield of ferrous ions (due to the decrease in the radical yield) as the X-ray energy decreases.<sup>71</sup> The yields of the °OH, were also studied in the soft X-ray range, using plasmid DNA strand breaks or using specific fluorescent probes sensitive to °OH.<sup>69,72,27</sup> In these studies, the production yield of the °OH is shown to decrease with an increase in photon energy up to 1 keV, reaching a minimum around 1 keV, and the yield starts to increase thereafter. In addition, these studies highlight the fact that soft X-rays behave like high-LET particles.<sup>71</sup> These studies point out the significance of the low energy electrons, i.e. the secondary electrons that produce radicals very close to each other. Around 1 keV, the tracks are very dense, leading to recombination reactions and thereby resulting in a minimum in the °OH yield.

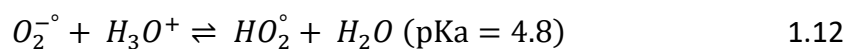
As mentioned, the fate of  $H_2O^{2+}$ , remains unexplored. Nevertheless, the studies available in the literature have explored the dissociation of  $H_2O^{2+}$  in high LET tracks, using heavy ions. These studies show that superoxide ( $HO_2^\circ$ ) is one of the resulting species when  $H_2O^{2+}$  dissociates.

### 1.3.2. Superoxide radical production from multiple ionization

Over the years, °OH was considered to be the primary species contributing in the radiation damage to biomolecules<sup>18,73</sup> and recent studies reflected the significance of low-energy electrons in causing radiation damage.<sup>74,75</sup> However,  $HO_2^\circ$  is considered as a secondary player in radiation damage, compared to °OH radicals and the low-energy electrons.<sup>76</sup> This is because superoxide is mainly produced by the reaction of dissolved oxygen and  $e_{aq}^-$  (reaction 1.11) and its contribution in radiation toxicity is usually not considered.<sup>76</sup> Depending upon the pH of the solution, superoxide can be produced in its protonated form or in the anionic form (see

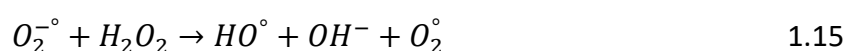
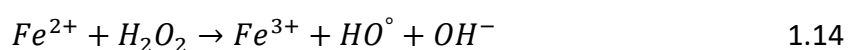


reaction 1.12). At the physiological pH ranges, the anion radical (superoxide radical) form thus dominates.



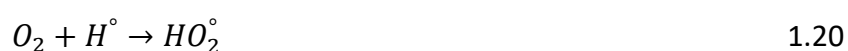
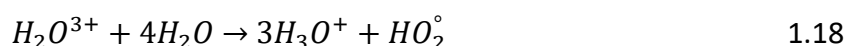
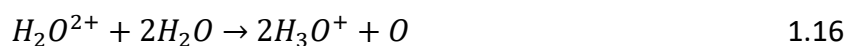
Superoxide radical is a paramagnetic species having a low reactivity.<sup>77</sup> It is one of the major products of the primary oxidase sources (for example, NADPH oxidase or respiratory chain) of reactive oxygen species (ROS).

Due to the chemical diversity in the biological system and the fact that superoxide radical can act either as an oxidant or a reductant, finding a target to either reduce or oxidize is easy for superoxide. This species has the ability to oxidize sulfite and initiate the free radical chain oxidation, thereby causing an indirect damage.<sup>78</sup> It is biologically toxic since it can inactivate the [4Fe-4S] cluster containing enzymes that play a crucial role in the metabolic pathways,<sup>79</sup> by oxidizing them at their active sites. These Fe-S clusters are of importance as they are cofactors of proteins that pose vital roles in the multicellular processes such as respiration, photosynthesis, gene regulation and nitrogen fixation.<sup>79</sup> These enzymes include fumarases A and B, dihydroxy acid dehydratase etc. that are rapidly oxidized via  $O_2^{\cdot -}$  resulting in the loss of Fe that generates hydroxyl radical, which is highly reactive, leading to what is referred to as Fenton-chemistry. In vitro,  $O_2^{\cdot -}$  acts as a reductant towards the Fe(III) and generates Fe(II), which can further reduce hydrogen peroxide (see equations 1.13 and 1.14). The overall reaction is given by equation 1.15.



This excess generation of free radicals like  $HO^{\cdot}$  under conditions of increased or uncontrolled levels of iron causes significant oxidative damage to lipids, proteins, and DNA. It can also act as a chain propagator in reactions like autoxidation of small sugars by a free radical pathway.<sup>78</sup> Therefore it is crucial to quantify the superoxide radicals generated during radiolysis because it can be toxic in the body and it is one of the main reasons for oxidative stress.<sup>80</sup>

The production of  $\text{HO}_2^\circ$  in the heavy ion radiolysis has been interpreted as the signature of the energetic processes occurring in dense tracks.<sup>81</sup> In early 1960s, Kupperman first suggested that  $\text{HO}_2^\circ$  can be produced by a reaction between a small yield of oxygen atoms and the  $^\circ\text{OH}$  in the ionization tracks (reaction 1.17).<sup>82</sup> Its yield is shown to increase as a function of LET.



In 1997, Ferradini and Jay G erin suggested that the triple ionization of water can directly result in the production of  $\text{HO}_2^\circ$  (reactions 1.18).<sup>81</sup> In addition to this, they also suggested the mechanism, earlier proposed by Kupperman, where the reaction between the O atom (formed after the dissociation of  $\text{H}_2\text{O}^{2+}$ , see reaction 1.16) and its consecutive reaction with  $^\circ\text{OH}$  radicals (formed after the dissociation of  $\text{H}_2\text{O}^+$ , see reaction 1.7) results in the  $\text{HO}_2^\circ$  production, as shown in reaction 1.17. The probability of the reaction 1.18, however, is less compared to reactions 1.16 and 1.17. The triple ionization, however, is shown to be favourable in the irradiation of gas-phase water with  $\text{Xe}^{44+}$ .<sup>81</sup>

It should be noted that the oxygen atom produced in reaction 1.16 can be in either its singlet (lowest excited state) or triplet state (ground state). The singlet and triplet states of the oxygen resulting from the doubly ionized water dissociation has been investigated using theoretical<sup>83</sup> studies (see section 1.3.3) and experimental studies.<sup>84</sup> The experimental study is based on the use of cold target recoil ion momentum spectroscopy, to discuss the dissociation of doubly ionized water molecules.<sup>84</sup> The experiments indicate two dissociation pathways of doubly ionized water molecule, one resulting in an  $\text{OH}^+$  and  $\text{H}^+$  while the other resulting in the dissociation shown in reaction 1.16. Another set of experiments<sup>81,85,86</sup> reported in the literature has shown that the superoxide formation can only occur when the oxygen is present in its triplet state. This is because the triplet state is inert with respect to water, which is not

the case for singlet oxygen. The singlet oxygen is shown to react with water, in the physico-chemical stage, resulting in the direct formation of  $\text{H}_2\text{O}_2$ .<sup>85</sup>

One must not forget that the formation of superoxide radicals can also occur via oxidation of  $\text{H}_2\text{O}_2$  using  $^{\circ}\text{OH}$  (see equation 1.19). It should be noted that the reactions 1.16, 1.17, 1.18 and 1.19 occur even in anoxic conditions (absence of molecular oxygen).

### 1.3.3. Theoretical studies to understand multiple ionization and $\text{HO}_2^{\circ}$ production

Ab-initio Molecular Dynamics (AIMD)<sup>87,61</sup> and Kinetic Monte-Carlo (KMC) simulations<sup>88,89,90,91</sup> are widely used to investigate radiolysis processes, ionization tracks and radical production. KMC simulations can allow to simulate the different stages (physical, physico-chemical and chemical). These simulations are also used to model the diffusion and reactions in the radiation-induced spurs.<sup>92</sup> However, certain input parameters, like interaction cross sections, dissociation pathways and diffusion and rate constants, are required in advance to perform such simulations. These parameters therefore have to be found experimentally or using Molecular Dynamics (MD) simulations.<sup>93,94</sup> AIMD, on the other hand, allows following the time evolution of a system comprising of few hundred atoms for up to sub-nanosecond physical timescale.<sup>95</sup> It doesn't require initial parameters, as the forces acting on the nuclei are computed by performing first-principle electronic structure calculations.<sup>96</sup> AIMD simulations are therefore a useful tool to simulate the dissociation of charged systems (like ionized water molecule) and also, to understand the effects of ROS on biomolecules embedded in water.<sup>97,98,99</sup>

To support the experimental findings, the investigation of the multiple ionization events has also been explored using simulation.<sup>21,68,81,61,100</sup> Apart from the fact that the proportion of multiple ionization events increases with the increase in the LET,<sup>60</sup> the studies for high LET ions have reported that multiple ionization is responsible for superoxide formation.<sup>81,101</sup> Studies have also pointed out that this formation occurs via the reaction between the oxygen atom and the  $^{\circ}\text{OH}$  in the ionization tracks, as shown from reaction 1.16 and 1.17.<sup>64</sup> The KMC simulations in liquid water suggest that the dissociation of the  $\text{H}_2\text{O}^{2+}$  results in the formation of two solvated protons and an oxygen atom that is left at its original location.<sup>60,68</sup> Similar conclusions have been made using the simulations, where the authors present the calculations of the triply differential cross-section for one-photon double ionization.<sup>83</sup> As

observed via the experimental studies, it has been shown using the simulations that the oxygen atom (formed in reaction 1.16), can be either in its triplet ground state or singlet state. The study points out that the radical yield of superoxide is higher when the proportion of triplet over singlet oxygen is higher, indicating the significance of triplet oxygen in the formation of  $\text{HO}_2^\circ$ .<sup>60,68</sup>

These dissociation studies, for liquid water have also been reported using the Time-Dependent Density Functional Theory (TDDFT),<sup>102</sup> and Car-Parinello Molecular Dynamics (CPMD),<sup>61</sup> where it is highlighted that the dissociation of  $\text{H}_2\text{O}^{2+}$  results in the formation of three atomic fragments within 4 fs, oxygen atom and two hydronium ions.<sup>102</sup> The probability of the oxygen atom to react with the  $^\circ\text{OH}$  to give superoxide radical is significant, due to the abundance of  $^\circ\text{OH}$  in the high LET tracks ( $2.5 \text{ H}_2\text{O}^+$ , which dissociate to give  $^\circ\text{OH}$ , within 1.5 nm sphere radius of the  $\text{H}_2\text{O}^{2+}$ ).<sup>61</sup> Additionally, the authors also precise that the simulation without multiple ionizations results in negligible superoxide production.<sup>61</sup> All these experiments as well as the simulations for heavy ions have pointed out that the multiple ionization (especially double ionization) results in the production of superoxide radical. The yield of superoxide radical in the dense ionization tracks is reported to be around  $0.005 \mu\text{mol/J}$ .<sup>103,68</sup> A significant objective of this work is to measure the yield of superoxide in the soft X-ray energy range.

#### **1.4. Spectroscopy- A good tool to study the interaction of photons with solute**

As mentioned in the previous section, the majority of radiation damage in living systems arises from indirect effects, where the radicals produced after water irradiation trigger the chemistry of the biomolecules. However, it is important to acknowledge that direct effects can also lead to severe damage. The interaction of the photons and the biomolecules follows similar stages as observed in the indirect effects.<sup>104</sup> The first stage is the physical stage, where the radiation interacts directly with the biomolecule instead of solvent water molecules, and results in its excitation or ionization within less than a femtosecond. The second stage accounts for the physical chemical events that include the fragmentation of the biomolecules, the formation of radical species and their recombination. However, the notion of track in such interactions is not used, but rather local events. Therefore, it can be noted that the timescale of direct radiation damage (starts within few fs) significantly differs from that of radiation-induced

biological damage through indirect effects (starts within few  $\mu\text{s}$ , depends upon the distance between the ionized/excited molecule and the biomolecule), as it involves the direct ionization of target biomolecules.<sup>105,106,107,108</sup>

Both, theoretically and experimentally, there are studies reporting the effect of soft X-rays on the biomolecules, either in the solid (dry) state or in the gas phase. In the solid state, there are studies reporting the decomposition of amino acids, in powder form, as a result of soft X-ray interaction.<sup>109</sup> The studies of radiation-induced damage on dry DNA plasmid (nanometer thick layer) has also been reported.<sup>110,111</sup> Studies are also reported on the DNA films, using X-ray photoelectron spectroscopy,<sup>112</sup> reporting the breakage of the DNA backbone as well as the fragmentation of nucleobases. In the gas phase, the fragmentation of glycine (a simplest amino acid), thymidine or Uracil, have been reported using the photoelectron-photoion coincidence experiments.<sup>113,114,115,116</sup>

However, these studies are scarce for biomolecules in aqueous solutions. Following the fast direct events (fs to ps) is challenging, both experimentally and theoretically. Theoretically, to monitor these effects, both MC simulation and AIMD simulation can be performed, as in the case of water radiolysis. However, owing to the large size of the biomolecules, carrying out such simulations is very demanding in terms of both, computational resources and time.<sup>117</sup> Therefore, most of the studies focus on investigating the building blocks of biomolecules. Experimentally, in recent years, there has been a sharp increase in techniques and detection methods to monitor radiation-induced effects on biomolecules, especially with the dawn of fourth generation synchrotrons. Some of these experimental techniques include spectroscopy,<sup>118,119,120</sup> microscopy,<sup>121</sup> and more. Spectroscopy can be an excellent tool to study these fast events.

#### 1.4.1. Soft X-ray spectroscopic techniques

As the dominant interaction of soft X-rays with the targeted atom is via core-shell photoionization (above the K-edge threshold of the atom) or core-excitation, they facilitate core-level spectroscopy studies.<sup>122</sup> Such studies allow the understanding of chemical bonding states of an atom (local chemical environment), the composition of the test sample, etc. To perform the core-level studies, different techniques are employed in spectroscopy. These include X-ray Photoelectron Spectroscopy (XPS) and X-ray Absorption Spectroscopy (XAS), which will be

discussed in the following sections. However, since the core-hole created during the interaction of the photon is not stable, it decays via different pathways (see figure 1.4, 1.5 and 1.6) that can be studied using Auger Electron Spectroscopy (AES) or X-ray Emission Spectroscopy (XES), which is beyond the scope of our current discussion. It must be noticed that all these techniques are concerned with the physical stage, discussing the electronic structure of the molecule and not concerning the nuclear geometry change following the X-ray absorption.

#### 1.4.1.1. X-ray Photoelectron Spectroscopy

##### 1.4.1.1.i. Principle

The technique XPS, also known as Electron Spectroscopy for Chemical Analysis (ESCA), allows the study of core hole via ionization of the electron from the core shell. XPS performed with soft X-rays is a surface-sensitive technique based on the principle of the photoelectric effect (explained in section 1.2.1). The basics of the XPS technique were already known in 1914,<sup>123</sup> however, the technique was later developed by Kai Siegbahn (Nobel Prize, 1981) and his co-workers at the University of Uppsala, in mid 1960s.<sup>124</sup>

The basics of XPS can be depicted in three main steps.

*Step 1* is the absorption of the incoming photon energy ( $h\nu$ ) by the atom and creation a photoelectron (PE) upon ionization, given the photon energy is above the absorption K-edge threshold.

*Step 2* is the fate of the PE that has a non-negligible probability to travel through the sample surface without seeing its initial kinetic energy modified. This ejected photoelectron has a certain amount of kinetic energy ( $E_k$ ) that depends on  $h\nu$  and the binding energy ( $BE$ ) of the core-shell electron and the work function of the sample ( $\varphi_{sample}$ ), which is the energy difference between the Fermi level of the sample and the vacuum level at the surface (see equation 1.22). The electrons kinetic energy is measured thanks to high-resolution electron analyzers (like the hemispherical electron analyzer explained in chapter 2). However, the measured kinetic energy  $E_{k,mes}$  is related to the work function of the analyzer ( $\varphi_{analyzer}$ ). If a good electric contact is established between the sample and the analyzer, so that their Fermi levels are aligned, the equation 1.23 holds true. This results in the equation 1.24.

$$E_k = h\nu - BE - \varphi_{sample} \quad 1.22$$

$$E_{k,mes} + \varphi_{analyzer} = E_k + \varphi_{sample} \quad 1.23$$

$$E_{k,mes} = h\nu - BE - \varphi_{analyzer} \quad 1.24$$

All electrons created in the sample also have a probability to undergo inelastic collision with the medium and lose progressively their kinetic energies.

For the range of kinetic energies of electrons released via soft X-ray ionization, the value of their inelastic mean free path (the average distance that an electron can travel in a medium without losing its energy) is small, in order of few nanometers. Also, even if this soft X-rays can penetrate few micrometers in the medium (see figure 1.7), only the electrons emitted from the extreme surface will be detected. It is why soft X-ray XPS is a surface sensitive technique, compared to conventional table top XPS, which creates more energetic electrons, due to their high energy X-ray lamps.

The escaping PE can also interact with the remaining electrons of the atom, which leads to energy loss of the PE. This is seen as low intensity peaks in the XPS spectrum, called the satellite peaks. These peaks can result either via a shake-up or shake-off processes. In the shake-up process, the PE that is being ejected can interact with the valence electron that fills the core-hole vacancy and while doing so the PE losses some of its kinetic energy. The shake-up peaks therefore appear at a higher binding energy to the main peak.<sup>125</sup> The shake-up satellite peaks provide insights on the energy difference of the occupied and the unoccupied energy states of the system.<sup>126</sup> The shake-off originate because of loss of an additional electron from the outer shell.<sup>125</sup>

*Step 3* involves the stabilization of the core-hole. When the PE is ejected, a vacancy is created in the core level. Depending upon the lifetime of the core-hole, the system relaxes by different decay mechanisms (see figures 1.4 and 1.6).

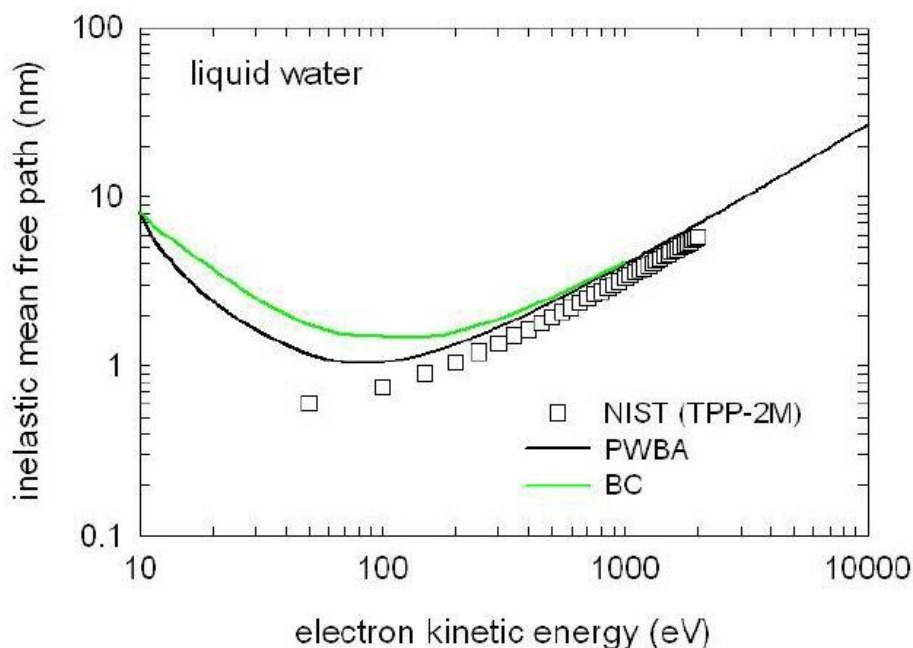


**Figure 1.9:** IMFP of electrons in liquid water. The figure is taken from the reference [127], depicting the variation in the IMFP from the energy range of 10 eV to 10 keV, using calculations.

The emitted electrons (PE and Auger electrons) have a specific inelastic mean free path (IMFP) that decreases with an increase in the pressure<sup>128</sup> and therefore, an ultra-high vacuum ( $10^{-7}$  mbar to  $10^{-10}$  mbar) is essential to perform high resolution spectroscopy measurements. It also ensures a clean sample surface. Theoretical calculations are able to predict the IMFP in the liquids<sup>127,129,130</sup> (see figure 1.9). Additionally, different measurements are reported in the literature to predict the IMFP in liquid water<sup>131,132</sup> and other aqueous salt solutions.<sup>129</sup> However, new techniques like NAP-XPS (described in Chapter 2) have made it possible to perform the XPS analysis at pressure in few 10's of mbar range in the analysis chamber.<sup>133</sup>

#### 1.4.1.1.ii. Understanding the XPS spectrum

Typically, the XPS spectra represent the intensity of the PE (counts or counts per second) as a function of  $BE$  (eV), usually decreasing from the left to the right of the horizontal axis, which can be determined from the measured PE kinetic energy by rearranging the terms in equation 1.23. The binding energy of the electron ejected from the sample is defined by the Coulombic interactions between the electrons and the nuclei. The presence of an electronegative or electropositive atom around the target atom changes the chemical environment of the atoms (changes in electronic density). This can result either in a slight increase (loss of electron) or a



decrease (gain of electron) in the  $BE$ , changing the peak position. This change in the peak position (shift in the  $BE$  of the electron) is referred to as the chemical shift or the binding energy shift.<sup>134,135,128</sup> The concept of chemical shift is one of the features that makes XPS a very powerful technique. Therefore, determining the accurate peak position for different atoms in XPS allows to distinguish the atoms in their different electronic states, characterize the unknown samples, etc. When fitting the XPS spectrum, it is therefore important to perform calibration (of both,  $h\nu$  and  $BE$ ) to accurately determine the peak position.

Another striking feature about XPS spectra is the peak intensity (or the area under the peak) that provides a quantitative information. The ratio of the different peaks indicates the ratio in which the atoms of the respective peaks are present in the system, i.e. the intensity provides the relative abundance of atoms in the system.<sup>136</sup> Additionally, by measuring the intensity of the elements at different depths of the sample (by varying the photon energy, thus the kinetic energy of the emitted electron and thus its IMFP), it is possible to disentangle the interfacial and bulk properties.<sup>137,138</sup> It should be emphasized at this point that the peak area or the intensity is a relative term. This is because not all the electrons emitted from the system are detected, due to some scattering within the molecular system or the surrounding medium.<sup>139,140</sup> Only the electrons that belong to a certain energy range determined using the selected energy value, pass energy ( $E_{pass}$ ), can go through the detector. The higher the  $E_{pass}$  value is, the larger the detected counts are and hence the higher the intensity is.<sup>141</sup> However, a higher  $E_{pass}$  also means a lower resolution. Therefore, choosing the value of  $E_{pass}$  is a compromise between the resolution and the detectable counts. Usually, a higher  $E_{pass}$  is used for survey spectra, which gives a first-hand information on the different elements present in the system. To obtain the high resolution spectrum, a low  $E_{pass}$  is then used.

XPS technique also allows to analyze the valence band spectrum (one electron removed from valence shell). It provides information about the valence electron that play a crucial role in chemical reactions,<sup>142</sup> allowing the determination of the ionization threshold<sup>1</sup> for a sample and providing insights on the density of states (DOS). This can be eventually compared to the simulation studies (for instance, Density Functional Theory, DFT).<sup>143</sup>

---

<sup>1</sup> Minimum energy required to remove electron the most loosely bound electron.

#### 1.4.1.2. X-ray absorption spectroscopy

The XAS is an absorption technique where the energy of the incoming photons is just sufficient to result in an excitation of the core-electron in one of the unoccupied electronic states, and could lead in resonant core-excitation process. It therefore allows the study of the core-hole created via excitation rather than ionization. It should be noted that the state of the system after the core-hole creation in XAS is neutral rather than being positively charged, as is the case in XPS.<sup>144</sup>

The XAS spectra present the absorption intensity as a function of photon energy.<sup>145</sup> XAS is divided into two regions of study. The first is Near Edge X-ray Absorption Fine Structure (NEXAFS), where the absorption of the photons occurs very close to the absorption edges. It provides information on the electronic structure by allowing to explore the unoccupied Molecular Orbitals (MOs).<sup>144</sup> The second is Extended X-ray Absorption Fine Structure (EXAFS), where the absorption of the photons occurs well above the absorption edges (typically 50 eV above or more) and bring information on the chemical surrounding of a specific type of atom.<sup>146</sup> The core-hole created after the excitation is stabilized by different de-excitation pathways (see figures 1.5 and 1.6). The different stages involved in generation of a NEXAFS spectrum (photo absorption, excited state creation and relaxation) can be monitored depending upon the way the NEXAFS spectrum is recorded. Partial electron yield (PEY) is one of the ways to quantify the photo-absorption stage by detecting the processes that follow the photo-absorption.<sup>147</sup> The term partial, here, refers to the fact that only the electrons with a certain kinetic energy will be detected and not all of the electrons. PEY spectra can be obtained by integrating over the KE of the 2D absorption maps (intensity of electrons as a function of KE and photon energy).<sup>148</sup>

#### 1.4.2. Studies of biomolecules using soft X-ray spectroscopic techniques

Soft X-ray photoelectron spectroscopy studies have primarily focused on studying the building blocks of biomolecules/proteins, i.e. amino acids (also referred to as the bottom-up approach) in the solid phase<sup>149,150,151</sup> as well as in the gas phase.<sup>152,153,154</sup> Similar studies have also been performed for larger biomolecules (e.g. DNA plasmids or nucleotides) where thin films of the sample were exposed to the energy source of XPS.<sup>155,156,157,158,110</sup> These studies characterize the radiation-induced fragmentation, changes in the structural and electronic properties of

the biomolecules and the single or double strand breaks of DNA, in particular. NEXAFS studies have also been carried out to characterize the radiation-induced modifications on the properties of the irradiated sample.<sup>159,160,161,162,163</sup> These studies discuss the NEXAFS spectra using partial electron yield mode and they include, for instance, the determination of the chemical state of oligonucleotide molecules before and after soft X-ray irradiation around the phosphorus (P) and sulfur (S) K-edges<sup>159</sup> or determining the electronically excited state of protonated cysteine molecule around the sulfur (S) K-edge.<sup>160</sup>

Solvation can play a crucial role in the behavior and reactivity of biomolecules. Since biomolecules are surrounded by water in real-life, studying radiation damage in liquid phase is crucial. Owing to the poor penetration soft X-rays in liquids (few  $\mu\text{m}$ , depending upon the energy) and the difficulty of using liquid samples under vacuum ( $10^{-6}$  to  $10^{-10}$  mbar), the spectroscopic studies in the liquid phase have been limited to those having a vapor pressure less than 1 Torr (performed using 'rotating disk' or 'liquid beams').<sup>164</sup> This meant a difficulty in performing spectroscopic studies of water (vapor pressure = 20 Torr at room temperature) and other aqueous samples. With the development of liquid micro jets under vacuum,<sup>165,166,167</sup> it is now possible to perform spectroscopic studies of liquids with vapor pressure higher than 1 Torr. Other setups devised for liquid phase experiments include the use of liquid cell that can be in either of the configurations, static<sup>168</sup> and flowing.<sup>169</sup> These liquid cells are mainly used for absorption studies to obtain near edge X-ray absorption fine structures (NEXAFS) and resonance measurements.<sup>170,171</sup> However the use of liquid micro jets (cylindrical) for the absorption studies provides an alternative, in addition to benefiting from the window-less X-ray absorption measurements.<sup>167</sup> Studies have also been reported for measuring liquid samples using a liquid flatjet system, for absorption studies in the transmission mode (as cylindrical jets are thicker) or for XPS studies.<sup>172</sup> The recent advancements in the field of near ambient pressure XPS (NAP-XPS) have allowed to probe the radiation induced damage to DNA and other biomolecules in near ambient pressure (few 10s of mbar) conditions, in the liquid phase.<sup>120</sup>

There are an increasing number of theoretical studies to support the XPS and XAS studies.<sup>173,151,174,46</sup> These theoretical studies use Ab-initio Molecular Dynamics (AIMD) and Hartree-Fock simulations to obtain NEXAFS spectra,<sup>175,173</sup> Auger spectra,<sup>170</sup> core-XPS spectra,<sup>176</sup> etc..

These studies shed light on various decay pathways that occur upon photon absorption or photoionization, as well as the resulting changes in physical and chemical properties. They indicate that bond cleavage and fragmentation can occur in liquids as is also observed in solid and gas phase spectroscopy. In addition, there are some changes reported in the local electronic structures influenced by the surrounding solvent molecules.<sup>150,177</sup> However, our understanding of the specific effects caused by solvation remains limited.

### 1.5. Research Objectives

Over the last century, scientists have been trying to understand the interaction of photons with matter. This has led to a great knowledge in different photon energy range including Ultraviolet (UV) light, which majorly results in excitation events, and highly penetrating electromagnetic radiations (hard X-rays or Gamma rays) that produce sparsely ionizing tracks.

As stated earlier, little is known about the poorly penetrating soft X-rays (0.2 keV – 2 keV) (lying between the UV and hard X-ray). Soft X-rays were shown to behave like high LET particles,<sup>27</sup> resulting in dense ionization tracks. Moreover, they interact dominantly via inner shell ionization and thus trigger multiple ionization events. In addition, the soft X-ray energy range holds great potential in the field of radiobiology for studying both direct and indirect effects of radiation.<sup>122</sup>

**The objective of the thesis is two-fold.**

1. The first objective is to study the indirect effects of soft X-rays, i.e. their interaction with pure water, as water plays a crucial role in radiobiology. The focus is on studying the possible formation of a radical species ( $\text{HO}_2^\circ$ ) after the reaction of the dissociation product of a doubly ionized water molecule (produced after the Auger effect, in the femtosecond timescale) with its surrounding, in the dense ionization tracks. In addition to the poor penetration of soft X-rays, the radical yield in this energy range is extremely low. To overcome these limitation, this work presents the development of a state-of-the-art highly sensitive detection technique, i.e. a microfluidic cell coupled with an in-line UV detection cell. These experiments were performed at the Metrologie beamline, SOLEIL synchrotron. A complementary theoretical AIMD simulations is also presented to understand the mechanism of the formation of  $\text{HO}_2^\circ$  in the dense tracks. This is modeled using TDDFT and CPMD methods, from femtosecond to picosecond timescale.

The following questions are addressed (in chapter 3 and 4) in the context of indirect effects:

- *What is the effect of an inner-shell ionization on water molecules upon soft X-ray irradiation in the liquid?*
- *What are the reaction pathways of doubly ionized water in soft X-ray tracks?*
- *How to measure the extremely low production yield of superoxide radicals in the soft X-ray ionization tracks?*

2. *The second objective of the thesis is to understand the direct effects of soft X-rays, i.e. their initial interaction with solvated biomolecules.* The timescale of the direct effects is different compared to the indirect effects, the former being faster. To study these ultrafast effects, the experiments performed on solvated biomolecules are presented, from the simple peptide (Glycine) to one that mimic the peptidic bond (*Glycylglycine*), using soft X-ray spectroscopy techniques (XPS and XAS). These experiments are possible thanks to *the state-of-the-art under vacuum liquid microjet setup at the PLEIADES beamline, SOLEIL synchrotron.* A study on the electronic properties of the biomolecules and how these properties are affected by solvation, is presented. A theoretical counterpart, i.e. *AIMD simulations to determine the different (Kohn-Sham) electronic states of a biomolecule embedded in liquid water,* which allows the interpretation of the resonance studies of the solvated biomolecules, is also discussed.

The following questions are addressed (in chapter 5) in the in the context of direct effects:

- *What is the effect of solvation on the electronic structure of the solute?*
- *How is the energy given to the biomolecules dissipated?*

## References

- (1) US EPA, O. *Radiation Sources and Doses*. <https://www.epa.gov/radiation/radiation-sources-and-doses> (accessed 2023-07-03).
- (2) University, © Stanford; Stanford; Complaints, C. 94305 C. *Radiation Protection Guidance For Hospital Staff – Stanford Environmental Health & Safety*. <https://ehs.stanford.edu/manual/radiation-protection-guidance-hospital-staff> (accessed 2023-05-14).
- (3) Tonnessen, B. H.; Pounds, L. Radiation Physics. *J. Vasc. Surg.* **2011**, *53* (1, Supplement), 6S-8S. <https://doi.org/10.1016/j.jvs.2010.05.138>.
- (4) 31105382023.Pdf. <https://www.iaea.org/sites/default/files/publications/magazines/bulletin/bull31-1/31105382023.pdf> (accessed 2023-06-14).
- (5) Donya, M.; Radford, M.; ElGuindy, A.; Firmin, D.; Yacoub, M. H. Radiation in Medicine: Origins, Risks and Aspirations. *Glob. Cardiol. Sci. Pract.* **2014**, *2014* (4), 437–448. <https://doi.org/10.5339/gcsp.2014.57>.
- (6) Meli, J. A. Interactions of Charged Particles: Elastic Coulomb Scattering. **2020**. [https://doi.org/10.1063/9780735421882\\_003](https://doi.org/10.1063/9780735421882_003).
- (7) Gazis, E. The Ionizing Radiation Interaction with Matter, the X-Ray Computed Tomography Imaging, the Nuclear Medicine SPECT, PET and PET-CT Tomography Imaging. In *Medical Imaging - Principles and Applications*; IntechOpen, 2019. <https://doi.org/10.5772/intechopen.84356>.
- (8) Saldaña, G.; Reyes, U.; Salazar, H.; Oscar, M.; Moreno, E.; Conde, R. High Density Devices Applied to a Gamma-Camera Implementation; 2012. <https://doi.org/10.5772/33990>.
- (9) Kharisov, B.; Kharissova, O. Main Ionizing Radiation Types and Their Interaction with Matter.; 2013.
- (10) Sharma, N. K.; Sharma, R.; Mathur, D.; Sharad, S.; Minhas, G.; Bhatia, K.; Anand, A.; Ghosh, S. P. Role of Ionizing Radiation in Neurodegenerative Diseases. *Front. Aging Neurosci.* **2018**, *10*.
- (11) Thierry-Chef, I.; Cardis, E.; Damilakis, J.; Frija, G.; Hierath, M.; Hoeschen, C. Medical Applications of Ionizing Radiation and Radiation Protection for European Patients, Population and Environment. *EPJ Nucl. Sci. Technol.* **2022**, *8*, 44. <https://doi.org/10.1051/epjn/2022044>.
- (12) 0000160760\_001.Pdf. [https://hal.science/hal-02507250v1/file/0000160760\\_001.PDF](https://hal.science/hal-02507250v1/file/0000160760_001.PDF) (accessed 2023-05-15).
- (13) Desouky, O.; Ding, N.; Zhou, G. Targeted and Non-Targeted Effects of Ionizing Radiation. *J. Radiat. Res. Appl. Sci.* **2015**, *8* (2), 247–254. <https://doi.org/10.1016/j.jrras.2015.03.003>.
- (14) Tsai, J.-Y.; Chen, F.-H.; Hsieh, T.-Y.; Hsiao, Y.-Y. Effects of Indirect Actions and Oxygen on Relative Biological Effectiveness: Estimate of DSB Induction and Conversion Induced by Gamma Rays and Helium Ions. *J. Radiat. Res. (Tokyo)* **2015**, *56* (4), 691–699. <https://doi.org/10.1093/jrr/rrv025>.
- (15) Swarts, S. G.; Gilbert, D. C.; Sharma, K. K.; Razskazovskiy, Y.; Purkayastha, S.; Naumenko, K. A.; Bernhard, W. A. Mechanisms of Direct Radiation Damage in DNA, Based on a Study of the Yields of Base Damage, Deoxyribose Damage, and Trapped Radicals in d(GCACGCGTGC)2. *Radiat. Res.* **2007**, *168* (3), 367–381. <https://doi.org/10.1667/RR1058.1>.
- (16) Swarts, S. G.; Becker, D.; Sevilla, M.; Wheeler, K. T. Radiation-Induced DNA Damage as a Function of Hydration. II. Base Damage from Electron-Loss Centers. *Radiat. Res.* **1996**, *145* (3), 304–314. <https://doi.org/10.2307/3578986>.
- (17) Becker, D.; Sevilla, M. D. 3 - The Chemical Consequences of Radiation Damage to DNA. In *Advances in Radiation Biology*; Lett, J. T., Sinclair, W. K., Eds.; Advances in Radiation

- Biology; Elsevier, 1993; Vol. 17, pp 121–180. <https://doi.org/10.1016/B978-0-12-035417-7.50006-4>.
- (18) Balasubramanian, B.; Pogożelski, W. K.; Tullius, T. D. DNA Strand Breaking by the Hydroxyl Radical Is Governed by the Accessible Surface Areas of the Hydrogen Atoms of the DNA Backbone. *Proc. Natl. Acad. Sci. U. S. A.* **1998**, *95* (17), 9738–9743. <https://doi.org/10.1073/pnas.95.17.9738>.
- (19) Singh, A.; Singh, H. Time-Scale and Nature of Radiation-Biological Damage: Approaches to Radiation Protection and Post-Irradiation Therapy. *Prog. Biophys. Mol. Biol.* **1982**, *39*, 69–107. [https://doi.org/10.1016/0079-6107\(83\)90014-7](https://doi.org/10.1016/0079-6107(83)90014-7).
- (20) Bertolet, A.; Ramos-Méndez, J.; McNamara, A.; Yoo, D.; Ingram, S.; Henthorn, N.; Warmenhoven, J.-W.; Faddegon, B.; Merchant, M.; McMahon, S. J.; Paganetti, H.; Schuemann, J. Impact of DNA Geometry and Scoring on Monte Carlo Track-Structure Simulations of Initial Radiation-Induced Damage. *Radiat. Res.* **2022**, *198* (3), 207–220. <https://doi.org/10.1667/RADE-21-00179.1>.
- (21) Meesungnoen, J. *Effect of Multiple Ionization on the Radiolysis of Liquid Water Irradiated with Heavy Ions a Theoretical Study Using Monte-Carlo Simulations*; Université de Sherbrooke, 2007.
- (22) Dikomey, E.; Dahm-Daphi, J.; Brammer, I.; Martensen, R.; Kaina, B. Correlation between Cellular Radiosensitivity and Non-Repaired Double-Strand Breaks Studied in Nine Mammalian Cell Lines. *Int. J. Radiat. Biol.* **1998**, *73* (3), 269–278. <https://doi.org/10.1080/095530098142365>.
- (23) Chatzipapas, K. P.; Papadimitroulas, P.; Emfietzoglou, D.; Kalospyros, S. A.; Hada, M.; Georgakilas, A. G.; Kagadis, G. C. Ionizing Radiation and Complex DNA Damage: Quantifying the Radiobiological Damage Using Monte Carlo Simulations. *Cancers* **2020**, *12* (4), 799. <https://doi.org/10.3390/cancers12040799>.
- (24) Richardson, D. B. Occupational Health Risks in Nuclear Power. In *Encyclopedia of Energy*; Cleveland, C. J., Ed.; Elsevier: New York, 2004; pp 489–496. <https://doi.org/10.1016/B0-12-176480-X/00439-3>.
- (25) Steel, G. G.; Down, J. D.; Peacock, J. H.; Stephens, T. C. Dose-Rate Effects and the Repair of Radiation Damage. *Radiother. Oncol. J. Eur. Soc. Ther. Radiol. Oncol.* **1986**, *5* (4), 321–331. [https://doi.org/10.1016/s0167-8140\(86\)80181-5](https://doi.org/10.1016/s0167-8140(86)80181-5).
- (26) Niemantsverdriet, M.; van Goethem, M.-J.; Bron, R.; Hogewerf, W.; Brandenburg, S.; Langendijk, J. A.; van Luijk, P.; Coppes, R. P. High and Low LET Radiation Differentially Induce Normal Tissue Damage Signals. *Int. J. Radiat. Oncol.* **2012**, *83* (4), 1291–1297. <https://doi.org/10.1016/j.ijrobp.2011.09.057>.
- (27) Huart, L.; Nicolas, C.; Kaddissy, J. A.; Guigner, J.-M.; Touati, A.; Politis, M.-F.; Mercere, P.; Gervais, B.; Renault, J.-P.; Hervé du Penhoat, M.-A. Soft X-Ray Radiation and Monte Carlo Simulations: Good Tools to Describe the Radiation Chemistry of Sub-keV Electrons. *J. Phys. Chem. A* **2020**, *124* (10), 1896–1902. <https://doi.org/10.1021/acs.jpca.9b10539>.
- (28) Bearden, J. A.; Burr, A. F. Reevaluation of X-Ray Atomic Energy Levels. *Rev. Mod. Phys.* **1967**, *39* (1), 125–142. <https://doi.org/10.1103/RevModPhys.39.125>.
- (29) Hertz, H. Ueber Sehr Schnelle Elektrische Schwingungen. *Ann. Phys.* **1887**, *267* (7), 421–448. <https://doi.org/10.1002/andp.18872670707>.
- (30) Einstein, A. Über Einen Die Erzeugung Und Verwandlung Des Lichtes Betreffenden Heuristischen Gesichtspunkt. *Ann. Phys.* **1905**, *322* (6), 132–148. <https://doi.org/10.1002/andp.19053220607>.
- (31) Brown, M. A.; Faubel, M.; Winter, B. X-Ray Photo- and Resonant Auger-Electron Spectroscopy Studies of Liquid Water and Aqueous Solutions. *Annu. Rep. Sect. C Phys. Chem.* **2009**, *105* (0), 174–212. <https://doi.org/10.1039/B803023P>.

- (32) Carley, A. F. Surface Analysis: X-Ray Photoelectron Spectroscopy. In *Encyclopedia of Materials: Science and Technology*; Buschow, K. H. J., Cahn, R. W., Flemings, M. C., Ilschner, B., Kramer, E. J., Mahajan, S., Veyssi re, P., Eds.; Elsevier: Oxford, 2001; pp 8991–8996. <https://doi.org/10.1016/B0-08-043152-6/01621-1>.
- (33) Valli res, S. Dose Enhancement with Nanoparticles in Radiotherapy Using Gold-Doxorubicin Conjugates, 2016. <https://doi.org/10.13140/RG.2.2.24027.77601>.
- (34) Huart, L. Inner Shell Ionization Effects on Molecules of Biological Interest in an Aqueous Medium. phdthesis, Sorbonne Universit , 2022. <https://tel.archives-ouvertes.fr/tel-03725615> (accessed 2022-09-02).
- (35) Sankari, A.; Str hlman, C.; Sankari, R.; Partanen, L.; Laksman, J.; Kettunen, J. A.; Galv n, I. Fdez.; Lindh, R.; Malmqvist, P.- .; Sorensen, S. L. Non-Radiative Decay and Fragmentation in Water Molecules after 1a<sub>1</sub>–14a<sub>1</sub> Excitation and Core Ionization Studied by Electron-Energy-Resolved Electron–Ion Coincidence Spectroscopy. *J. Chem. Phys.* **2020**, *152* (7), 074302. <https://doi.org/10.1063/1.5141414>.
- (36) Fogarty, R. M.; Palgrave, R. G.; Bourne, R. A.; Handrup, K.; Villar-Garcia, I. J.; Payne, D. J.; Hunt, P. A.; Lovelock, K. R. J. Electron Spectroscopy of Ionic Liquids: Experimental Identification of Atomic Orbital Contributions to Valence Electronic Structure. *Phys. Chem. Chem. Phys.* **2019**, *21* (35), 18893–18910. <https://doi.org/10.1039/C9CP02200G>.
- (37) Gel’ mukhanov, F.; Odelius, M.; Polyutov, S. P.; F hlisch, A.; Kimberg, V. Dynamics of Resonant X-Ray and Auger Scattering. *Rev. Mod. Phys.* **2021**, *93* (3), 035001. <https://doi.org/10.1103/RevModPhys.93.035001>.
- (38) Jahnke, T.; Hergenbahn, U.; Winter, B.; D rner, R.; Fr hling, U.; Demekhin, P. V.; Gokhberg, K.; Cederbaum, L. S.; Ehresmann, A.; Knie, A.; Dreuw, A. Interatomic and Intermolecular Coulombic Decay. *Chem. Rev.* **2020**, *120* (20), 11295–11369. <https://doi.org/10.1021/acs.chemrev.0c00106>.
- (39) Slav c ek, P.; Winter, B.; Cederbaum, L. S.; Kryzhevoi, N. V. Proton-Transfer Mediated Enhancement of Nonlocal Electronic Relaxation Processes in X-Ray Irradiated Liquid Water. *J. Am. Chem. Soc.* **2014**, *136* (52), 18170–18176. <https://doi.org/10.1021/ja5117588>.
- (40) Huart, L.; Nicolas, C.; Herv  du Penhoat, M.-A.; Guigner, J.-M.; Gosse, C.; Palaudoux, J.; Lefran ois, S.; Mercere, P.; Dasilva, P.; Renault, J.-P.; Chevillard, C. A Microfluidic Dosimetry Cell to Irradiate Solutions with Poorly Penetrating Radiations: A Step towards Online Dosimetry for Synchrotron Beamlines. *J. Synchrotron Radiat.* **2021**, *28* (3), 778–789. <https://doi.org/10.1107/S1600577521002691>.
- (41) Henke, B. L.; Gullikson, E. M.; Davis, J. C. X-Ray Interactions: Photoabsorption, Scattering, Transmission, and Reflection at E = 50–30,000 eV, Z = 1–92. *At. Data Nucl. Data Tables* **1993**, *54* (2), 181–342. <https://doi.org/10.1006/adnd.1993.1013>.
- (42) *X-Ray Attenuation Length*. [https://henke.lbl.gov/optical\\_constants/atten2.html](https://henke.lbl.gov/optical_constants/atten2.html) (accessed 2023-06-22).
- (43) *Glycylglycine | 556-50-3*. ChemicalBook. [https://www.chemicalbook.com/ChemicalProductProperty\\_EN\\_CB3704259.htm](https://www.chemicalbook.com/ChemicalProductProperty_EN_CB3704259.htm) (accessed 2023-07-24).
- (44) Honkim ki, V.; Sleight, J.; Suortti, P. Characteristic X-Ray Flux from Sealed Cr, Cu, Mo, Ag and W Tubes. *J. Appl. Crystallogr.* **1990**, *23* (5), 412–417. <https://doi.org/10.1107/S0021889890006082>.
- (45) Ishikawa, T. Accelerator-Based X-Ray Sources: Synchrotron Radiation, X-Ray Free Electron Lasers and Beyond. *Philos. Trans. R. Soc. Math. Phys. Eng. Sci.* **2019**, *377* (2147), 20180231. <https://doi.org/10.1098/rsta.2018.0231>.
- (46) Smith, J. W.; Saykally, R. J. Soft X-Ray Absorption Spectroscopy of Liquids and Solutions. *Chem. Rev.* **2017**, *117* (23), 13909–13934. <https://doi.org/10.1021/acs.chemrev.7b00213>.



- (47) Adjei, D.; Wiecheć, A.; Wachulak, P.; Getachew, M.; Lekki, J.; Kwiatek, W.; Bartnik, A.; Davidkova, M.; Vyšín, L.; Juha, L.; Pina, L.; Fiedorowicz, H. DNA Strand Breaks Induced by Soft X-Ray Pulses from a Compact Laser Plasma Source. *Radiat. Phys. Chem.* **2015**, *120*. <https://doi.org/10.1016/j.radphyschem.2015.11.021>.
- (48) Cornforth, M. N.; Schillaci, M. E.; Goodhead, D. T.; Carpenter, S. G.; Wilder, M. E.; Sebring, R. J.; Raju, M. R. Radiobiology of Ultrasoft X Rays: III. Normal Human Fibroblasts and the Significance of Terminal Track Structure in Cell Inactivation. *Radiat. Res.* **1989**, *119* (3), 511–522. <https://doi.org/10.2307/3577522>.
- (49) Alberts, B.; Johnson, A.; Lewis, J.; Raff, M.; Roberts, K.; Walter, P. The Chemical Components of a Cell. In *Molecular Biology of the Cell. 4th edition*; Garland Science, 2002.
- (50) Reinspach, J. High-Resolution Nanostructuring for Soft X-Ray Zone-Plate Optics. **2011**.
- (51) Kirz, J.; Jacobsen, C.; Howells, M. Soft X-Ray Microscopes and Their Biological Applications. *Q. Rev. Biophys.* **1995**, *28* (1), 33–130. <https://doi.org/10.1017/S0033583500003139>.
- (52) Sakakura, T.; Uemura, S.; Hino, M.; Kiyomatsu, S.; Takatsuji, Y.; Yamasaki, R.; Morimoto, M.; Haruyama, T. Excitation of H<sub>2</sub>O at the Plasma/Water Interface by UV Irradiation for the Elevation of Ammonia Production. *Green Chem.* **2018**, *20* (3), 627–633. <https://doi.org/10.1039/C7GC03007J>.
- (53) Li, J.; Zhang, Q.; Chen, B.; Wang, L.; Zhu, R.; Yang, J. Hydrogen Peroxide Formation in Water during the VUV/UV Irradiation Process: Impacts and Mechanisms of Selected Anions. *Environ. Res.* **2021**, *195*, 110751. <https://doi.org/10.1016/j.envres.2021.110751>.
- (54) Bulak, M.; Paardekooper, D. M.; Fedoseev, G.; Chuang, K.-J.; Terwisscha Van Scheltinga, J.; Eistrup, C.; Linnartz, H. Quantification of O<sub>2</sub> Formation during UV Photolysis of Water Ice: H<sub>2</sub>O and H<sub>2</sub>O:CO<sub>2</sub> Ices. *Astron. Astrophys.* **2022**, *657*, A120. <https://doi.org/10.1051/0004-6361/202141875>.
- (55) Nikogosyan, D. N.; Oraevsky, A. A.; Rupasov, V. I. Two-Photon Ionization and Dissociation of Liquid Water by Powerful Laser UV Radiation. *Chem. Phys.* **1983**, *77* (1), 131–143. [https://doi.org/10.1016/0301-0104\(83\)85070-8](https://doi.org/10.1016/0301-0104(83)85070-8).
- (56) Dupuy, R.; Féraud, G.; Bertin, M.; Romanzin, C.; Philippe, L.; Putaud, T.; Michaut, X.; Cimino, R.; Baglin, V.; Fillion, J.-H. Desorption of Neutrals, Cations, and Anions from Core-Excited Amorphous Solid Water. *J. Chem. Phys.* **2020**, *152*, 054711. <https://doi.org/10.1063/1.5133156>.
- (57) Svoboda, V.; Michiels, R.; LaForge, A. C.; Med, J.; Stienkemeier, F.; Slavíček, P.; Wörner, H. J. Real-Time Observation of Water Radiolysis and Hydrated Electron Formation Induced by Extreme-Ultraviolet Pulses. *Sci. Adv.* **2020**, *6* (3), eaaz0385. <https://doi.org/10.1126/sciadv.aaz0385>.
- (58) TCS-42\_web.Pdf. [https://www-pub.iaea.org/MTCD/Publications/PDF/TCS-42\\_web.pdf](https://www-pub.iaea.org/MTCD/Publications/PDF/TCS-42_web.pdf) (accessed 2023-06-14).
- (59) V, N. R. C. (US) C. on the B. E. of I. R. (BEIR. Background Information and Scientific Principles. In *Health Effects of Exposure to Low Levels of Ionizing Radiation: Beir V*; National Academies Press (US), 1990.
- (60) Gervais, B.; Beuve, M.; Olivera, G. H.; Galassi, M. E. Numerical Simulation of Multiple Ionization and High LET Effects in Liquid Water Radiolysis. *Radiat. Phys. Chem.* **2006**, *75* (4), 493–513. <https://doi.org/10.1016/j.radphyschem.2005.09.015>.
- (61) Gageot, M. P.; Vuilleumier, R.; Stia, C.; Galassi, M. E.; Rivarola, R.; Gervais, B.; Politis, M. F. A Multi-Scale Ab Initio Theoretical Study of the Production of Free Radicals in Swift Ion Tracks in Liquid Water. *J. Phys. B At. Mol. Opt. Phys.* **2007**, *40* (1), 1. <https://doi.org/10.1088/0953-4075/40/1/001>.

- (62) Appleby, A.; Schwarz, H. A. Radical and Molecular Yields in Water Irradiated by .Gamma.-Rays and Heavy Ions. *J. Phys. Chem.* **1969**, *73* (6), 1937–1941. <https://doi.org/10.1021/j100726a048>.
- (63) LaVerne, J. A. OH Radicals and Oxidizing Products in the Gamma Radiolysis of Water. *Radiat. Res.* **2000**, *153* (2), 196–200. [https://doi.org/10.1667/0033-7587\(2000\)153\[0196:ORAOP\]2.0.CO;2](https://doi.org/10.1667/0033-7587(2000)153[0196:ORAOP]2.0.CO;2).
- (64) LaVerne, J. A.; Schuler, R. H. Track Effects in the Radiolysis of Water: HO<sub>2</sub> Production by 200-800 MeV Carbon Ions. *J. Phys. Chem.* **1992**, *96* (18), 7376–7378. <https://doi.org/10.1021/j100197a044>.
- (65) Baldacchino, G.; Bouffard, S.; Balanzat, E.; Gardès-Albert, M.; Abedinzadeh, Z.; Jore, D.; Deycard, S.; Hickel, B. Direct Time-Resolved Measurement of Radical Species Formed in Water by Heavy Ions Irradiation. *Nucl. Instrum. Methods Phys. Res. Sect. B Beam Interact. Mater. At.* **1998**, *146* (1), 528–532. [https://doi.org/10.1016/S0168-583X\(98\)00463-7](https://doi.org/10.1016/S0168-583X(98)00463-7).
- (66) Camazzola, G.; Boscolo, D.; Scifoni, E.; Dorn, A.; Durante, M.; Krämer, M.; Abram, V.; Fuss, M. C. TRAX-CHEMxt: Towards the Homogeneous Chemical Stage of Radiation Damage. *Int. J. Mol. Sci.* **2023**, *24* (11), 9398. <https://doi.org/10.3390/ijms24119398>.
- (67) Le Caër, S. Water Radiolysis: Influence of Oxide Surfaces on H<sub>2</sub> Production under Ionizing Radiation. *Water* **2011**, *3* (1), 235–253. <https://doi.org/10.3390/w3010235>.
- (68) Gervais, B.; Beuve, M.; Olivera, G. H.; Galassi, M. E.; Rivarola, R. D. Production of HO<sub>2</sub> and O<sub>2</sub> by Multiple Ionization in Water Radiolysis by Swift Carbon Ions. *Chem. Phys. Lett.* **2005**, *410* (4–6), 330–334. <https://doi.org/10.1016/j.cplett.2005.05.057>.
- (69) Vyšín, L.; Wachulak, P.; Toufarová, M.; Medvedev, N.; Voronkov, R. A.; Bartnik, A.; Fiedorowicz, H.; Juha, L. Chemical Dosimetry in the “Water Window”: Ferric Ions and Hydroxyl Radicals Produced by Intense Soft X Rays. *Radiat. Res.* **2020**, *193* (4), 372–382. <https://doi.org/10.1667/RR15520.1>.
- (70) Freyer, J. P.; Schillaci, M. E.; Raju, M. R. Measurement of the G-Value for 1.5 keV X-Rays. *Int. J. Radiat. Biol.* **1989**, *56* (6), 885–892. <https://doi.org/10.1080/09553008914552361>.
- (71) Watanabe, R.; Usami, N.; Kobayashi, K. Oxidation Yield of the Ferrous Ion in a Fricke Solution Irradiated with Monochromatic Synchrotron Soft X-Rays in the 1.8-10 keV Region. *Int. J. Radiat. Biol.* **1995**, *68* (2), 113–120. <https://doi.org/10.1080/09553009514551011>.
- (72) Fulford, J.; Bonner, P.; Goodhead, D. T.; Hill, M. A.; O’Neill. Experimental Determination of the Dependence of OH Radical Yield on Photon Energy: A Comparison with Theoretical Simulations. *J. Phys. Chem. A* **1999**, *103* (51), 11345–11349. <https://doi.org/10.1021/jp993087n>.
- (73) Hahn, M. B.; Dietrich, P. M.; Radnik, J. In Situ Monitoring of the Influence of Water on DNA Radiation Damage by Near-Ambient Pressure X-Ray Photoelectron Spectroscopy. *Commun. Chem.* **2021**, *4* (1), 1–8. <https://doi.org/10.1038/s42004-021-00487-1>.
- (74) Alizadeh, E.; Sanz, A. G.; García, G.; Sanche, L. Radiation Damage to DNA: The Indirect Effect of Low Energy Electrons. *J. Phys. Chem. Lett.* **2013**, *4* (5), 820–825. <https://doi.org/10.1021/jz4000998>.
- (75) Alizadeh, E.; Orlando, T. M.; Sanche, L. Biomolecular Damage Induced by Ionizing Radiation: The Direct and Indirect Effects of Low-Energy Electrons on DNA. *Annu. Rev. Phys. Chem.* **2015**, *66* (1), 379–398. <https://doi.org/10.1146/annurev-physchem-040513-103605>.
- (76) Rajpal, A.; Huart, L.; Nicolas, C.; Chevillard, C.; Guigner, J.-M.; Dasilva, P.; Mercere, P.; Gervais, B.; Hervé du Penhoat, M.-A.; Renault, J.-P. Superoxide Production under Soft X-Ray Irradiation of Liquid Water. *J. Phys. Chem. B* **2023**, *127* (19), 4277–4285. <https://doi.org/10.1021/acs.jpcc.3c00932>.
- (77) Krumova, K.; Cosa, G. Chapter 1 Overview of Reactive Oxygen Species. **2016**, 1–21. <https://doi.org/10.1039/9781782622208-00001>.

- (78) 5\_Superoxide-Radical-and-Superoxide-Dismutases.Pdf.
- (79) The Impact of O(2) on the Fe-S Cluster Biogenesis .Pdf.
- (80) Giacco, F.; Brownlee, M. Oxidative Stress and Diabetic Complications. *Circ. Res.* **2010**, *107* (9), 1058–1070. <https://doi.org/10.1161/CIRCRESAHA.110.223545>.
- (81) Ferradini, C.; Jay-Gerin, J.-P. DOES MULTIPLE IONIZATION INTERVENE FOR THE PRODUCTION OF HO<sub>2</sub> RADICALS IN HIGH-LET LIQUID WATER RADIOLYSIS? 5.
- (82) Appleby, A.; Schwarz, H. A. Radical and Molecular Yields in Water Irradiated by  $\gamma$ -Rays and Heavy Ions. *J. Phys. Chem.* **1969**, *73* (6), 1937–1941. <https://doi.org/10.1021/j100726a048>.
- (83) Streeter, Z. L.; Yip, F. L.; Lucchese, R. R.; Gervais, B.; Rescigno, T. N.; McCurdy, C. W. Dissociation Dynamics of the Water Dication Following One-Photon Double Ionization. I. Theory. *Phys. Rev. A* **2018**, *98* (5), 053429. <https://doi.org/10.1103/PhysRevA.98.053429>.
- (84) Reedy, D.; Williams, J. B.; Gaire, B.; Gatton, A.; Weller, M.; Menssen, A.; Bauer, T.; Henrichs, K.; Burzynski, Ph.; Berry, B.; Streeter, Z. L.; Sartor, J.; Ben-Itzhak, I.; Jahnke, T.; Dörner, R.; Weber, Th.; Landers, A. L. Dissociation Dynamics of the Water Dication Following One-Photon Double Ionization. II. Experiment. *Phys. Rev. A* **2018**, *98* (5), 053430. <https://doi.org/10.1103/PhysRevA.98.053430>.
- (85) Taube, H. Photochemical Reactions of Ozone in Solution. *Trans. Faraday Soc.* **1957**, *53*, 656. <https://doi.org/10.1039/tf9575300656>.
- (86) Amichai, O.; Treinin, A. Chemical Reactivity of O(3P) Atoms in Aqueous Solution. *Chem. Phys. Lett.* **1969**, *3* (8), 611–613. [https://doi.org/10.1016/0009-2614\(69\)85123-7](https://doi.org/10.1016/0009-2614(69)85123-7).
- (87) Iftimie, R.; Minary, P.; Tuckerman, M. E. Ab Initio Molecular Dynamics: Concepts, Recent Developments, and Future Trends. *Proc. Natl. Acad. Sci.* **2005**, *102* (19), 6654–6659. <https://doi.org/10.1073/pnas.0500193102>.
- (88) Spothem-Maurizot, M.; Davidková, M. Radiation Damage to DNA in DNA–Protein Complexes. *Mutat. Res. Mol. Mech. Mutagen.* **2011**, *711* (1), 41–48. <https://doi.org/10.1016/j.mrfmmm.2011.02.003>.
- (89) Baba, K.; Kusumoto, T.; Okada, S.; Ishikawa, M. A Simulation-Based Study on Water Radiolysis Species for 1H<sup>+</sup>, 4He<sup>2+</sup>, and 12C<sup>6+</sup> Ion Beams with Multiple Ionization Using Geant4-DNA. *J. Appl. Phys.* **2021**, *129* (24), 244702. <https://doi.org/10.1063/5.0054665>.
- (90) Bernal, M. A.; Bordage, M. C.; Brown, J. M. C.; Davidková, M.; Delage, E.; El Bitar, Z.; Enger, S. A.; Francis, Z.; Guatelli, S.; Ivanchenko, V. N.; Karamitros, M.; Kyriakou, I.; Maigne, L.; Meylan, S.; Murakami, K.; Okada, S.; Payno, H.; Perrot, Y.; Petrovic, I.; Pham, Q. T.; Ristic-Fira, A.; Sasaki, T.; Štěpán, V.; Tran, H. N.; Villagrasa, C.; Incerti, S. Track Structure Modeling in Liquid Water: A Review of the Geant4-DNA Very Low Energy Extension of the Geant4 Monte Carlo Simulation Toolkit. *Phys. Med.* **2015**, *31* (8), 861–874. <https://doi.org/10.1016/j.ejmp.2015.10.087>.
- (91) Plante, I. A Monte-Carlo Step-by-Step Simulation Code of the Non-Homogeneous Chemistry of the Radiolysis of Water and Aqueous Solutions. Part I: Theoretical Framework and Implementation. *Radiat. Environ. Biophys.* **2011**, *50*, 389–403. <https://doi.org/10.1007/s00411-011-0367-8>.
- (92) Clifford, P.; Green, N. J. B.; Pilling, M. J. Monte Carlo Simulation of Diffusion and Reaction in Radiation-Induced Spurs. Comparisons with Analytic Models. *J. Phys. Chem.* **1982**, *86* (8), 1322–1327. <https://doi.org/10.1021/j100397a022>.
- (93) Frongillo, Y.; Goulet, T. MONTE CARLO SIMULATION OF FAST ELECTRON AND PROTON TRACKS IN LIQUID WATER—II. NONHOMOGENEOUS CHEMISTRY.
- (94) Battaile, C. C.; Srolovitz, D. J.; Butler, J. E. A Kinetic Monte Carlo Method for the Atomic-Scale Simulation of Chemical Vapor Deposition: Application to Diamond. *J. Appl. Phys.* **1997**, *82* (12), 6293–6300. <https://doi.org/10.1063/1.366532>.

- (95) He, X.; Zhu, Y.; Epstein, A.; Mo, Y. Statistical Variances of Diffusional Properties from Ab Initio Molecular Dynamics Simulations. *Npj Comput. Mater.* **2018**, *4* (1), 1–9. <https://doi.org/10.1038/s41524-018-0074-y>.
- (96) Andrade, X.; Castro, A.; Zueco, D.; Alonso, J. L.; Echenique, P.; Falceto, F.; Rubio, A. A Modified Ehrenfest Formalism for Efficient Large-Scale Ab Initio Molecular Dynamics. *J. Chem. Theory Comput.* **2009**, *5* (4), 728–742. <https://doi.org/10.1021/ct800518j>.
- (97) Hervé du Penhoat, M.-A.; Hamila, A.; Gageot, M.-P.; Vuilleumier, R.; Fujii, K.; Yokoya, A.; Politis, M.-F. Ab Initio Molecular Dynamics Simulations to Interpret the Molecular Fragmentation Induced in Deoxyribose by Synchrotron Soft X-Rays. *Quantum Beam Sci.* **2019**, *3* (4), 24. <https://doi.org/10.3390/qubs3040024>.
- (98) Omar, K. A.; Hasnaoui, K.; de la Lande, A. First-Principles Simulations of Biological Molecules Subjected to Ionizing Radiation. *Annu. Rev. Phys. Chem.* **2021**, *72* (1), 445–465. <https://doi.org/10.1146/annurev-physchem-101419-013639>.
- (99) Kohanoff, J.; McAllister, M.; Tribello, G. A.; Gu, B. Interactions between Low Energy Electrons and DNA: A Perspective from First-Principles Simulations. *J. Phys. Condens. Matter* **2017**, *29* (38), 383001. <https://doi.org/10.1088/1361-648X/aa79e3>.
- (100) Meesungnoen, J.; Filali-Mouhim, A.; Ayudhya, N. S. N.; Mankhetkorn, S.; Jay-Gerin, J.-P. Multiple Ionization Effects on the Yields of HO<sub>2</sub>/O<sub>2</sub><sup>-</sup> and H<sub>2</sub>O<sub>2</sub> Produced in the Radiolysis of Liquid Water with High-LET 12C<sup>6+</sup> Ions: A Monte-Carlo Simulation Study. *Chem. Phys. Lett.* **2003**, *377* (3), 419–425. [https://doi.org/10.1016/S0009-2614\(03\)01101-1](https://doi.org/10.1016/S0009-2614(03)01101-1).
- (101) Olivera, G. H.; Caraby, C.; Jardin, P.; Cassimi, A.; Adoui, L.; Gervais, B. Multiple Ionization in the Earlier Stages of Water Radiolysis. *Phys. Med. Biol.* **1998**, *43* (8), 2347–2360. <https://doi.org/10.1088/0031-9155/43/8/025>.
- (102) Tavernelli, I.; Gageot, M. P.; Vuilleumier, R.; Stia, C.; Du Penhoat, M. A. H.; Politis, M. F. Time-Dependent Density Functional Theory Molecular Dynamics Simulations of Liquid Water Radiolysis. *ChemPhysChem* **2008**, *9* (14), 2099–2103. <https://doi.org/10.1002/cphc.200800177>.
- (103) Baldacchino, G.; Deycard, S. Direct Observation of HO<sub>2</sub>/O<sub>2</sub><sup>-</sup> Free Radicals Generated in Water by a High-Line Energy Transfer Pulsed Heavy-Ion Beam. 6.
- (104) 38544\_Lopez\_Tarifa\_Pablo.Pdf. [https://repositorio.uam.es/bitstream/handle/10486/6364/38544\\_Lopez\\_Tarifa\\_Pablo.pdf?sequence=1](https://repositorio.uam.es/bitstream/handle/10486/6364/38544_Lopez_Tarifa_Pablo.pdf?sequence=1) (accessed 2023-07-04).
- (105) Hieda, K. DNA Damage Induced by Vacuum and Soft X-Ray Photons from Synchrotron Radiation. 7.
- (106) Raju, M. R.; Carpenter, S. G.; Chmielewski, J. J.; Schillaci, M. E.; Wilder, M. E.; Freyer, J. P.; Johnson, N. F.; Schor, P. L.; Sebring, R. J.; Goodhead, D. T. Radiobiology of Ultrasoft X Rays: I. Cultured Hamster Cells (V79). *Radiat. Res.* **1987**, *110* (3), 396–412. <https://doi.org/10.2307/3577007>.
- (107) Fayard, B.; Touati, A.; Abel, F.; Penhoat, M. A. H. du; Despiney-Bailly, I.; Gobert, F.; Ricoul, M.; L'Hoir, A.; Politis, M. F.; Hill, M. A.; Stevens, D. L.; Sabatier, L.; Sage, E.; Goodhead, D. T.; Chetioui, A. Cell Inactivation and Double-Strand Breaks: The Role of Core Ionizations, as Probed by Ultrasoft X Rays. *Radiat. Res.* **2002**, *157* (2), 128–140. [https://doi.org/10.1667/0033-7587\(2002\)157\[0128:CIADSB\]2.0.CO;2](https://doi.org/10.1667/0033-7587(2002)157[0128:CIADSB]2.0.CO;2).
- (108) Herve du Penhoat, M. A.; Fayard, B.; Abel, F.; Touati, A.; Gobert, F.; Despiney-Bailly, I.; Ricoul, M.; Sabatier, L.; Stevens, D. L.; Hill, M. A.; Goodhead, D. T.; Chetioui, A. Lethal Effect of Carbon K-Shell Photoionizations in Chinese Hamster V79 Cell Nuclei: Experimental Method and Theoretical Analysis. *Radiat. Res.* **1999**, *151* (6), 649–658.

- (109) Zubavichus et al. - 2004 - Soft X-Ray-Induced Decomposition of Amino Acids A.Pdf. [http://xrm.phys.northwestern.edu/research/pdf\\_papers/2004/zubavichus\\_radiation\\_2004.pdf](http://xrm.phys.northwestern.edu/research/pdf_papers/2004/zubavichus_radiation_2004.pdf) (accessed 2023-07-26).
- (110) Fromm, M.; Boulanouar, O. Low Energy Electrons and Ultra-Soft X-Rays Irradiation of Plasmid DNA. Technical Innovations. *Radiat. Phys. Chem.* **2016**, *128*, 44–53. <https://doi.org/10.1016/j.radphyschem.2016.05.025>.
- (111) Touati, A.; Penhoat, M.; Fayard, B.; Champion, C.; Abel, F.; Gobert, F.; Lamoureux, M.; Politis, M.; Martins, L.; Ricoul, M.; Sabatier, L.; Sage, E.; Chetioui, A. Biological Effects Induced by K Photo-Ionisation in and near Constituent Atoms of DNA. *Radiat. Prot. Dosimetry* **2002**, *99*, 83–84. <https://doi.org/10.1093/oxfordjournals.rpd.a006845>.
- (112) Ptasinska, S.; Stypczynska, A.; Nixon, T.; Mason, N.; Klyachko, D.; Sanche, L. X-Ray Induced Damage in DNA Monitored by X-Ray Photoelectron Spectroscopy. *J. Chem. Phys.* **2008**, *129*, 065102. <https://doi.org/10.1063/1.2961027>.
- (113) Chiarinelli, J.; Bolognesi, P.; Domaracka, A.; Rousseau, P.; Castrovilli, M. C.; Richter, R.; Chatterjee, S.; Wang, F.; Avaldi, L. Insights into the Dissociative Ionization of Glycine by PEPICO Experiments. *Phys. Chem. Chem. Phys.* **2018**, *20* (35), 22841–22848. <https://doi.org/10.1039/C8CP03473G>.
- (114) Itälä, E.; Kooser, K.; Rachlew, E.; Huels, M. A.; Kukk, E. Soft X-Ray Ionization Induced Fragmentation of Glycine. *J. Chem. Phys.* **2014**, *140* (23), 234305. <https://doi.org/10.1063/1.4882648>.
- (115) Itälä, E.; Huels, M. A.; Rachlew, E.; Kooser, K.; Hägerth, T.; Kukk, E. A Comparative Study of Dissociation of Thymidine Molecules Following Valence or Core Photoionization. *J. Phys. B At. Mol. Opt. Phys.* **2013**, *46* (21), 215102. <https://doi.org/10.1088/0953-4075/46/21/215102>.
- (116) Itälä, E.; Ha, D. T.; Kooser, K.; Nömmiste, E.; Joost, U.; Kukk, E. Fragmentation Patterns of Core Ionized Uracil. *Int. J. Mass Spectrom.* **2011**, *306* (1), 82–90. <https://doi.org/10.1016/j.ijms.2011.07.006>.
- (117) Haag, N.; Liu, B.; Nielsen, S. B.; Zettergren, H.; Hvelplund, P.; Manil, B.; Huber, B. A.; Johansson, H. A. B.; Schmidt, H. T.; Cederquist, H. Collisions with Biomolecules Embedded in Small Water Clusters. *J. Phys. Conf. Ser.* **2009**, *194* (1), 012053. <https://doi.org/10.1088/1742-6596/194/1/012053>.
- (118) Nag, N.; Sasidharan, S.; Saudagar, P.; Tripathi, T. Chapter 1 - Fundamentals of Spectroscopy for Biomolecular Structure and Dynamics. In *Advanced Spectroscopic Methods to Study Biomolecular Structure and Dynamics*; Saudagar, P., Tripathi, T., Eds.; Academic Press, 2023; pp 1–35. <https://doi.org/10.1016/B978-0-323-99127-8.00002-7>.
- (119) Balog, E. R. M. Chapter 8 - Spectroscopic Investigation of Biomolecular Dynamics Using Light Scattering Methods. In *Advanced Spectroscopic Methods to Study Biomolecular Structure and Dynamics*; Saudagar, P., Tripathi, T., Eds.; Academic Press, 2023; pp 211–226. <https://doi.org/10.1016/B978-0-323-99127-8.00011-8>.
- (120) Hahn, M. B.; Dietrich, P. M.; Radnik, J. In Situ Monitoring of the Influence of Water on DNA Radiation Damage by Near-Ambient Pressure X-Ray Photoelectron Spectroscopy. *Commun. Chem.* **2021**, *4* (1), 1–8. <https://doi.org/10.1038/s42004-021-00487-1>.
- (121) Pu, S.; Gong, C.; Robertson, A. W. Liquid Cell Transmission Electron Microscopy and Its Applications. *R. Soc. Open Sci.* **2020**, *7* (1), 191204. <https://doi.org/10.1098/rsos.191204>.
- (122) Smith, N. V. Science with Soft X-Rays. *Phys. Today* **2000**, *54* (1).
- (123) Hagström, S.; Nordling, C.; Siegbahn, K. Electron Spectroscopy for Chemical Analyses. *Phys. Lett.* **1964**, *9*, 235–236. [https://doi.org/10.1016/0031-9163\(64\)90062-9](https://doi.org/10.1016/0031-9163(64)90062-9).

- (124) Siegbahn, K. *ESCA; Atomic, Molecular and Solid State Structure Studied by Means of Electron Spectroscopy*; Nova acta Regiae Societatis Scientiarum Upsaliensis; Almqvist & Wiksells: Uppsala, 1967.
- (125) Persson, P.; Lunell, S.; Szöke, A.; Ziaja, B.; Hajdu, J. Shake-up and Shake-off Excitations with Associated Electron Losses in X-Ray Studies of Proteins. *Protein Sci. Publ. Protein Soc.* **2001**, *10* (12), 2480–2484.
- (126) Bancroft, G. M.; Boyd, B. D.; Creber, D. K. Shake-up Satellite Structure in the x-Ray Photoelectron Spectra (ESCA) of Metal Hexacarbonyls. *Inorg. Chem.* **1978**, *17* (4), 1008–1013. <https://doi.org/10.1021/ic50182a042>.
- (127) Nikjoo, H.; Uehara, S.; Emfietzoglou, D.; Brahme, A. Heavy Charged Particles in Radiation Biology and Biophysics. *New J. Phys.* **2008**, *10*, 075006. <https://doi.org/10.1088/1367-2630/10/7/075006>.
- (128) Boucly, A. Catalytical Reactions and Environmental Chemistry Modifications as Seen by Synchrotron Radiation NAP-XPS.
- (129) Olivieri, G.; Parry, K. M.; Powell, C. J.; Tobias, D. J.; Brown, M. A. Quantitative Interpretation of Molecular Dynamics Simulations for X-Ray Photoelectron Spectroscopy of Aqueous Solutions. *J. Chem. Phys.* **2016**, *144* (15), 154704. <https://doi.org/10.1063/1.4947027>.
- (130) Emfietzoglou, D.; Kyriakou, I.; Garcia-Molina, R.; Abril, I. Inelastic Mean Free Path of Low-Energy Electrons in Condensed Media: Beyond the Standard Models. *Surf. Interface Anal.* **2017**, *49* (1), 4–10. <https://doi.org/10.1002/sia.5878>.
- (131) Thürmer, S.; Seidel, R.; Faubel, M.; Eberhardt, W.; Hemminger, J. C.; Bradforth, S. E.; Winter, B. Photoelectron Angular Distributions from Liquid Water: Effects of Electron Scattering. *Phys. Rev. Lett.* **2013**, *111* (17), 173005. <https://doi.org/10.1103/PhysRevLett.111.173005>.
- (132) Gadeyne, T.; Zhang, P.; Schild, A.; Wörner, H. J. Low-Energy Electron Distributions from the Photoionization of Liquid Water: A Sensitive Test of Electron Mean Free Paths. *Chem. Sci.* **2022**, *13* (6), 1675–1692. <https://doi.org/10.1039/D1SC06741A>.
- (133) Salmeron, M.; Schlogl, R. Ambient Pressure Photoelectron Spectroscopy: A New Tool for Surface Science and Nanotechnology. *Surf. Sci. Rep.* **2008**, *63* (4), 169–199. <https://doi.org/10.1016/j.surfrep.2008.01.001>.
- (134) Ramirez, L. P. Electronic Structure of Interfaces Studied by in Situ Real-Time XPS.
- (135) Dao, A. T. N.; Mott, D. M.; Maenosono, S. Characterization of Metallic Nanoparticles Based on the Abundant Usages of X-Ray Techniques. In *Handbook of Nanoparticles*; Aliofkhazraei, M., Ed.; Springer International Publishing: Cham, 2016; pp 217–244. [https://doi.org/10.1007/978-3-319-15338-4\\_13](https://doi.org/10.1007/978-3-319-15338-4_13).
- (136) Shard, A. G. Practical Guides for X-Ray Photoelectron Spectroscopy: Quantitative XPS. *J. Vac. Sci. Technol. A* **2020**, *38* (4), 041201. <https://doi.org/10.1116/1.5141395>.
- (137) Gray, A. X.; Papp, C.; Ueda, S.; Balke, B.; Yamashita, Y.; Plucinski, L.; Minár, J.; Braun, J.; Ylvisaker, E. R.; Schneider, C. M.; Pickett, W. E.; Ebert, H.; Kobayashi, K.; Fadley, C. S. Probing Bulk Electronic Structure with Hard X-Ray Angle-Resolved Photoemission. *Nat. Mater.* **2011**, *10* (10), 759–764. <https://doi.org/10.1038/nmat3089>.
- (138) Powell, C. J. Practical Guide for Inelastic Mean Free Paths, Effective Attenuation Lengths, Mean Escape Depths, and Information Depths in x-Ray Photoelectron Spectroscopy. *J. Vac. Sci. Technol. A* **2020**, *38* (2), 023209. <https://doi.org/10.1116/1.5141079>.
- (139) Travnikova, O.; Patanen, M.; Söderström, J.; Lindblad, A.; Kas, J. J.; Vila, F. D.; Céolin, D.; Marchenko, T.; Goldsztejn, G.; Guillemin, R.; Journal, L.; Carroll, T. X.; Børve, K. J.; Declava, P.; Rehr, J. J.; Mårtensson, N.; Simon, M.; Svensson, S.; Sæthre, L. J. Energy-Dependent Relative Cross Sections in Carbon 1s Photoionization: Separation of Direct Shake and

- Inelastic Scattering Effects in Single Molecules. *J. Phys. Chem. A* **2019**, *123* (35), 7619–7636. <https://doi.org/10.1021/acs.jpca.9b05063>.
- (140) Nordlund, D.; Ogasawara, H.; Bluhm, H.; Takahashi, O.; Odelius, M.; Nagasono, M.; Pettersson, L. G. M.; Nilsson, A. Probing the Electron Delocalization in Liquid Water and Ice at Attosecond Time Scales. *Phys. Rev. Lett.* **2007**, *99* (21), 217406. <https://doi.org/10.1103/PhysRevLett.99.217406>.
- (141) Crist, B. V. *FWHM Peak-width vs Pass Energy (ER)*. The XPS Library of Monochromatic XPS Spectra. <https://xpslibrary.com/fwhm-peak-width-vs-pass-energy-er/> (accessed 2023-06-25).
- (142) Seidel, R.; Winter, B.; Bradforth, S. E. Valence Electronic Structure of Aqueous Solutions: Insights from Photoelectron Spectroscopy. *Annu. Rev. Phys. Chem.* **2016**, *67* (1), 283–305. <https://doi.org/10.1146/annurev-physchem-040513-103715>.
- (143) Krishna, D. N. G.; Philip, J. Review on Surface-Characterization Applications of X-Ray Photoelectron Spectroscopy (XPS): Recent Developments and Challenges. *Appl. Surf. Sci. Adv.* **2022**, *12*, 100332. <https://doi.org/10.1016/j.apsadv.2022.100332>.
- (144) Duncan, D. A. Synchrotron-Based Spectroscopy In On-Surface Polymerization of Covalent Networks. In *Encyclopedia of Interfacial Chemistry*; Wandelt, K., Ed.; Elsevier: Oxford, 2018; pp 436–445. <https://doi.org/10.1016/B978-0-12-409547-2.13768-0>.
- (145) *Core Level Spectroscopy*. <https://www-ssrl.slac.stanford.edu/nilssongroup/corelevel.html> (accessed 2023-06-23).
- (146) *Extended X-ray absorption fine structure (EXAFS) - Online Dictionary of Crystallography*. [https://dictionary.iucr.org/Extended\\_X-ray\\_absorption\\_fine\\_structure\\_\(EXAFS\)](https://dictionary.iucr.org/Extended_X-ray_absorption_fine_structure_(EXAFS)) (accessed 2023-06-23).
- (147) *Scattering Methods for Condensed Matter Research: Towards Novel Applications at Future Sources*; Angst, M., Forschungszentrum Jülich, Eds.; Lecture notes of the ... IFF spring school; Forschungszentrum Jülich: Jülich, 2012.
- (148) Miteva, T.; Kryzhevoi, N. V.; Sisourat, N.; Nicolas, C.; Pokapanich, W.; Saisopa, T.; Songsiriritthigul, P.; Rattanachai, Y.; Dreuw, A.; Wenzel, J.; Palaudoux, J.; Öhrwall, G.; Püttner, R.; Cederbaum, L. S.; Rueff, J.-P.; Céolin, D. The All-Seeing Eye of Resonant Auger Electron Spectroscopy: A Study on Aqueous Solution Using Tender X-Rays. *J. Phys. Chem. Lett.* **2018**, *9* (15), 4457–4462. <https://doi.org/10.1021/acs.jpcllett.8b01783>.
- (149) Bozack, M. J.; Zhou, Y.; Worley, S. D. Structural Modifications in the Amino Acid Lysine Induced by Soft X-ray Irradiation. *J. Chem. Phys.* **1994**, *100* (11), 8392–8398. <https://doi.org/10.1063/1.466786>.
- (150) Yang, C.; Meng, Y.; Xie, B.; Xia, S. Impacts of Solvation on Photo-Damage of Polypeptides: Modulation and Biological Implications. *J. Photochem. Photobiol. B* **2021**, *220*, 112214. <https://doi.org/10.1016/j.jphotobiol.2021.112214>.
- (151) Clark, D. T.; Peeling, J.; Colling, L. An Experimental and Theoretical Investigation of the Core Level Spectra of a Series of Amino Acids, Dipeptides and Polypeptides. *Biochim. Biophys. Acta BBA - Protein Struct.* **1976**, *453* (2), 533–545. [https://doi.org/10.1016/0005-2795\(76\)90149-5](https://doi.org/10.1016/0005-2795(76)90149-5).
- (152) V, F.; O, P.; R, R.; M, C.; Kc, P.; V, C. Photoemission and Photoabsorption Spectroscopy of Glycyl-Glycine in the Gas Phase. *J. Phys. Chem. A* **2009**, *113* (40). <https://doi.org/10.1021/jp906843j>.
- (153) Zhang, W.; Carravetta, V.; Plekan, O.; Feyer, V.; Richter, R.; Coreno, M.; Prince, K. C. Electronic Structure of Aromatic Amino Acids Studied by Soft X-Ray Spectroscopy. *J. Chem. Phys.* **2009**, *131* (3), 035103. <https://doi.org/10.1063/1.3168393>.

- (154) Li, H.; Hua, W.; Lin, Z.; Luo, Y. First-Principles Study on Core-Level Spectroscopy of Arginine in Gas and Solid Phases. *J. Phys. Chem. B* **2012**, *116* (42), 12641–12650. <https://doi.org/10.1021/jp302309u>.
- (155) Kummer, K.; Vyalikh, D. V.; Gavrila, G.; Preobrajenski, A. B.; Kick, A.; Bönsch, M.; Mertig, M.; Molodtsov, S. L. Electronic Structure of Genomic DNA: A Photoemission and X-Ray Absorption Study. *J. Phys. Chem. B* **2010**, *114* (29), 9645–9652. <https://doi.org/10.1021/jp1013237>.
- (156) Xiao, F.; Luo, X.; Fu, X.; Zheng, Y. Cleavage Enhancement of Specific Chemical Bonds in DNA by Cisplatin Radiosensitization. *J. Phys. Chem. B* **2013**, *117* (17), 4893–4900. <https://doi.org/10.1021/jp400852p>.
- (157) Kundu, S.; Schaible, M. J.; McKee, A. D.; Orlando, T. M. Direct Damage of Deoxyadenosine Monophosphate by Low-Energy Electrons Probed by X-Ray Photoelectron Spectroscopy. *J. Phys. Chem. B* **2020**, *124* (9), 1585–1591. <https://doi.org/10.1021/acs.jpcc.9b08971>.
- (158) Rosenberg, R. A.; Symonds, J. M.; Vijayalakshmi, K.; Mishra, D.; Orlando, T. M.; Naaman, R. The Relationship between Interfacial Bonding and Radiation Damage in Adsorbed DNA. *Phys. Chem. Chem. Phys.* **2014**, *16* (29), 15319–15325. <https://doi.org/10.1039/C4CP01649A>.
- (159) Narita, A.; Fujii, K.; Baba, Y.; Shimoyama, I. Use of a DNA Film on a Self-Assembled Monolayer for Investigating the Physical Process of DNA Damage Induced by Core Electron Ionization. *Int. J. Radiat. Biol.* **2016**, *92* (11), 733–738. <https://doi.org/10.1080/09553002.2016.1179812>.
- (160) Gopakumar, G.; Svensson, P. H. W.; Grånäs, O.; Brena, B.; Schwob, L.; Unger, I.; Saak, C.-M.; Timm, M.; Bülow, C.; Kubin, M.; Zamudio-Bayer, V.; Lau, J. T.; von Issendorff, B.; Abid, A. R.; Lindblad, A.; Danielsson, E.; Koerfer, E.; Coleman, C.; Björneholm, O.; Lindblad, R. X-Ray Induced Fragmentation of Protonated Cystine. *J. Phys. Chem. A* **2022**, *126* (9), 1496–1503. <https://doi.org/10.1021/acs.jpca.1c10158>.
- (161) Zubavichus, Y.; Shaporenko, A.; Grunze, M.; Zharnikov, M. Innershell Absorption Spectroscopy of Amino Acids at All Relevant Absorption Edges. *J. Phys. Chem. A* **2005**, *109* (32), 6998–7000. <https://doi.org/10.1021/jp0535846>.
- (162) Zubavichus, Y.; Zharnikov, M.; Schaporenko, A.; Grunze, M. NEXAFS Study of Glycine and Glycine-Based Oligopeptides. *J. Electron Spectrosc. Relat. Phenom.* **2004**, *134* (1), 25–33. <https://doi.org/10.1016/j.elspec.2003.09.006>.
- (163) Plekan, O.; Feyer, V.; Richter, R.; Coreno, M.; de Simone, M.; Prince, K. C.; Carravetta, V. An X-Ray Absorption Study of Glycine, Methionine and Proline. *J. Electron Spectrosc. Relat. Phenom.* **2007**, *155* (1), 47–53. <https://doi.org/10.1016/j.elspec.2006.11.004>.
- (164) Siegbahn, H.; Siegbahn, K. ESCA Applied to Liquids. *J. Electron Spectrosc. Relat. Phenom.* **1973**, *2* (3), 319–325. [https://doi.org/10.1016/0368-2048\(73\)80023-4](https://doi.org/10.1016/0368-2048(73)80023-4).
- (165) Faubel, M.; Steiner, B.; Toennies, J. P. Photoelectron Spectroscopy of Liquid Water, Some Alcohols, and Pure Nonane in Free Micro Jets. *J. Chem. Phys.* **1997**, *106* (22), 9013–9031. <https://doi.org/10.1063/1.474034>.
- (166) Muccignat, D. L.; Stokes, P. W.; Cocks, D. G.; Gascooke, J. R.; Jones, D. B.; Brunger, M. J.; White, R. D. Simulating the Feasibility of Using Liquid Micro-Jets for Determining Electron–Liquid Scattering Cross-Sections. *Int. J. Mol. Sci.* **2022**, *23* (6), 3354. <https://doi.org/10.3390/ijms23063354>.
- (167) Winter, B. Liquid Microjet for Photoelectron Spectroscopy. *Nucl. Instrum. Methods Phys. Res. Sect. Accel. Spectrometers Detect. Assoc. Equip.* **2009**, *601* (1–2), 139–150. <https://doi.org/10.1016/j.nima.2008.12.108>.
- (168) Guo, J.-H.; Kastanov, S.; Soderstrom, J.; Glans, P.-A.; West, M.; Learmonth, T.; Chiou, J.-W.; Luo, Y.; Nordgren, J.; Smith, K.; Pong, W.-F.; Cheng, H.; Griffiss, J. M. Electronic Structure



- Study of the Bases in DNA Duplexes by in Situ Photon-in/Photon-out Soft X-Ray Spectroscopy. *J. Electron Spectrosc. Relat. Phenom.* **2010**, *181* (2), 197–201. <https://doi.org/10.1016/j.elspec.2010.05.014>.
- (169) Nappini, S.; D'Amario, L.; Favaro, M.; Dal Zilio, S.; Salvador, F.; Betz-Güttner, E.; Fondacaro, A.; Piš, I.; Romanzin, L.; Gambitta, A.; Bondino, F.; Lazzarino, M.; Magnano, E. Soft X-Ray Spectroscopies in Liquids and at Solid–Liquid Interface at BACH Beamline at Elettra. *Rev. Sci. Instrum.* **2021**, *92* (1), 015115. <https://doi.org/10.1063/5.0025326>.
- (170) Liegener, C. -M.; Bakhshi, A. K.; Chen, R.; Ladik, J. Theoretical Auger Spectra of the Glycine Ion in Solution. *J. Chem. Phys.* **1987**, *86* (11), 6039–6045. <https://doi.org/10.1063/1.452492>.
- (171) Reinert and Geurts - Eingereicht Am 18.08.2016 Bei Der Fakultät Für Ph.Pdf. [https://opus.bibliothek.uni-wuerzburg.de/opus4-wuerzburg/frontdoor/deliver/index/docId/14711/file/Benkert\\_Andreas\\_glycine.pdf](https://opus.bibliothek.uni-wuerzburg.de/opus4-wuerzburg/frontdoor/deliver/index/docId/14711/file/Benkert_Andreas_glycine.pdf) (accessed 2023-06-05).
- (172) Ekimova, M.; Quevedo, W.; Faube, M.; Wernet, P.; Nibbering, E. A Liquid Flatjet System for Solution Phase Soft-x-Ray Spectroscopy. *Struct. Dyn.* **2015**, *2*. <https://doi.org/10.1063/1.4928715>.
- (173) Wilks, R. G.; MacNaughton, J. B.; Kraatz, H.-B.; Regier, T.; Blyth, R. I. R.; Moewes, A. Comparative Theoretical and Experimental Study of the Radiation-Induced Decomposition of Glycine. *J. Phys. Chem. A* **2009**, *113* (18), 5360–5366. <https://doi.org/10.1021/jp900794v>.
- (174) Rehr, J. J.; Albers, R. C. Theoretical Approaches to X-Ray Absorption Fine Structure. *Rev. Mod. Phys.* **2000**, *72* (3), 621–654. <https://doi.org/10.1103/RevModPhys.72.621>.
- (175) Sanchez-Gonzalez, A.; Barillot, T. R.; Squibb, R. J.; Kolorenč, P.; Agaker, M.; Averbukh, V.; Bearpark, M. J.; Bostedt, C.; Bozek, J. D.; Bruce, S.; Montero, S. C.; Coffee, R. N.; Cooper, B.; Cryan, J. P.; Dong, M.; Eland, J. H. D.; Fang, L.; Fukuzawa, H.; Guehr, M.; Ilchen, M.; Johnsson, A. S.; Liekhus-S, C.; Marinelli, A.; Maxwell, T.; Motomura, K.; Mucke, M.; Natan, A.; Osipov, T.; Östlin, C.; Pernpointner, M.; Petrovic, V. S.; Robb, M. A.; Sathe, C.; Simpson, E. R.; Underwood, J. G.; Vacher, M.; Walke, D. J.; Wolf, T. J. A.; Zhaunerchyk, V.; Rubensson, J.-E.; Berrah, N.; Bucksbaum, P. H.; Ueda, K.; Feifel, R.; Frasiniski, L. J.; Marangos, and J. P. Auger Electron and Photoabsorption Spectra of Glycine in the Vicinity of the Oxygen K-Edge Measured with an X-FEL. *J. Phys. B At. Mol. Opt. Phys.* **2015**, *48* (23), 234004. <https://doi.org/10.1088/0953-4075/48/23/234004>.
- (176) C. Castrovilli, M.; Bolognesi, P.; Bodo, E.; Mattioli, G.; Cartoni, A.; Avaldi, L. An Experimental and Theoretical Investigation of XPS and NEXAFS of 5-Halouracils. *Phys. Chem. Chem. Phys.* **2018**, *20* (9), 6657–6667. <https://doi.org/10.1039/C8CP00026C>.
- (177) Freiwald, M.; Cramm, S.; Eberhardt, W.; Eisebitt, S. Soft X-Ray Absorption Spectroscopy in Liquid Environments. *J. Electron Spectrosc. Relat. Phenom.* **2004**, *137–140*, 413–416. <https://doi.org/10.1016/j.elspec.2004.02.165>.



## CONTENTS CHAPTER 2

---

<b>Chapter 2: Materials and Methods</b> .....	<b>40</b>
<b>2.1. Chemical products</b> .....	<b>47</b>
<b>2.2. Gamma irradiation</b> .....	<b>48</b>
2.2.1. Gamma dosimetry .....	49
<b>2.3. Synchrotron Soft X-ray irradiation</b> .....	<b>51</b>
2.3.1. Synchrotron light source .....	51
2.3.2. SOLEIL Beamlines.....	53
2.3.2.1. METROLOGIE beamline.....	53
2.3.2.2. TEMPO beamline.....	54
2.3.2.3. PLEIADES beamline.....	55
<b>2.4. Experimental set and analysis techniques</b> .....	<b>56</b>
2.4.1. In-air beam extraction at METROLOGIE beamline: IRAD setup .....	56
2.4.2. Microfluidic cell design and set-up.....	58
2.4.2.1. Original cell design .....	59
2.4.2.2. Microfluidic set-up .....	60
2.4.3. Optical Interferometry.....	61
2.4.4 UV-visible spectrophotometry .....	62
2.4.4.1. Principle.....	62
2.4.4.2. Off-line UV analysis .....	63
2.4.4.2.i. Absorbance measurements in transmission .....	63
2.4.4.2.ii. Absorbance measurements in reflectance.....	64
2.4.4.3. Post-processing.....	64
2.4.4.3.i. Absorbance to Yield .....	64
2.4.4.3.ii. Band gap measurement.....	65

2.4.5. XPS analysis.....	65
2.4.5.1. Hemispherical electron analyzer.....	66
2.4.5.2. Solid XPS.....	67
2.4.5.2.i. Setup.....	67
2.4.5.2.ii. Data acquisition and calibration method.....	67
2.4.5.3. NAP-XPS.....	67
2.4.5.4. Liquid microjet XPS.....	69
2.4.5.4.i. Setup.....	69
2.4.5.4.ii. Data treatment and Calibration.....	71
<b>2.5. Theoretical methods .....</b>	<b>73</b>
2.5.1. General concepts.....	73
2.5.1.1. Classical Molecular Dynamics.....	73
2.5.1.2. Ab-Initio Molecular Dynamics.....	75
2.5.1.3. Born-Oppenheimer approximation .....	76
2.5.1.4. Born-Oppenheimer molecular dynamics.....	77
2.5.1.5. Car–Parrinello Molecular Dynamics .....	78
2.5.1.6. Density Functional Theory.....	78
2.5.1.7. Plane-wave basis set .....	80
2.5.1.8. Concept of Pseudopotential.....	81
2.5.1.9. Time-Dependent Density Functional Theory.....	82
2.5.1.10. Ehrenfest-TDDFT .....	83
2.5.2. Modelling the doubly ionized species .....	83
2.5.2.1. The investigated systems and computational details .....	83
2.5.2.2. Preparation of the system prior to double ionization.....	85
2.5.2.3. Modeling the prepared systems .....	87
2.5.2.4. Data analysis .....	90
2.5.2.2.i. Bader charge analysis.....	90
2.5.2.2.ii. Density of states calculation.....	91
2.5.2.2.iii. Trajectory/Geometrical analysis .....	91
2.5.2.5. Typical CPU time.....	92
<b>References.....</b>	<b>93</b>

## Chapter 2: Materials and Methods

This chapter provides a comprehensive overview of the chemicals, irradiation sources, and various experimental techniques used in this thesis. We describe the different synchrotron beamlines where the experiments were conducted and briefly discuss the methods of detecting the superoxide radical, determining the yield, and calculating the dose and its uncertainty. Additionally, we discuss the computational approaches employed in this work, as well as the choice of our simulation systems.

**Table 2.1:** List of chemicals used in the thesis, along with their specification, brand name and reference.

Chemical	Brand name	Reference
Ferrous Ammonium Sulfate, ACS reagent, 99%	Sigma-Aldrich	215406
NaCl, ACS reagent, $\geq 99.0\%$	Sigma-Aldrich	S9888
Sulphuric acid ( $H_2SO_4$ )	Sigma-Aldrich	ARK2197
Cytochrome C from bovine heart ( $\geq 95\%$ , powder, $-20^\circ C$ )	Sigma-Aldrich	C3131
Water Soluble Tetrazole Salt (WST8), 99.67%	MedChemExpress	HY-D0831
Phosphate buffer solution (1 M, pH = 7.4 at $25^\circ C$ )	Sigma-Aldrich	P3619-1GA
Superoxide Dismutase (SOD) from bovine erythrocytes ( $\geq 3,000$ units/mg protein, BioReagent, lyophilized powder)	Sigma-Aldrich	S5395
Catalase from bovine liver ( lyophilized powder, $\geq 10,000$ units/mg protein)	Sigma-Aldrich	232-577-1
Ethanol (Laboratory Reagent, 96%)	Sigma-Aldrich	200-578-6
Potassium Chloride (KCl) (ACS reagent, 99.0-100.5%)	Sigma-Aldrich	231-211-8
Glycine ( BioUltra, for molecular biology, $\geq 99.0\%$ , 1.03 g/mL at $20^\circ C$ )	Sigma-Aldrich	200-272-2
Glycylglycine ( BioUltra, $\geq 99.5\%$ )	Sigma-Aldrich	209-127-8
Barium Sulphate ( $BaSO_4$ ) (ReagentPlus <sup>®</sup> , 99%)	Sigma-Aldrich	231-784-4

**Table 2.2:** List of devices/instruments used in the thesis, along with their specifications and supplier.

Product	Supplier	Specification
<i>Devices</i>		
Millex-GP Syringe Filter Unit	Sigma Aldrich (Ref: SLGP033RS)	Polyethersulfone, 0.22 $\mu\text{m}$ pore size syringe filter, 10 bar max. inlet pressure and 45 $^{\circ}\text{C}$ max temperature
Captair Pyramid: Transportable glove bag	Erlab	US patent no. 6851769
Gammacell <sup>®</sup> 3000	Best Theratronics	Cesium-137 gamma source
Silicon frame with silicon nitride window for 'Exit window)	FASTEC, Northampton, UK	Silicon frame = 10 $\times$ 10 $\text{mm}^2$ , 500 $\mu\text{m}$ thick and Silicon nitride window = 1 $\text{mm} \times$ 1 $\text{mm}$ , 150 $\text{nm}$ thick
YAG:Ce crystal	Crytur, Turnov, Czech Republic	50 $\mu\text{m}$ thick Scintillator crystal
CCD camera	AcA2500-20gm, Basler, Ahrensburg, Germany	High quality imaging used in this work to record beam shape
Photodiode	International Radiation Detector, Torrance, California, USA	AXUV-100G Ti/C Coating ( $\sim 190 \pm 19$ $\text{nm}$ Titanium, $\sim 50 \pm 5$ $\text{nm}$ Carbon and $\sim 7$ $\text{nm}$ Silicon dioxide films)
x-z Translation table	Brétigny/Orge, France	Standard translation table, AXMO, MNT9 model, 0.2 $\text{mm}$ precise
Optical level	Wild HeerBrugg, Heerbrugg, Switzerland	
Silicon chip for microfluidic cell without $\text{Si}_3\text{N}_4$ membrane	Silson, Southam, UK	6 $\text{mm} \times$ 3 $\text{mm}$ large, 200 $\mu\text{m}$ thick silicon chip
Silicon chip for microfluidic cell with $\text{Si}_3\text{N}_4$ membrane	Silson, Southam, UK	6 $\text{mm} \times$ 3 $\text{mm}$ large, 200 $\mu\text{m}$ thick silicon chip with 300 $\mu\text{m} \times$ 1 $\text{mm}$ $\text{Si}_3\text{N}_4$ membrane (low internal stress, $\leq 250$ $\text{MPa}$ )
Metal holder for microfluidic cell	Gavard, Arrou, France	polytetrafluoroethylene, PTFE 2.8 $\text{cm} \times$ 4.2 $\text{cm}$

Microfluidic devices (pressure controller, flowmeters, M-switch, PEEK or Teflon tube)	FLUIGENT smart microfluidics	Details of the products are available on the website of fluigent
Optical interferometer	Smart WLI Schaefer GmbH, Germany	Used for performing interferometry measurements
Quartz cuvette	Hellma Analytics	1mm path length, High Precision cell
Integrating sphere	Shimadzu (Ref: ISR-2600PLUS)	Measurement of solid samples using a UV-VIS spectrophotometer
UV spectrophotometer	Shimadzu	UV-2550
Laboratory XPS		Kratos AIX ULTRA DLD spectrometer A monochromatic Al K $\alpha$ X-ray source (1486.6 eV, 150 W)
Hemispherical analyzer	SPECS Scienta	Phoibos 150 VG-Scienta R4000WA
Silicon photomultiplier (SiPM)	KETEK GmbH <sup>1</sup>	PM3315-WB active area of 3 × 3 mm <sup>2</sup>
Electronic card	KETEK GmbH	PEPCB-EVAL-MCX-P
Deuterium-Tungsten Halogen Source	Ocean Insights	DH2000 wavelength range: 190 nm – 2500 nm
QE Pro spectrometer	IDIL Fibres Optiques	Efficient analog to digital converter (18 bit) - allows the measurement of a variation of 1/262144 in optical intensity (minimal measurable optical density of 2.10 <sup>-5</sup> )
In-line UV detection cell	IDIL fibre Optiques	SMA-Z Cell, FIA Z cell series Optical path = 2.5 mm
PTFE AF mini degassing chamber	imChem (Ref: P3105)	PEEK chamber including a gas permeable Teflon tube. Standard 100 $\mu$ l systec AF degassing chamber, 0,5 mL/min Not compatible to hexanes and other alkanes
<i>Softwares</i>		
Microfluidic Automation tool: MAT', and 'All In One (A.i.O)'	FLUIGENT smart microfluidics	MAT: for developing and running time based protocols and A.i.O: For

		real time control of pressure and flow rates, version 19.0.0.1
OceanView	Ocean Insights	Software for spectroscopy application. Copyright © 2013 Ocean Optics, Version 1.6.7 and version 2.0
IGOR pro	WaveMetrics	Scientific Data analysis, Version 9.01
UVprobe	Shimadzu	Multifunctional UV spectroscopy software, Version 2.70, Copyright ©1998-2018 Shimadzu Corporation
CasaXPS	Casa Software Ltd	Processing Software for XPS and more, Version 2.3.24, Copyright © 1999-2021 Casa Software Ltd
UCSF Chimera	Regents of the University of California	Version 1.16, copyright 2000-2020 by Regents of the University of California
Gromacs	University of Groningen, Uppsala universite	High-performance molecular dynamics package, Version 2020.1
<i>Computing platform</i>		
MeSU	HPCaVe group Sorbonne University, France	Used computing resources: Alpha, Beta
Occigen	GENCI/CINES	HPE Cray EX4000
Jean-Zay	GENCI/IDRIS	HPE SGI 8600



## 2.1. Chemical products

For the experiments performed in the oxic condition (aerated), samples were prepared in air, at room temperature. The list of the samples used in this work is mentioned below and is also presented in the table 2.1 along with the references. For the anoxic condition, samples were prepared in a transportable glove bag (see table 2.2 for reference), under an argon atmosphere. The samples were kept under the argon atmosphere for approximately 3 hours, filtered, put in the sample tube, capped, sealed with paraffin. The samples are then ready for the irradiation.

**Fricke solution:** Air-saturated Fricke solution (1 mM  $(\text{NH}_4)\text{Fe}_2(\text{SO}_4)_2$ , 0.4 M  $\text{H}_2\text{SO}_4$ , 1 mM NaCl) was prepared using high-purity ferrous ammonium sulfate, NaCl and sulphuric acid, in triple distilled water. The solution was covered in aluminum foil to avoid the degradation in light.<sup>2</sup>

**Phosphate buffer:** 1 M, pH 7.4 (25 °C) phosphate buffer solution was used. It was diluted to 10 mM using Milli-Q water and it was used to maintain the pH of the samples.

**Ferri-Cytochrome C:** Solution of cytochrome C (from bovine heart) was prepared with varying concentrations (7.7  $\mu\text{M}$ , 15.4  $\mu\text{M}$ , 23.1  $\mu\text{M}$ , 30.8  $\mu\text{M}$ , 46.2  $\mu\text{M}$  and 61.5  $\mu\text{M}$ ) in 10 mM Phosphate buffer. The solutions were filtered using the Millex-GP Syringe Filter Unit (0.22  $\mu\text{m}$ , polyethersulfone). They were used as a chemical probe for superoxide detection. The molar extinction coefficient ( $\epsilon$ ) of cytochrome C was 106,100  $\text{M}^{-1}\text{cm}^{-1}$  and 27,700  $\text{M}^{-1}\text{cm}^{-1}$  at 410 nm and 550 nm, respectively.<sup>3,4,5</sup>

**Water Soluble Tetrazole Salt (WST8):** WST8<sup>6</sup> was also used as a chemical probe for superoxide detection. All WST8 aqueous solutions, from 100  $\mu\text{M}$  to 500  $\mu\text{M}$ , were prepared in Milli-Q water. The solutions were filtered using the Millex-GP Syringe Filter Unit (0.22  $\mu\text{m}$ , polyethersulfone). The pH of the solutions was measured to be 5. The molar extinction coefficient ( $\epsilon$ ) of WST8 was 30,700  $\text{M}^{-1}\text{cm}^{-1}$  at 460 nm.<sup>7</sup>

**Superoxide Dismutase (SOD):** The enzyme, SOD (from bovine erythrocytes), was used to dismutate superoxide radical anions. Solution of concentration 0.15  $\mu\text{M}$  to 3.1  $\mu\text{M}$  were prepared in phosphate buffer.

**Catalase:** Catalase from bovine liver<sup>8,9</sup> (0.15  $\mu\text{M}$  to 3.1  $\mu\text{M}$ ) was used to dismutate hydrogen peroxide.

**Sodium Chloride (NaCl):** Sodium Chloride was used as an OH scavenger in the chemical detection system.

**Ethanol:** Ethanol was used as an OH scavenger in the chemical detection system.

**Potassium Chloride (KCl):** 50 mM KCl solution was used as a reference solution in XPS measurements. Its solution was prepared in Milli-Q water.

**Glycine:** The powdered form of Glycine was used for solid XPS. 1 M of Glycine was prepared in 50 mM KCl solution, for liquid XPS. The solution had a pH of 7 at 22 °C.

**Glycylglycine:** The powdered form of Glycylglycine was used for solid XPS. 1 M solution of glycylglycine was prepared in 50 mM KCl solution, for liquid XPS. The solution had a pH of 7 at 22 °C.

**Barium Sulphate (BaSO<sub>4</sub>):** BaSO<sub>4</sub> was used as a reference for performing solid state UV analysis.

## 2.2. Gamma irradiation

In this work, gamma rays were used as a reference radiation. All the gamma irradiation experiments were performed using a Cesium-137 gamma source (Gammacell® 3000, *Best Theratronics*)<sup>10</sup> available at LIONS, CEA Saclay, France. Cesium-137, discovered in the late 1930s by Glenn T. Seaborg and his coworker, Margaret Melhase, undergoes a radioactive decay by beta emission and gamma radiations to Barium-137. The energy of the emitted gamma rays is 662 keV.<sup>11</sup>

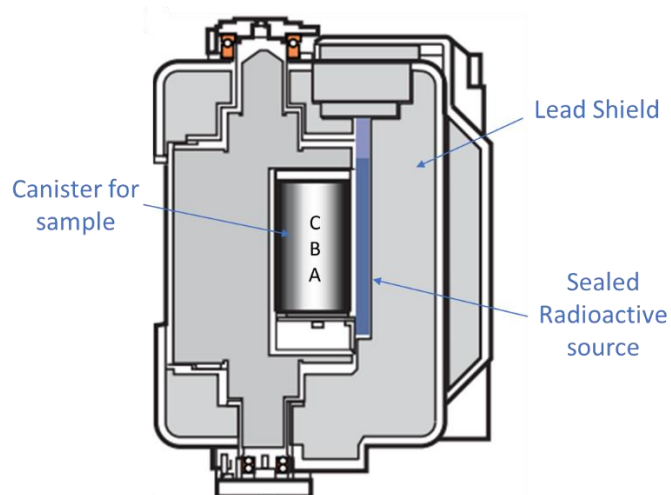


**Figure 2.1:** Side view of Gammacell® 3000<sup>10</sup>. The samples can be placed in the canister for irradiation. Positions A, B and C (not to scale) in the canister refer to the three different heights at which the sample was placed for irradiation.

As Cesium-137 gamma rays have a high penetration and are dangerous to human health, the design of the Gammacell is such that the sealed Cs-137 source is shielded by lead (Pb). The sample to be irradiated is placed in a canister. The entire design can be seen in figure 2.1.

### 2.2.1. Gamma dosimetry

The Cs-137 radionuclide has a half-life of 30.07 years.<sup>12</sup> The dose rate of the source thus changes with time. In addition, depending upon the height of the sample in the canister, the dose received by the sample varies. Therefore, to determine the dose delivered to the solutions by the source, a Fricke dosimeter was used.

The Fricke solution is a standard chemical dosimetry solution. Fricke dosimetry is also referred to as ferrous sulphate dosimetry, because the process involves the oxidation of ferrous ions ( $\text{Fe}^{2+}$ ) to ferric ions ( $\text{Fe}^{3+}$ ) upon irradiation. The Fricke solution was irradiated in glass vials, placed at three different heights in the canister: positions A (6 cm), B (9 cm) and C (13 cm). The absorbance of the oxidized Fricke solution, i.e.  $\text{Fe}^{3+}$ , can be measured by the increase in the UV signal at 304nm. The dose delivered to the sample can be estimated using equation (2.1),

$$D = \frac{\Delta A}{\varepsilon_{\text{Fe}^{3+}}^{304 \text{ nm}} G(\text{Fe}^{3+}) \rho l} \quad 2.1$$

where  $\Delta A$  is the difference between the measured absorbance of irradiated and non-irradiated samples,  $G(\text{Fe}^{3+})$  is the radiation chemical yield of ferric ions, i.e.  $1.55 \times 10^{-6}$  mol/J and  $\varepsilon_{\text{Fe}^{3+}}^{304 \text{ nm}}$  is the molar extinction coefficient of ferric ions at 304 nm, which is equal to  $2174 \text{ M}^{-1}\text{cm}^{-1}$ .<sup>2,13</sup> The density of the solution,  $\rho$ , is  $1.023 \text{ g.cm}^{-3}$  at  $25^\circ\text{C}$  and the path length of the UV cell,  $l$ , is 1 cm.

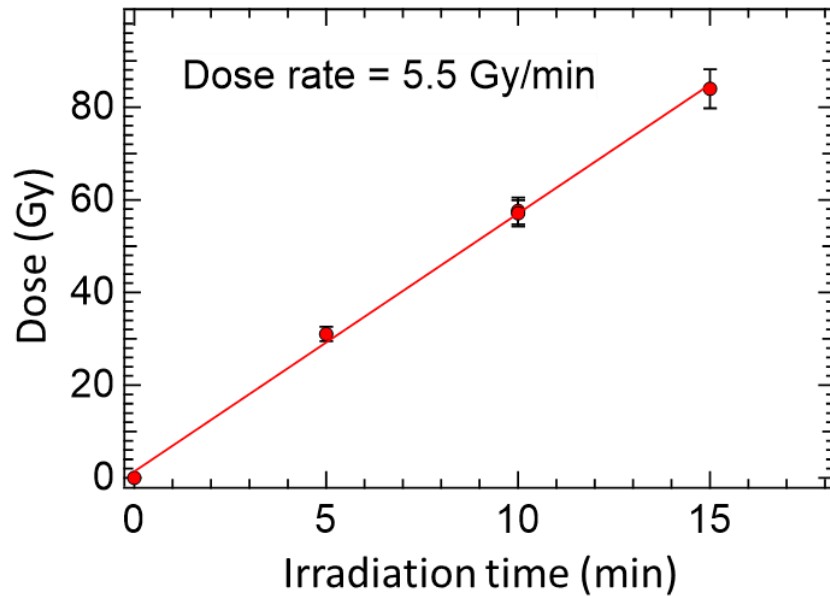


**Figure 2.2:** Fricke Dosimetry-Variation in the dose (Gy) delivered to the Fricke solution (250  $\mu$ l) as a function of irradiation time (min), at a height of 9 cm (position B) in the canister.

Equation (2.1) was used to calculate the dose delivered to the solution as a function of irradiation time. The table 2.3 shows the variation in the dose rate as the position of the sample inside the canister (placed in the gamma cell) changes.

**Table 2.3:** Variation in dose rate inside the Gamma cell with respect to sample volume and position in the canister.

Volume of Fricke solution irradiated ( $\mu$ l)	Dose rate (Gy/min)		
	Position A (6 cm)	Position B (9 cm)	Position C (13 cm)
150	4.23	5.23	5.14
250	4.14	5.51	4.73
400	4.41	5.90	4.92

In all the gamma irradiation experiments conducted in this work, the 250  $\mu$ l sample was placed at position B. Therefore, the dose rate employed to determine the dose delivered to the sample was 5.5 Gy/min (see table 2.3), with a percentage error in the dosimetry of approximately 5%.

### 2.3. Synchrotron Soft X-ray irradiation

In this section, I briefly describe the synchrotron light source. I also discuss the characteristics of the soft X-ray beamlines of synchrotron SOLEIL that were used in this work.

#### 2.3.1. Synchrotron light source

Synchrotron light sources are a type of particle accelerator and are among the most powerful tools in modern scientific research, providing researchers with intense beams of light in the X-ray, ultraviolet, and infrared regions of the electromagnetic spectrum. Synchrotron light sources work by accelerating charged particles, typically electrons, to nearly the speed of light and then forcing them to travel in a circular path using magnetic fields. As the charged particles travel along their circular path, they experience a force perpendicular to both their direction of motion and the direction of the magnetic field. This force is known as the Lorentz force. During this circular motion, the relativistic charged particle emits synchrotron radiation (SR), as its velocity direction is continually changing. This radiation is collected and used for a wide range of scientific applications.

Over the years, there have been numerous advancements in synchrotron light source technology, including the development of new accelerator designs, improvements in beamline instrumentation, and advances in data analysis and computational techniques. One of the most significant advancements in synchrotron light source technology has been the development of third-generation light sources, which are characterized by their high brightness and coherence. In recent years, there has also been a growing interest in developing fourth-generation light sources, which aim to further increase the brightness and coherence of synchrotron light sources.<sup>14,15</sup>

There are several key components in a synchrotron light source. Here, we describe these components for SOLEIL, which is the French national 2.75 GeV third generation synchrotron.

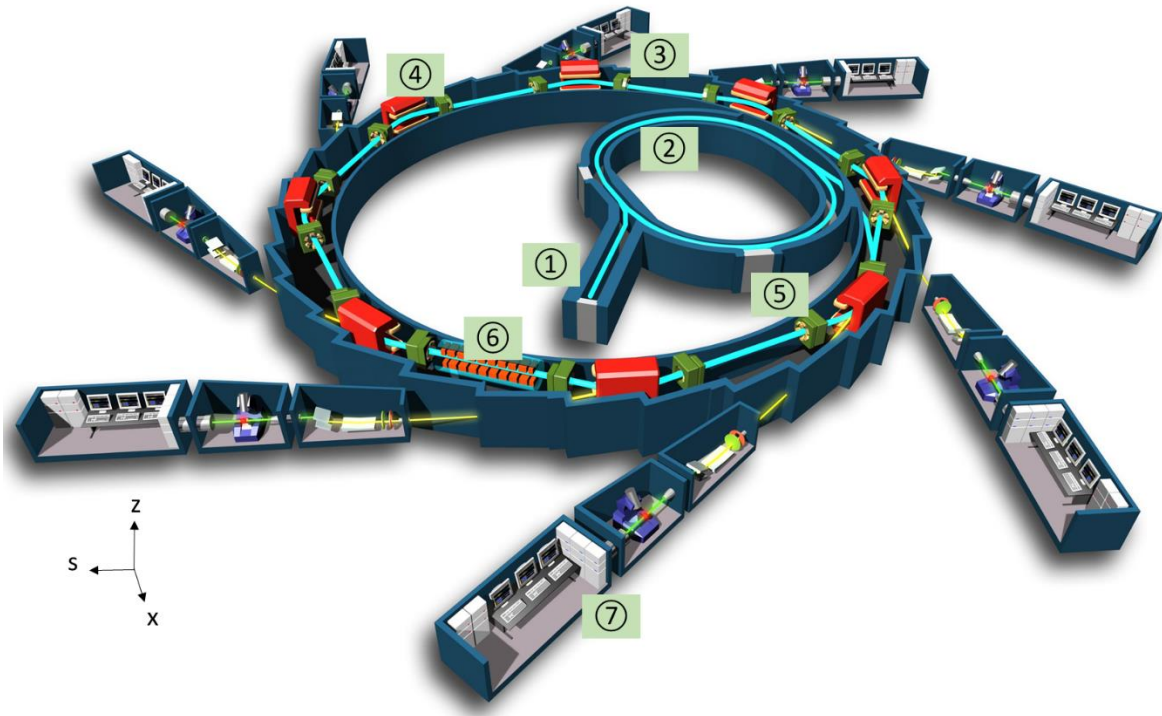


**Figure 2.3:** Schematic diagram of SOLEIL synchrotron, following a 7 step process to produce synchrotron radiation.<sup>16</sup>

SOLEIL is an electron-based synchrotron (see figure 2.3). Its first component is a 16 m long linear accelerator (linac) (①), where the electron beam emitted by an electron gun is accelerated. The second component is called a Booster (②) that accelerates the electron beam in a circular path, preparing the beam for the main ring of the synchrotron i.e. the storage ring (③), which has a circumference of 354 m. In this ring, the presence of bending magnets (④) facilitates the circular trajectory of the electrons by bending the electron beam using magnetic field. Another important component in producing SR is the radiofrequency (RF) cavity (⑤). It is tuned to a specific frequency that matches the rotational frequency of the charged particle and it compensates for the energy losses of the electron beam when it emits SR. Since SOLEIL is a third-generation synchrotron, it uses insertion devices, including wigglers and undulators (⑥), which produce more intense SR than a conventional bending magnet and can be designed to optimize its emission on a desired energy range. Finally, the emitted SR are used at the beamlines having the so called 'end stations' (⑦), where different set-ups are installed for specific experimental analysis.

In this work, all the soft X-ray experiments were performed at the beamlines of SOLEIL synchrotron that are detailed in the following section.

### 2.3.2. SOLEIL Beamlines

#### 2.3.2.1. METROLOGIE beamline

The METROLOGIE beamline is a bending magnet beamline with two optical branches dedicated to X-UV and hard X-rays energy ranges from few eV to 40 keV (monochromatic) with an access to white beam. The beamline is operated under vacuum ( $P = 10^{-8}$  mbar). In this work, we use the XUV (soft X-ray) branch of the METROLOGIE beamline (see figure 2.4).

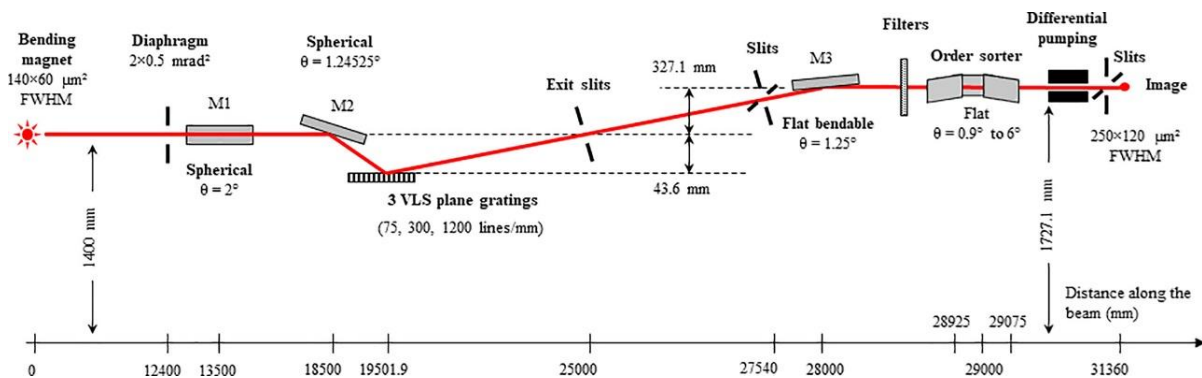


**Figure 2.4** : Scheme of the X-UV branch of the METROLOGIE beamline (image adapted from 17).

Depending upon the energy of the beam, the photon flux at the soft X-ray branch can vary from  $10^9$  to  $10^{12}$  photons/s. The different energies can be selected thanks to the three gratings (Varied Line Spacing plane gratings) present in the beamline (see figure 2.4). The branch operates from 30 eV to 1800 eV and is equipped with a lower order sorter that facilitates the removal of higher order light with a rejection rate of 0.1% (filters such as Boron  $0.4 \mu\text{m}$  can be chosen depending upon the working photon energy). Thanks to the higher order light rejection, the resulting spectral purity is more than 99 % over the entire energy range. The output beam is well focused and collimated ( $25 \mu\text{m} \times 120 \mu\text{m}$  FWHM focused beam). Typically, the spectral resolution<sup>1</sup> is few 10's of eV. The beamline is well suited to perform experiments at the low photon flux regimes and high spectral purity.

<sup>1</sup> Resolution refers to the ability of an instrument to separate and resolve adjacent peaks. It is defined using the fit parameter, FWHM (Full Width at Half Maximum).

### 2.3.2.2. TEMPO beamline

To observe the radiation damage on aqueous amino acid (Glycine) and dipeptide (Glycylglycine) samples, we chose to perform X-ray Photoelectron spectroscopy experiments using the TEMPO (Time resolved Experiments on Materials with PhotOelectron spectroscopy) beamline (beamline energy range = 50 to 1500 eV). It is an undulator beamline. The beamline comprises various elements, including slits, gratings, vertical and spherical mirrors (see figure 2.5). The mirrors in the extraction section allow to focus the beam horizontally and vertically on the entrance slit (EnS). The gratings and the two spherical mirrors (M2a and M2b) in the monochromator section focus the beam on the exit slit (ExS).<sup>18,19</sup>

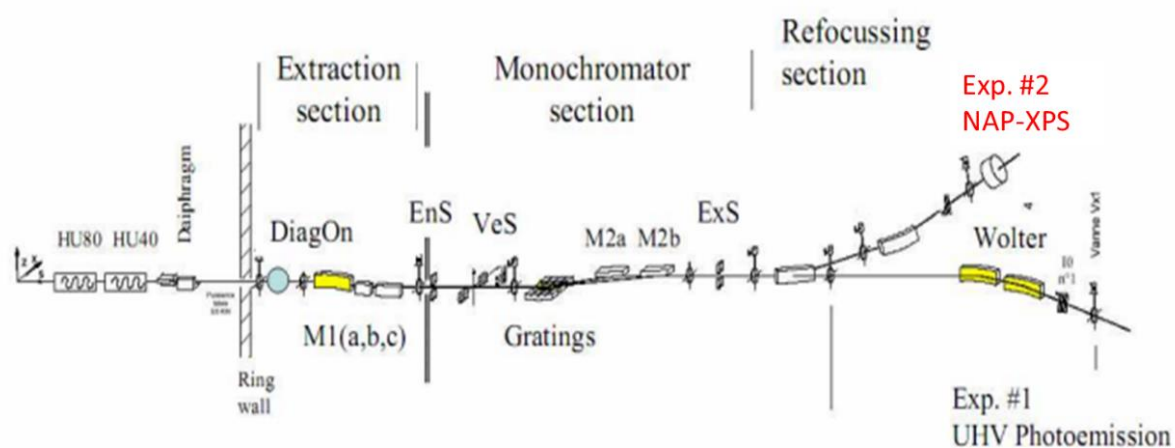


**Figure 2.5:** Schematic of the TEMPO beamline having two end station for UHV photoemission and NAP-XPS experiments.

Thanks to the different combinations of the available gratings and mirrors, it was possible to access the entire energy range of the beamline. The resulting monochromatic beam can then be used at the two end stations,<sup>18</sup> one to perform UHV Photoemission experiments and the other for NAP-XPS (Near-Ambient Pressure X-ray Photoelectron Spectroscopy).

At the NAP-XPS end station, it is possible to perform experiments with pressures as high as 20 mbar.<sup>19</sup> The analysis is facilitated using a SPECS Phoibos 150-NAP electron analyzer. Since the experiments are performed at high pressures, the analyzer and the beamline are protected using a differential pumping system. The working principle and the set-up of the NAP-XPS technique is given in section 2.4.5.3.



### 2.3.2.3. PLEIADES beamline

The PLEIADES (Polarized Light source for Electron and Ion Analysis from Diluted Excited Specie) beamline is an undulator beamline (HU80 and HU256) covering an energy range from 10 eV to 1000 eV. The schematic of the beamline is shown on figure 2.6. It generates ultra-high resolution soft X-rays with a resolving power of  $10^5$  at 50 eV and is dedicated to performing spectroscopy experiments in different physical states of the matter (gases, nanoparticles, liquids, etc.). The PLEIADES beamline has three branches: ① The MAIA branch, ② the central branch with one open port for users and ③ a branch with two end stations and one open port for the users.

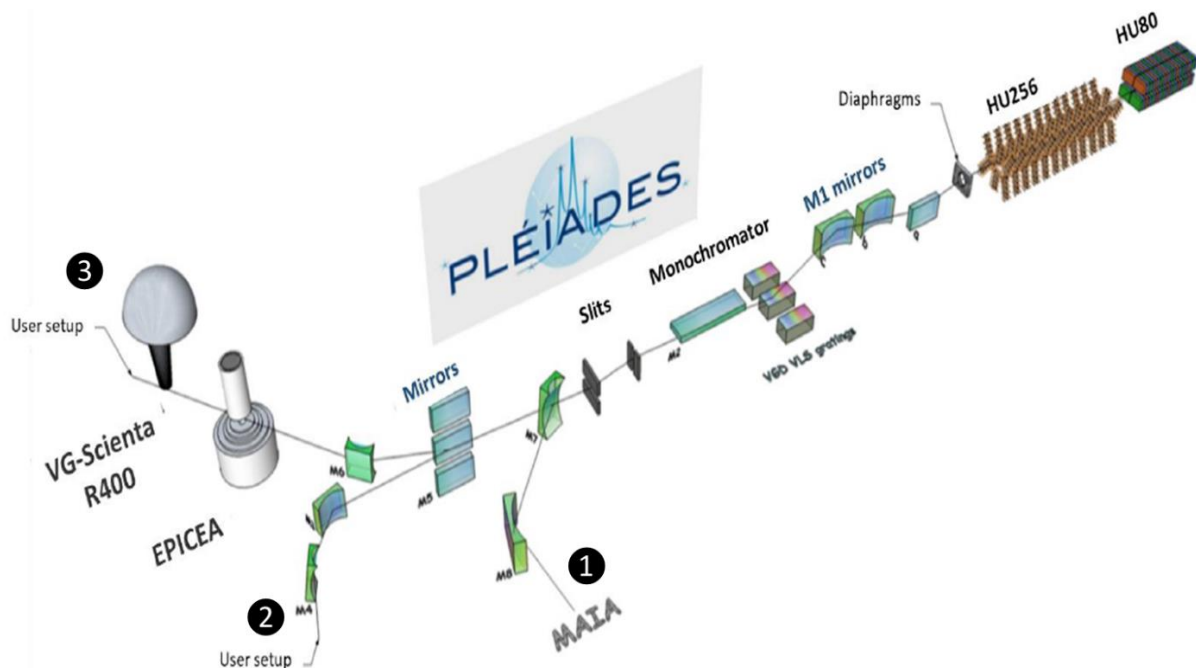


**Figure 2.6:** Schematic of the PLEIADES beamline displaying the three branches for performing experiments with high resolution soft X-rays.

In this work we have used the central branch (②) where the beam spot size is  $50 \text{ (H)} \times 30 \text{ (V)} \mu\text{m}^2$ , and the VG-Scienta R4000 of branch ③, where the spot size is  $180 \text{ (H)} \times 100 \text{ (V)} \mu\text{m}^2$ . The beam size can however be adjusted vertically using the exit slits after the monochromator. Since it is an undulator beamline, the fine tuning of the photon energy can be done by simply varying the magnetic field of the undulator. The undulator can be tuned (maximizing photon flux) or de-tuned (reduces the photon flux) with the monochromator.

Unlike METROLOGIE, this beamline is not equipped to reject higher order light, however, the photon flux is higher ( $10^{13}$  photons/s).

## 2.4. Experimental set-up and analysis techniques

### 2.4.1. In-air beam extraction at METROLOGIE beamline: IRAD setup

All the soft X-ray irradiation experiments conducted at METROLOGIE beamline, were performed in air ( $P = 1$  bar), using a microfluidic device (see section 2.4.2). Since the beamline is under vacuum ( $P = 10^{-8}$  mbar), the beam had to be extracted. This was possible thanks to a previously developed IRAD set-up (IMPMC, Sorbonne Université) (see figure 2.7). This set-up was initially developed for irradiating samples of biological interest at the Laboratoire pour l'Utilisation du Rayonnement Électromagnétique (LURE)<sup>20</sup> and was later adapted for the soft X-ray beamline at synchrotron SOLEIL.<sup>21</sup> Its installation was done behind the focal point of the beamline. The IRAD set-up has a three-stage differential pumping system that allows to reach a pressure of  $10^{-7}$  mbar behind the Silicon Nitride window from a pressure of  $10^{-8}$  mbar in the beamline. The differential pumping is facilitated thanks to the ionic and Turbomolecular pumps. Along the set-up, there are several diaphragms ( $A = 5$  mm,  $B = 3$  mm and  $C = 1$  mm). The set-up terminates with a Silicon Nitride square window ( $1$  mm  $\times$   $1$  mm,  $150$  nm thick) in a square silicon frame ( $10$  mm  $\times$   $10$  mm,  $500$   $\mu$ m thick) (FASTEC, Northampton, UK),<sup>22,23,20</sup> which is transparent to soft X-rays, referred to as the 'Exit window'. The differential pumping stage helps to protect the beamline and the storage ring, in case the Exit window breaks.

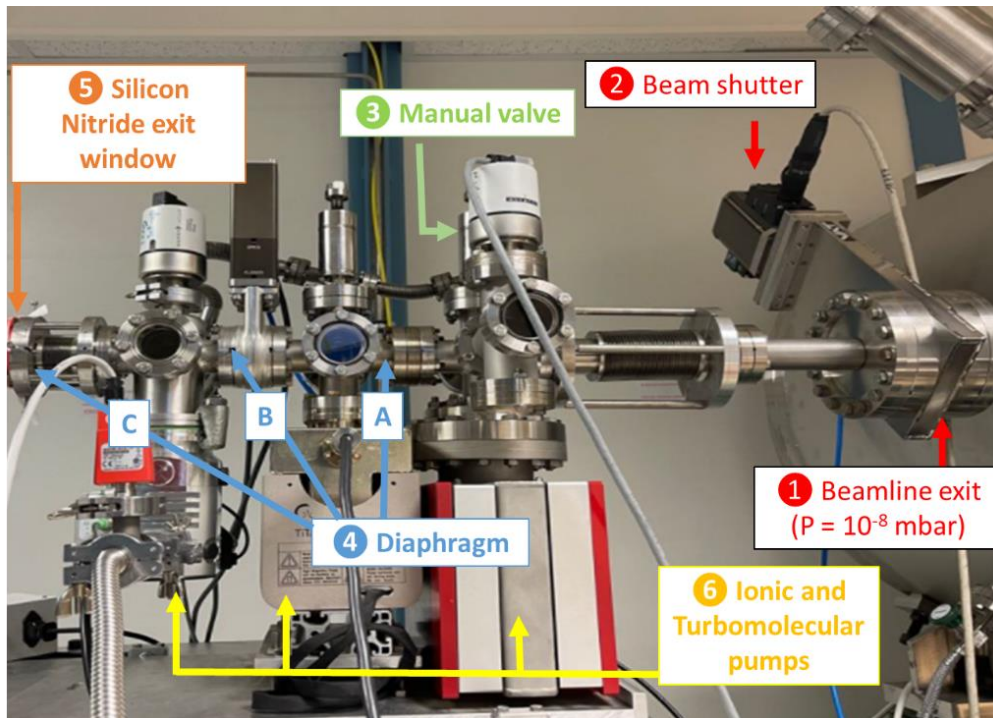


**Figure 2.7:** IRAD set-up installed at the front end of the METROLOGIE beamline, having a differential pumping system. It allows the extraction of beam under vacuum to air. The exit of the IRAD set-up is the 150 nm thick silicon nitride window, transparent to soft X-rays.

Thanks to the translation table of the IRAD setup, the microfluidic cell along with other alignment devices, namely a YAG:Ce crystal installed on a CCD camera and a photodiode (for specifications of the devices, refer to table 2.2 and for more details on the microfluidic cell, see section 2.4.2 and 3.2.1) could be installed in the front of the exit window of the IRAD setup. These devices could be translated in front of the exit window, thanks to the software for the translation table (software developed by Emmanuel Robert, PLEIADES beamline of SOLEIL synchrotron, France) that allowed the precise moment in the  $x$ ,  $s$  and  $z$  direction with respect to the beam. The  $T_s$  axis is parallel to the synchrotron beam,  $T_z$  is the vertical axis and  $T_x$  is perpendicular to  $T_s$  and  $T_z$ . The distance at which these devices were placed with respect to the exit window are shown in the figure 2.8. The relative distance (along the  $x$  and  $z$  plane) between these devices were measured prior to mounting them in front of the exit window, using the optical level.

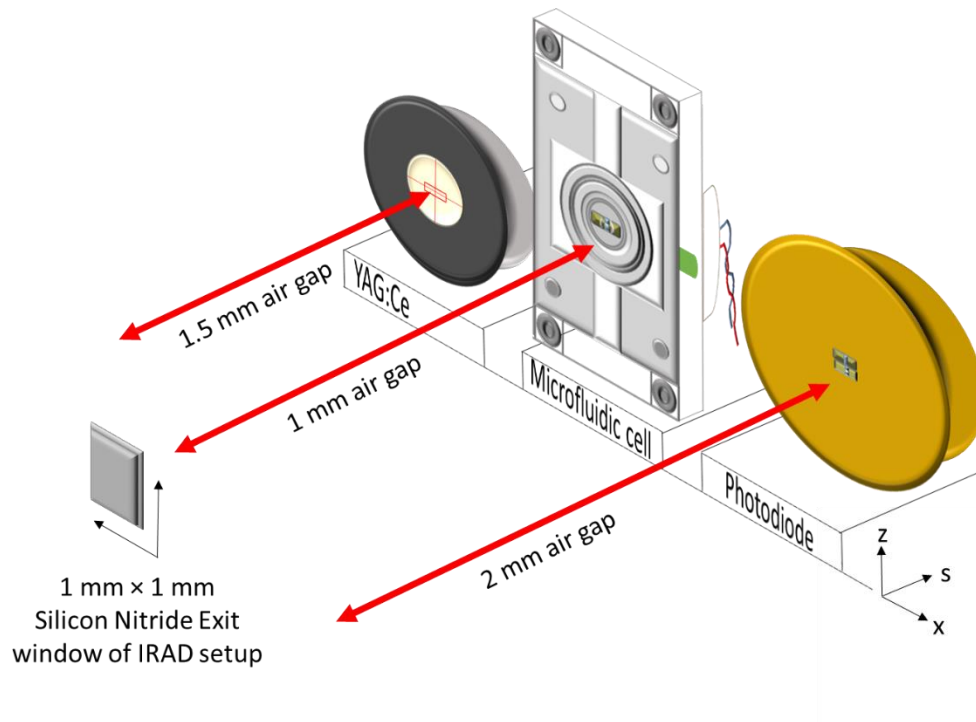


**Figure 2.8:** The installation of the microfluidic cell, YAG:Ce and the photodiode (placed at a known distance from each other) on the translation table, in front of the exit window of the IRAD setup. It should be noted that the distances shown in the figure are not with the sensitive surface of the devices but with the outer measurable surface of the device. The translation table allows the movement of the devices in front of the exit window along different axis, with a greater movement possible in Ts direction.

#### 2.4.2. Microfluidic cell design and set-up

As described in the introduction, soft X-ray beams are strongly attenuated in liquid media and hence, they cannot travel beyond few 10's of micrometers in aqueous solutions. Samples were thus irradiated in a microfluidic cell (5.3  $\mu\text{m}$  in depth), instead of a conventional irradiation cell (few mm to cm in depth), in order to have a relatively homogeneous depth-dose distribution.

This section describes the microfluidic cell design that is adapted from the microfluidic cell first developed for STXM measurements in a vacuum microscope chamber of the HERMES beamline, by Corinne Chevillard (CEA, Saclay), Charlie Gosse (LPN-CNRS, Marcoussis), Stéphane Le François (Synchrotron SOLEIL, Saint-Aubin) and Stefan Stanescu (Synchrotron SOLEIL, Saint-Aubin).<sup>24,24</sup> The cell was then adapted to use at METROLOGIE beamline during L.

Huart thesis, in collaboration with Corinne Chevillard.<sup>1</sup> The modifications introduced in the original cell design (to irradiate aqueous solutions with soft X-rays<sup>25</sup>) will be detailed. In addition, the microfluidic set-up that facilitates the flow and irradiation of samples will also be described.

#### 2.4.2.1. Original cell design

The original cell<sup>24,25,26</sup> was made of two silicon chips (6 mm x 3 mm large, 200  $\mu\text{m}$  thick) (Silson, Southam, UK) that were sandwiched between two elastomers, polymer polydimethylsiloxane (PDMS gaskets), as can be seen in the exploded view of the microfluidic cell in figure 2.9a. The PDMS gaskets allowed a firm sealing for the two silicon chips under the required pressure conditions (up to 2 bar). The front silicon chip (facing the beam) had a 150 nm thick and 300  $\mu\text{m}$  x 1 mm large silicon nitride ( $\text{Si}_3\text{N}_4$ ) membrane (low internal stress,  $\leq 250$  MPa) in its center, for the beam to pass. The back silicon chip had two side holes to allow the fluid to flow through the microfluidic channel (using the fluidic connections, see figure 2.9a). The microfluidic channel was formed thanks to the hollow SU-8-photoresist rectangular spacer on the front silicon chip) resulting in a channel depth of 5.3  $\mu\text{m}$ . This entire assembly was assembled on a metal holder (polytetrafluoroethylene, PTFE) (Gavard, Arrou, France). To compress the PDMS and tighten the assembly in the metal holder, a clamping system comprising stainless steel hollow bolt and a brass nut was used.<sup>26</sup>

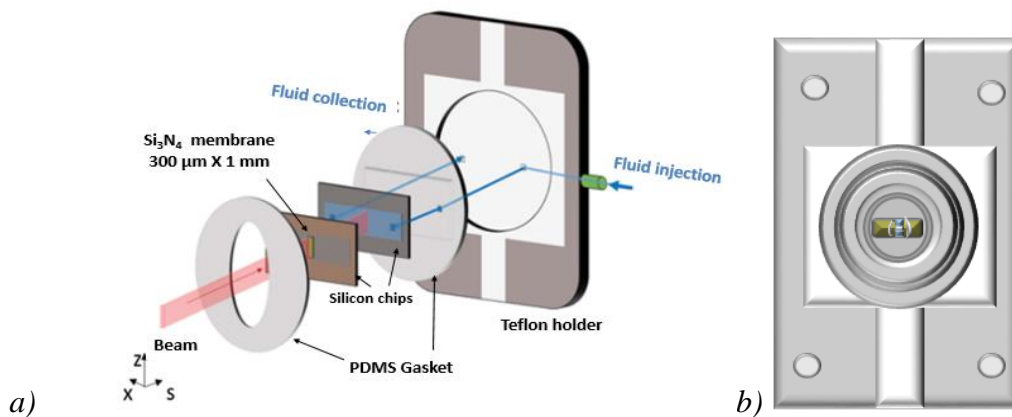


**Figure 2.9:** a) Exploded view and b) assembled front view of the original microfluidic cell design with one  $\text{Si}_3\text{N}_4$  membrane on the front silicon chip. The two silicon chips are packed between two PDMS gaskets that prevent leakage of the flowing sample.

This initial design did not allow the beam transmission through the cell, making it difficult to align the cell with respect to the beam (described later in this section). In order to speed up the process of alignment, modifications were introduced in the cell design (see section 3.2.1.1 of chapter 3).

#### 2.4.2.2. Microfluidic set-up

The microfluidic cell enables the sample to flow through it and the sample is automatically renewed during the irradiation process. To accurately control the flow of the sample in the microfluidic cell, a set-up consisting of various microfluidic devices was used (see figure 2.10). These devices (pressure controller, bidirectional flowmeters, 2-switch valves, bidirectional 10-position M-switch and PEEK or teflon tubes) were purchased from “FLUIGENT smart microfluidics”. The FLUIGENT softwares, namely ‘Microfluidic Automation tool’, ‘ESS control’ and ‘All In One (A.i.O)’ were used to write and to automate the irradiation protocols and time based fluidic programs (sample injection, changes in flowrate or pressure after certain time duration, cleaning of the cell).

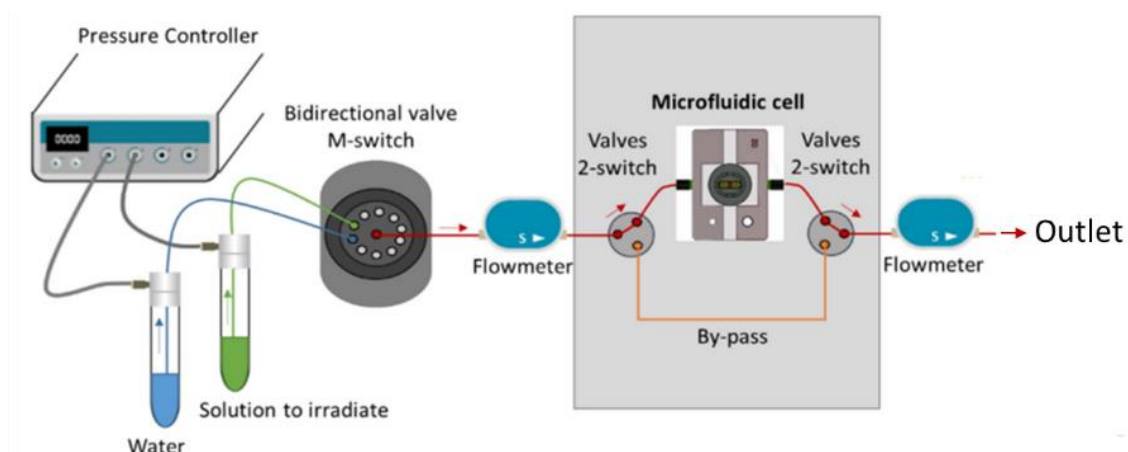


**Figure 2.10:** Microfluidic set-up comprising of various microfluidic devices that allow to control the flow of sample through the microfluidic cell. The figure shows the two paths that the liquid can flow through, the microfluidic cell and the bypass.

The set-up comprises of sample reservoirs or tubes, and a specific sample can be selected thanks to the 10-position M-switch valve. Thanks to the ‘MFCS™ pressure controller’, the flowrate of the sample in the microfluidic channel can be maintained at a desired value during the experiments. The pressure controller allows to work with compressed air (for oxic conditions) as well as with nitrogen gas (for anoxic conditions). The flowrate can be monitored

on the 'bidirectional flow units' or the flowmeters. Depending upon the sensor diameter of the flowmeter (S or M), the inner volume and the maximum pressure resistance changes. The connections between the devices are made using PEEK or Teflon tubes. The flowmeter is then connected to a 2-switch bidirectional valve that allows the sample to flow either through the microfluidic cell or through the bypass. The bypass is a path in the circuit with low hydrodynamic resistance facilitating a faster injection of the sample and a faster cleaning of the channel. The last device in the channel is another flowmeter to monitor the outlet flowrate that helps to verify if there is leakage in the channel. The devices used for our set-up are compatible for low pressure (up to 2 bar) and they provide reliable and repeatable experimental condition. The sample flowing through the microfluidic cell is irradiated and at the outlet, it can be collected for post-analysis, or in-line analysis (see section 3.2.2 of chapter 3).

The calibration of the flow Units (see Appendix I.III.) was performed to have an accurate flowrate measurement for each sample that was crucial for dose determination (see section 3.2.3.).

#### 2.4.3. Optical Interferometry

The application of pressure in the microfluidic channel, to facilitate the flow of the sample, results in the deformation of the membrane. To measure this deformation (or bulging) we employ a technique called "Optical Interferometry." This well-established method involves splitting coherent light into multiple beams using beam splitters or other optical components. These beams follow separate paths before recombining, creating an interference pattern based on their phase relationship. Constructive interference produces bright fringes, while destructive interference leads to dark fringes. Fringes represent the distinct patterns of light and dark regions resulting from wave interference. By capturing and analyzing the fringe pattern using techniques like image processing, interferometric data analysis algorithms, or Fourier transform methods, we can extract quantitative information such as surface profiles and thickness.

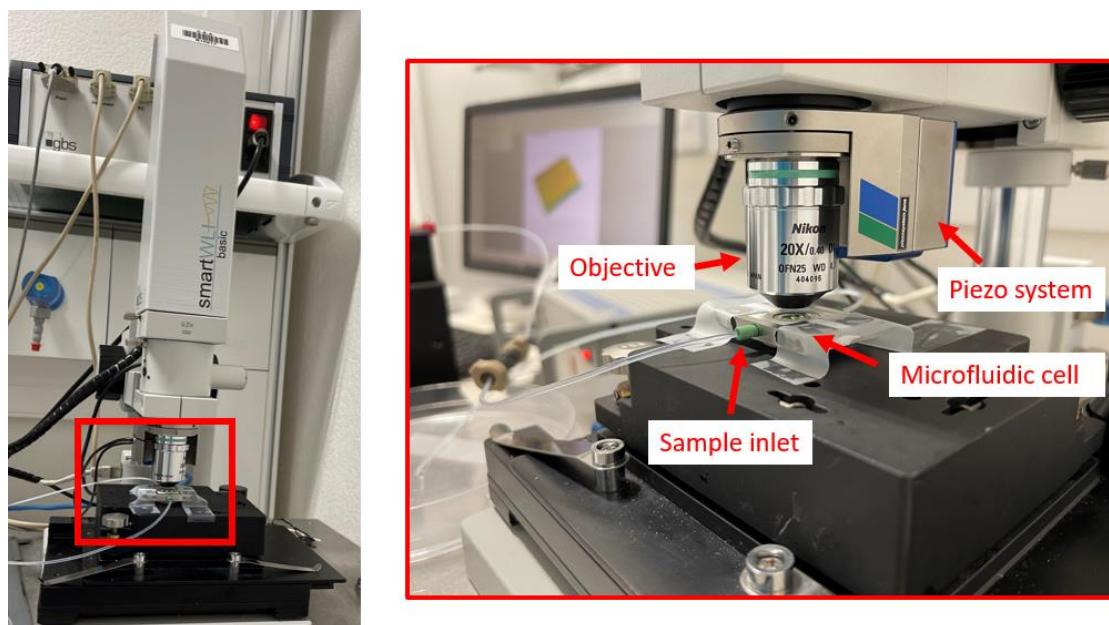


**Figure 2.11:** Experimental setup to measure interference patterns on the bulging membrane of the microfluidic cell using an optical interferometer (smartWLI, Germany) with a 20X objective. b) Pattern of the fringes when the sample is not flowing (left) and when it is flowing through the microfluidic cell (right).

The interferometry measurements in the work were performed using an optical interferometer from Smart WLI Schaefer GmbH, Germany, with a changeable objective (10X and 20X were used in the measurements), the setup for which is shown in the figure 2.11.

#### 2.4.4. UV-visible spectrophotometry

In this section, we discuss the UV- visible spectroscopy technique, used to perform absorbance and band gap measurements for samples. Firstly, the basic principle of the technique is described. It is followed by discussion on the absorbance measurements for the liquid samples in the transmission mode and reflectance measurements for the solid sample, using a conventional UV spectrophotometer. Lastly, the post processing of these measurements to determine the yield and band gap of the sample, is detailed.

##### 2.4.4.1. Principle

UV-Vis spectroscopy is a technique that involves the absorption of light in the ultraviolet-visible region (UV-Vis) of the electromagnetic spectrum. It is based on the principle that when light passes through a sample, specific wavelengths are absorbed, leading to electronic



transition of electrons. The energy required for this transition is specific to the molecule and it is related to the band gap of the molecule (difference between highest occupied molecular orbital, HOMO, and the lowest unoccupied molecular orbital, LUMO). This technique is governed by the Beer-Lambert law that provides a relation between the absorbance ( $A$ ) of the sample and its concentration ( $c$ ), at a given wavelength ( $\lambda$ ) and path length ( $l$ ). The Beer Lambert law can be given by the equation 2.2.

$$A = \varepsilon_{\lambda}cl \quad 2.2$$

The absorption of light by the sample is measured using a spectrophotometer, which generates a spectrum of light absorbed by the sample as a function of wavelength.

#### 2.4.4.2. Off-line UV analysis

##### 2.4.4.2.i. Absorbance measurements in transmission

UV spectra were measured using a conventional UV spectrophotometer Shimadzu UV-2550 available at LIONS, CEA Saclay, France, and a 1mm quartz cuvette (High Precision cell, Hellma Analytics), transparent to UV. The software used to record the spectra was *UVprobe*. The wavelength range over which the spectra were recorded is 190 nm - 600 nm, with a slow single-mode scan speed. The slit width was kept as 2 nm with a sample interval of 1 nm.

For liquid samples, ultra-pure water was used for base line correction. The absorbance at the wavelength of interest (460 nm for WST-8 formazan) was subtracted with the absorbance at 600 nm wavelength (the wavelength where the absorbance remained the same throughout). The resulting delta absorbance or optical density (OD) was used for calculations of the yield, explained in section 2.4.4.3.

The UV-vis spectra of all gamma-irradiated samples, reported in this work, were obtained using an off-line UV-vis spectrophotometer. However, for the irradiated sample from soft X-rays, the analysis was performed using an in-line UV setup and its development and use is detailed in chapter 3.

### 2.4.4.2.ii. Absorbance measurements in reflectance

To record the UV-visible spectra of the powdered solid sample, the measurements were made in the reflectance mode, available in the *UVprobe* software. The reflectance measurements were made using an integrating sphere (see figure 2.12).<sup>27,28</sup>

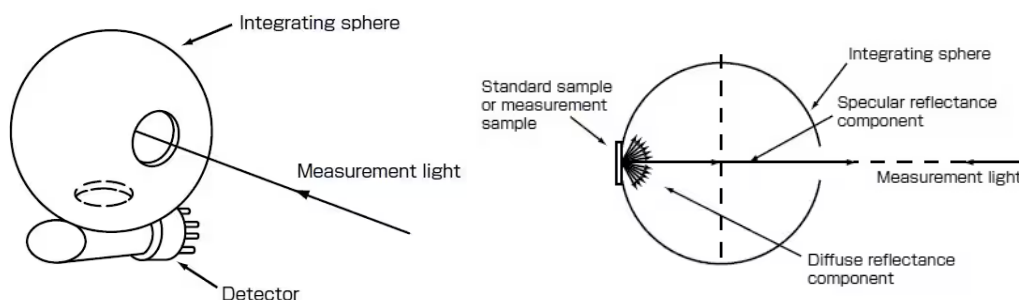


**Figure 2.12:** Schematic representation of integrating sphere (image on the right) and the diffuse reflectance measurements (measurement light is irradiated at 0°, on the sample), on the left, used for measurement of the UV-vis spectra in reflectance. Images are taken from Shimadzu’s website.<sup>27</sup>

The baseline correction was performed by using BaSO<sub>4</sub> powder as a reference sample. The reflectance values of the sample were recorded as the light gets reflected by the solid sample, unlike in the liquid sample. The reflectance values of the sample (R) are then transformed into a quantity proportional to the absorbance (KM), using Kubelka-Munk transformation (see equation 2.3).<sup>29</sup>

$$KM = \frac{(1-R)^2}{2R} \quad 2.3$$

### 2.4.4.3. Post-processing

#### 2.4.4.3.i. Absorbance to Yield

The yield of the radiolysis products can be defined by the amount of the product formed per 100 eV of the absorbed energy. However, it can also be expressed as ‘M Gy<sup>-1</sup>’ or in its SI unit ‘mol/J’. All the yield values in this work are reported in μmol/J. The conversion factor can be given as, 1 M Gy<sup>-1</sup> = 9648000 molecule/100 eV and 1 molecule/100 eV = 0.10364 μmol/J.<sup>30</sup>

The first step was to determine the concentration (M), for a given irradiation dose, from the delta absorbance values (see section 2.4.4.2.), using the Lambert-Beer law (see equation 2.2). The concentration was calculated at each dose (Gy) and each concentration value was divided by the dose (Gy) at which it was obtained. The resulting quantity, the yield, has the unit 'M Gy<sup>-1</sup>'. This value is then converted to the more conventional unit for yield, i.e. μmol/J.

#### 2.4.4.3.ii. Band gap measurement

The UV-vis spectroscopy allows to estimate the band gap of samples. This is possible by generating a Tauc plot. The Tauc relation can be expressed by equation 2.4.

$$(\alpha h\nu)^{1/\gamma} = B(h\nu - E_g) \quad 2.4$$

Where  $\alpha$  is the molar absorption coefficient, which is energy dependent,  $h$  is the Planck constant,  $\nu$  is the frequency of light,  $\gamma$  is dependent upon the electronic transition and can be equivalent to either 0.5 or 2 for direct or indirect band gap measurements, respectively,<sup>31,32</sup>  $B$  is a constant and  $E_g$  is the band gap energy. In this work, the indirect band gap measurements ( $\gamma = 2$ ) are reported.

The Tauc plot was obtained by calculating  $\alpha$  at each wavelength, thanks to the values obtained via the recorded absorption spectra. The photon energy was plotted on the x-axis. The value of the band gap was obtained by extrapolating the first onset curve to the x-axis.<sup>32</sup>

#### 2.4.5. XPS analysis

In this section, we will focus on X-ray Photoelectron Spectroscopy (XPS) analysis technique, used to study dipeptide solutions after interaction with soft X-rays. It is a surface-sensitive technique based on the principle of the photoelectric effect (see section 1.2.1 of chapter 1).

We describe here the commonly used analyzer for XPS measurements. Additionally, we will delve into the solid-state XPS and liquid-state XPS techniques (NAP-XPS and liquid microjet XPS), along with the data treatment and calibrations performed for them.

### 2.4.5.1. Hemispherical electron analyzer

Hemispherical electron analyzer is a widely used analyzer for techniques like XPS to perform high resolution measurements. It allows to analyze the energy and momentum of electrons emitted from a sample surface. The set-up of the analyzer comprises several elements as shown in figure 2.13.

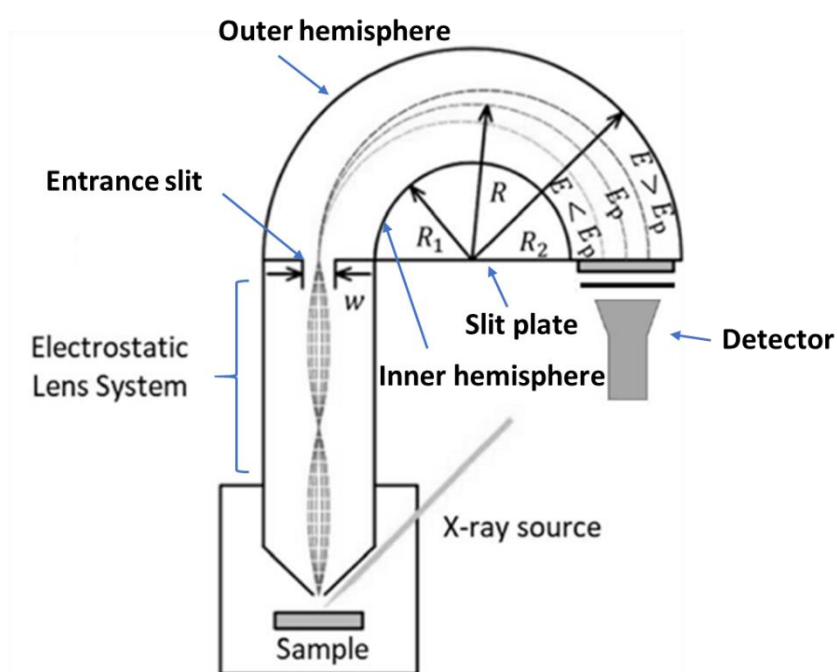


**Figure 2.13:** Schematic of XPS setup with a hemispherical electron analyzer.<sup>33</sup>

The very first stage is the sample holder where the sample is positioned/oriented to face the center of the analyzer entrance. Upon irradiation with the X-ray source (X-ray tubes or synchrotron radiation) the emitted electron enters the electrostatic lens system where the electrons are focused to the entrance slit of the hemispherical analyzer.<sup>34</sup> The hemispherical analyzer typically has two concentric hemispheres (inner and outer) that operate at different potentials to maintain the trajectory of the electrons. The trajectories of the electrons are dispersed, based upon their kinetic energy, and an XPS spectra is acquired using a detector (CCD etc.). The voltages on which the hemispheres operate defines the pass energy (linked to the range of kinetic energies of the electrons that can be detected on the detector). The slow moving electrons remain closer to the inner hemisphere and vice versa.<sup>35</sup>

### 2.4.5.2. Solid XPS

We performed solid-state XPS of the samples (Glycine and Glycylglycine) as a reference XPS study to understand the chemical structure of the molecules in the absence of water molecules and to compare to our liquid XPS data. This allows a better understanding of the effect of hydration. The laboratory XPS set-up used, is detailed below.

#### 2.4.5.2.i Setup

The solid-state XPS spectra were recorded using the Kratos AIX ULTRA DLD spectrometer<sup>36</sup> with a monochromatic Al K $\alpha$  X-ray source (1486.6 eV, 150 W) at LICSEN, CEA Saclay, France. All the solid-state XPS measurements were performed by Jocelyn Leroy. The sample was deposited on a gold substrate in electrical contact with the hemispherical electron analyzer and the analysis area of the sample was (300  $\times$  700)  $\mu\text{m}^2$ . In order to minimize or avoid the charge effect on the measurements, the charge neutralization system was used.<sup>37</sup> All the spectra were recorded with a hybrid lens mode.

#### 2.4.5.2.ii. Data acquisition and calibration method

To obtain an overview of the composition of the sample, the survey spectrum was recorded at pass energy of 160 eV and an energy step of 1 eV. The binding energy scale calibration of the spectra was performed with respect to Au 4f<sub>7/2</sub> at a binding energy of 84 eV for the gold substrate. The verification of the alignment of the Fermi level was done using the C 1s peak of hydrocarbons at 284.8 eV.<sup>38, 39, 40</sup> High-resolution core and valence level spectra of the sample were recorded at a pass energy of 20 eV and an energy step of 0.05 eV.

All the spectra were corrected for the work function (the minimum energy required to remove an electron from the sample, in vacuum) of the analyzer that is equal to -4.69 eV. The binding energies of the solid-state XPS spectra are reported with respect to the Fermi level of gold. The resolution of the spectra (core and valence spectra) recorded at the pass energy of 20 eV is 0.35 eV (measured previously for the same spectral conditions).<sup>1</sup>

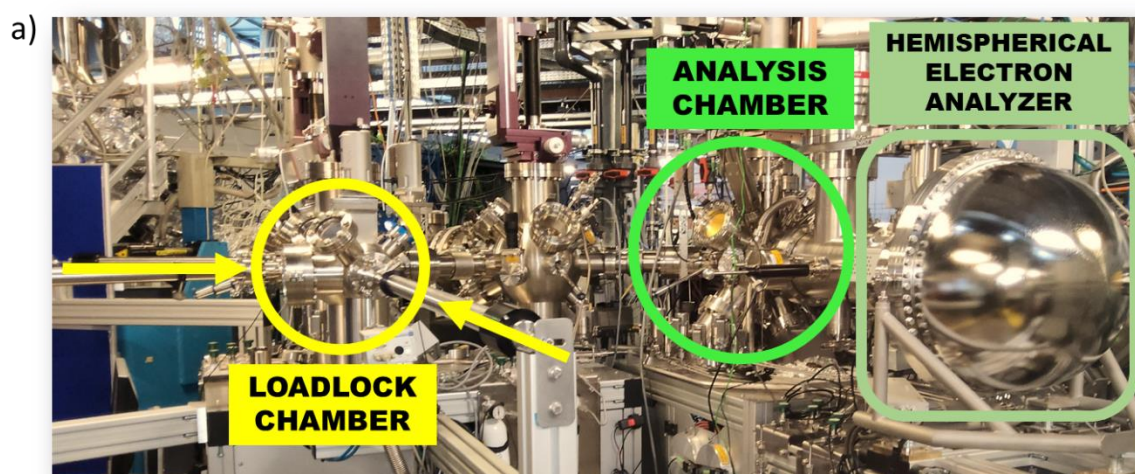
### 2.4.5.3. NAP-XPS

Traditional XPS requires the sample to be under high vacuum conditions, preventing the study of samples under realistic conditions. The advancements in the field of spectroscopic studies

have allowed to perform XPS measurements in the near ambient pressure condition. The technique is known as the near ambient pressure X-ray photoelectron spectroscopy (NAP-XPS), working at pressures up to few 10's of millibar. It should be however noted that NAP-XPS has some limitations, such as a lower resolution and sensitivity compared to traditional XPS due to the presence of the gas environment.

The experimental setup used to perform the NAP-XPS (TEMPO beamline, SOLEIL synchrotron) is shown in the figure 2.14 a. The first stage of the setup is the 'Load Lock Chamber', where the sample was loaded. Powdered sample was secured within the copper rings fixed on the sample holder (Figure 2.14 b) and mounted onto a horizontal manipulator in the 'Load Lock Chamber'. The sample was then transferred through a series of chambers to reach the 'Analysis Chamber', where it was repositioned vertically (see figure 2.14 c). This vertical orientation was necessary to ensure that the sample faced the analyzer at the good working distance of the NAP lens and that the beam was focused precisely at the sample. As the hemispherical analyzer (Phoibos 150 from specs) is positioned horizontally, this step was crucial to enable accurate analysis of the sample.<sup>41</sup>

The vertical manipulator in the analysis chamber was capable of translating in 5 axis, to optimize the signal. The sample surface was approximately 1 mm away from the NAP analyzer's aperture entrance, which had a diameter of 0.3 mm (see figure 2.14 c). Additionally, the SR beam entrance angle was set to 54° relative to the axis of the analyzer.



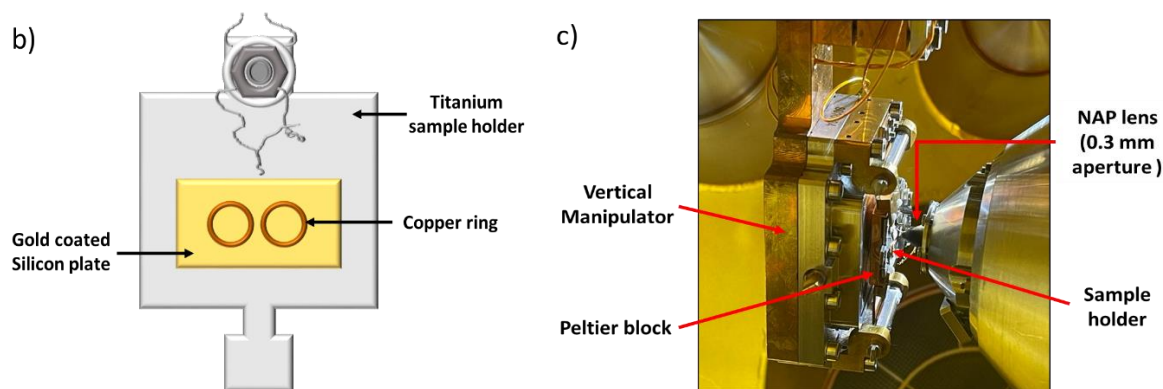


**Figure 2.14:** a) NAP-XPS end station; b) Sample holder; c) Sample analysis using NAP lens of 0.3 mm aperture set-up at TEMPO beamline, SOLEIL synchrotron.

For our study, we maintained a working pressure range of 5 to 7 millibars and a temperature of 278 K during NAP-XPS measurements, to allow a droplet formation. The Peltier block in contact with the sample holder on the vertical manipulator allowed us to achieve such a low temperature. The sample remained static on the holder, oriented at a particular angle relative to the SR beam and NAP lens. This enabled us to monitor the evolution of the liquid XPS spectra with the irradiation time and to observe any radiation damage.

#### 2.4.5.4. Liquid microjet XPS

Liquid-jet XPS is an alternative technique for conducting liquid XPS spectroscopy. However, unlike NAP-XPS, liquid-jet XPS measurements are carried out in high vacuum. One significant difference between these two techniques is that liquid-jet XPS involves renewing the liquid sample continuously. As a result, radiation damage is not expected to be observed in the recorded spectra, given the high flow rate.<sup>42</sup> The set-up used for performing such measurements was available at PLEIADES beamline and is explained below.

##### 2.4.5.4.i. Setup

All the liquid microjet XPS measurements were carried out at the PLEIADES beamline of SOLEIL synchrotron, France. The liquid microjet set-up (see figure 2.15) is detailed elsewhere.<sup>43,42</sup> Briefly, the set-up consists of a glass capillary with a 60  $\mu\text{m}$  orifice diameter used to create a liquid jet. The jet is collected using a heated catcher, which is maintained at a temperature of approximately 80°C to prevent the solution from freezing inside of it. A titanium skimmer (entrance of 300  $\mu\text{m}$ ) is used to direct the electrons towards the hemispherical analyzer. The

liquid jet, generated from the nozzle, and the skimmer are aligned perpendicularly, allowing the emitted electrons to be selectively directed based upon the applied pass energy.

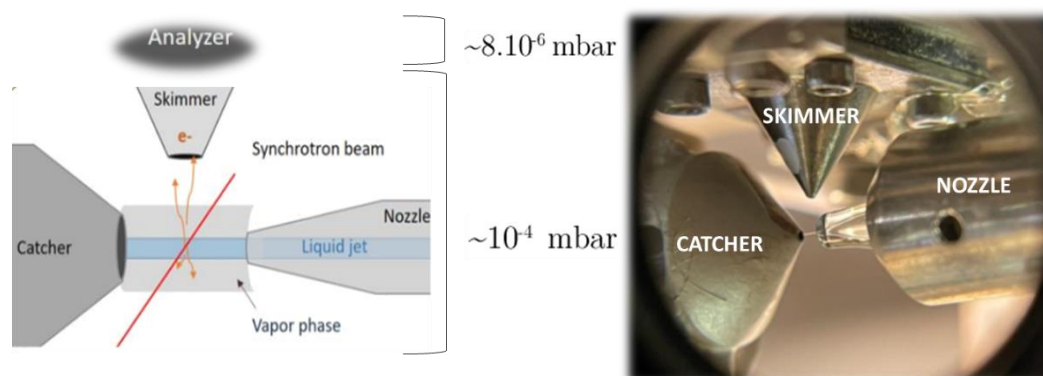


**Figure 2.15:** Schematic diagram (left) and experimental image (right) of the liquid jet XPS setup at PLEIADES beamline to perform high-resolution spectroscopy of liquid samples.

The nozzle holder is mounted on a two-axis translational stage to center the jet compared to the catcher hole. This geometry is set on an aluminum holder that comprises two differential tubes of 1 mm diameter holes aligned for the beam entrance and exit. The entire set-up is then placed in an aluminum box with three holes, two of them aligned to each other as well as to the two holes of the aluminum holder (beam entrance and exit). The third hole, made with a titanium insert and centered compared to the skimmer axis, allows the emitted electrons to pass towards the hemispherical electron analyzer. The analyzer lens axis, the SR beam and the jet are mutually perpendicular, thanks to the three-axis translation stage of the aluminum box. The jet was placed at the working distance of the electron analyzers. Two different electron analyzers were used during this work. The first one is a VG-Scienta R4000WA and the second one is a HV Phoibos 150 from Specs. The jet was electrically grounded using a metallic connector in the upstream of the glass-nozzle to overcome the charging effect that can result in unstable in the spectra.

The entire set-up is placed under vacuum and therefore, the pressure in the liquid micro-jet chamber (aluminum box) was  $\sim 10^{-4}$  mbar and the pressure in the spectrometer chamber was  $\sim 10^{-5}$  mbar. To maintain such high vacuum condition, pumping is done using the primary and secondary pumps, as well as two cold traps filled with liquid nitrogen mounted on the liquid microjet chamber and the spectrometer chamber. The sample can be collected for further analysis, outside the vacuum chamber, thanks to the catcher, in glass bottles pumped below



10 mbar and stored at 4 °C. Throughout the experiment, the flowrate of the injected liquid was maintained to 3 mL/min.

#### *2.4.5.4.ii. Data treatment and Calibration*

The recorded spectra had contributions from both liquid and gas phases (present around the jet). Elimination of the gas phase was however possible thanks to the polarization of the jet (by applying a certain voltage),<sup>43</sup> so that the main contribution was from the liquid phase.

The total experimental resolution of the spectra recorded at 100 eV, 400 eV and 600 eV (Pass energy = 50 eV and monochromator slit size = 25  $\mu\text{m}$ ) was 0.1 eV, 0.3 eV and 0.3 eV respectively. The calibration of the spectra at 100 eV and 400 eV was done with respect to the gas phase  $\text{H}_2\text{O}^+$  band, 1b1,<sup>44</sup> at 12.62 eV. The spectra recorded at 600 eV were calibrated against the O 1s gas phase peak of water at 539.8 eV.<sup>45, 46, 47</sup> The procedure for the gas phase values extraction, according to the 2D images recorded with the spectrometers is detailed elsewhere.<sup>42</sup> The energies are reference with respect to the vacuum level and all spectra were recorded with Linear Vertical (LV) polarization mode. The photon energy calibration was done using different gases (Kr 3d at  $h\nu = 91.2$  eV,<sup>48</sup>  $\text{N}_2 \pi^*$  at  $h\nu = 400.9$  eV,<sup>49</sup> Ar 2p at  $h\nu = 244.4$  eV<sup>50</sup>). All the spectra were corrected for the work function of the analyzer that is equal to -4.8 eV.

The nitrogen and carbon flux calibration for all the spectra was carefully performed. For nitrogen, the flux calibration was performed by dividing the measured electron intensity by the current read on a photodiode (from 394 eV to 410 eV), at the respective photon energies. However, for carbon, since the photodiode response can also be affected by the carbon contamination, on the photodiode itself, over the region from 280 eV to 310 eV, we measure total electron yield of neon that should display a smooth decrease according to the photon energy in this region. Thus, all the feature observed are only due to carbon contamination on the different beamline optics. Then knowing the ionization cross-section of the neon, it is easy to perform flux correction by multiplying the measured electron intensity with normalized neon yield and the normalized cross-section of neon, at the respective photon energies.<sup>51</sup>

All the graphs are plotted using the commercial software CasaXPS and Igor Pro. The peaks were fitted using the Voight-type function, which is the function given by the convolution of a

Lorentz distribution and a Gaussian distribution. The line shape SGL is used to do the fit that is the Gaussian/Lorentzian sum formula wherein the contribution of each distribution can be defined. We use SGL(30) that involves 30 % of Lorentzian contribution and 70 % Gaussian contribution. The background used in the fit was Tougaard for carbon XPS spectra and Linear for nitrogen XPS spectra.

The Secondary electron cut off spectra (SECO) were recorded at the photon energy,  $h\nu = 91.2$  eV (Pass energy = 10 eV and monochromator slit size = 5  $\mu\text{m}$ ) and with the total resolution of 0.1 eV. The spectra were fitted with an erf step function<sup>52</sup> to accurately determine the work function of the aqueous sample and the function is detailed elsewhere.<sup>52,53,54</sup>

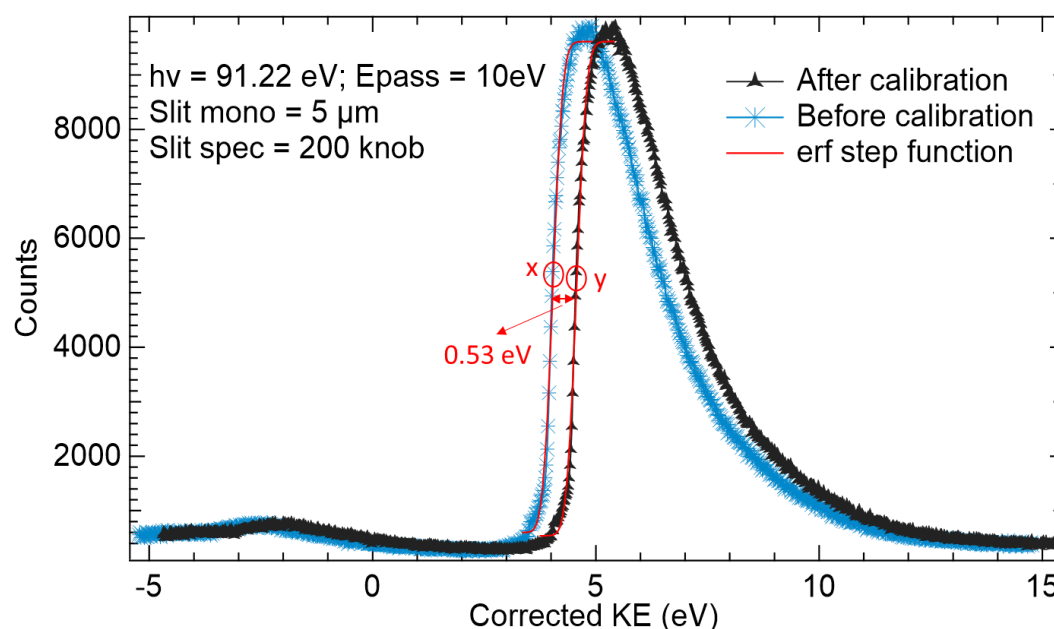


**Figure 2.16:** Secondary electron cut off spectra for 50 mM KCl solution before calibration (blue curve) and after calibration (black curve). The value of the work function obtained (before calibration =  $x$  and after calibration =  $y$ ) from the fitting function is shown by a red curve. The reported spectra were recorded at the bias of -50 V (subtracted on figure).

The SECO spectra were recorded at the bias of -50 V. For energy calibration, work function of KCl solution, determined from the fit of SECO spectrum, was compared with the value present in the literature (4.6 eV).<sup>52</sup> The KCl spectrum, before and after the calibration, is shown in figure 2.16. The obtained calibration factor of 0.53 eV was used for the glycine and

Glycylglycine SECO spectra (see chapter 5). The SECO spectra are plotted and analyzed using the commercial software Igor Pro.

## **2.5. Theoretical Methods**

### **2.5.1. General concepts**

Simulation techniques are a method widely used to analyze systems having real-world applications. Simulations also serve as the best tool to provide complementary knowledge alongside the experiments.<sup>55,56</sup> In addition, they can be very advantageous in scenarios where the system of study is quite complex or where experimental conditions are harsh or difficult to replicate,<sup>57</sup> or can even suggest new experiments to perform.

In the following sections, we emphasize the key concepts for understanding molecular dynamics (MD) simulations. MD is one of the principal computer simulation techniques to model the time evolution of a system of atoms or molecules, using different levels of theories and approximations. The atoms and molecules can be treated either classically or quantum mechanically, depending on the type of information one wants to extract. MD simulations can be used to investigate a wide range of phenomena, such as the behavior of isolated or liquid-phase biomolecules, different properties of liquids (thermodynamic, surface, spectroscopic, dynamic, electronic etc.),<sup>58,59</sup> solids (thermal, elastic, defects, electronic etc.)<sup>60,61</sup> and interfaces (interfacial interactions, tension, thermal transport, electronic etc.)<sup>62</sup>.

In this work, we model the fragmentation dynamics of doubly ionized systems (water and water-dipeptide systems) and study the interaction of the dissociation products with surrounding molecules in the simulation box. The electronic density of states (DOS) calculations are also performed to interpret the photoelectron spectroscopy results. The simulation techniques used in this work are described in the following sections.

#### **2.5.1.1. Classical Molecular Dynamics (MD)**

Standard or classical MD is one of the principal theoretical tools to study complex system. In this approach, the atoms or ions are treated classically and the quantum mechanical effects are entirely neglected. The instantaneous force on the atoms is calculated using force fields that define the interactions between atoms. These interaction potentials are based on

empirical data or independent electronic structure calculations. Pair-additive potentials (e.g. Lennard-Jones potential) are used to model the non-bonded interactions between the atoms.<sup>63,64</sup> Once the initial positions and velocities for all the particles (atoms or ions) are specified in the system, the forces acting on each particle are calculated, which in turn gives the new positions and velocities of the particles using Newton's equations.

Different types of algorithms can be used to move the particles in time. For instance, the positions and velocities at time  $t + \delta t$  may be deduced using the velocity Verlet algorithm (see equations 2.5 and 2.6):

$$\vec{r}_i(t + \delta t) = \vec{r}_i(t) + \delta t \vec{v}_i(t) + \frac{\delta t^2}{2m_i} \vec{F}_i(t) \quad 2.5$$

$$\vec{v}_i(t + \delta t) = \vec{v}_i(t) + \frac{\delta t}{2m_i} [\vec{F}_i(t) + \vec{F}_i(t + \delta t)] \quad 2.6$$

Where  $t$  is time,  $\delta t$  is the time step,  $\vec{F}_i$  is the sum of all forces acting on the particle  $i$ .  $\vec{r}_i$  and  $\vec{v}_i$  are the position and velocity of the particle  $i$ , respectively, and  $m_i$  is the mass of the particle  $i$ .

One can use various software packages to perform classical MD, such as GROMACS,<sup>65</sup> CHARMM,<sup>66</sup> or AMBER.<sup>67</sup> In this work, the presented classical MD simulations were performed using GROMACS 2020.1. The classical approach allows the study of large systems comprising millions of atoms for a timescales as long as a few microseconds. For instance, different trajectories were calculated for a system having tens of thousands of atoms (like DNA or other biomolecules), with each trajectories more than one microsecond.<sup>68,69,70</sup> But this method does not take into account the electrons explicitly. In addition, in classical MD, the stretching of the covalent bonds mostly relies on a harmonic function (see figure 2.17).<sup>2</sup> This implies that one cannot study the reactions dynamics as the bond-breaking and bond-forming is not possible.<sup>71</sup>

---

<sup>2</sup> GROMACS uses other functions or potentials as well, including Morse potential, Cubic potential, etc. for bond stretching and Cosine potential, Restricted potential etc., for bond angle.

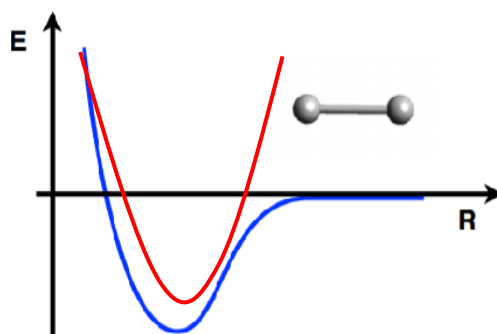


**Figure 2.17:** The plot of potential energy ( $E$ ) vs the interatomic distance ( $R$ ) between two covalently bonded atoms. The harmonic potential (red curve) is a good approximation for the exact potential between two covalently bonded atoms (blue curve) around its minimum, in the vicinity of the equilibrium inter-atomic distance.<sup>72</sup> It however does not allow the study of bond-breaking and bond-forming.

To obtain more information on the properties of the system, such as electronic structures or reaction mechanisms, the quantum mechanical nature of the electrons must be taken into account. *Ab-initio* Molecular Dynamics (AIMD) simulation is one such type of MD simulation (see section 2.5.1.2). This method, unlike classical MD, allows the study of bond breaking and forming, though it can only be used to study smaller systems ( $\sim 100$ s of atoms) for the timescale of a few 10's- 100's picoseconds.

### 2.5.1.2. *Ab-Initio Molecular Dynamics*

AIMD simulations are used in various fields of sciences, for instance to study electronic polarization effects,<sup>73,74</sup> reaction mechanisms, many-body forces, etc.<sup>75,14</sup> Liquid water, in particular, has attracted a lot of attention due to its importance in chemistry, biology but also others scientific fields.<sup>76,77</sup> AIMD proves to be an ideal approach to understand this simple molecules in its condensed phase, which has a rather complex chemistry.<sup>78</sup> In this work, we use the AIMD approach to study water and water-dipeptide mixtures.

In the AIMD approach, the electrons are treated as quantum particles, and the nuclei are treated classically. The forces acting on the nuclei are directly computed from the electronic structure, which is calculated 'on the fly', as the system evolves in time.<sup>79</sup>

The system at a fixed time can be parameterized in terms of the coordinates of the  $N_n$  nuclei ( $\vec{R} = \vec{R}_1, \vec{R}_2 \dots, \vec{R}_n$ ) and the  $N_e$  relevant electrons ( $\vec{r} = \vec{r}_1, \vec{r}_2 \dots, \vec{r}_{N_e}$ ). The quantum molecular system is characterized by a wavefunction  $\Phi(\vec{r}, \vec{R}, t)$  whose evolution is determined by the time-dependent Schrodinger equation (TDSE) (see equation 2.7).

$$i\hbar \frac{d\Phi(\vec{r}, \vec{R}, t)}{dt} = \hat{H}_T \Phi(\vec{r}, \vec{R}, t) \quad 2.7$$

Where  $\hat{H}_T$ , the non-relativistic Hamiltonian operator, is defined by:

$$\hat{H}_T = \hat{T}_N(\vec{R}) + \hat{V}_{NN}(\vec{R}) + \hat{T}_e(\vec{r}) + \hat{V}_{eN}(\vec{r}, \vec{R}) + \hat{V}_{ee}(\vec{r}) \quad 2.8$$

In equation 2.8,  $\hat{T}_N(\vec{R})$  and  $\hat{T}_e(\vec{r})$  represent the kinetic energy operators for the nuclei and electrons, respectively.  $\hat{V}_{eN}(\vec{r}, \vec{R})$ ,  $\hat{V}_{NN}(\vec{R})$  and  $\hat{V}_{ee}(\vec{r})$  are the potential energy operators for the nuclear-electron attraction, the nuclear-nuclear repulsion and the electron-electron repulsion, respectively. An equivalent notation for equation 2.8 is given by:

$$\hat{H}_T = \hat{T}_N(\vec{R}) + \hat{H}_e(\vec{r}, \vec{R}) \quad 2.9$$

where  $\hat{H}_e(\vec{r}, \vec{R})$  is the electronic Hamiltonian.

A particular solution of the TDSE can be found separating the electronic and nuclear variables from time. The total wavefunction solutions (stationary states) of the TDSE can be written as:

$$\Phi(\vec{r}, \vec{R}, t) = \Psi(\vec{r}, \vec{R}) \exp\left(\frac{-i}{\hbar} Et\right) \quad 2.10$$

where  $E$  is the energy of the system and  $\psi(\vec{r}, \vec{R})$  is an Eigen function of the time-independent Schrödinger (TISE) equation:

$$\hat{H}_T \psi(\vec{r}, \vec{R}) = E \psi(\vec{r}, \vec{R}) \quad 2.11$$

### 2.5.1.3. Born-Oppenheimer approximation

The Born Oppenheimer approximation is a concept in quantum mechanics that refers to the use of time-scale separation of the fast and slow degrees of freedom in order to solve the

time-dependent Schrödinger equation (equation 2.7). It applies to any system that evolves slowly compared to the relevant time scales of the underlying physics.<sup>80</sup> It assumes that the electronic motion and the nuclear motion can be treated separately, with the electrons moving in the field generated by the nuclei, which are considered to be fixed. In other words, because electrons are lighter than nuclei, they move and relax faster. Hence, they arrange themselves instantaneously to the position of the nuclei, which in turn move on the electronic potential energy surface.<sup>81</sup>

#### **2.5.1.4. Born-Oppenheimer molecular dynamics (BOMD)**

BOMD is a type of MD simulation that uses the Born-Oppenheimer approximation to separate the electronic and nuclear motion in a molecule. In this approach, the static electronic structure is calculated at each molecular dynamics step based on the fixed positions of the nuclei at that instant of time. Quantum mechanical methods, such as the density functional theory (DFT), described in section 2.5.1.6., are used to determine the solutions of the electronic TISE for clamped nuclei at positions ( $\vec{R}$ ):

$$\hat{H}_e \psi_0(\vec{r}; \vec{R}) = E_0(\vec{R}) \psi_0(\vec{r}; \vec{R}) \quad 2.12$$

Where  $\psi_0(\vec{r}; \vec{R})$  is the electronic wavefunction and  $E_0(\vec{R})$  is the energy, here referring to the electronic ground state, as determined using DFT (see section 2.5.1.6.), but this scheme could be applied to an excited electronic state although without considering any interferences with other states nor with itself.

The motion of the nuclei is determined by numerically solving the classical equations of motion:

$$M_i \ddot{R}_i = -\nabla_i E_k(\vec{R}) = \vec{F}_i (i = 1, \dots, N_n) \quad 2.13$$

The forces acting on the nuclei are calculated using the Hellman-Feynman theorem (equation 2.14).

$$\vec{F}_i(t) = -\langle \psi_0 | \nabla_i \hat{H}_e | \psi_0 \rangle \quad 2.14$$

Although BOMD can provide insight into the chemical reaction mechanisms, it is still computationally expensive as an evaluation of the electronic wavefunction is included at each time step.

#### **2.5.1.5. Car–Parrinello molecular dynamics (CPMD)**

The CPMD method, introduced in 1985,<sup>82</sup> is a starting point for combining on-the-fly electronic structure calculations to MD and statistical physics. The CPMD approach is not as time expensive as the standard BOMD simulations. It differs from BOMD in the way that the electronic variables are treated as dynamical degrees of freedom in an extended Lagrangian formalism, complete with fictitious electronic masses and velocities.<sup>83</sup> In the Car–Parrinello (CP) approach to AIMD, the electronic structure is described using the Kohn–Sham formulation of the density functional theory (DFT) and the Kohn–Sham orbitals are expanded in a plane wave basis. It is an iterative diagonalization approach that is used to minimize the total energy functional and is useful in a variety of physical and chemical applications.<sup>9, 84</sup>

In CPMD, the electron configuration must be in the ground state corresponding to the initial nuclear configuration, as it doesn't allow us to propagate the excited state. By choosing a small enough fictitious mass, the CPMD trajectories, derived from the extended Lagrangian, reproduce very closely the true (Born Oppenheimer) nuclear trajectories.

#### **2.5.1.6. Density functional theory**

The density-functional theory was developed by Hohenberg, Kohn and Sham (1964-1965).<sup>85,86</sup> DFT is the method of choice for first-principles electronic structure calculations in condensed phase and complex molecular environments. DFT-based approaches are used in a variety of disciplines ranging from condensed matter physics, to chemistry, materials science, biochemistry and biophysics. It is one way to solve the Schrödinger equation of the N-electrons system.

$$\hat{H}_{el} = \hat{T}_e(\vec{r}) + \hat{V}_{ee}(\vec{r}) + \hat{V}_{ext}(\vec{r}) \quad 2.15$$

Where  $\hat{H}_{el}$  is the electronic Hamiltonian (note that  $\hat{V}_{NN}(\vec{R})$  is not included here) and  $\hat{V}_{ext}(\vec{r})$  is the potential energy operator due to the interaction of the electrons with any other external



source, be it the nuclei, an external magnetic field, laser etc. Generally,  $\hat{V}_{ext}(\vec{r}) = \hat{V}_{eN}(\vec{r}, \vec{R})$ , i.e. the interaction between the electrons and the nuclei (as in equation 2.8).

DFT is based on the electron probability density function  $\rho(\vec{r}_M)$ , which is defined for a given normalized electronic wavefunction  $\Psi(\vec{r})$  as:

$$\rho(\vec{r}_M) = N \int |\Psi(\vec{r}_M, \vec{r}_2, \dots, \vec{r}_{N_e})|^2 d\vec{r}_2 \dots \vec{r}_{N_e} \quad 2.16$$

where  $\vec{r}_M$  is the position vector at point M. The principle of DFT is to determine the ground state wavefunction, which is uniquely determined by  $\hat{V}_{ext}(\vec{r})$ , which is also uniquely determined by the electron density (see equation 2.17).

$$\hat{V}_{ext}(\vec{r}) \Leftrightarrow \rho(\vec{r}_M) \quad 2.17$$

The ground state energy is a functional (function of a function) of the electron density (see equation 2.18).

$$E[\rho] = T_e[\rho] + V_{ee}[\rho] + V_{ext}[\rho] \quad 2.18$$

Where  $T_e[\rho]$  is the kinetic energy functional,  $V_{ee}[\rho]$  is the electron-electron repulsion energy functional and  $V_{ext}[\rho]$  is the external interaction energy functional. In the Kohn-Sham (KS) method, a fictitious system of  $N_e$  non-interacting electrons is introduced. The corresponding Hamiltonian is:

$$\hat{H}_S = \hat{T}_e + \hat{V}_S \quad 2.19$$

where  $\hat{V}_S$  is the external potential operator such that the ground state density of the non-interacting system is equal to the ground state density of the real (interacting) system. For the real system, we can rewrite the expression of the energy (2.18) in terms of quantities of the reference non-interacting system:

$$E[\rho] = T_s[\rho] + V_{eeH}[\rho] + V_{ext}[\rho] + (T_e[\rho] - T_s[\rho]) + (V_{ee}[\rho] - V_{eeH}[\rho]) \quad 2.20$$

Where  $T_s[\rho]$  is the mean kinetic energy of the non-interacting system at the same density ( $\rho$ ) as that of the interacting system and,  $V_{eeH}$  is the classical Coulomb Hartree term.

$$E[\rho] = T_s[\rho] + V_{eeH}[\rho] + V_{ext}[\rho] + E_{xc}[\rho] \quad 2.21$$

$$E[\rho] = T_s[\rho] + \frac{1}{2} \iint \frac{\rho(\vec{r}_{M_1})\rho(\vec{r}_{M_2})}{|\vec{r}_{M_1} - \vec{r}_{M_2}|} d\vec{r}_{M_1} d\vec{r}_{M_2} + \int \rho(\vec{r}_M) V_{ext}(\vec{r}_M) d\vec{r}_M + E_{xc}[\rho] \quad 2.22$$

Where  $E_{xc}$  is the final exchange correlation term. For the interacting system with  $N_e$  electrons, the differentiation of the energy functional yields the final form of the KS potential ( $v_{KS}$ ), also called effective potential. Thus, the Schrödinger equation for the set of non-interacting electrons moving under this external potential is given by:

$$[T + v_{KS}] \phi_i(\mathbf{r}) = \epsilon_i \phi_i(\mathbf{r}) \quad \epsilon_1 < \epsilon_2 < \dots < \epsilon_{N_e} \quad 2.23$$

where  $i$  runs to the number of electrons. This set of equations, known as Kohn-Sham equations, are one-particle equations and the solution to these is the Kohn-Sham orbitals. Each of these orbitals ( $\phi_i$ ) is associated with an energy value (Kohn-Sham energy,  $\epsilon_i$ ) given from the 'eigenvalue'.<sup>87</sup>

The term  $E_{xc}$  comprises of all the unknowns. It is the one that prevents DFT from being an exact method. It can therefore be determined using the equation 2.24, where it is defined as an integral of a function  $F$  that depends on the density, the functional Generalized Gradient Approximation (GGA)<sup>88</sup>, the functional meta-GGA<sup>89</sup> and so on.

$$E_{xc}[\rho] = \int d\vec{r} F(\rho(\vec{r}), \nabla\rho(\vec{r}), \nabla^2\rho(\vec{r}), \dots) \quad 2.24$$

Depending upon the system under investigation, we can change the quality of this approximation by truncating at different points. If this expression is used till its first term, this would lead to a Local density approximation (LDA). Though LDA works quite well in many cases (metals and semiconductors), in general underestimates the exchange energy and gives poor results for molecules. To improve this, both the density and its first derivative are included that gives a GGA and if the double derivative of density is also included, it results in a meta-GGA. GGA, as e.g. the BP (Becke-Perdew)<sup>90,91</sup> or the BLYP<sup>92</sup> functional, is proved to give quite accurate results. Apart from these functionals, hybrid functionals (such as B3LYP<sup>93</sup>) that include part of the exact HF exchange, are also broadly used.

### **2.5.1.7. Plane wave basis set**

In DFT, a basis set expansion is used to express the unknown Kohn-Sham (Molecular) Orbitals. Basis sets used in practical calculations are STO (exponential: Slater-type orbitals), GTO (Gaussian-type orbitals) and Plane waves. One of the most commonly used basis sets is the plane wave basis set.<sup>94</sup> According to the Bloch's theorem, the wavefunction ( $\Psi_j$ ) of an electron

in a band  $j$  can be written as a product of a cell-periodic part ( $f_k(\vec{r})$ ) and a wave like part ( $\exp(j\vec{k}\vec{r})$ ) as shown below:

$$\Psi_j(\vec{r}) = \exp(j\vec{k}\vec{r})f_k(\vec{r}) \quad 2.25$$

Where  $\vec{k}$  is the wave vector and  $\vec{r}$  is the position of the electron. Due to its periodicity, the function  $f_j$  can be expanded using a discrete set of plane waves whose wave vectors are reciprocal lattice vectors  $\vec{G}$  of the crystal. The size of the basis set is determined by inserting a cut-off:

$$E_{kin} = \left(\frac{h}{2\pi}\right)^2 \frac{1}{2m_e} \vec{G}^2 \leq E_{cut} \quad 2.26$$

that includes all plane waves whose kinetic energy ( $E_{kin}$ ) is below a defined limit  $E_{cut}$ .

Plane waves do not depend on nuclear positions so, unlike localized basis sets, correction terms are not needed for the calculation of forces. This type of basis set has some advantages over the Slater or Gaussian functions as it can be used for all atomic species and also at the end the convergence can be tested easily.<sup>95</sup> It can also be applied to non-periodic systems such as isolated systems.

In this work, for all the CPMD simulations, the plane wave basis set was used.

### **2.5.1.8. Concept of Pseudopotential**

Dealing with large systems can induce a lot of complexities and be computationally very expensive. New methods were thus devised to minimize these problems wherever possible. One such method was the introduction of the concept of pseudopotential. Since plane waves are not good for localized systems, core electrons and the strong ionic Coulomb potential are replaced by a weaker pseudopotential that acts on a set of pseudo wavefunction. This approximation is valid as only the valence electrons participate in the orbital overlapping during bond making while the core electrons remain localized to the nucleus of their atom. This approach of pseudopotential theory was earlier used for solid-state physics and later applied elsewhere.<sup>82,75</sup> It enables a reduction of the basis set's size that leads to effective speedup of calculation as it decreases the number of electrons taken into consideration, which in turn decreases the number of degrees of freedom.

### 2.5.1.9. Time-dependent Density functional theory

DFT allows the study of the ground state properties of a system. However, predicting the excited state properties, like the energy loss of the system, photoionization, absorption etc., where the system evolves with time, is possible using Time Dependent Density Functional theory (TDDFT).

We consider  $N_e$  electron systems that are governed by the nonrelativistic, time-dependent many-body Schrödinger equation:

$$i\left(\frac{\hbar}{2\pi}\right)\frac{d\psi(\vec{r},t)}{dt} = \hat{H}_{el}(t)\psi(\vec{r},t) \quad 2.27$$

where the electronic Hamiltonian  $\hat{H}_{el}(t) = \hat{T}_e(\vec{r}) + \hat{V}_{ee}(\vec{r}) + \hat{V}_{ext}(\vec{r},t)$ , includes a time-dependent external potential  $\hat{V}_{ext}(\vec{r},t)$ .

TDDFT is based on the Runge-Gross theorem,<sup>96,97</sup> which is an extension of Hohenberg and Kohn theorem. It establishes a one-to-one correspondence, between the external time-dependent potentials and the time-dependent one-body densities, for a given initial many-body state wavefunction:

$$\hat{V}_{ext}(\vec{r},t) \Leftrightarrow \rho(\vec{r},t) \quad 2.28$$

The idea is then to solve the TDSE of a non-interacting system that produces the same density as the interacting system. Time-dependent Kohn-Sham equations are then derived featuring an effective single-particle potential, such that the non-interacting system reproduces the exact density.

The TDDFT approach has proven to be very successful in the study of various chemical and physical processes, such as chemical reactions, photochemistry, and electronic structure of complex molecules.

### 2.5.1.10. Ehrenfest-TDDFT

Ehrenfest MD is a semi-classical MD that can be obtained from the time-dependent Schrödinger equation (equation 2.27). In mean-field Ehrenfest dynamics, the total wavefunction  $\Phi(\vec{r}, \vec{R}, t)$  is the product of a time-dependent electronic wavefunction and a

time-dependent nuclear wavefunction (and a phase factor). This allows to obtain two time-dependent differential equations, one for the electrons and the other nuclei. Each of them undergoes evolution influenced by time-dependent average potentials generated by each other. These average potentials provide a feedback interaction between the electronic and nuclear parts.<sup>97</sup> The classical limit is then taken for the nuclei motion. In Ehrenfest MD, the two time-dependent coupled differential equations for the electronic and nuclear dynamics are solve simultaneously.

TDDFT-MD uses a TDDFT approach to solve the electron's equation (see section 2.5.1.9). The time step required for TDDFT MD is two to three order of magnitude smaller than that in CPMD or BOMD. This is because of the electronic motion, which is faster than that of the nuclei.<sup>98</sup> TDDFT is thus computationally expensive and it is difficult to perform such calculations for large systems or even longer simulations for small system. It allows the electrons to evolve on arbitrary non-adiabatic states unlike BOMD or CPMD.<sup>99</sup>

Ehrenfest-TDDFT provides an orthogonalization-free alternative to CP AIMD, in addition to allowing the simulation of the excited state.<sup>99,97</sup> The Ehrenfest-TDDFT simulations performed in this work, use the code implemented in CPMD software and developed by Ivano Tavernelli.<sup>100</sup>

## 2.5.2. Modelling the doubly ionized species

### **2.5.2.1. The investigated systems and computational details**

The aim of the computational approach is to study doubly ionized species and provide a numerical counter-part to the thesis. Here, we list all the computational details and hypothesis used, from the building of the system of doubly ionized species to the analysis of the various reaction pathways in the aqueous medium.

All calculations have been performed using the plane-wave Kohn–Sham-based DFT code CPMD,<sup>101,102</sup> where the TDDFT scheme has been implemented.<sup>100</sup> This work was performed using HPC resources from GENCI-CINES/IDRIS (Grants 2019-085014 to 2023-085014) and the MESU supercomputer from Sorbonne University.

**Table 2.4:** List of systems studied in this work along with the simulation box size and available valence electrons in the system.

Systems studied	Box size (Å)	Number of valence electrons
a) HO <sup>°</sup> + 63 H <sub>2</sub> O (target system)	12.43	511
b) 64 H <sub>2</sub> O (control system)	12.43	512
c) Glycylglycine + 123 H <sub>2</sub> O	15.77	1036
d) Glycine + 43 H <sub>2</sub> O	11.31	374
e) Formamide + 60 H <sub>2</sub> O	12.36	498

The systems studied in this work are listed in see table 2.4. The local spin density approximation (LSD) was used for the system having an °OH, due to the presence of an unpaired electron.<sup>103</sup> For pure water system (control system), both spin-restricted and spin-unrestricted wavefunctions were used (to observe the difference, if any), whereas only spin-restricted wavefunctions were used for the other systems. Self-interaction correction was not taken into account for our simulation, as the effect of the error due to self-interaction is prominent in small simulation box (for instance, a system of 31 H<sub>2</sub>O + °OH, where the oxygen atoms of °OH and neighboring water molecule can interact).<sup>103</sup> This effect is minimized in simulations with the large box size like ours, as suggested by the authors.<sup>103,104</sup> Core electrons were replaced by pseudopotentials of the Trouiller-Martins form.<sup>105</sup> The Kleinman-Bylander<sup>106</sup> integration scheme is used for all types and the plane-wave basis set was truncated at an energy cut-off of 90 Ry. The exchange and correlation energy was calculated using the generalized gradient approximation (GGA) functional Becke–Lee–Yang–Parr (BLYP).<sup>107,108</sup> The time step for TDDFT simulation was 0.005 au and the time step for CPMD simulations was 0.25 au, and the fictitious mass was 6.25 au.

#### 2.5.2.2. Preparation of the system prior to double ionization

The *control system* (64 H<sub>2</sub>O) was already equilibrated prior to my Master thesis, by running a 2 ps CP MD, during which rescaling of velocities was applied. Because of a wave function optimization issue, the center of mass velocity increased during this part of the equilibration. The mean kinetic energy of the atoms in the center of mass frame was therefore 27 meV. The

equilibration was continued by a 1.45 ps BO MD, during which a rescaling of velocities was applied, and then a 0.12 ps BO MD, without rescaling of velocities. As will be discussed in chapter 4, the Coulomb explosion of  $\text{H}_2\text{O}^{2+}$  in liquid water results in a very fast and high local Kinetic Energy increase (up to 5.8 eV) resulting in hot atom chemistry, due to collisions with the two emitted H/H<sup>+</sup> atoms. As a consequence, we don't expect the equilibration temperature to have an impact on the conclusions drawn from Chapter 4. This will be checked in the future by running a few tests on a system by equilibrating it with controlled center of mass velocity.

The equilibrated *control system* was then directly used for performing the analysis in pure water. This configuration was also used to prepare the *target system* ( $^{\circ}\text{OH} + 63 \text{ H}_2\text{O}$ ). A hydrogen atom was removed from one of the neutral water molecules resulting in a box containing 63 water molecules, and an OH radical (see figure 2.18).

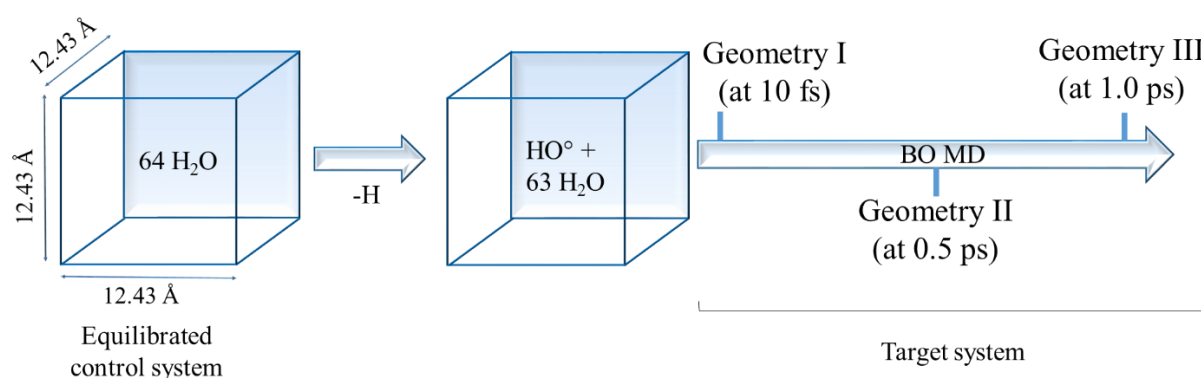


**Figure 2.18:** Preparation of starting geometries (I, II and III) of the target system, prior to double ionization. The first step corresponds to the removing of a hydrogen atom from a water molecule to have a hydroxyl radical in liquid water and it is followed by the equilibration step of 1 ps, using BO MD.

The deaerated system ( $\text{HO}^{\circ} + 63 \text{ H}_2\text{O}$ ) was equilibrated for one picosecond, by performing a BO MD of the neutral system with a 0.012 fs time step, allowing the  $\text{HO}^{\circ}$  to relax in the simulation box.<sup>109,110,111</sup> The average temperature was  $300 \pm 9 \text{ K}$ . Three different geometries (atomic positions and velocities) were chosen along this equilibration, to serve as an input for performing the dissociation analysis in deaerated water: Geometry I (at 10 fs, the non-equilibrated  $^{\circ}\text{OH}$ ), Geometry II (at 0.5 ps, the partially equilibrated  $^{\circ}\text{OH}$ ) and Geometry III (at 1.0 ps, fully equilibrated  $^{\circ}\text{OH}$ ).<sup>103</sup>

For systems c = 'Glycylglycine + 123 H<sub>2</sub>O', d = 'Glycine + 43 H<sub>2</sub>O' and e = 'Formamide + 60 H<sub>2</sub>O', the pdb files of biomolecule (Gly-Gly, Glycine and formamide) were extracted from the protein data bank and 'H' atoms were added to the structure using an interactive program 'Chimera' (version 1.16, copyright 2000-2020 by Regents of the University of California) for visualizing and analyzing molecular structures. The file was saved in the '.mol2' format and thanks to the server 'swissparam',<sup>112</sup> the topology file was generated. The generated topology file was used as an input for the high-performance molecular dynamics package, Gromacs 2020.1.<sup>113</sup> The biomolecule was centered in the box and the box size was defined by specifying its distance from the edge of the box. This distance was defined by keeping in mind that the biomolecule should not interact with its periodic image, i.e. this distance should be greater than the cut-off radius used for the non-bonded interactions. In the next step, solvent water molecules were added using the three-point solvent model, spc216.gro.<sup>114</sup> Further, the system was relaxed by the energy optimization step, ensuring that the starting geometry for the biomolecule and the surrounding water molecules was correct. The next step was to conduct the equilibration, which is usually a two-step process, NPT (Number of Particles, Volume and Temperature) and NVT (Number of Particles, Pressure and Temperature) to stabilize the temperature and pressure of the system, which was targeted to be 300 K and 1 bar, respectively.

A 100 ns classical molecular dynamics simulation, with a time step of 1 fs, was then performed at the desired temperature and pressure, to ensure the preparation of the system is good. The output configuration of the system was in 'gro' format. Thanks to the python code (see appendix II.I.), it was converted into a readable format for the CPMD package. The average temperature was 318 K for systems 'c' and 'd', and 295 K for system 'e' after the equilibration in Gromacs.

### **2.5.2.3. Modeling the prepared systems**

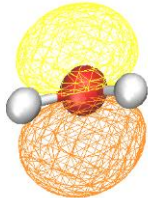
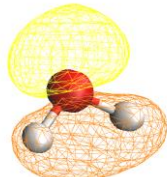
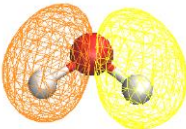
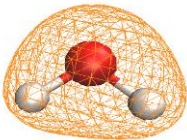
Two protocols were used to study the dynamics of a doubly ionized molecule embedded in liquid water. These protocols are detailed elsewhere (Protocol A<sup>115</sup> and Protocol B<sup>111</sup>) for pure water. Here, we explain briefly these protocols for the target system (HO<sup>o</sup> + 63 H<sub>2</sub>O) and extend its use to other systems of interest listed in section 2.5.2.1.



**Protocol A (TDDFT + CPMD)**

The first step of the protocol A was to create an initial non-stationary electronic state by removing two electrons from the Highest Occupied Molecular Orbital (HOMO), 1b1 molecular orbital (which is the most probable final state, 1b1<sup>-2</sup>),<sup>116</sup> of a specific water molecule in the sample (W42, see figure 2.19) in proximity to the OH radical. All the other molecules were kept neutral, thanks to the use of effective Wannier MO associated with each water molecule.<sup>117</sup> The contour of the Wannier MO centered on W42 are shown in table 2.5.

**Table 2.5:** Effective Wannier MO centered on W42. The other water molecules in the simulation box are hidden for clear visuals. The Wannier MO contours are represented with an iso-value of ( $\pm 0.06$ ), where the orange color denotes positive value and the yellow color denotes a negative value.

Wannier MO of W42	Energy (eV)	Contour
1b1	-3.98	
3a1	-5.98	
1b2	-8.71	
2a1	-21.13	

The time evolution of the system,  $\text{OH} + \text{H}_2\text{O}^{2+} + 62 \text{H}_2\text{O}$ , was then modelled for 30 fs using TDDFT MD. As a second step, different configurations along the TDDFT MD were chosen as an input configuration to switch to the ground-state CPMD. The time at which the switch was made from TDDFT to CPMD was the so-called switch time (see figure 2.19, protocol A). The geometry at the switch time was used as the starting geometry for the next step, i.e. the CPMD simulation for  $\sim 1$  ps.

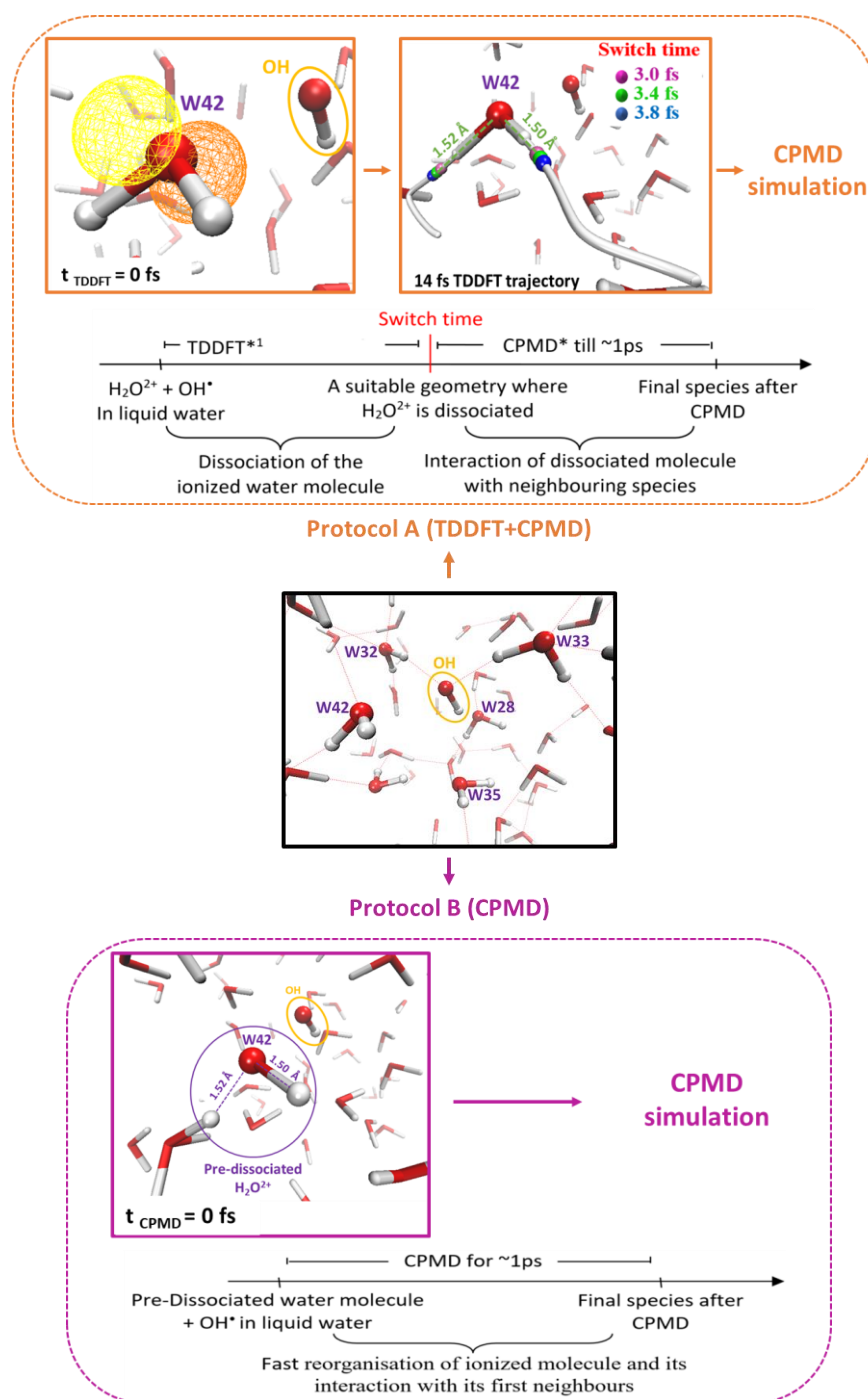


**Figure 2.19:** The scheme shows two protocols, A and B, used in our study to understand the dissociation of a doubly ionized water molecule in proximity of an OH radical in liquid water. The scheme presents the analysis of the target system. The water molecules selected in the first and the second hydration sphere of  $^{\circ}\text{OH}$ , to perform dissociation studies, are labeled in purple. The two protocols are explained using one of the scenarios under investigation, i.e. W42 as the dissociating doubly ionized water molecule. The OH dissociation length, labelled in protocol A and B corresponds to that at 3.4 fs after the TDDFT trajectory.

### Protocol B (CPMD)

Since TDDFT MD are time expensive, it becomes impractical to perform many simulations using the protocol A. An alternate protocol,<sup>111</sup> was therefore used to make an extensive study of the doubly ionized systems of interest.

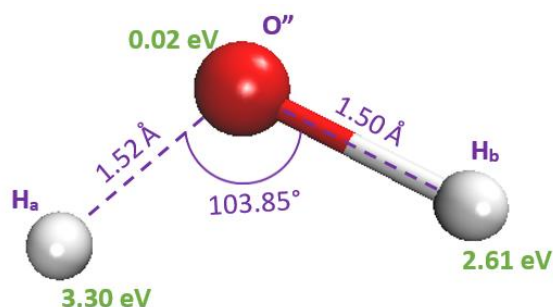


**Figure 2.20:** The parameters of the pre-dissociated water molecule, W42, selected for protocol B.

The starting system, in protocol B, was a pre-dissociated water molecule located in proximity of the OH radical in liquid water (see figure 2.19). The parameters of the pre-dissociated water molecule (O-H lengths, HOH angle and the velocities of the three atoms) (see figure 2.20) were extracted from the configuration (atomic position and velocities) of the molecule W42 at 3.4 fs switch time in protocol A.<sup>111</sup> To perform the statistics, 5 different water molecules, present in the first and second hydration sphere (which have been shown to play a big role in dynamics and interactions<sup>118,119</sup>) of the OH segment, were substituted with the parameters of the pre-dissociated water molecule. Two cases, where the dissociating water molecule was far from the hydroxyl radical were also studied. The evolution of the system was then followed entirely using CPMD for around 1 ps.

#### 2.5.2.4. Data analysis

##### 2.5.2.4.i. Bader charge analysis

Bader charge analysis is based on the Quantum Theory of Atoms In Molecules (QTAIM), developed by Richard Bader,<sup>120</sup> which provides a way to divide the molecules into atoms based on the electron density. The Bader analysis is based on the zero-flux surface, which is a boundary surface that separates regions of space around each atom where the electron density flows towards or away from the atom. It is a fast and robust way to analyze the charge,

by partitioning the electron density of a molecule into atomic contributions. It is very useful in understanding the chemical and mechanical properties.<sup>120</sup>

To analyze the charge using this method, the first step is to analyze the density of the system, obtained from the *ab-initio* calculation. Using the Bader algorithm (algorithm bound by zero-flux surface), the electron density is segregated. By integrating the electron density within each atomic basin (region where majority of the electron density associated with that atom is located), the charge on each atom can be identified.

All the charge analysis reported in this work are performed using this method.

In the case of polar bonds, for instance the O-H bond, owing to the electronegativity of the oxygen atom, the hydrogen atom attains a partial positive charge. Since the Bader charge analysis determines the boundaries around each atom and calculates the electron charge associated with each atomic region (Bader volume),<sup>121</sup> the charge analysis of H can be difficult around the oxygen atom. The Bader analysis method, therefore, poses limitations in accurately determining the electrostatic potentials and the dipole moments, given that the higher multipole moments are not taken into account.<sup>121</sup>

#### 2.5.2.4.ii. Density of states calculation

Density of States (DOS) provides information about the allowed energy levels available to electrons in the system and provides information about the occupancy of each of these energy levels. In this work, we perform the DOS calculations using the following equation.<sup>117</sup>

$$D(\varepsilon) = \langle \delta(\varepsilon - \hat{H}_s) \rangle \quad 2.29$$

Where  $D(\varepsilon)$  is the density of states as a function of energy,  $\varepsilon$ , and  $\hat{H}_s$  is the self-consistent one-electron KS Hamiltonian. To determine DOS, the first step is to calculate the ground state electronic wavefunction for several configurations (25 configurations, at an interval of 720 fs until 18 ps) along a CPMD trajectory of the neutral system. The files are then used to determine KS eigenvalues (the energy levels of the KS orbitals, see section 2.5.1.6).

For each energy interval (0.2 eV), the number of electronic states falling within that interval is counted. This count is then divided by the width of the energy interval to obtain the DOS. The resulting DOS is often presented as a graph or plot, with energy on the x-axis and the DOS on

the y-axis. To compare the DOS of system with different size, the DOS values are also divided by the number of electrons present in the system (see table 2.4).

#### 2.5.2.4.iii. Trajectory/Geometrical analysis

All the trajectory analysis carried out in this work was visualized using the visualizing software VMD<sup>122</sup> and all the figures for the simulation are prepared using this software. During a certain trajectory, dynamic bonds are used (one of the features of VMD) to follow the bond breaking and bon-making, with a defined bond length ( $r_{O-H}$ ) criterion (see equations 2.30 and 2.31).

$$OH \text{ bond} = \begin{cases} \text{not broken, } r_{O-H} < 1.4 \\ \text{broken, } r_{O-H} \geq 1.4 \end{cases} \quad 2.30$$

$$OO \text{ bond} = \begin{cases} \text{not broken, } r_{O-O} < 1.8 \\ \text{broken, } r_{O-O} \geq 1.8 \end{cases} \quad 2.31$$

For the H-bond, the geometrical criteria used were: the O-O bond distance ( $r_{O-O}$ )  $< 3 \text{ \AA}$  and the angle ( $\beta$ )  $< 20^\circ$ . The angle  $\beta$  was the angle of the donated hydrogen from the line joining both oxygen atoms (from donating and withdrawing water molecule) (see figure 2.21). These criteria are the default values used in VMD.

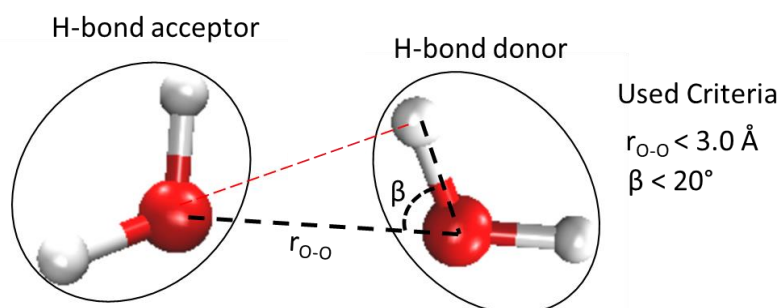


**Figure 2.21:** The criteria used for defining the H-bond in the present work: The bond distance ( $r_{O-O}$ ) between the oxygen atom of the accepting and donating water molecule is less than  $3 \text{ \AA}$  and the angle  $\beta$  is less than  $20^\circ$ .

The information on the Bader charges (thanks to the density calculation) and Kinetic energy (thanks to the velocities of the atoms) of the atoms was extracted from the trajectory.

#### 2.5.2.5. Typical CPU time

One of the key differences between the computational methods, TDDFT MD and CPMD or BOMD is the computational time. In terms of practical sense, it is one of the main limitation

factors and hence the choice has to be a compromise between the computational cost and the information required from the simulation. The comparison between their CPU time is indicated in the table 2.6. The reported computational times in table 2.6 are for the target system modelled using the CPMD code<sup>82</sup> in its version v.3.17, run on Occigen (CINES), GENCI.

**Table 2.6:** Comparison of CPU time for the target system ( $\text{HO}^\circ + 63 \text{H}_2\text{O}$ ) using TDDFT MD (0.18 fs) and CPMD (120 fs).

Computational method	Processors	Time-step (au)	Total steps	Steps/min	Total CPU time (hr)
TDDFT MD	48	0.005	1500	1.3	19.7
CP MD	48	0.25	20000	21.4	15.6

## References

- (1) Huart, L. Inner Shell Ionization Effects on Molecules of Biological Interest in an Aqueous Medium. phdthesis, Sorbonne Université, 2022. <https://tel.archives-ouvertes.fr/tel-03725615> (accessed 2022-09-02).
- (2) deAlmeida, C. E.; Ochoa, R.; de Lima, M. C.; David, M. G.; Pires, E. J.; Peixoto, J. G.; Salata, C.; Bernal, M. A. A Feasibility Study of Fricke Dosimetry as an Absorbed Dose to Water Standard for <sup>192</sup>Ir HDR Sources. *PLoS One* **2014**, *9* (12), e115155. <https://doi.org/10.1371/journal.pone.0115155>.
- (3) Margoliash, E.; Frohwirt, N. Spectrum of Horse-Heart Cytochrome c. *Biochem J* **1959**, *71* (3), 570–572. <https://doi.org/10.1042/bj0710570>.
- (4) Absorption Spectra and Some Other Properties of Cytochrome c and of Its Compounds with Ligands. *Proc. R. Soc. Lond. B* **1962**, *156* (965), 429–458. <https://doi.org/10.1098/rspb.1962.0049>.
- (5) Zabinski-Snopko, R. M.; Czerlinski, G. H. Spectrophotometric Titrations of Ferricytochrome C with Ferrihexacyanide in the pH Range 5 to 7. *J Biol Phys* **1981**, *9* (3), 155–167. <https://doi.org/10.1007/BF01988248>.
- (6) Tiwari, K.; Wavdhane, M.; Haque, S.; Govender, T.; Kruger, H. G.; Mishra, M. K.; Chandra, R.; Tiwari, D. A Sensitive WST-8-Based Bioassay for PEGylated Granulocyte Colony Stimulating Factor Using the NFS-60 Cell Line. *Pharm Biol* **2015**, *53* (6), 849–854. <https://doi.org/10.3109/13880209.2014.943248>.
- (7) Chamchoy, K.; Pakotiprapha, D.; Pumirat, P.; Leartsakulpanich, U.; Boonyuen, U. Application of WST-8 Based Colorimetric NAD(P)H Detection for Quantitative Dehydrogenase Assays. *BMC Biochemistry* **2019**, *20* (1), 4. <https://doi.org/10.1186/s12858-019-0108-1>.
- (8) Schroeder, W. A.; Shelton, J. R.; Shelton, J. B.; Olson, B. M. SOME AMINO ACID SEQUENCES IN BOVINE-LIVER CATALASE. *Biochim Biophys Acta* **1964**, *89*, 47–65. [https://doi.org/10.1016/0926-6569\(64\)90100-2](https://doi.org/10.1016/0926-6569(64)90100-2).
- (9) Sund, H.; Weber, K.; Mölbert, E. [Dissociation of beef liver catalase in its subunits]. *Eur J Biochem* **1967**, *1* (4), 400–410. <https://doi.org/10.1111/j.1432-1033.1967.tb00088.x>.
- (10) *Best Theratronics Products - Gammacell 1000/3000*. [http://www.theratronics.ca/product\\_gamma.html](http://www.theratronics.ca/product_gamma.html) (accessed 2023-05-08).
- (11) Russell, B. C.; Croudace, I. W.; Warwick, P. E. Determination of <sup>135</sup>Cs and <sup>137</sup>Cs in Environmental Samples: A Review. *Analytica Chimica Acta* **2015**, *890*, 7–20. <https://doi.org/10.1016/j.aca.2015.06.037>.
- (12) Duncan, D. *Half Lives Explained*. <https://dec.alaska.gov/eh/radiation/half-lives-explained/> (accessed 2023-05-08).
- (13) Klassen, N. V.; Shortt, K. R.; Seuntjens, J.; Ross, C. K. Fricke Dosimetry: The Difference between G(Fe<sup>3+</sup>) for <sup>60</sup>Co Gamma-Rays and High-Energy x-Rays. *Phys Med Biol* **1999**, *44* (7), 1609–1624. <https://doi.org/10.1088/0031-9155/44/7/303>.
- (14) Schlachter, A. S. Third-Generation Synchrotron Light Sources. In *New Directions in Research with Third-Generation Soft X-Ray Synchrotron Radiation Sources*; Schlachter, A. S., Wuilleumier, F. J., Eds.; NATO ASI Series; Springer Netherlands: Dordrecht, 1994; pp 1–22. [https://doi.org/10.1007/978-94-011-0868-3\\_1](https://doi.org/10.1007/978-94-011-0868-3_1).
- (15) Bilderback, D. H.; Elleaume, P.; Weckert, E. Review of Third and next Generation Synchrotron Light Sources. *J. Phys. B: At. Mol. Opt. Phys.* **2005**, *38* (9), S773. <https://doi.org/10.1088/0953-4075/38/9/022>.



- (16) *SOLEIL in 3 questions | French national synchrotron facility*. <https://www.synchrotron-soleil.fr/en/about-us/what-soleil/soleil-3-questions> (accessed 2023-05-09).
- (17) Meuris, A.; Schneider, B.; Allaire, H.; Baudin, D.; Cojocari, I.; Da Silva, P.; Doumayrou, E.; Götz, D.; Ferrando, P.; Laurent, P.; Lortholary, M.; Mercère, P.; Pinsard, F.; Prieur, M.; Pichon, T.; Provost, L.; Renaud, D.; Renault-Tinacci, N.; Tollet, T.; Visticot, F. Characterization of the Focal Plane of the Microchannel X-Ray Telescope at the Metrology Beamline of SOLEIL Synchrotron for the Space Astronomy Mission SVOM. *Nuclear Instruments and Methods in Physics Research Section A: Accelerators, Spectrometers, Detectors and Associated Equipment* **2023**, *1048*, 167909. <https://doi.org/10.1016/j.nima.2022.167909>.
- (18) Polack, F.; Silly, M.; Chauvet, C.; Lagarde, B.; Bergeard, N.; Izquierdo, M.; Chubar, O.; Krizmancic, D.; Ribbens, M.; Duval, J. -P.; Basset, C.; Kubsky, S.; Sirotti, F. TEMPO: A New Insertion Device Beamline at SOLEIL for Time Resolved Photoelectron Spectroscopy Experiments on Solids and Interfaces. *AIP Conference Proceedings* **2010**, *1234* (1), 185–188. <https://doi.org/10.1063/1.3463169>.
- (19) Tissot, H.; Olivieri, G.; Gallet, J.-J.; Bournel, F.; Silly, M. G.; Sirotti, F.; Rochet, F. Cation Depth-Distribution at Alkali Halide Aqueous Solution Surfaces. *J. Phys. Chem. C* **2015**, *119* (17), 9253–9259. <https://doi.org/10.1021/jp512695c>.
- (20) Herve du Penhoat, M. A.; Fayard, B.; Abel, F.; Touati, A.; Gobert, F.; Despiney-Bailly, I.; Ricoul, M.; Sabatier, L.; Stevens, D. L.; Hill, M. A.; Goodhead, D. T.; Chetioui, A. Lethal Effect of Carbon K-Shell Photoionizations in Chinese Hamster V79 Cell Nuclei: Experimental Method and Theoretical Analysis. *Radiat Res* **1999**, *151* (6), 649–658.
- (21) Huart, L.; Nicolas, C.; Kaddissy, J. A.; Guigner, J.-M.; Touati, A.; Politis, M.-F.; Mercere, P.; Gervais, B.; Renault, J.-P.; Hervé du Penhoat, M.-A. Soft X-Ray Radiation and Monte Carlo Simulations: Good Tools to Describe the Radiation Chemistry of Sub-keV Electrons. *J. Phys. Chem. A* **2020**, *124* (10), 1896–1902. <https://doi.org/10.1021/acs.jpca.9b10539>.
- (22) Gobert, F. -n.; Lamoureux, M.; Penhoat, M. -a. H. du; Ricoul, M.; Boissière, A.; Touati, A.; Abel, F.; Politis, M. -f.; Fayard, B.; Guigner, J. M.; Martins, L.; Testard, I.; Sabatier, L.; Chetioui, A. Chromosome Aberrations and Cell Inactivation Induced in Mammalian Cells by Ultrasoft X-rays: Correlation with the Core Ionizations in DNA. *International Journal of Radiation Biology* **2004**, *80* (2), 135–145. <https://doi.org/10.1080/09553000310001654710>.
- (23) Fayard, B.; Touati, A.; Abel, F.; Penhoat, M. A. H. du; Despiney-Bailly, I.; Gobert, F.; Ricoul, M.; L’Hoir, A.; Politis, M. F.; Hill, M. A.; Stevens, D. L.; Sabatier, L.; Sage, E.; Goodhead, D. T.; Chetioui, A. Cell Inactivation and Double-Strand Breaks: The Role of Core Ionizations, as Probed by Ultrasoft X Rays. *rare* **2002**, *157* (2), 128–140. [https://doi.org/10.1667/0033-7587\(2002\)157\[0128:CIADSB\]2.0.CO;2](https://doi.org/10.1667/0033-7587(2002)157[0128:CIADSB]2.0.CO;2).
- (24) Gosse, C.; Stanescu, S.; Frederick, J.; Lefrançois, S.; Vecchiola, A.; Moskura, M.; Swaraj, S.; Belkhou, R.; Watts, B.; Haltebourg, P.; Blot, C.; Daillant, J.; Guenoun, P.; Chevillard, C. A Pressure-Actuated Flow Cell for Soft X-Ray Spectromicroscopy in Liquid Media. *Lab Chip* **2020**, *20* (17), 3213–3229. <https://doi.org/10.1039/C9LC01127G>.
- (25) Huart, L.; Nicolas, C.; Hervé du Penhoat, M.-A.; Guigner, J.-M.; Gosse, C.; Palaudoux, J.; Lefrançois, S.; Mercere, P.; Dasilva, P.; Renault, J.-P.; Chevillard, C. A Microfluidic Dosimetry Cell to Irradiate Solutions with Poorly Penetrating Radiations: A Step towards Online Dosimetry for Synchrotron Beamlines. *J Synchrotron Rad* **2021**, *28* (3), 778–789. <https://doi.org/10.1107/S1600577521002691>.

- (26) Creemer, J. F.; Santagata, F.; Morana, B.; Mele, L.; Alan, T.; Iervolino, E.; Pandraud, G.; Sarro, P. M. An All-in-One Nanoreactor for High-Resolution Microscopy on Nanomaterials at High Pressures. In *2011 IEEE 24th International Conference on Micro Electro Mechanical Systems*; 2011; pp 1103–1106. <https://doi.org/10.1109/MEMSYS.2011.5734622>.
- (27) *Integrating Spheres*. <https://www.shimadzu.com/an/service-support/technical-support/analysis-basics/fundamentals-uv/integratingspheres.html> (accessed 2023-07-18).
- (28) Murphy, A. Modified Kubelka-Munk Model for Calculation of the Reflectance of Coatings with Optically-Rough Surfaces. *Journal of Physics D: Applied Physics* **2006**, *39*, 3571. <https://doi.org/10.1088/0022-3727/39/16/008>.
- (29) George, P.; Chowdhury, P. Complex Dielectric Transformation of UV-Vis Diffuse Reflectance Spectra for Estimating Optical Band-Gap Energies and Materials Classification. *Analyst* **2019**, *144* (9), 3005–3012. <https://doi.org/10.1039/C8AN02257G>.
- (30) Butarbutar, S.; Meesungnoen, J.; Guzonas, D.; Stuart, C.; Jay-Gerin, J.-P. Modeling the Radiolysis of Supercritical Water by Fast Neutrons: Density Dependence of the Yields of Primary Species at 400°C. *Radiation research* **2014**, *182*. <https://doi.org/10.1667/RR13715.1>.
- (31) Pankove, J. I. *Optical Processes in Semiconductors*; Prentice-Hall: Englewood Cliffs, N.J, 1971.
- (32) Makuła, P.; Pacia, M.; Macyk, W. How To Correctly Determine the Band Gap Energy of Modified Semiconductor Photocatalysts Based on UV–Vis Spectra. *J. Phys. Chem. Lett.* **2018**, *9* (23), 6814–6817. <https://doi.org/10.1021/acs.jpcllett.8b02892>.
- (33) Butterfly, B. *Electron Spectroscopy for Surfaces Analysis*. FindLight Blog. <https://www.findlight.net/blog/electron-spectroscopy-for-surface-analysis/> (accessed 2023-05-11).
- (34) Introduction. In *Handbook of Mineral Spectroscopy*; Klopogge, J. T., Wood, B. J., Eds.; Elsevier, 2021; pp xiii–xxv. <https://doi.org/10.1016/B978-0-12-804522-0.02001-0>.
- (35) Dogan, M.; Ulu, M.; Gennarakis, G. G.; Zouros, T. J. M. Experimental Energy Resolution of a Paracentric Hemispherical Deflector Analyzer for Different Entry Positions and Bias. *Review of Scientific Instruments* **2013**, *84* (4), 043105. <https://doi.org/10.1063/1.4798592>.
- (36) *AXIS Supra+ X-ray photoelectron spectrometer*. <https://www.kratos.com/products/axis-supra-xps-surface-analysis-instrument> (accessed 2023-05-09).
- (37) Baer, D. R.; Artyushkova, K.; Cohen, H.; Easton, C. D.; Engelhard, M.; Gengenbach, T. R.; Greczynski, G.; Mack, P.; Morgan, D. J.; Roberts, A. XPS Guide: Charge Neutralization and Binding Energy Referencing for Insulating Samples. *Journal of Vacuum Science & Technology A* **2020**, *38* (3), 031204. <https://doi.org/10.1116/6.0000057>.
- (38) Bashouti, M.; Paska, Y.; Puniredd, S. R.; Stelzner, T.; Christiansen, S.; Haick, H. Silicon Nanowires Terminated with Methyl Functionalities Exhibit Stronger Si-C Bonds than Equivalent 2D Surfaces. *Physical chemistry chemical physics : PCCP* **2009**, *11*, 3845–3848. <https://doi.org/10.1039/b820559k>.
- (39) Tissot, H.; Gallet, J.-J.; Bournel, F.; Olivieri, G.; Silly, M. G.; Sirotti, F.; Boucly, A.; Rochet, F. The Electronic Structure of Saturated NaCl and NaI Solutions in Contact with a Gold Substrate. *Top Catal* **2016**, *59* (5), 605–620. <https://doi.org/10.1007/s11244-015-0530-6>.

- (40) Greczynski, G.; Hultman, L. The Same Chemical State of Carbon Gives Rise to Two Peaks in X-Ray Photoelectron Spectroscopy. *Sci Rep* **2021**, *11* (1), 11195. <https://doi.org/10.1038/s41598-021-90780-9>.
- (41) Ramirez, L. P. Electronic Structure of Interfaces Studied by in Situ Real-Time XPS.
- (42) Renault, J.-P.; Huart, L.; Milosavljević, A. R.; Bozek, J. D.; Palaudoux, J.; Guigner, J.-M.; Marichal, L.; Leroy, J.; Wien, F.; Hervé Du Penhoat, M.-A.; Nicolas, C. Electronic Structure and Solvation Effects from Core and Valence Photoelectron Spectroscopy of Serum Albumin. *IJMS* **2022**, *23* (15), 8227. <https://doi.org/10.3390/ijms23158227>.
- (43) Malerz, S.; Trinter, F.; Hergenbahn, U.; Ghrist, A.; Ali, H.; Nicolas, C.; Saak, C.-M.; Richter, C.; Hartweg, S.; Nahon, L.; Lee, C.; Goy, C.; M. Neumark, D.; Meijer, G.; Wilkinson, I.; Winter, B.; Thürmer, S. Low-Energy Constraints on Photoelectron Spectra Measured from Liquid Water and Aqueous Solutions. *Physical Chemistry Chemical Physics* **2021**, *23* (14), 8246–8260. <https://doi.org/10.1039/D1CP00430A>.
- (44) Truong, S. Y.; Yench, A. J.; Juarez, A. M.; Cavanagh, S. J.; Bolognesi, P.; King, G. C. Threshold Photoelectron Spectroscopy of H<sub>2</sub>O and D<sub>2</sub>O over the Photon Energy Range 12–40eV. *Chemical Physics* **2009**, *355* (2–3), 183–193. <https://doi.org/10.1016/j.chemphys.2008.12.009>.
- (45) Winter, B.; Aziz, E. F.; Hergenbahn, U.; Faubel, M.; Hertel, I. V. Hydrogen Bonds in Liquid Water Studied by Photoelectron Spectroscopy. *J. Chem. Phys.* **2007**, *126* (12), 124504. <https://doi.org/10.1063/1.2710792>.
- (46) Sankari, R.; Ehara, M.; Nakatsuji, H.; Senba, Y.; Hosokawa, K.; Yoshida, H.; De Fanis, A.; Tamenori, Y.; Aksela, S.; Ueda, K. Vibrationally Resolved O 1s Photoelectron Spectrum of Water. *Chemical Physics Letters* **2003**, *380* (5), 647–653. <https://doi.org/10.1016/j.cplett.2003.08.108>.
- (47) Nishizawa, K.; Kurahashi, N.; Sekiguchi, K.; Mizuno, T.; Ogi, Y.; Horio, T.; Oura, M.; Kosugi, N.; Suzuki, T. High-Resolution Soft X-Ray Photoelectron Spectroscopy of Liquid Water. *Phys. Chem. Chem. Phys.* **2011**, *13* (2), 413–417. <https://doi.org/10.1039/C0CP01636E>.
- (48) Saito, N.; Suzuki, I. Photon W Value for Krypton in the M-Shell Transition Region. *Radiation research* **2001**, *156*, 317–323. [https://doi.org/10.1667/0033-7587\(2001\)156\[0317:PWVFKI\]2.0.CO;2](https://doi.org/10.1667/0033-7587(2001)156[0317:PWVFKI]2.0.CO;2).
- (49) Koike, M.; Nakada, R.; Kajitani, I.; Usui, T.; Tamenori, Y.; Sugahara, H.; Kobayashi, A. In-Situ Preservation of Nitrogen-Bearing Organics in Noachian Martian Carbonates. *Nat Commun* **2020**, *11* (1), 1988. <https://doi.org/10.1038/s41467-020-15931-4>.
- (50) Lizzit, S.; Zampieri, G.; Kostov, K. L.; Tyuliev, G.; Larciprete, R.; Petaccia, L.; Naydenov, B.; Menzel, D. Charge Transfer from Core-Excited Argon Adsorbed on Clean and Hydrogenated Si(100): Ultrashort Timescales and Energetic Structure. *New J. Phys.* **2009**, *11* (5), 053005. <https://doi.org/10.1088/1367-2630/11/5/053005>.
- (51) Marr, G. V.; West, J. B. Absolute Photoionization Cross-Section Tables for Helium, Neon, Argon, and Krypton in the VUV Spectral Regions. *Atomic Data and Nuclear Data Tables* **1976**, *18* (5), 497–508. [https://doi.org/10.1016/0092-640X\(76\)90015-2](https://doi.org/10.1016/0092-640X(76)90015-2).
- (52) Pérez Ramírez, L.; Boucly, A.; Saudrais, F.; Bournel, F.; Gallet, J.-J.; Maisonhaute, E.; Milosavljević, A. R.; Nicolas, C.; Rochet, F. The Fermi Level as an Energy Reference in Liquid Jet X-Ray Photoelectron Spectroscopy Studies of Aqueous Solutions. *Phys. Chem. Chem. Phys.* **2021**, *23* (30), 16224–16233. <https://doi.org/10.1039/D1CP01511G>.
- (53) Thürmer, S.; Malerz, S.; Trinter, F.; Hergenbahn, U.; Lee, C.; Neumark, D. M.; Meijer, G.; Winter, B.; Wilkinson, I. Accurate Vertical Ionization Energy and Work Function

- Determinations of Liquid Water and Aqueous Solutions. *Chem. Sci.* **2021**, *12* (31), 10558–10582. <https://doi.org/10.1039/D1SC01908B>.
- (54) Schultz, T. A Unified Secondary Electron Cut-off Presentation and Common Mistakes in Photoelectron Spectroscopy. *Electron. Struct.* **2022**, *4* (4), 044002. <https://doi.org/10.1088/2516-1075/ac9ffb>.
- (55) Greenwald, M. Beyond Benchmarking—How Experiments and Simulations Can Work Together in Plasma Physics. *Computer Physics Communications* **2004**, *164* (1–3), 1–8. <https://doi.org/10.1016/j.cpc.2004.06.001>.
- (56) Kästner, J.; Arnold, E. When Can a Computer Simulation Act as Substitute for an Experiment? A Case-Study from Chemistry.
- (57) McLean, C.; Lee, Y. T.; Jain, S.; Hutchings, C. *Modeling and Simulation of Hazardous Material Releases for Homeland Security Applications*, 0 ed.; NIST IR 7786; National Institute of Standards and Technology: Gaithersburg, MD, 2011; p NIST IR 7786. <https://doi.org/10.6028/NIST.IR.7786>.
- (58) Mirmohammadi, S. A.; Shen, L.; Gan, Y. A Reliable Approach for Calculating Thermophysical Properties of Liquid Using Molecular Dynamics Simulations. *Chemical Physics Letters* **2018**, *712*, 44–53. <https://doi.org/10.1016/j.cplett.2018.09.048>.
- (59) Bursulaya, B. D.; Kim, H. J. Spectroscopic and Dielectric Properties of Liquid Water: A Molecular Dynamics Simulation Study. *The Journal of Chemical Physics* **1998**, *109* (12), 4911–4919. <https://doi.org/10.1063/1.477102>.
- (60) Garkul, A.; Stegailov, V. Molecular Dynamics Analysis of Elastic Properties and New Phase Formation during Amorphous Ices Transformations. *Sci Rep* **2022**, *12* (1), 13325. <https://doi.org/10.1038/s41598-022-17666-2>.
- (61) Chen, Y.; Morishita, K. Molecular Dynamics Simulation of Defect Production in Fe Due to Irradiation. *Nuclear Materials and Energy* **2022**, *30*, 101150. <https://doi.org/10.1016/j.nme.2022.101150>.
- (62) Das, A.; Ali, Sk. M. Understanding of Interfacial Tension and Interface Thickness of Liquid/Liquid Interface at a Finite Concentration of Alkyl Phosphate by Molecular Dynamics Simulation. *Journal of Molecular Liquids* **2019**, *277*, 217–232. <https://doi.org/10.1016/j.molliq.2018.12.116>.
- (63) Hospital, A.; Goñi, J. R.; Orozco, M.; Gelpi, J. L. Molecular Dynamics Simulations: Advances and Applications. *AABC* **2015**, *8*, 37–47. <https://doi.org/10.2147/AABC.S70333>.
- (64) Brooks, C. L.; Case, D. A.; Plimpton, S.; Roux, B.; van der Spoel, D.; Tajkhorshid, E. Classical Molecular Dynamics. *J. Chem. Phys.* **2021**, *154* (10), 100401. <https://doi.org/10.1063/5.0045455>.
- (65) Welcome to GROMACS — GROMACS webpage <https://www.gromacs.org/documentation>. <https://www.gromacs.org/> (accessed 2023-05-23).
- (66) CHARMM: Home. <https://www.charmm.org/> (accessed 2023-05-23).
- (67) The Amber Molecular Dynamics Package. <https://ambermd.org/> (accessed 2023-05-23).
- (68) Klepeis, J. L.; Lindorff-Larsen, K.; Dror, R. O.; Shaw, D. E. Long-Timescale Molecular Dynamics Simulations of Protein Structure and Function. *Current Opinion in Structural Biology* **2009**, *19* (2), 120–127. <https://doi.org/10.1016/j.sbi.2009.03.004>.
- (69) Pérez, A.; Luque, F. J.; Orozco, M. Dynamics of B-DNA on the Microsecond Time Scale. *J. Am. Chem. Soc.* **2007**, *129* (47), 14739–14745. <https://doi.org/10.1021/ja0753546>.

- (70) Plimpton, S. Computational Limits of Classical Molecular Dynamics Simulations. *Computational Materials Science* **1995**, *4* (4), 361–364. [https://doi.org/10.1016/0927-0256\(95\)00037-1](https://doi.org/10.1016/0927-0256(95)00037-1).
- (71) González, M. A. Force Fields and Molecular Dynamics Simulations. *JDN* **2011**, *12*, 169–200. <https://doi.org/10.1051/sfn/201112009>.
- (72) Lemma, T. Investigation of Protein-Drug Interaction Using Capillary Isoelectric Focusing with Whole Column Imaging Detection and Spectroscopic Techniques. **2023**.
- (73) Tuckerman, M. E. Ab Initio Molecular Dynamics: Basic Concepts, Current Trends and Novel Applications. *J. Phys.: Condens. Matter* **2002**, *14* (50), R1297. <https://doi.org/10.1088/0953-8984/14/50/202>.
- (74) *Modern Methods and Algorithms of Quantum Chemistry. Proc,2: Proceedings*, 2. ed.; NIC series; NIC: Jülich, 2000.
- (75) Car, R. Introduction to Density-Functional Theory and Ab-Initio Molecular Dynamics. *Quantitative Structure-Activity Relationships* **2002**, *21* (2), 97–104. [https://doi.org/10.1002/1521-3838\(200207\)21:2<97::AID-QSAR97>3.0.CO;2-6](https://doi.org/10.1002/1521-3838(200207)21:2<97::AID-QSAR97>3.0.CO;2-6).
- (76) Vuilleumier, R. Density Functional Theory Based Ab Initio Molecular Dynamics Using the Car-Parrinello Approach. In *Computer Simulations in Condensed Matter Systems: From Materials to Chemical Biology Volume 1*; Ferrario, M., Ciccotti, G., Binder, K., Eds.; Lecture Notes in Physics; Springer: Berlin, Heidelberg, 2006; pp 223–285. [https://doi.org/10.1007/3-540-35273-2\\_7](https://doi.org/10.1007/3-540-35273-2_7).
- (77) Vassilev, P.; Hartnig, C.; Koper, M. T. M.; Frechard, F.; van Santen, R. A. Ab Initio Molecular Dynamics Simulation of Liquid Water and Water–Vapor Interface. *J. Chem. Phys.* **2001**, *115* (21), 9815–9820. <https://doi.org/10.1063/1.1413515>.
- (78) Chen, M.; Ko, H.-Y.; Remsing, R. C.; Calegari Andrade, M. F.; Santra, B.; Sun, Z.; Selloni, A.; Car, R.; Klein, M. L.; Perdew, J. P.; Wu, X. Ab Initio Theory and Modeling of Water. *Proc Natl Acad Sci U S A* **2017**, *114* (41), 10846–10851. <https://doi.org/10.1073/pnas.1712499114>.
- (79) Iftimie, R.; Minary, P.; Tuckerman, M. E. Ab Initio Molecular Dynamics: Concepts, Recent Developments, and Future Trends. *Proceedings of the National Academy of Sciences* **2005**, *102* (19), 6654–6659. <https://doi.org/10.1073/pnas.0500193102>.
- (80) Rebane, K. K. The Adiabatic Approximation. In *Impurity Spectra of Solids: Elementary Theory of Vibrational Structure*; Rebane, K. K., Ed.; Springer US: Boston, MA, 1970; pp 1–33. [https://doi.org/10.1007/978-1-4684-1776-0\\_1](https://doi.org/10.1007/978-1-4684-1776-0_1).
- (81) *9.2 The Born-Oppenheimer Approximation*. [https://web1.eng.famu.fsu.edu/~dommelen/quantum/style\\_a/bo.html](https://web1.eng.famu.fsu.edu/~dommelen/quantum/style_a/bo.html) (accessed 2023-04-09).
- (82) Car, R.; Parrinello, M. Unified Approach for Molecular Dynamics and Density-Functional Theory. *Phys. Rev. Lett.* **1985**, *55* (22), 2471–2474. <https://doi.org/10.1103/PhysRevLett.55.2471>.
- (83) Wang, L.-P.; Song, C. Car-Parrinello Monitor for More Robust Born-Oppenheimer Molecular Dynamics. <https://doi.org/10.26434/chemrxiv.8217362.v2>.
- (84) Tuckerman, M. E. Ab Initio Molecular Dynamics: Basic Concepts, Current Trends and Novel Applications. *Journal of physics. Condensed matter : an Institute of Physics journal* **2002**, *14* (50), R1297–R1355. <https://doi.org/10.1088/0953-8984/14/50/202>.
- (85) Hohenberg, P.; Kohn, W. Inhomogeneous Electron Gas. *Phys. Rev.* **1964**, *136* (3B), B864–B871. <https://doi.org/10.1103/PhysRev.136.B864>.

- (86) Kohn, W.; Sham, L. J. Self-Consistent Equations Including Exchange and Correlation Effects. *Phys. Rev.* **1965**, *140* (4A), A1133–A1138. <https://doi.org/10.1103/PhysRev.140.A1133>.
- (87) Stowasser, R.; Hoffmann, R. What Do the Kohn–Sham Orbitals and Eigenvalues Mean? *J. Am. Chem. Soc.* **1999**, *121* (14), 3414–3420. <https://doi.org/10.1021/ja9826892>.
- (88) Perdew, J. P.; Burke, K.; Ernzerhof, M. Generalized Gradient Approximation Made Simple. *Phys. Rev. Lett.* **1996**, *77* (18), 3865–3868. <https://doi.org/10.1103/PhysRevLett.77.3865>.
- (89) Tao, J.; Perdew, J. P.; Staroverov, V. N.; Scuseria, G. E. Climbing the Density Functional Ladder: Nonempirical Meta–Generalized Gradient Approximation Designed for Molecules and Solids. *Phys. Rev. Lett.* **2003**, *91* (14), 146401. <https://doi.org/10.1103/PhysRevLett.91.146401>.
- (90) Becke, A. D. Density-Functional Exchange-Energy Approximation with Correct Asymptotic Behavior. *Phys. Rev. A* **1988**, *38* (6), 3098–3100. <https://doi.org/10.1103/PhysRevA.38.3098>.
- (91) Perdew, J. P. Density-Functional Approximation for the Correlation Energy of the Inhomogeneous Electron Gas. *Phys. Rev. B* **1986**, *33* (12), 8822–8824. <https://doi.org/10.1103/PhysRevB.33.8822>.
- (92) Lee, C.; Yang, W.; Parr, R. G. Development of the Colle-Salvetti Correlation-Energy Formula into a Functional of the Electron Density. *Phys. Rev. B* **1988**, *37* (2), 785–789. <https://doi.org/10.1103/PhysRevB.37.785>.
- (93) Tirado-Rives, J.; Jorgensen, W. L. Performance of B3LYP Density Functional Methods for a Large Set of Organic Molecules. *J. Chem. Theory Comput.* **2008**, *4* (2), 297–306. <https://doi.org/10.1021/ct700248k>.
- (94) Bockstedte, M.; Kley, A.; Neugebauer, J.; Scheffler, M. Density-Functional Theory Calculations for Poly-Atomic Systems: Electronic Structure, Static and Elastic Properties and Ab Initio Molecular Dynamics. *Computer Physics Communications* **1997**, *107* (1), 187–222. [https://doi.org/10.1016/S0010-4655\(97\)00117-3](https://doi.org/10.1016/S0010-4655(97)00117-3).
- (95) Francis, G. P.; Payne, M. C. Finite Basis Set Corrections to Total Energy Pseudopotential Calculations. *J. Phys.: Condens. Matter* **1990**, *2* (19), 4395–4404. <https://doi.org/10.1088/0953-8984/2/19/007>.
- (96) Runge, E.; Gross, E. K. U. Density-Functional Theory for Time-Dependent Systems. *Phys. Rev. Lett.* **1984**, *52* (12), 997–1000. <https://doi.org/10.1103/PhysRevLett.52.997>.
- (97) Curchod, B. F. E.; Rothlisberger, U.; Tavernelli, I. Trajectory-Based Nonadiabatic Dynamics with Time-Dependent Density Functional Theory. *ChemPhysChem* **2013**, *14* (7), 1314–1340. <https://doi.org/10.1002/cphc.201200941>.
- (98) Alonso, J. L.; Castro, A.; Echenique, P.; Rubio, A. On the Combination of TDDFT with Molecular Dynamics: New Developments. In *Fundamentals of Time-Dependent Density Functional Theory*; Marques, M. A. L., Maitra, N. T., Nogueira, F. M. S., Gross, E. K. U., Rubio, A., Eds.; Lecture Notes in Physics; Springer Berlin Heidelberg: Berlin, Heidelberg, 2012; Vol. 837, pp 301–315. [https://doi.org/10.1007/978-3-642-23518-4\\_15](https://doi.org/10.1007/978-3-642-23518-4_15).
- (99) Andrade, X.; Castro, A.; Zueco, D.; Alonso, J. L.; Echenique, P.; Falceto, F.; Rubio, A. A Modified Ehrenfest Formalism for Efficient Large-Scale Ab Initio Molecular Dynamics. *J. Chem. Theory Comput.* **2009**, *5* (4), 728–742. <https://doi.org/10.1021/ct800518j>.
- (100) Tavernelli \*, I.; Röhrig, U. F.; Rothlisberger, U. Molecular Dynamics in Electronically Excited States Using Time-Dependent Density Functional Theory. *Molecular Physics* **2005**, *103* (6–8), 963–981. <https://doi.org/10.1080/00268970512331339378>.

- (101) *GitHub - CPMD-code/CPMD: The CPMD code is a parallelized plane wave / pseudopotential implementation of Density Functional Theory, particularly designed for ab-initio molecular dynamics.* <https://github.com/CPMD-code/CPMD> (accessed 2023-05-22).
- (102) Hervé Du Penhoat, M.-A.; Kamol Ghose, K.; Gageot, M.-P.; Vuilleumier, R.; Fujii, K.; Yokoya, A.; Politis, M.-F. Investigation of the Fragmentation of Core-Ionised Deoxyribose: A Study as a Function of the Tautomeric Form. *Phys. Chem. Chem. Phys.* **2015**, *17* (48), 32375–32383. <https://doi.org/10.1039/C5CP05196G>.
- (103) Codorniu-Hernández, E.; Kusalik, P. G. Mobility Mechanism of Hydroxyl Radicals in Aqueous Solution via Hydrogen Transfer. *J. Am. Chem. Soc.* **2012**, *134* (1), 532–538. <https://doi.org/10.1021/ja208874t>.
- (104) Lundberg, M.; Siegbahn, P. E. M. Quantifying the Effects of the Self-Interaction Error in DFT: When Do the Delocalized States Appear? *J. Chem. Phys.* **2005**, *122* (22), 224103. <https://doi.org/10.1063/1.1926277>.
- (105) Troullier, N.; Martins, J. L. Efficient Pseudopotentials for Plane-Wave Calculations. *Phys. Rev. B* **1991**, *43* (3), 1993–2006. <https://doi.org/10.1103/PhysRevB.43.1993>.
- (106) Kleinman, L.; Bylander, D. M. Efficacious Form for Model Pseudopotentials. *Phys. Rev. Lett.* **1982**, *48* (20), 1425–1428. <https://doi.org/10.1103/PhysRevLett.48.1425>.
- (107) Becke, A. D. Density-Functional Exchange-Energy Approximation with Correct Asymptotic Behavior. *Phys. Rev. A* **1988**, *38* (6), 3098–3100. <https://doi.org/10.1103/PhysRevA.38.3098>.
- (108) Lee, C.; Yang, W.; Parr, R. G. Development of the Colle-Salvetti Correlation-Energy Formula into a Functional of the Electron Density. *Phys. Rev. B* **1988**, *37* (2), 785–789. <https://doi.org/10.1103/PhysRevB.37.785>.
- (109) Khalack, J. M.; Lyubartsev, A. P. Solvation Structure of Hydroxyl Radical by Car-Parrinello Molecular Dynamics. *J. Phys. Chem. A* **2005**, *109* (2), 378–386. <https://doi.org/10.1021/jp0461807>.
- (110) Vassilev, P.; Louwse, M. J.; Baerends, E. J. Hydroxyl Radical and Hydroxide Ion in Liquid Water: A Comparative Electron Density Functional Theory Study. *J. Phys. Chem. B* **2005**, *109* (49), 23605–23610. <https://doi.org/10.1021/jp044751p>.
- (111) Gageot, M. P.; Vuilleumier, R.; Stia, C.; Galassi, M. E.; Rivarola, R.; Gervais, B.; Politis, M. F. A Multi-Scale Ab Initio Theoretical Study of the Production of Free Radicals in Swift Ion Tracks in Liquid Water. *Journal of Physics B: Atomic, Molecular and Optical Physics* **2007**, *40* (1), 1. <https://doi.org/10.1088/0953-4075/40/1/001>.
- (112) Zoete, V.; Cuendet, M. A.; Grosdidier, A.; Michielin, O. SwissParam: A Fast Force Field Generation Tool for Small Organic Molecules. *Journal of Computational Chemistry* **2011**, *32* (11), 2359–2368. <https://doi.org/10.1002/jcc.21816>.
- (113) Lemkul, J. A. From Proteins to Perturbed Hamiltonians: A Suite of Tutorials for the GROMACS-2018 Molecular Simulation Package [Article v1.0]. *Living Journal of Computational Molecular Science* **2019**, *1* (1), 5068–5068. <https://doi.org/10.33011/livecoms.1.1.5068>.
- (114) *Molecular dynamics simulation of a small protein using GROMACS — GROMACS tutorials* <https://tutorials.gromacs.org documentation>. <https://tutorials.gromacs.org/docs/md-intro-tutorial.html> (accessed 2023-05-22).
- (115) Tavernelli, I.; Gageot, M. P.; Vuilleumier, R.; Stia, C.; Du Penhoat, M. A. H.; Politis, M. F. Time-Dependent Density Functional Theory Molecular Dynamics Simulations of

- Liquid Water Radiolysis. *ChemPhysChem* **2008**, *9* (14), 2099–2103.  
<https://doi.org/10.1002/cphc.200800177>.
- (116) Carravetta, V.; gren, H. Stieltjes Imaging Method for Molecular Auger Transition Rates: Application to the Auger Spectrum of Water. *Phys. Rev. A* **1987**, *35* (3), 1022–1032. <https://doi.org/10.1103/PhysRevA.35.1022>.
- (117) Hunt, P.; Sprik, M.; Vuilleumier, R. Thermal versus Electronic Broadening in the Density of States of Liquid Water. *Chemical Physics Letters* **2003**, *376* (1), 68–74. [https://doi.org/10.1016/S0009-2614\(03\)00954-0](https://doi.org/10.1016/S0009-2614(03)00954-0).
- (118) Zhang, L.; Wang, L.; Kao, Y.-T.; Qiu, W.; Yang, Y.; Okobiah, O.; Zhong, D. Mapping Hydration Dynamics around a Protein Surface. *Proc Natl Acad Sci U S A* **2007**, *104* (47), 18461–18466. <https://doi.org/10.1073/pnas.0707647104>.
- (119) Makkos, E.; Kerridge, A.; Kaltsoyannis, N. The Importance of Second Shell Effects in the Simulation of Hydrated Sr<sup>2+</sup> Hydroxide Complexes. *Dalton Transactions* **2015**, *44* (25), 11572–11581. <https://doi.org/10.1039/C5DT01110H>.
- (120). <https://theory.cm.utexas.edu/henkelman/research/bader/> (Accessed 2023-05-24).
- (121) Choudhuri, I.; Truhlar, D. G. Calculating and Characterizing the Charge Distributions in Solids. *J. Chem. Theory Comput.* **2020**, *16* (9), 5884–5892. <https://doi.org/10.1021/acs.jctc.0c00440>.
- (122) Humphrey, W.; Dalke, A.; Schulten, K. VMD: Visual Molecular Dynamics. *Journal of Molecular Graphics* **1996**, *14* (1), 33–38. [https://doi.org/10.1016/0263-7855\(96\)00018-5](https://doi.org/10.1016/0263-7855(96)00018-5).





## CONTENT CHAPTER 3

---

Chapter 3: Experimental approach for HO <sub>2</sub> <sup>°</sup> detection .....	103
3.1. Optimizing the chemical detection system with reference $\gamma$ source .....	105
3.1.1. Optimizing the conditions for the chemical detection system.....	106
3.1.2. Optimizing concentration of the probe and enzymes.....	110
3.1.3. Irradiation using reference gamma source .....	112
3.2. Irradiation using soft X-rays .....	114
3.2.1. Microfluidic cell: A solution for poor penetrating soft X-rays .....	114
3.2.1.1. Modified cell design .....	114
3.2.2.1. Alignment of the modified microfluidic cell.....	115
3.2.2.1.i. First version of the alignment protocol .....	115
3.2.2.1.ii. Second version of the alignment protocol.....	119
3.2.2. In-line UV analysis: A solution for low radical yield .....	123
3.2.2.1. In-line UV detection cell .....	123
3.2.2.2. Coupling microfluidic set-up and in-line UV detection cell .....	125
3.2.2.3. Automating the in-line UV detection.....	126
3.2.3. Dose calculation .....	128
3.2.3.1. Photodiode flux ( $\phi_{\text{photodiode}}$ ) .....	129
3.2.3.2. Transmission through front Silicon nitride ( $T_{\text{Si}_3\text{N}_4}$ ) membrane.....	130
3.2.3.3. Transmission through sample ( $T_{\text{sample}}$ ) .....	130
3.2.4. Uncertainty calculation .....	134
3.2.5. Superoxide detection upon irradiation with soft X-rays .....	136
3.2.5.1. Yields from direct pathway.....	136
3.2.5.2. Yields from indirect pathway.....	141
3.3. Conclusion .....	144
References .....	145

## Chapter 3: Experimental approach for HO<sub>2</sub><sup>°</sup> detection

In this chapter, our primary focus is directed towards the detection and quantification of HO<sub>2</sub><sup>°</sup>, produced as a result of K-shell ionization of water molecules when exposed to soft X-ray irradiation. The chapter is divided into three main components. The initial section addresses the choice of the chemical detection system followed by its optimization using the reference gamma source. The second section delves into the experimental developments wherein the modification introduced in the microfluidic set-up is detailed along with the development of an 'in-line' UV detection set-up, to facilitate the experiments with synchrotron soft X-rays. Finally, the key results of the quantification of HO<sub>2</sub><sup>°</sup> produced during irradiation are presented.

### 3.1. Optimizing the chemical detection system with reference $\gamma$ source

In section 1.3.2 of Chapter 1, we discussed the importance of superoxide radicals and the need for its quantification. Various methods have been devised to detect and quantify HO<sub>2</sub><sup>°</sup>, including lucigenin and luminol assays, electron paramagnetic resonance, high performance liquid chromatography (HPLC) coupled with mass spectrometry (MS), and chemical probes for fluorescence and UV absorbance measurements.<sup>1,2,3,4,5</sup> One widely employed technique for superoxide detection is the use of UV-vis probes that interact selectively with the superoxide radical and undergo reduction. The reduction of the probe results in a conjugated structure that produces a characteristic signal in the UV absorption spectrum. The reduced probe acts as an indicator for the presence of superoxide radical. Among the popular probes, Nitroblue Tetrazolium (NBT), Cytochrome C (Cyt C) and Water Soluble Tetrazole (WST) Salts have been extensively used.<sup>6,7,3</sup> However, it has been reported that the NBT assay has limitations due to the insolubility of its reduced formazan product, while the Cyt C probe lacks sensitivity.<sup>6</sup> During our previous experiments using Cyt C, we not only encountered a lack of sensitivity but also observed a contamination of the microfluidic channel due to Cyt C aggregation, leading to cell fouling. Unlike the other tetrazolium salts that have a low solubility of their formazan products (like NBT), WST salts are free from such limitation.<sup>8</sup> Considering these factors, we opted for WST salts as a reliable choice for our experiments.

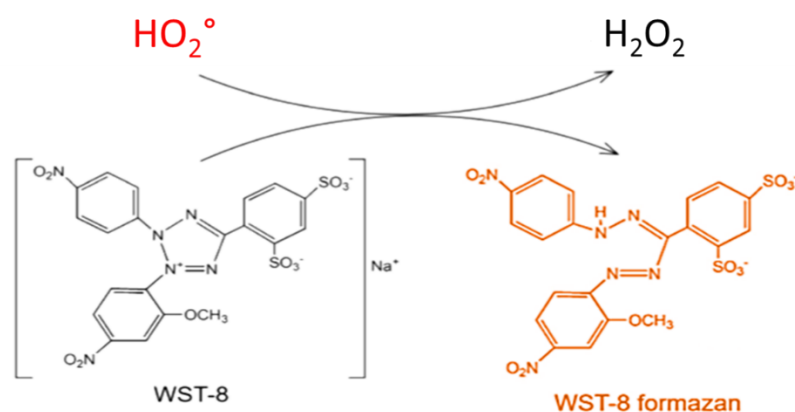


**Figure 3.1:** WST8 reducing to its formazan product.

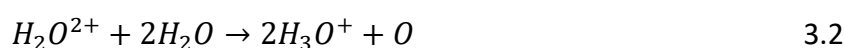
WST salts react selectively with superoxide species and undergo reduction, forming formazan products (see figure 3.1) with absorbance maxima in the range of 430 nm to 550 nm. Among the range of WST salts available ('WST-1', 'WST-3', 'WST-4', 'WST-5', 'WST-8' and 'WST-9'),<sup>9,10</sup> WST-8 stands out due to its exceptional sensitivity and specificity.<sup>7</sup>

It is important to note that the molar extinction coefficient ( $\epsilon$ ) of reduced WST-8 ( $\epsilon_{460} = 30700\text{M}^{-1}\text{cm}^{-1}$ ) surpasses that of other WST salts and reduced Cyt C ( $\epsilon_{550} = 27700\text{M}^{-1}\text{cm}^{-1}$ ), resulting in higher intensity and therefore higher sensitivity of detection.

Therefore, all superoxide detection experiments were conducted using WST-8 as the chemical probe.

### 3.1.1. Optimizing the conditions for the chemical detection system

The production of superoxide can occur via various pathways as reported in section 1.3.2. of Chapter 1. In the present work, we focus on quantifying the production of superoxide by the indirect pathway (reaction 3.1), i.e. the reduction of molecular oxygen by aqueous electrons, as well as by the direct pathway (reaction 3.2 and 3.3) that refers to the production of superoxide as a result of the dissociation of  $\text{H}_2\text{O}^{2+}$  and its intra track reactions. As mentioned in section 1.3.2. of Chapter 1, superoxide ( $\text{pK}_a = 4.8$ ) can be present in its protonated form ( $\text{HO}_2^\bullet$ ) or in the anionic form ( $\text{O}_2^{\bullet-}$ ), depending upon the pH of the solution. Since the pH of our prepared solution is 5, both forms of superoxide are in equilibrium.





To determine the superoxide produced from the two pathways of interest, it was essential to be able to chemically suppress (using scavengers) one of these two pathways. In addition, the probe, WST-8, selected as an indicator of superoxide production, can also be reduced by solvated electrons (see figure 3.2).

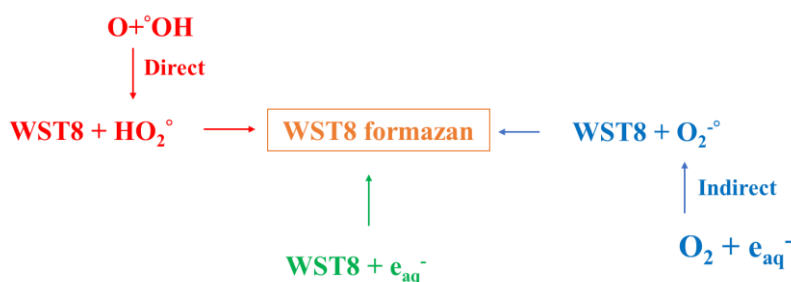


**Figure 3.2:** Different pathways for the reduction of the chemical probe, WST-8, to the formazan product that gives a characteristic signal in UV at 460 nm.

To identify unambiguously the contribution from the different reduction pathways of WST8, the experiments were conducted in different conditions (see table 3.1 and figures 3.3 and 3.4) to optimize the chemical detection system. Simultaneously, the concentrations of the different components within the chemical detection system were also optimized (see section 3.1.2). Here, we first present the optimization of the experimental conditions.

**Table 3.1:** Different experimental conditions used to identify the contribution from different reaction pathways for the reduction of the chemical probe, WST8. Different chemicals that were used are Superoxide Dismutase (SOD), Catalase, NaCl and Ethanol. All these conditions were tested using the Cs<sup>137</sup> gamma source.

S. no.	Condition	Contribution to reduction of WST8
1	Oxic	Direct HO <sub>2</sub> <sup>°</sup> + Indirect HO <sub>2</sub> <sup>°</sup> + Solvated electrons
2	Anoxic	Direct HO <sub>2</sub> <sup>°</sup> + Solvated electrons
3	Anoxic + SOD	Solvated electrons + peroxidase activity <sup>11</sup> due to SOD
4	Anoxic + SOD + Catalase	Solvated electrons
5	Anoxic + NaCl	Direct HO <sub>2</sub> <sup>°</sup> + Solvated electrons + negative contribution from OH, if any
6	Anoxic + Ethanol	Direct HO <sub>2</sub> <sup>°</sup> + Solvated electrons + negative contribution from OH, if any

In the oxic condition (Condition 1, table 3.1), HO<sub>2</sub><sup>°</sup> is produced via all the pathways shown in the figure 3.2. The complete absorption spectra of WST-8 irradiated in oxic conditions (orange curve, figure 3.3) shows a considerable increase in the absorption around 460 nm. The absorption values at 460 nm were extracted from the absorption spectra to calculate the yield, as explained in section 2.4.4.3. of chapter 2, and is presented in the figure 3.4.

However, in the anoxic condition (Condition 2), the contribution from the indirect pathway, shown in blue in figure 3.2, was eliminated. This can be seen by the reduction in its absorption band (green curve, figure 3.3).

Upon addition of Superoxide Dismutase (SOD) in the anoxic condition (Condition 3), all the superoxide produced in the sample, upon irradiation, was eliminated from the system as SOD selectively removes superoxide from the solution by catalyzing its dismutation<sup>12, 2, 13, 14</sup> into

molecular oxygen and hydrogen peroxide (Reaction 3.4). Hence, the formazan product was formed only due to solvated electrons, as shown in green in figure 3.2.



SOD has a side activity as a peroxidase,<sup>11</sup> which could possibly lead to side reactions in the presence of H<sub>2</sub>O<sub>2</sub>, as indicated by reaction 1.19 in section 1.3.2. of Chapter 1. Therefore, to eliminate the peroxidase activity,<sup>15,16,17</sup> we introduced an enzyme that facilitates the removal of peroxidase, i.e. catalase, (Condition 4).<sup>18</sup> Reaction (3.5) indicates the dismutation reaction of hydrogen peroxide, catalyzed by catalase.

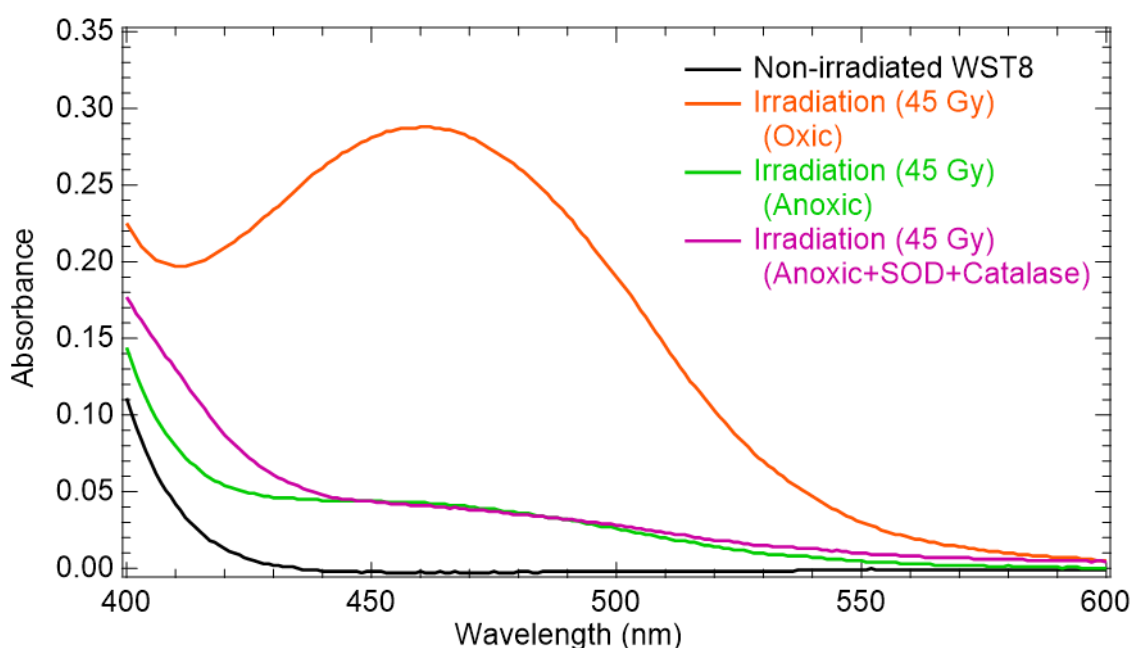
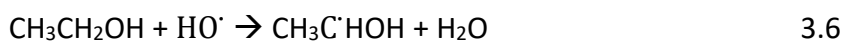


**Figure 3.3:** The absorption spectrum, from 400 nm to 600 nm, at different irradiation conditions. The concentration of WST-8 was 300  $\mu\text{M}$  and the concentration of SOD and catalase was 0.62  $\mu\text{M}$ . The samples were irradiated at 45 Gy using the gamma source with the dose rate of 5.5 Gy/min. The dose response curve for some of the condition is given in the appendix I.II.

In condition 4, the contribution was therefore just from the solvated electrons. The difference between HO<sub>2</sub><sup>•</sup> yields measured in condition 2 and in condition 4 therefore gave the contribution from the direct pathway, i.e. the HO<sub>2</sub><sup>•</sup> yield resulting from the dissociation of doubly ionized water molecules, in which we are interested.

Some additional tests were done using NaCl (10 mM) and ethanol (10 mM) (which are effective scavenger for OH<sup>°</sup>), conditions 5 and 6, respectively, in order to investigate the role of OH radicals, if any. Reaction (3.6) shows the scavenging reaction of OH<sup>°</sup> by ethanol.<sup>17,19,20</sup>



The yield with and without °OH scavengers was found to be the same, hence, we could safely consider that there was no/negligible contribution from °OH.

Therefore, conditions that are important for further consideration to determine the HO<sub>2</sub><sup>°</sup> produced via the direct and indirect pathways are conditions 1, 2 and 4.

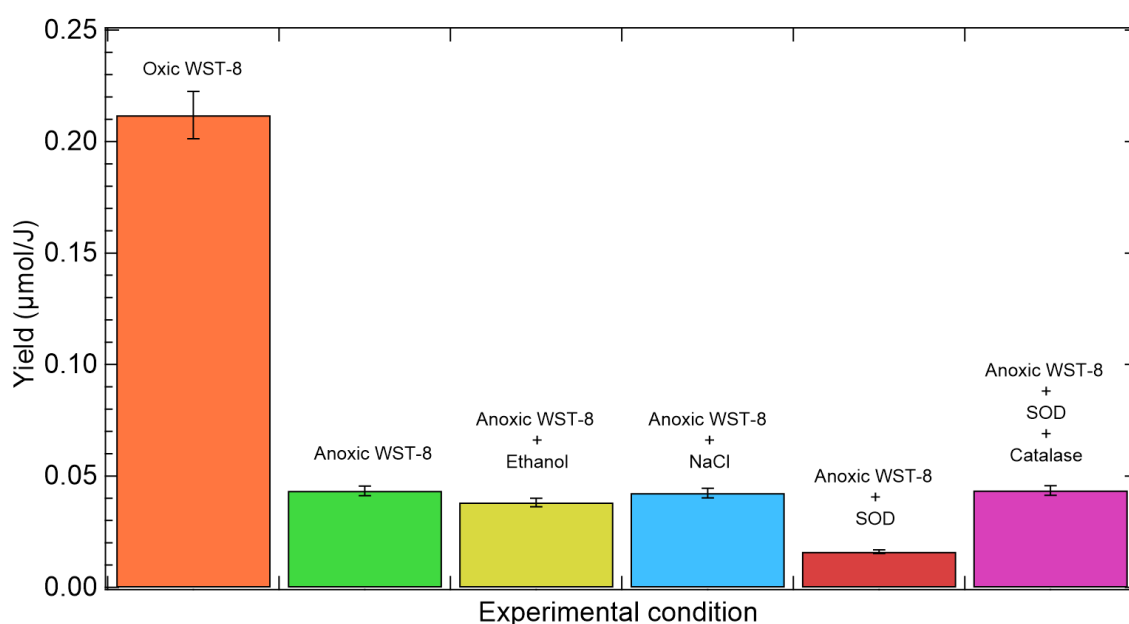


**Figure 3.4:** Validation of the chemical system, when irradiated at 45 Gy, with the gamma source (5.5 Gy/min) in different conditions. The yields were calculated from the absorbance values at 460 nm recorded using the conventional UV-vis spectrophotometer (see figure 3.3 for complete absorption spectra). The yields reported in the figure are an average of 5 data points and their standard deviation is plotted as error bars.

### 3.1.2. Optimizing concentration of the probe and enzymes

The components of the chemical detection system are the chemical probe (WST8) and the SOD and catalase enzymes. The next step was to find their optimal concentrations. Since the samples were to be irradiated in a microfluidic cell for the soft X-rays experiments, the choice of the optimal concentration was based on the thumb rule of microfluidics: To use a



microfluidic system for as long as possible, the solutions should be as dilute as possible to minimize the contamination of the microfluidic channel that could eventually lead to flow impairment.

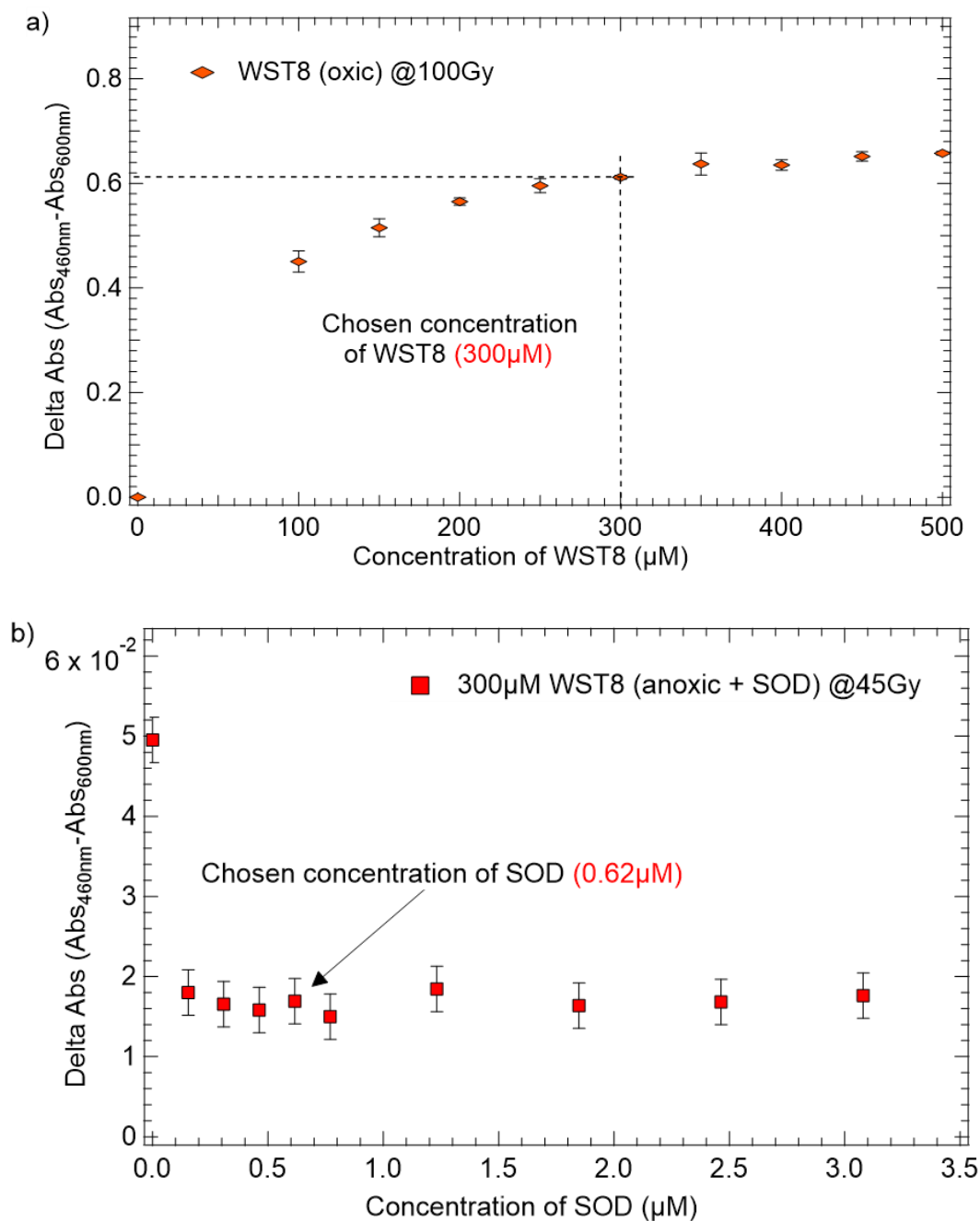


**Figure 3.5:** Variation in absorbance of the probe, WST8, a) as a function of its concentration, ranging from 100  $\mu\text{M}$  to 500  $\mu\text{M}$ , irradiated at 100 Gy; b) as a function of SOD concentration (from 0  $\mu\text{M}$  to 3.1  $\mu\text{M}$ ) with 300  $\mu\text{M}$  WST8 concentration, irradiated at 45 Gy, when irradiated by a Cs-gamma source. The absorbance values plotted in the figure are an average of 5 data points and the error bars correspond to their standard deviation.

WST8 solutions were irradiated with a Cs<sup>137</sup> gamma source under oxic conditions, varying the WST8 concentration between 0 and 500 μM. The dose was 100 Gy, which is the maximum value until which the absorbance was a linear function of the dose. A plateau was reached after 300 μM WST8 concentration suggesting it to be the minimum concentration to ensure the efficient capture of the superoxide species present in the irradiated sample. Hence, this concentration was chosen to be the optimum one (Figure 3.5 a). Such a low concentration also allowed to minimize the eventual interactions of WST8 with °OH.

Further, 300 μM WST8 solutions were irradiated at a dose of 45 Gy under anoxic conditions. Absorbance measurements were performed by varying the enzyme (SOD) concentration (see figure 3.5 b). The choice of the SOD concentration was such that the concentration should be as low as possible and yet sufficient to dismutate HO<sub>2</sub><sup>°</sup> and have a detectable absorbance signal. Therefore, it was chosen to be 0.62 μM, which is around 500 times lower than the WST8 concentration and sufficient to capture the HO<sub>2</sub><sup>°</sup>. For catalase as well, an equivalent concentration (0.62 μM) was chosen, to ensure that the peroxidase activity due to SOD was eliminated. Hereafter, all the experiments were performed with these specific concentrations.

### 3.1.3. Irradiation using reference gamma source

In the oxic condition (condition 1), the production yield of WST-8 formazan was found to be 0.21 (±0.01) μmol/J. As expected for a dilute scavenger like WST8, the measured yield was 20% lower than the theoretical radiolytic primary yield (0.26 μmol/J).<sup>21</sup> Therefore, the direct/indirect yield to be measured with soft X-rays as well, will be slightly underestimated. It must be noted at this point that the more classical cytochrome C (45 μM) reduction assay, in oxic conditions, gave an even lower yield of 0.17 (±0.01) μmol/J, upon gamma irradiation.<sup>22</sup>

The experiments were also performed in anoxic condition, without SOD (condition 2), and the absorbance at 460 nm decreased considerably as compared to the oxic condition (see figures 3.3 and 3.4). The formazan yield was found to be 0.043 (± 0.005) μmol/J. The difference between the yields in condition 1 and condition 2 was attributed as the *indirect* HO<sub>2</sub><sup>°</sup> yield.

As a next step, the formazan yield was measured in the anoxic condition, with SOD (condition 3) and was found to be 0.012 (± 0.002) μmol/J. The difference between the formazan yields in these two conditions (3 and 2) would be equal to the yield of direct HO<sub>2</sub><sup>°</sup> if the peroxidase activity of SOD is negligible. However, the difference between the two yields was around 0.03

μmol/J, in complete disagreement with the literature data that gave a direct superoxide yield value of about 0.002 μmol/J or less.<sup>23</sup> Therefore, we could not neglect the peroxidase activity of SOD and we had to consider the side reaction of formazan with hydrogen peroxide resulting after the catalytic dismutation of superoxide by SOD, as indicated in section 3.1.1.<sup>15</sup>

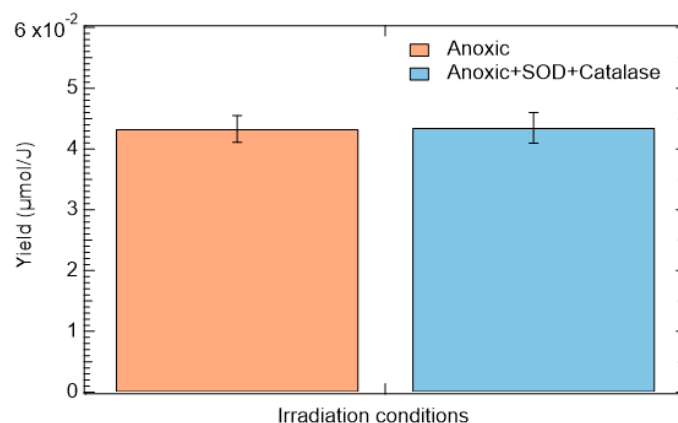


**Figure 3.6:** Average yield (of five data points per condition) of the reduced probe (300 μM) focusing on the two irradiation conditions which enable determining the direct HO<sub>2</sub><sup>•</sup> yield (among the six displayed in figure 3.4). The solutions were irradiated at 45 Gy, with a gamma source (5.5 Gy/min). The concentration of SOD and catalase were 500 times lower (0.62 μM). The error bars are standard deviation of the five data points for each condition.

The formazan yield was measured for the anoxic sample containing both SOD and catalase (Condition 4) to eliminate the effect of H<sub>2</sub>O<sub>2</sub> side reaction (3.5) and it was found to be 0.043 (± 0.005) μmol/J, which is the same as was observed in condition 2. This can also be observed in the absorption spectra in figure 3.3, where the absorbance at 460 nm is almost the same for these two conditions. It should be noted that the difference in the yields between anoxic/SOD and anoxic/SOD/catalase conditions (i.e. 0.03 μmol/J), can be attributed to H<sub>2</sub>O<sub>2</sub> reaction, with a yield that is one-third of the H<sub>2</sub>O<sub>2</sub> primary yield under gamma irradiation.<sup>24</sup>

The difference between the yield of formazan in anoxic (Condition 2) and anoxic/SOD/catalase (Condition 4) corresponded to the yield of *direct* superoxide. Considering the detection limit of the scavenging system used, we could only confirm that the direct superoxide production under gamma irradiation was below 0.005 μmol/J (See figure 3.6). For 200 MeV carbon ions (≤36 keV/μm)<sup>25</sup> and protons (≤1 keV/μm)<sup>23</sup> having LET similar to that of the gamma source (0.2 - 0.5 keV/μm),<sup>26</sup> the reported production yield of direct HO<sub>2</sub><sup>•</sup> (O + OH → HO<sub>2</sub><sup>•</sup>) are around 0.003 μmol/J.<sup>23, 25</sup>

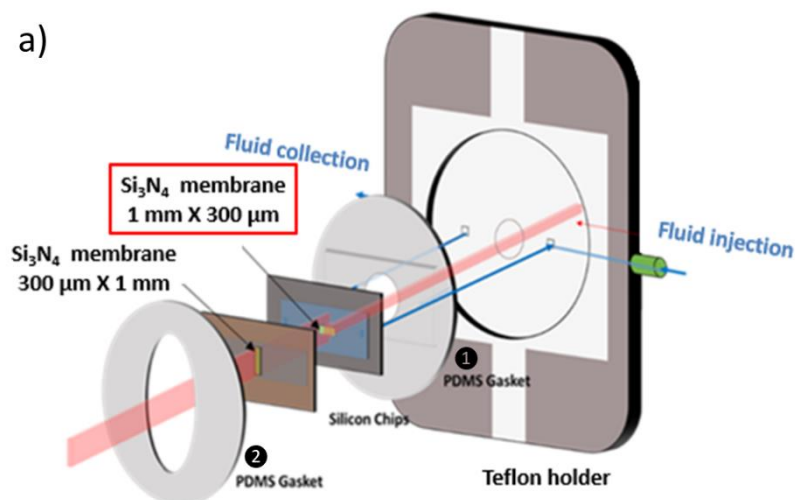
## 3.2. Irradiation using soft X-rays

### 3.2.1. Microfluidic cell: A solution for poor penetrating soft X-rays

#### 3.2.1.1. Modified cell design

As stated earlier, soft X-rays have a poor penetration (or strong attenuation) in liquid media. In order to overcome this limitation and thereby ensure a homogeneous dose distribution, the solutions were irradiated through a 150 nm-thick silicon membrane (entrance membrane), while flowing through a 5.3 μm-thick microfluidic channel (see figure 3.7). The original microfluidic cell design is elaborated in section 2.4.2.1 of chapter 2 and was developed in collaboration with C. Chevillard during L. Huart thesis.<sup>27</sup> Since both the beam and the entrance membrane are only 300 μm wide (along the X axis), it is crucial to ensure that they are properly aligned. The precise way to ensure this is to have a cell design that allows the transmission of a small fraction of the beam. Therefore, we introduced a modification in the original cell design.

A second Si<sub>3</sub>N<sub>4</sub> membrane (exit membrane) was thus added to the back silicon chip and this exit membrane was 200 nm thick and 1 mm x 300 μm large. It was rotated by 90 degrees with respect to the Si<sub>3</sub>N<sub>4</sub> membrane of the front silicon chip (see figure 3.7).



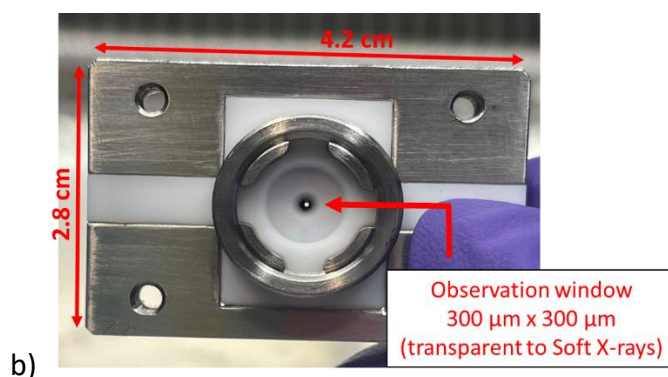


**Figure 3.7:** a) Exploded view of the modified microfluidic cell design having two Si<sub>3</sub>N<sub>4</sub> membranes b) back view of the assembled microfluidic cell, with a transparent square corresponding to the observation window, allowing the transmission of the beam.

Since both axis windows are perpendicular to each other, it forms a 300 μm x 300 μm square that is transparent to soft X-rays.<sup>28</sup> This square is referred to as the ‘observation window’. In addition, a 0.5 mm-diameter hole was punched onto the PDMS gasket ① to allow the beam to exit the cell.

### 3.2.2.1. Alignment of the modified microfluidic cell

#### 3.2.2.1.i. First version of the alignment protocol

As stated above, the soft X-rays pass through the front window of 300 μm x 1 mm, to irradiate the sample. Owing to the small dimension along the X axis, the precise alignment of the cell with respect to the beam is essential for irradiation. This alignment procedure is detailed in this section.

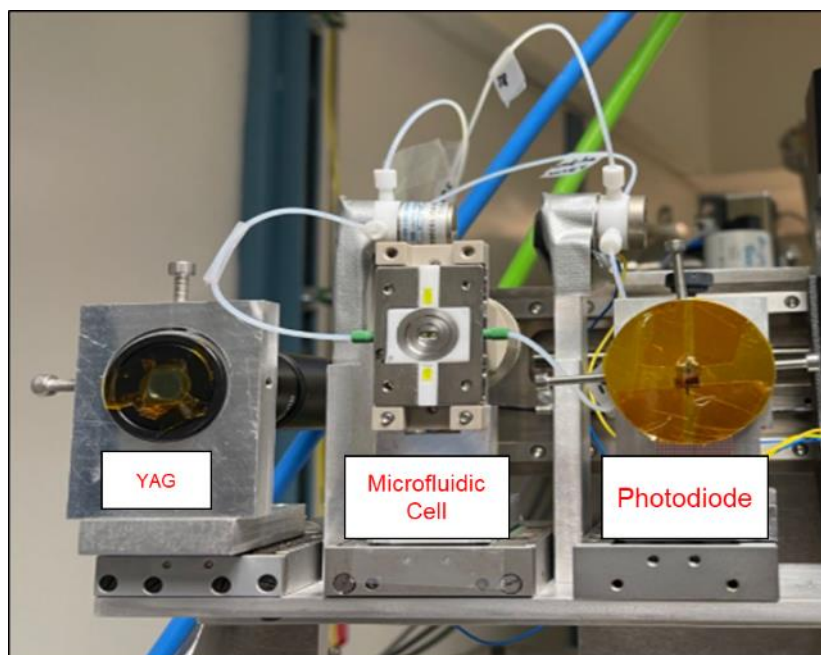


**Figure 3.8:** Installation of microfluidic cell and the alignment devices on the translation table of the IRAD setup (allowing the motion along different axis ( $T_s$ ,  $T_x$  and  $T_z$ )). The microfluidic cell is in the center with a scintillator (YAG:Ce) to its left and a photodiode with an aluminium mask to its right. Each device was also mounted on a one-direction manual translation device (along the  $T_s$ -axis).

The first alignment step was the installation of the microfluidic cell, a scintillator crystal (YAG:Ce) and a photodiode on a translation table (figure 3.8). The relative position of these device were first measured using an optical level (see figure 2.8, Chapter 2). The scintillator crystal (YAG:Ce) and a photodiode allowed the determination of the beam shape and position respectively.<sup>29,21</sup> The photodiode was also used for the dosimetry (see section 3.2.3.1).

Briefly, the 50  $\mu\text{m}$ -thick Scintillator crystal (YAG:Ce) was installed in front of a CCD camera that helped to convert X-rays into visible light. The alignment was possible thanks to engravings etched on the YAG crystal (etching of 0.3 mm x 1 mm, similar to the front membrane dimensions), allowing to visualize the beam's shape (see figure 3.9). By changing the monochromator vertical slit size, we could therefore control the centering of the beam and ensure that the beam was correctly aligned with respect to the diaphragms in the IRAD set-up (see section 2.4.1 of Chapter 2).

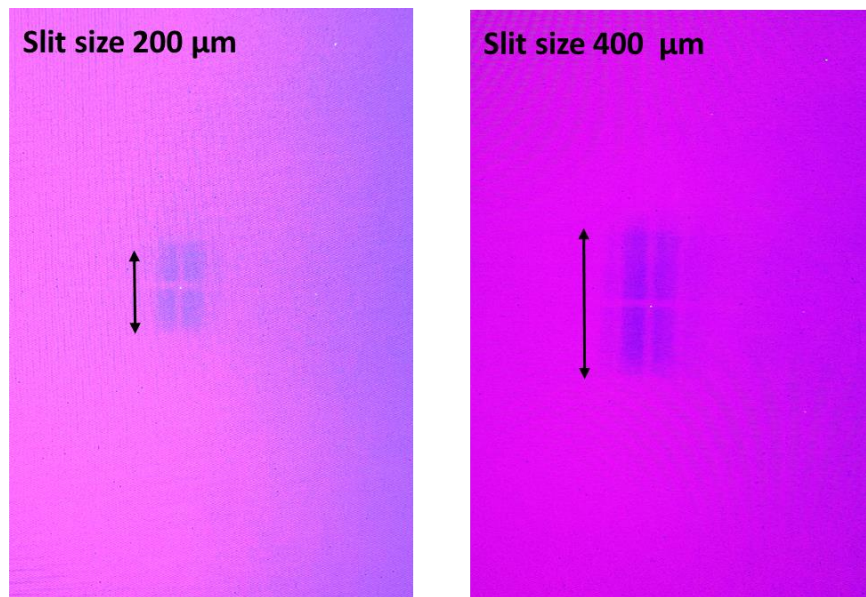


**Figure 3.9:** Beam shape visualized through the YAG crystal etched with the dimensions of the front silicon nitride membrane, captured using the CCD camera. The left and the right images were captured with the monochromator vertical slit size of 200  $\mu\text{m}$  and 400  $\mu\text{m}$ , respectively.

Another device used for the alignment was a photodiode (for specifications see table 2.2 in chapter 2), having a very stable quantum efficiency.<sup>30</sup> The photodiode was covered with an aluminium mask having two holes. Ghost Si<sub>3</sub>N<sub>4</sub> membranes were affixed on each of these holes, one broken and the other intact. Thanks to the translation table, horizontal (Tx) and vertical (Tz) scans were performed in front of the beam (see figure 3.10) to center the beam on these windows. The photodiode was then used to determine the beam flux (in photons/s) at its sensitive surface by measuring the current (in nano-ampere, nA) through the broken membrane window.

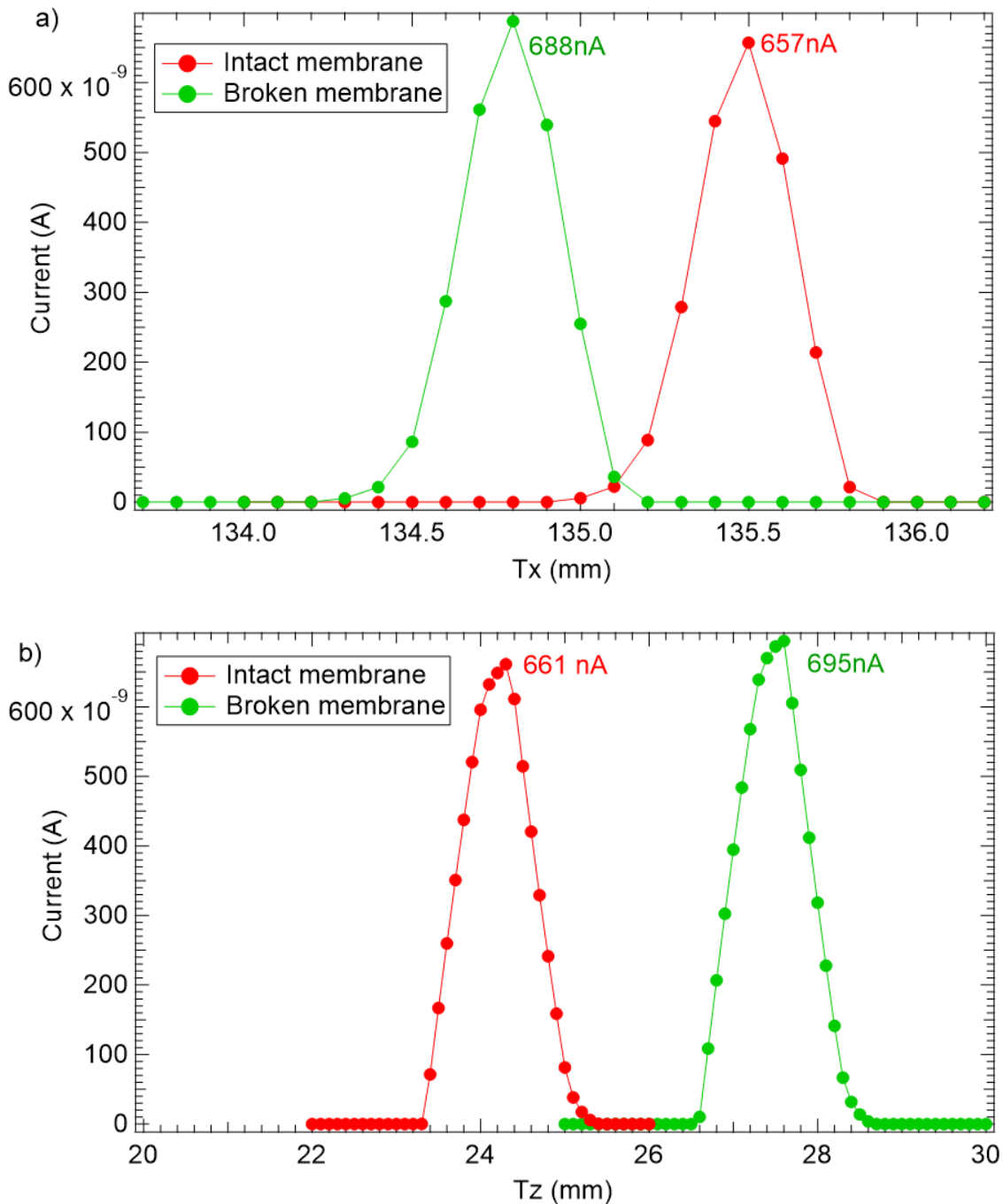


**Figure 3.10:** a) Tx and b) Tz scans on the Ghost membranes. The broken (green curves) and the intact (red curves) membranes taped on aluminum mask of the photodiode, at 1620eV with 500  $\mu\text{m}$  monochromator vertical slits and a Boron (0.4  $\mu\text{m}$ ) inline filter. The cell was translated horizontally (Tx), with a step of 0.05 mm and vertically (Tz) with a step of 0.1 mm, in front of the exit window of the IRAD set-up (in front of the synchrotron beam). The measurements are obtained with an air gap of 2 mm between the exit window of the IRAD setup and the aluminium mask of the photodiode.



The alignment scans provided the position of the ghost membranes centre. Knowing the relative positions of the center of microfluidic cell's front membrane and the center of the ghost membranes, allowed aligning the cell accurately. However, the uncertainty in the measurement of these distance were large (few  $\mu\text{m}$ ). The alignment was also refined using the chemical measurements<sup>31</sup> that took very long time (few hours).

In addition, the two alignment devices (the YAG:Ce and photodiode) described above allowed verifying the alignment before and after each irradiation. During the irradiation, however, the drifts in the cell position because of mechanical relaxation (for example, the mechanical relaxation due to the translation table) were difficult to account via these methods. In addition, every time the cell was replaced (due to the breaking of the cell membrane or cell clogging), the relative position of the cell with respect to these devices was to be determined again and the alignment procedure had to be repeated. This requires tedious amount of work. Hence, these points of concern motivated the instalment of a new device for alignment.

#### *3.2.2.1.ii. Second version of alignment protocol*

Thanks to the modified cell design, explained earlier, we introduced another device for ensuring accurate alignment in real time, i.e. even during irradiation. This device is composed of a scintillator (YAG:Ce from Crytur) and a Silicon photomultiplier (SiPM)<sup>27</sup> located behind the microfluidic cell. The transmitted beam was converted into visible light by the YAG:Ce crystal and then detected by the SiPM. The entire assembly, the microfluidic cell, the SiPM and the scintillator, were placed in a PEEK support (support first developed by Lucie Huart and later refined by collaboration with Stephane Lefrancois (Synchrotron SOLEIL, SMIS beamline) (See figure 3.11)).

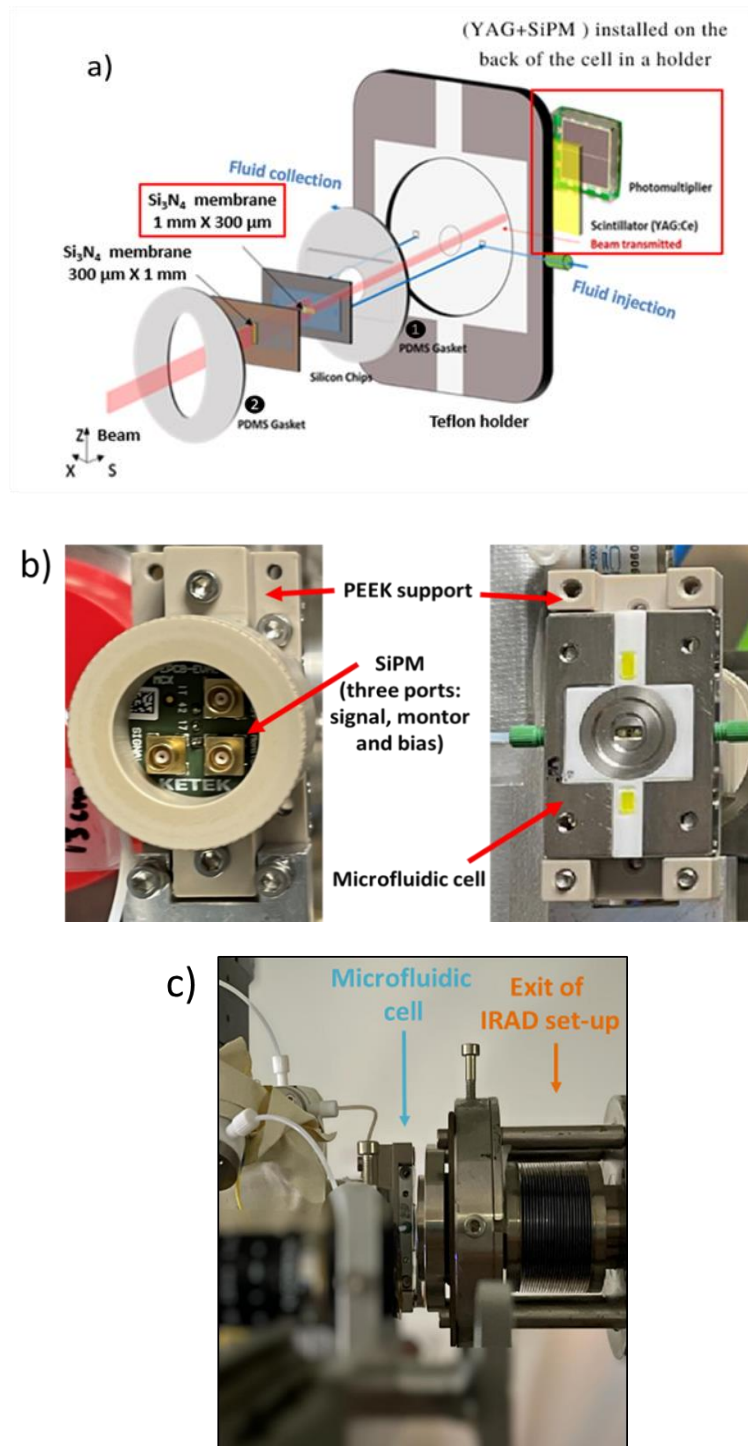


**Figure 3.11:** SiPM installed behind the cell, allowing the detection of transmitted beam, thanks to the scintillator that converts X-rays to visible light. a) Exploded view of the modified cell with the SiPM behind; Photograph of b) the cell support back (left) and front (right) made of PEEK, to support the YAG:Ce (not visible), the microfluidic cell and SiPM; c) the entire assembly (microfluidic cell with the SiPM in the support) placed at a distance of 1 mm from the exit window of the IRAD setup on the METROLOGIE beamline at synchrotron SOLEIL, for in-air irradiations experiments.

SiPM has high sensitivity, offering the possibility of single-photon detection (for specification, refer to table 2.2 of chapter 2). Experimentally, the saturation level of SiPM was found to be  $4 \times 10^5$  counts. Its introduction in the set-up allowed performing direct and fast alignment (*via* vertical and horizontal scans) of the microfluidic cell with respect to the SR beam, even in the presence of the sample. Therefore, it acted as a control of the cell position during the irradiation.

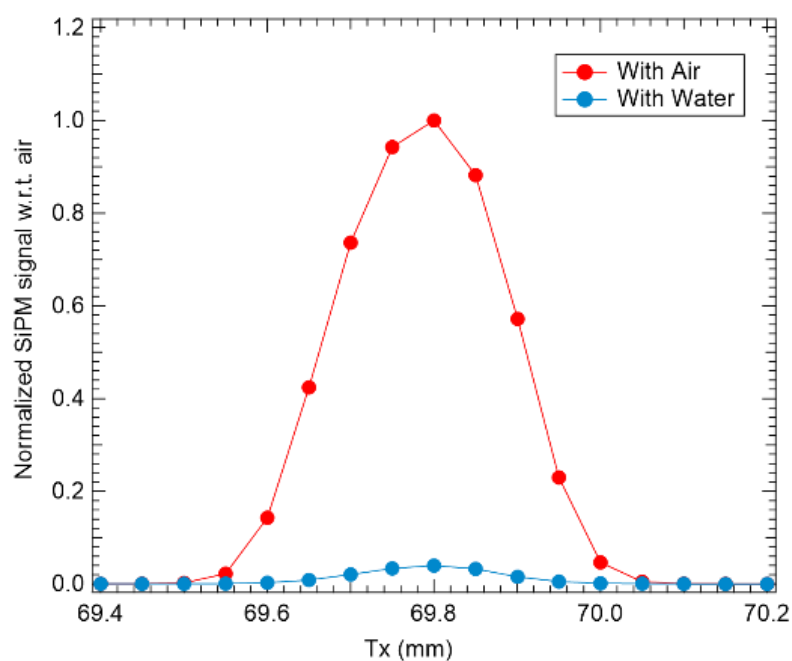


**Figure 3.12:** Attenuation of the SR beam in water (5  $\mu\text{l}/\text{min}$  flow rate) resulting in a reduction of the SiPM signal (blue curve) when compared to the SiPM signal when the cell is filled with air (red curve). Both the signals are normalized with respect to the SiPM signal in air. The cell was translated horizontally, with steps of 0.05 mm in front of the exit window of the IRAD set-up (i.e. in front of the synchrotron beam). Both the curves were normalized with respect to the SiPM signal in air, so that the maximum of the red curve (channel filled with air) is 1.

Firstly, vertical (Tz) and horizontal (Tx) scans were performed at a fixed monochromator slit size, to align the beam on the observation window. The figure 3.12 shows the evolution of the SiPM signal while translating the microfluidic cell along the horizontal (x) axis in front of the beam, when the cell is filled with air (red curve) or when water is flowing through the channel at a 5  $\mu\text{l}/\text{min}$  flowrate (blue curve). The position at the maximum of the curve corresponds to a correct alignment of the cell with respect to the beam. It should be noted that the SiPM

response was not linear, so that this method does not allow to measure the transmission of the flowing solution.

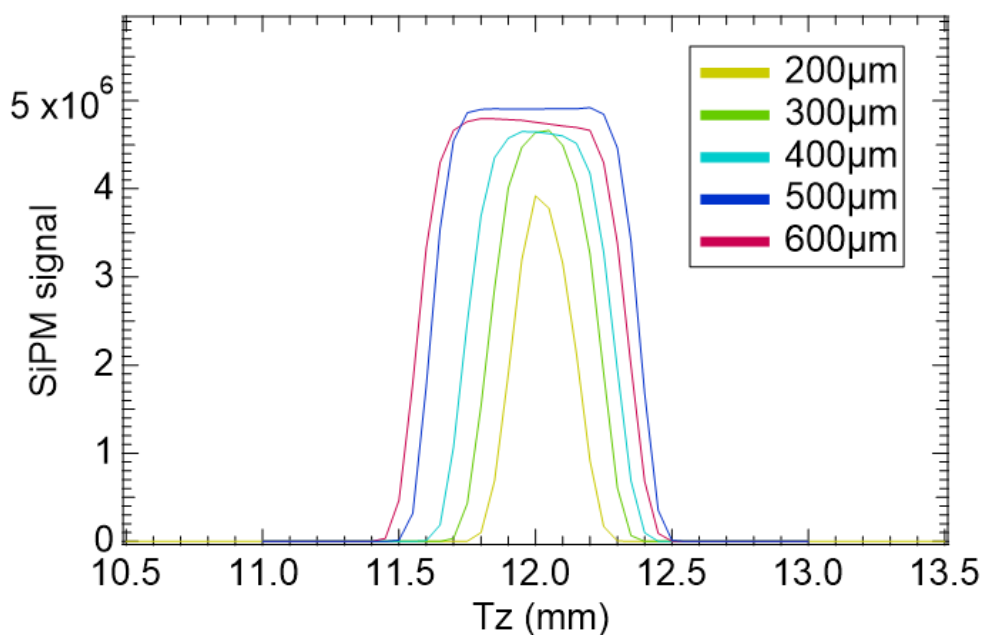


**Figure 3.13:** Variation in vertical width as a function of slit size of the beamline monochromator.

As a next step, vertical scans were performed at different exit slit sizes of the beamline monochromator (see figure 3.13). A decrease in the beam's vertical width upon decreasing the slit size was observed. The beam's center was independent of the slit size of the beamline monochromator, indicating an efficient beam centering.

The SiPM greatly facilitated the alignment (with and without the sample), resulting in a time efficient (within minutes) alignment as compared to that possible with the first version (few hours) of the alignment protocol. The SiPM signal variation as a function of flowrate of the sample was also measured (see appendix I.IV.). In addition, the first version did not allow the direct alignment of the cell and we had to rely on the distance measurements between the devices, as mentioned before. Using the SiPM removed the uncertainty arising due to these distance measurements and allowed to control the cell position, even during the irradiation experiments.

### 3.2.2. In-line UV analysis: A solution for low radical yield

#### **3.2.2.1. In-line UV detection cell**

The soft X-ray irradiation experiments using the above mentioned microfluidic cell address the limitation of poor penetration of the beam in a liquid medium. However, conducting such experiments poses another challenge due to significantly lower radical yields in the soft X-ray regime (compared to gamma rays).<sup>32,33</sup> It is important to emphasize that even with gamma irradiation, the yield of direct HO<sub>2</sub><sup>°</sup> was exceptionally low, falling below the detection limit of the chemical detection system, and therefore could not be recorded using a conventional UV spectrophotometer.

Consequently, measuring the low radical yields (in our case, for HO<sub>2</sub><sup>°</sup>) in soft X-ray experiments becomes extremely challenging when relying on collecting irradiated samples at the microfluidic channel's end and subsequently testing them using a UV spectrophotometer. This highlights the necessity for a highly sensitive analysis system capable of precisely measuring such subtle changes in yield.

A solution we propose in this work is the use of an In-line UV analysis technique, using a UV detection cell (see figure 3.14). It is available in different materials (stainless steel, PEEK, ultem, plexiglas, and Teflon), and we chose to work with the PEEK (polyetheretherketone) material. PEEK is a high-performance thermoplastic that is expected to minimize the absorption of products of irradiation.

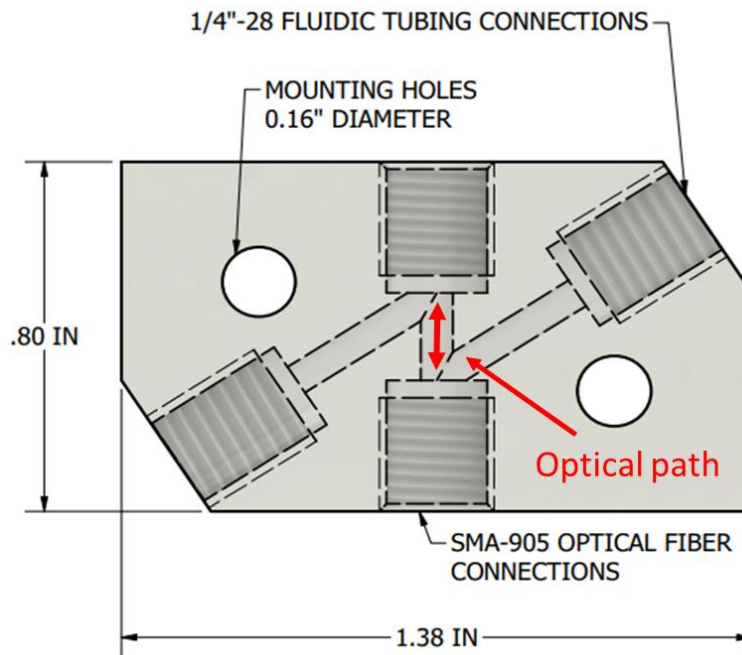


**Figure 3.14:** Schematic diagram of the UV detection cell having a Z-geometry. The cell has a PEEK outer body and provides the connections for optical fibers and the fluidics. The optical path of the cell is 2.5 mm. The image is taken from SMA-Z drawing of FIALab.

As shown in the figure 3.14, the detection cell (for specification see table 2.2, Chapter 2) uses UV-grade, fused silica windows (wavelength range from 190 nm to 1100 nm) and it has a Z geometry with a 2.5 mm optical path (2  $\mu$ l sample volume). The Z geometry minimizes the dead volume and also minimizes the formation of bubbles that can impair the measurements.<sup>34</sup>

### **3.2.2.2. Coupling microfluidic set-up and in-line UV detection cell**

The previously described UV detection cell was integrated to the microfluidic setup (microfluidic setup detailed in section 2.4.2 of chapter 2). It was positioned downstream to the microfluidic cell, as can be seen in the figure 3.15.

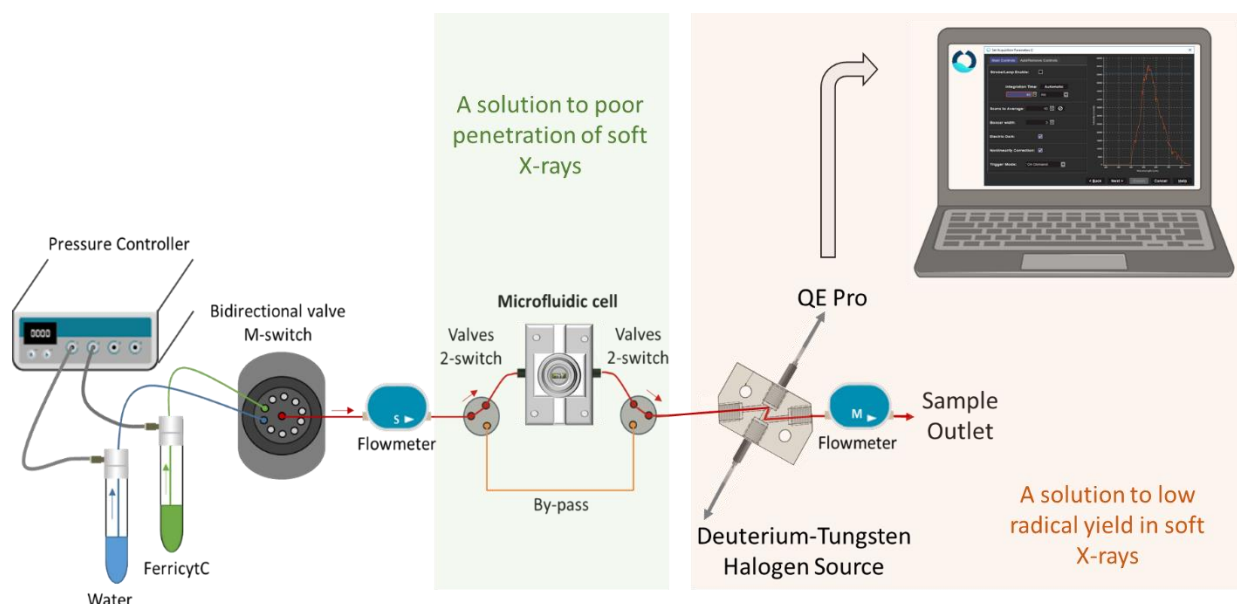


**Figure 3.15:** Sensitive detection system: Coupled microfluidic setup with in-line UV detection cell. The cell is connected to the spectrometer (QE pro) and the light source using the optical fibres, allowing detection of extremely low radical yields.

The two fluidic connections in the UV cell served as the inlet and outlet for the sample flowing in the microfluidic channel. It was possible to analyze the sample flowing in the UV cell thanks to the two optical fiber connections. One end of these fibers connected the UV cell to a Deuterium-Tungsten Halogen Source (wavelength range from 190 nm – 2500 nm, for reference, see table 2.2, Chapter 2), to illuminate the sample. This lamp was connected to an electrically filtered power supply to minimize intensity fluctuations. The other end was connected to the high-performance spectrophotometer, QE Pro (for reference, see table 2.2, Chapter 2). The QE Pro was chosen because it has a very efficient analog to digital converter (18 bit) that allows the measurement of a variation of  $1/262144$  in optical intensity (minimal measurable optical density of  $2 \cdot 10^{-5}$ ). In addition, thanks to the thermally cooled detector, it provides a very stable signal. Therefore, using this coupled setup, small changes in the absorbance values are detectable.

As described in section 3.2.2.1., the microfluidic cell is precisely positioned in front of the beam, which is extracted in air using the IRAD setup. The sample is then introduced into the coupled setup (figure 3.15) and allowed to flow at a desired flow rate. To capture the absorption spectra for both irradiated and non-irradiated samples, the beam shutter is initially manually opened and closed at regular intervals. The non-irradiated spectra are recorded both

before and after each irradiated spectrum in order to establish a real-time baseline. This approach allows for high sensitivity in detecting even small changes that occur upon irradiation.

The spectra are recorded using the 'OceanView' software. The initial step involves selecting appropriate acquisition parameters for the absorption spectra, such as average scans and integration time. This ensures that the lamp spectra, particularly at the desired wavelength (460 nm for WST-8 formazan), are not saturated during the whole acquisition. Subsequently, the signal for the reference solution is recorded. The software can then be used to launch the record for an entire spectrum of the sample, from 190 nm to 800 nm, or a time series spectrum at a particular wavelength.

### ***3.2.2.3. Automating the in-line UV detection***

After the successful coupling of the microfluidic set-up with the in-line UV detection cell, the next step was to automate the acquisition process. As mentioned in the previous section, the beam shutter was manually opened and closed to measure the signal of the irradiated and non-irradiated samples, respectively. However, to automate this process of beam off and beam on, a program was created (by Emmanuel Robert, PLEIADES beamline of SOLEIL synchrotron, France) using IGOR pro software that allowed the communication with the translation table where the microfluidic cell is placed. Using this program, the microfluidic cell could be aligned to the beam (center position obtained from the SiPM scan) as well as misaligned (by translating 2 mm along Tx) to cut off the irradiation. This was synchronised with the time evolution of the absorption signal at 460 nm.

The time of recording the signal for irradiated and non-irradiated signal, was 20-30 mins each. This time was calculated thanks to the hydrodynamic resistance measurement (see appendix I.III.) for the sample flowing through the microfluidic cell. The expected time for the sample to reach from the microfluidic cell to the UV detection cell was around 8 mins (depends on the length of the tubing between the two) at 5  $\mu$ L/min. This time could be experimentally measured by detecting a change in the signal at 460 nm and it was around 10 mins. It should be noted that the experimentally measured time was greater than the expected time due to the dilution effect and the former was referred to as the wait time (for the sample to reach the detection cell). Further, we wanted to record the sample for at least 10 mins



(accumulation time). This resulted in the synchronization of beam ON and beam OFF, with a time interval of 20 mins (wait time + accumulation time). This time could be increased (but not decreased) if more data points were to be collected in each interval. The synchronization can be seen (with time interval of 30 mins), in the figure 3.16, by the steps in the recorded raw data.

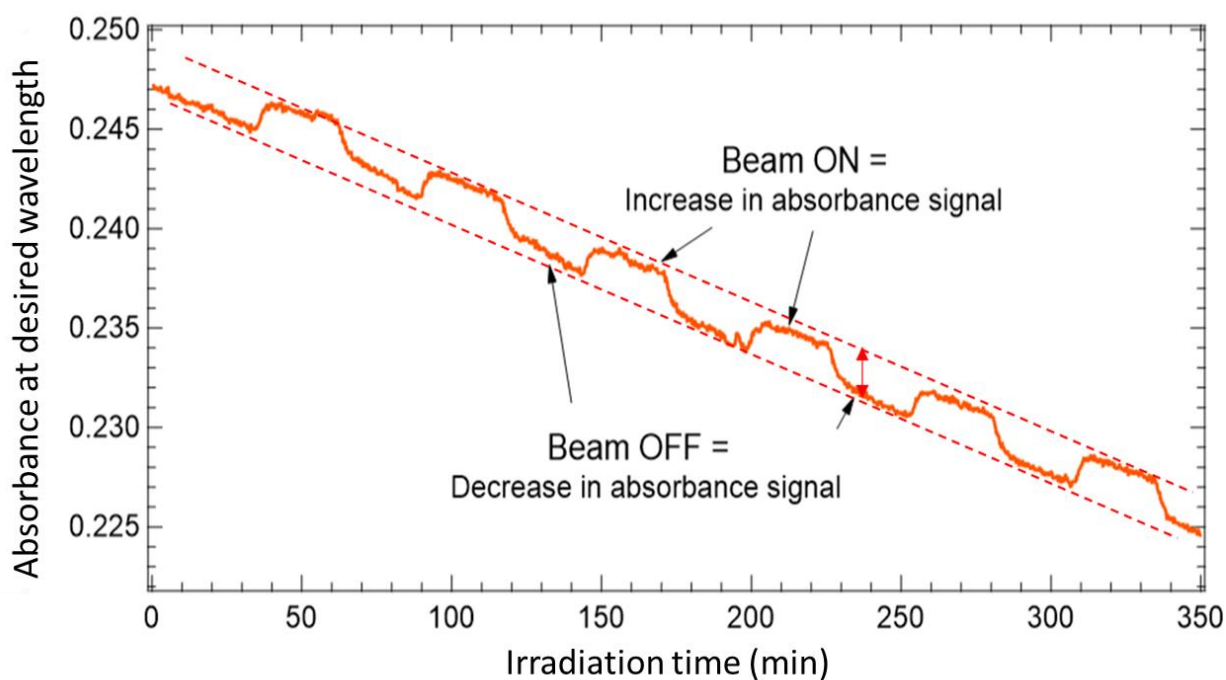


**Figure 3.16:** Experimental raw data obtained using the in-line detection set-up, recording the beam on (30 mins) and beam off (30 mins) absorbance signal. Depicted absorbance trace was monitored at the desired wavelength (460 nm) of the reduced product.

The recorded raw data may drift (see figure 3.16) because of fluctuations in lamp intensity and mechanical relaxations, including factors such as optical fiber connections and trapped microbubbles in the UV cell. To address the issue of microbubbles, the UV cell was regularly cleaned using ethanol. Additionally, the motion of optical fibers was restricted by securing them to a rigid support. The UV cell itself was secured on a support structure utilizing mounting holes incorporated into its design.

To take into account of such drift, a data treatment process was employed. This involved subtracting the absorbance signal at 460 nm with the absorbance signal at 800 nm, recorded as a function of time, to correct for variations in light intensity. By applying this correction, the drifts caused by lamp fluctuations and other mechanical factors were removed. Given that the

goal is to detect very small absorption changes, this correction step plays a vital role in ensuring accurate results. This data treatment was carried out using a custom Python code, enabling the analysis of thousands of spectra within few minutes, recorded during a single irradiation set. Following the data treatment, the absorbance variation as low as 10<sup>-4</sup> could be measured, not far from the maximal performance allowed by the QE pro detection system.

At this point, it should be noted that the absorption trace has a characteristic shape. The increase in the absorption is sharp, however, the decrease in the absorption trace is smooth and spread over a longer time. This is because of the dilution effect of the sample flowing through the cylindrical tubing.

### 3.2.3. Dose calculation

As described above, using the in-line UV analysis, we can accurately measure the absorbance values down to 10<sup>-4</sup>. An important step in calculating the yield of the radical produced (HO<sub>2</sub><sup>°</sup>) from the recorded absorbance values, is the estimation of the dose delivered to the sample during irradiation. Dose can be simply defined as energy deposited in the system per unit mass. The absorbed dose D can be given by the equation 3.1.<sup>29</sup>

$$D = \frac{E\Delta\phi_{solution}}{\rho Q} \quad 3.1$$

where E is the photon energy,  $\Delta\phi_{solution}$  is the number of photons absorbed in the solution per unit of time,  $\rho$  is the volumetric mass density of the solution, and Q is the flowrate. To determine  $\rho$  for each sample, multiple measurements are conducted by weighing different volumes of the sample and dividing their masses by their respective volumes. The dose delivered to the sample depends on the flow rate of the solution passing through the microfluidic channel. Lower flow rates result in a higher dose being delivered to the sample because it is exposed to the beam for a longer duration.

$$\Delta\phi_{solution} = T_{airgap} \cdot T_{Si_3N_4} \cdot (1 - T_{sample}) \cdot \phi_{photodiode} \quad 3.2$$

Unlike the other terms in equation 3.1, determining the value for  $\Delta\phi_{solution}$  is not straightforward. It depends on various other factors, as can be seen in the equation 3.2, where  $T_{air\ gap}$  is the transmission of beam through an air gap, through the cell's front silicon nitride membrane ( $T_{Si_3N_4}$ ) as well as through the sample ( $T_{sample}$ ). It must be noted that the air gap is

the distance between the sensitive surface of the photodiode and the air side of the Si<sub>3</sub>N<sub>4</sub> membrane of the microfluidic cell (along the beam axis direction). The transmission values through air and Si<sub>3</sub>N<sub>4</sub>, are available directly on the CXRO (Center for X-Ray Optics) website.<sup>35</sup>

$\phi_{\text{photodiode}}$  is the flux at the sensitive surface of the photodiode (used for alignment in section 3.2.2.1). The measurement of each term is explained below.

### 3.2.3.1. Photodiode flux ( $\phi_{\text{photodiode}}$ )

By recording the current measured through the broken window with the photodiode (see figure 3.17) and taking into account the beam transmission through the different coatings of the photodiode [Carbon (0.05  $\mu\text{m}$ ), Silicon Dioxide (0.007  $\mu\text{m}$ ) and Titanium (0.19  $\mu\text{m}$ )], the flux at the photodiode surface,  $\phi_{\text{photodiode}}$ , was calculated. The photodiode current was measured before and after each irradiation set, to account for changes in the flux, if any.

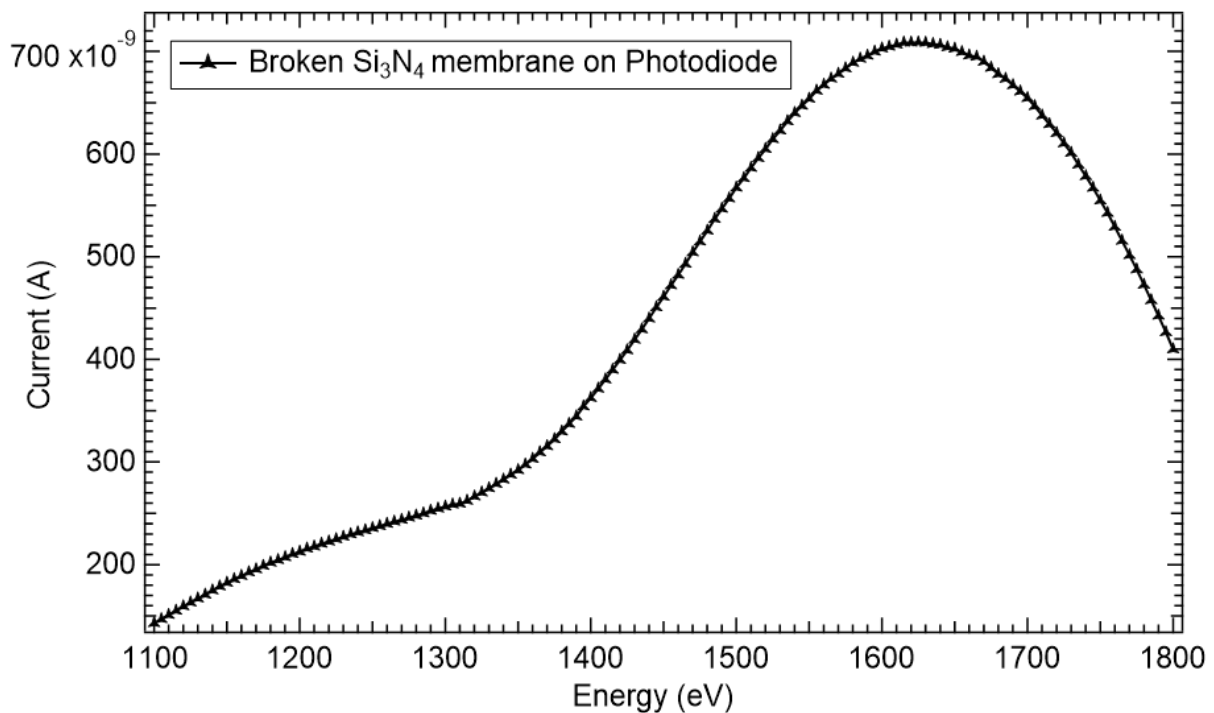


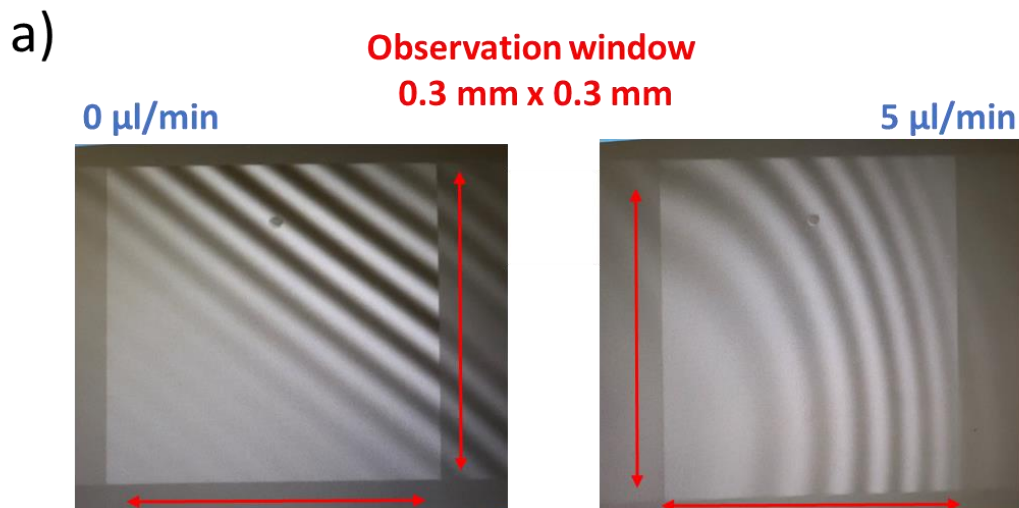
**Figure 3.17:** Variation in the current of the photodiode by varying the photon energy, at 500  $\mu\text{m}$  slit size, with a B (0.4  $\mu\text{m}$ ) inline filter, 4.06 mm air gap between the exit window of the IRAD setup and the photodiode sensitive area, measured through the broken ghost membrane.

### 3.2.3.2. Transmission through front Silicon nitride ( $T_{Si_3N_4}$ ) membrane

$T_{Si_3N_4}$  could be measured experimentally thanks to the use of the ghost membranes (broken and intact Si<sub>3</sub>N<sub>4</sub> membrane) fixed on the PD mask (explained in section 3.2.2.1). The ratio of maximum photodiode current through intact and broken membrane gives the transmission through the Si<sub>3</sub>N<sub>4</sub> membrane used ( $T_{Si_3N_4} = I_{intact} / I_{broken}$ ). The transmission values found were in comparable to those obtained from CXRO.<sup>35,28</sup>

### 3.2.3.3. Transmission through sample ( $T_{sample}$ )

To calculate the value of  $T_{sample}$ , the deformation (or the bulging) of the membrane has to be taken into account. The membrane can deform as pressure is applied to the microfluidic channel, for the sample to flow through it. This results in an increase in the sample volume inside the microfluidic cell that is being irradiated. The bulging of the membranes was measured through the interferometry measurements, performed at different flowrates, using an optical interferometer (see section 2.4.3). Linear fringes were observed when the solution was not flowing inside the cell, however, the fringes appeared curved when the solution was flowing through the cell. This can be seen in figure 3.18 a.



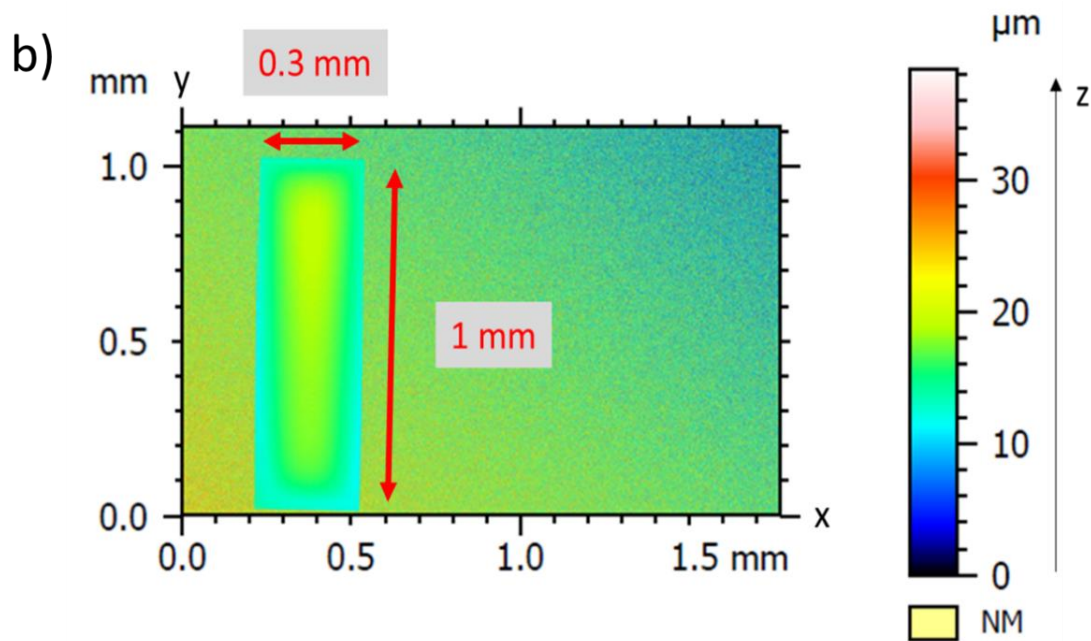


**Figure 3.18:** a) Pattern of the interference fringes when the sample is not flowing (left) and when it is flowing through the microfluidic cell (right) placed under the interferometer. b) 2D Image obtained from Interferometry representing the size of the membrane (1 mm x 0.3 mm) using a 10X objective by placing the microfluidic cell directly under the interferometer, for a flowrate of 5  $\mu\text{l}/\text{min}$ . The color scale in the figure corresponds to the z axis of the 2D image.

Subsequently, we measured the deformation of the membrane along the z-axis (figure 3.18 b) to understand the effect of applying pressure on the membranes. We observed that the maximum deformation of the membranes was around 8  $\mu\text{m}$  (see figure 3.19) per window. The deformation of both, the front and the back window increased linearly for low pressures and the variation in the deformation slowed down after 1100 mbar.

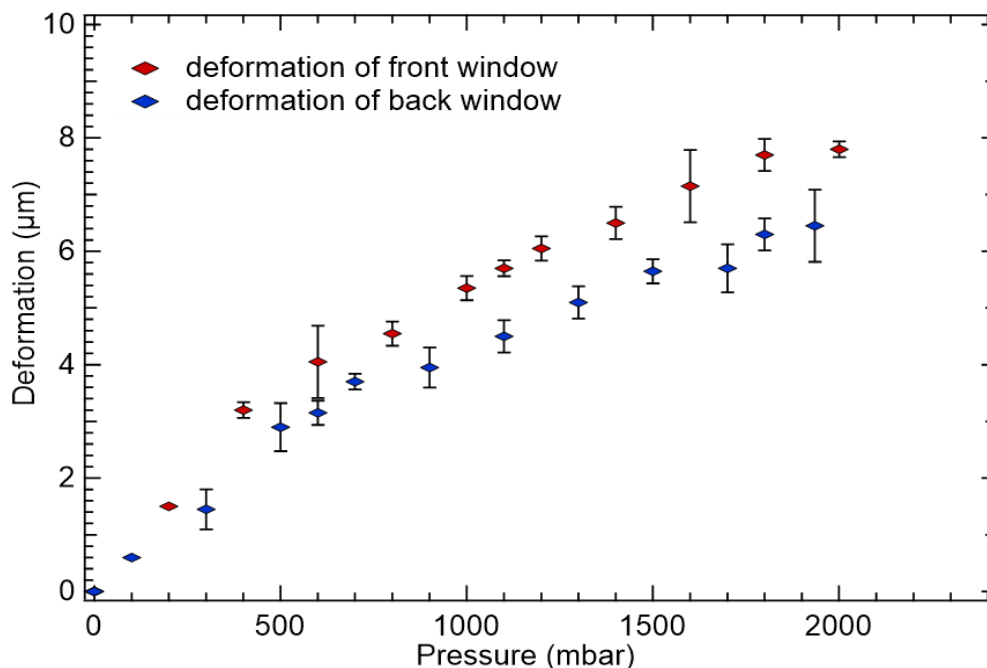


**Figure 3.19:** Deformation of the microfluidic cell's membranes, front and back, upon applying pressure for the sample to flow. Each reported values is an average of 3 data points, recorded at different times.

Using these deformation values ( $d$ ),  $T_{\text{sample}}$  was determined as follows. We calculated the transmission of the beam (using equation 3.3) assuming that the thickness of the solution ( $h$ ) was the same everywhere, either equal to  $5.3 \mu\text{m}$  (case of non-deformed membranes,  $h = 5.3 \mu\text{m}$ ) or equal to the maximum possible deformation ( $h = 5.3 \mu\text{m} + d$ ) (at the given flow rate). The average of these two values was taken as  $T_{\text{sample}}$ , and their difference divided by two as the uncertainty. This method gives an upper-bound to the uncertainty on this measurement.

$$T = \exp[-\mu(E)h] \quad 3.3$$

With all these factors into consideration, the absorbed dose was determined at the different photon energies (between 350 eV and 1700 eV) used in this work. The irradiation at 350 eV, 800 eV and 900 eV were performed at a single flowrate ( $5 \mu\text{l}/\text{min}$ ) and the dose values were 19.2 Gy, 82 Gy and 95 Gy, respectively. The dose delivered to the sample at photon energies above 1 keV were determined at three different experimental flowrates and are reported in table 3.2.

**Table 3.2:** Dose delivered (Gy) to the sample at different photon energies, as a function of flowrate

Photon Energy (eV)/Flowrate (μl/min)	1100	1200	1300	1400	1500	1600	1700	1800
13.5	8.40	9.19	8.74	9.70	12.38	13.06	10.55	5.89
10	11.33	12.39	11.78	13.05	16.62	17.50	14.11	7.86
5	22.51	24.40	22.92	25.02	31.37	32.52	25.83	14.18

The X-ray beam delivered by the diffraction grating contains unwanted higher-order radiation. The higher-order photon contributions were measured from air attenuation measurements and from the beam's transmission through in-line calibrated foils. The higher-order light contribution was negligible for photon energies above 1.1 keV, as can be seen from the blue curve in figure 3.20, where the photodiode current at 1280 eV decrease linearly as the distance between the microfluidic cell window and the exit window of the IRAD setup increases, with the minimum distance of 1 mm between the two. Below 1 keV, the higher-order light rejection devices (low pass filters) were not used in order to increase the dose. As a result, in the energy range, 400 eV to 700 eV, higher-order contamination was too large for measurements. At 890 eV and 800 eV, the dose was estimated considering the second order contribution that was found to be  $1.0 \pm 0.2\%$  and  $15.3 \pm 3.3\%$ , respectively. The contribution from the higher-order light at 890 eV is shown in the figure 3.20, where the curve deviates from linearity. For 350 eV, the dose was estimated taking into account the higher-order contributions, i.e. 2nd order contribution was  $39 \pm 14\%$ , 3rd order contribution was  $17 \pm 1\%$ , 4th order contribution was  $4 \pm 1\%$  and 5th order contribution was  $0.08 \pm 0.02\%$ .

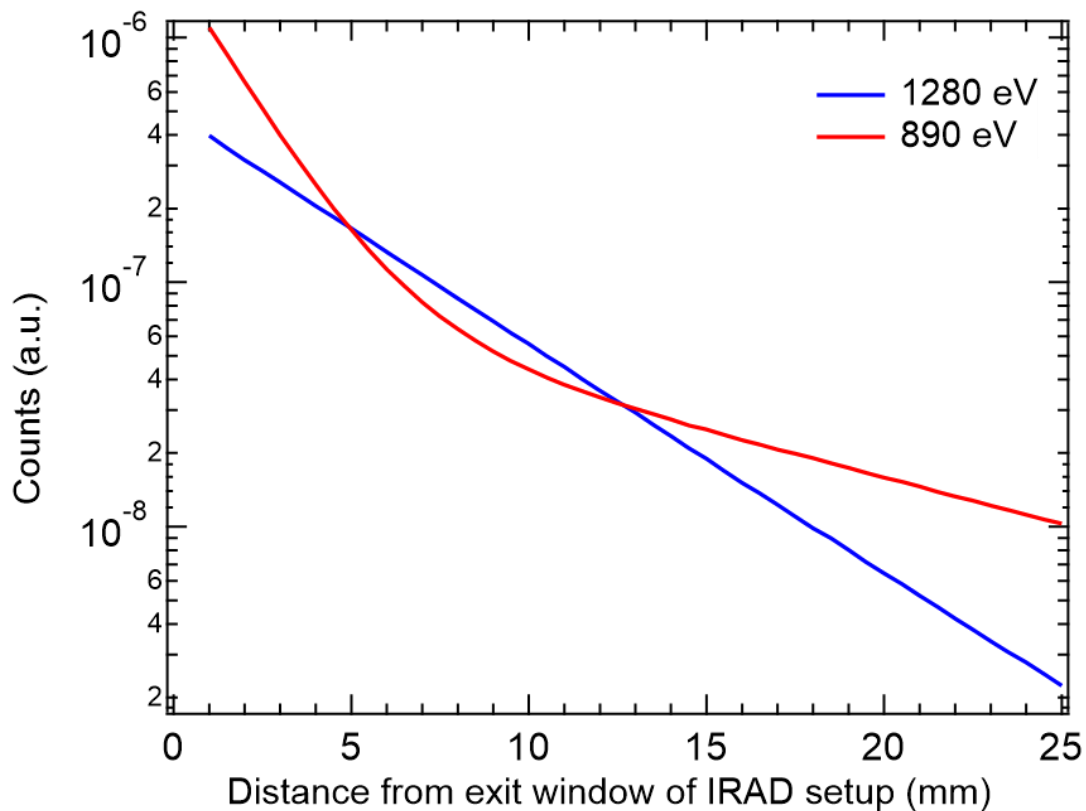


**Figure 3.20:** The decrease in the counts (i.e. the photodiode current in A) when the distance between the microfluidic cell window and the exit window of the IRAD setup increases. The minimum possible distance between the two is 1 mm, to avoid the breaking of the windows. The linear trend represents the absence of higher-order light at 1280 eV (blue curve) and the non-linear trend shows the contribution from higher-order light at 890 eV (red curve).

#### 3.2.4. Uncertainty calculation

The uncertainty in the dose values was calculated taking into consideration the different contributions listed in table 3.3.



**Table 3.3:** Uncertainty in dose calculation as a function of photon energy, as detailed in reference<sup>29</sup>.

<b>Photon energy (eV) / % Uncertainty</b>	<b>350</b>	<b>800</b>	<b>900</b>	<b>1100</b>	<b>1200</b>	<b>1300</b>	<b>1400</b>	<b>1500</b>	<b>1600</b>	<b>1700</b>	<b>1800</b>
<b>Photon flux</b>	6.3	8.6	6.7	4.4	3.8	3.4	3.7	5.1	7.4	10.3	13.4
<b>Air gap transmission from the photodiode to the cell membrane</b>	6.5	15.4	11.4	6.7	5.3	4.2	3.5	2.9	2.4	2.0	1.7
<b>Beam centering</b>	5.6	5.6	5.6	5.6	5.6	5.6	5.6	5.6	5.6	5.6	5.6
<b>Transmission of the silicon nitride membrane</b>	8.1	2.2	1.6	0.9	0.7	0.6	0.5	0.4	0.3	0.3	0.2
<b>Flow rate</b>	5.0	5.0	5.0	5.0	5.0	5.0	5.0	5.0	5.0	5.0	5.0
<b>Absorption of the solution*</b>	9.2	1.0	2.7	9.4	13.3	17.0	20.4	23.4	26.0	28.2	30.0
<b>Chemical dosimetry</b>	8.0	8.0	8.0	4.0	4.0	4.0	4.0	4.0	4.0	4.0	4.0
<b>Net uncertainty</b>	18.8	21.0	17.5	15.0	17.0	19.8	22.7	25.5	28.4	31.2	34.0

As specified in the previous section, the photon flux was measured using the photodiode. The uncertainty in this parameter was calculated thanks to the repeated measurements of photodiode current before and after each irradiation as well as by the uncertainty on the photodiode's coating (its thickness, quantum efficiency).<sup>31</sup> For the uncertainty on the air gap transmission between the photodiode and the cell membrane, estimation was made using the error on distance measurements via an optical level ( $\pm 0.2$  mm). The error in the positioning of the synchrotron beam with respect to the sample environment, accounted to be 5.6 %, was

assessed by calculating the effect of a 50 µm misalignment.<sup>29</sup> The pressure and the flowrate were recorded during each irradiation experiment, allowing to estimate the upper and lower bound of the flowrate. The uncertainty in flowrate was therefore calculated to be 5 %, and was deduced from the standard deviation of the flowrate values, recorded as a function of time, during irradiation.

The error on the transmission via the silicon nitride window was calculated using the uncertainty in the thickness ( $\pm 10$  %) and density (2.68 to 3.10 g/cm<sup>3</sup>) of the membrane, as well as the composition of silicon nitride membrane (from Si<sub>3</sub>N<sub>4</sub> to SiN), provided by the manufacturer. The uncertainty in the UV absorption measurements corresponds to the standard deviation of the absorption values, recorded at each photon energy. This value is doubled for the energies below 1 keV because the absorbance values at these energies were recorded only once and hence. The uncertainty values for the absorption of the solution are given for a flow rate of 5 µl/min. It should be noted that these uncertainty values increase with increasing flow rate (by increasing the pressure) due to the increase in the bulging of the membranes.

The maximum contribution to the uncertainty was from the absorption of the beam in the solution, except at 800 and 890 eV, as most of the dose is already absorbed prior to exiting the solution (in the channel).

### 3.2.5. Superoxide detection upon irradiation with soft X-rays

The soft X-ray irradiation experiments were performed using the above described setup, i.e. the microfluidic cell coupled with in-line UV setup. In this section we describe the yield measurements of both, direct and indirect HO<sub>2</sub><sup>°</sup> formation.

#### **3.2.5.1. Yields from direct pathway**

To measure the direct HO<sub>2</sub><sup>°</sup> production, all the irradiation experiments were performed at the photon energy of 1620 eV, where the maximum photon flux and higher spectral purity is reached on the soft X-ray branch of the METROLOGIE beamline (table 3.2, 1620 eV,  $1.18 \times 10^{10}$  photons/s after the cell Si<sub>3</sub>N<sub>4</sub> membrane). This choice was essential for the measurement of the extremely low production yield of superoxide coming from doubly ionized water molecules, to increase the signal of the reduced probe with respect to the background.

The effect of the irradiation on the sample was analyzed using the in-line UV detection scheme, described earlier. Figure 3.21 depicts the difference between the absorbance at the characteristic absorption wavelength of the probe, 460 nm, and the absorbance at 800 nm, recorded over time. It shows alternating sequences (every 20 mins) during which the flowing sample was not irradiated (background) and sequences during which it was irradiated. The sensitivity of the detection technique can be seen in the absorbance variations between the irradiated and non-irradiated solutions (or optical density), shown in figure 3.21, which are in the 10<sup>-4</sup> range, facilitating low radical yield detection that previously required the use of fluorescence probes.<sup>36</sup>

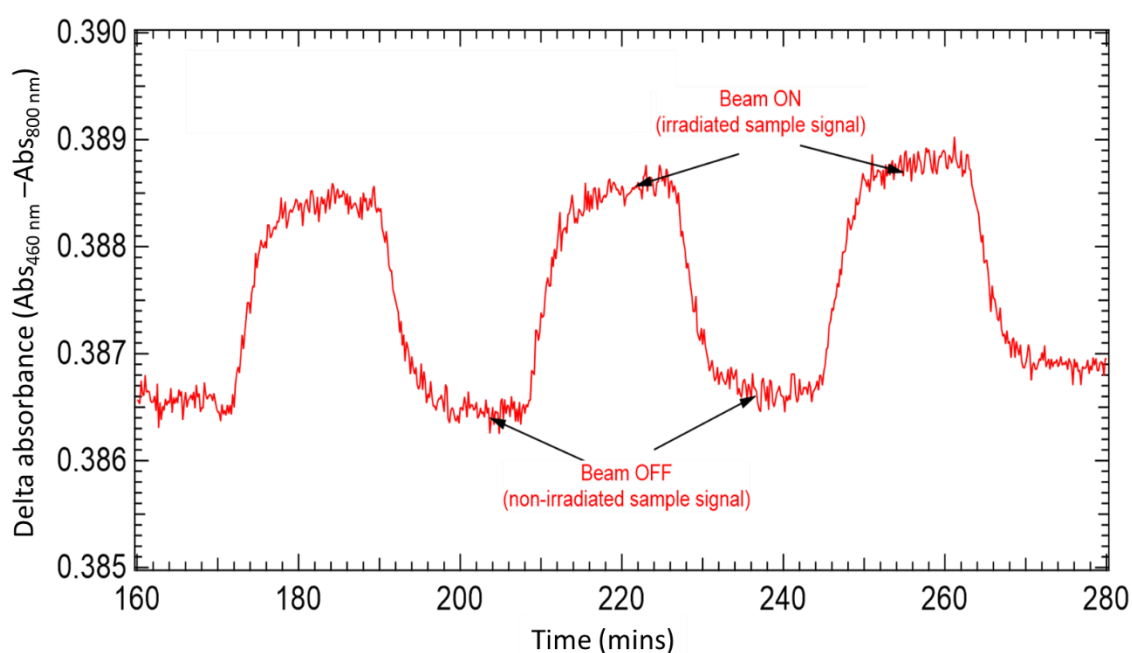


**Figure 3.21:** Experimental data obtained using the in-line detection set-up, after the data treatment (difference between the absorbance at 460 nm and that at 800 nm). The beam was periodically on and off. Absorbance were measured for a 300 μM WST8 solution in anoxic condition, without SOD and without catalase, at 5 μL/min corresponding to 32 Gy at 1620 eV. A horizontal translation of 2 mm of the microfluidic cell, compared to its optimized position in front of the synchrotron beam (69.8 mm in figure 3.12), gives us the beam off position (non-irradiated sample). This facilitated a real-time baseline correction (and the elimination of the baseline drift using the data treatment).

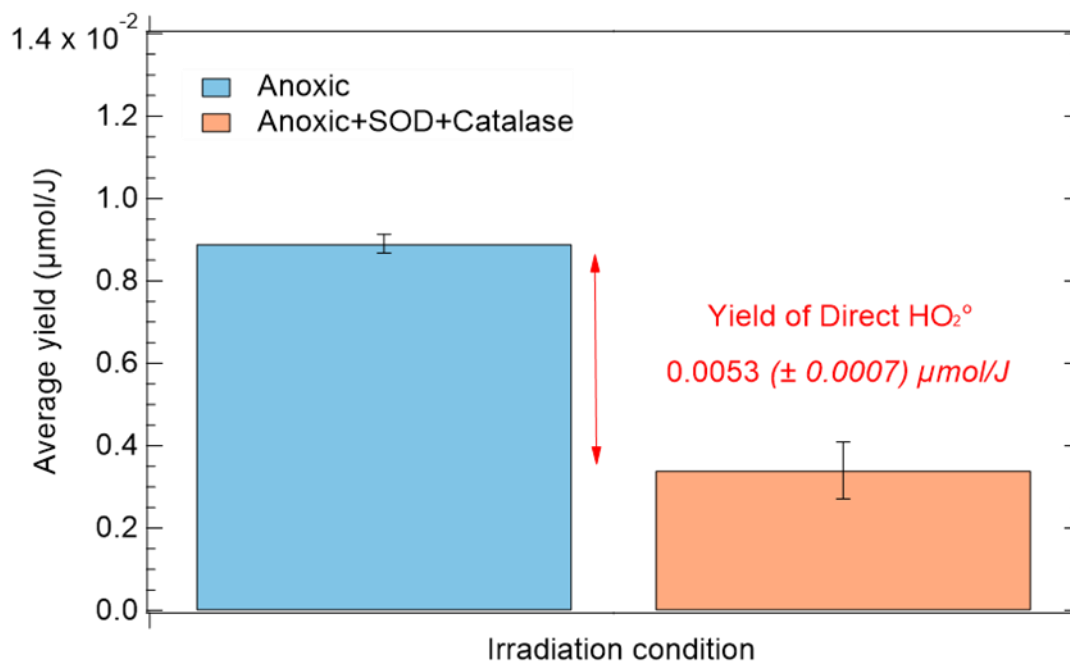


**Figure 3.22:** Yield of direct HO<sub>2</sub><sup>•</sup> production resulting from the difference of the yield of the reduced probe in anoxic (condition 2) and anoxic+SOD+catalase (condition 4), using synchrotron 1620 eV soft X-ray.

Multiple absorbance values (~10 data points for each condition) were recorded using a 5 μl/min flow rate, for each condition, and the yield was calculated. An average of these yield values, for both the conditions used (anoxic and anoxic/SOD/catalase conditions), is shown in figure 3.22. The yield of the direct HO<sub>2</sub><sup>•</sup>,  $G(\text{HO}_2^\bullet)$ , was found to be  $5.330 \times 10^{-9} (\pm 0.66 \times 10^{-9})$  M/Gy, i.e.  $0.0053 (\pm 0.0007) \mu\text{mol/J}$  by subtracting the HO<sub>2</sub><sup>•</sup> yield in the anoxic and anoxic/SOD/catalase conditions (see table 3.4).

Interestingly, the difference between the yield of superoxide obtained in anoxic/SOD and anoxic/SOD/catalase conditions, was negligible in the case of soft X-rays, unlike in the case of gamma radiation. This suggested that the H<sub>2</sub>O<sub>2</sub> production was negligible or not sufficient to reoxidize the formazan, during the soft X-ray irradiation.

At 1620 eV, core ionization is the most probable (~95%)<sup>37</sup>, so that almost each absorbed photon at this energy results in one core-shell ionization. Moreover, Auger transition probabilities are nearly 100% for oxygen atoms,<sup>38</sup> so that  $G(\text{H}_2\text{O}_2^{2+})$  is about  $0.006 \mu\text{mol/J}$  (one core ionization for 1620 eV deposited in the solution). This value is very near the  $G(\text{HO}_2^\bullet)$  of  $0.0053 \mu\text{mol/J}$  measured here. This indicates that with each double ionization we have one

superoxide production within experimental errors (conversion factor from H<sub>2</sub>O<sup>2+</sup> to HO<sub>2</sub><sup>°</sup>: 100% ± 30%). Therefore, we must envision that the reactions (3.2) and (3.3) are very efficient in our conditions, especially taking into account that some of the HO<sub>2</sub><sup>°</sup> can react with other radicals (like HO<sup>°</sup>) in the ionization tracks (see reaction 1.21, Chapter 1). But it could not be excluded that this reaction could also be even more efficient in the high LET ion tracks. This implies that nearly all doubly ionized water molecules dissociate to form an oxygen atom (as modeled using *ab initio* Molecular Dynamics<sup>39</sup>), and also, that the dense production of <sup>°</sup>OH radicals by the two secondary electrons close to the O atoms leads to a very efficient production of HO<sub>2</sub><sup>°</sup> (one per oxygen atom) *via* reaction (3.3). A similar conclusion (the very efficient production of HO<sub>2</sub><sup>°</sup> from O) was drawn from Monte Carlo simulations of heavy ions radiolysis, in which multiply ionized water molecules are formed at short impact parameter along the ion path, where the <sup>°</sup>OH radical density is large.<sup>23, 40</sup>

There could be other processes leading to the water double ionization, in addition to that formed by soft X-rays via Auger decay. One such process is the double ionization by electron impact, which has been studied theoretically in liquid water.<sup>41</sup> Calculated double over single ionization cross sections ratios allow a rough estimate of the electron impact double ionization contribution in the liquid phase.

In the direct double ionization, two electrons are emitted either originating from the same or two different molecular orbitals (MO) of the water molecule. Oubaziz *et al.* calculated that the double vs single ionization cross-section ratio increases steeply from 50 to 200 eV, and tends to a constant value of about 1.9 % for increasing impact energy.<sup>42</sup>

The W (mean energy to form an ion-electron pair) value of liquid water, was calculated as a function of incident electron energy (E) by dividing the given incident electron energy by the number of electrons produced during the slowing, including all secondary electrons.<sup>43</sup> The asymptotic W value (for high incident energies, i.e. E > 1 keV) is 25.4 eV, and remains below 30 eV for E > 100 eV. Assuming an H<sub>2</sub>O<sup>2+</sup>/H<sub>2</sub>O<sup>+</sup> ratio of 0.019, we would then have  $[(E_{\text{photo}} - 50) + (E_{\text{Auger}} - 50)] / W * 0.019 = \text{one double ionizations per photon absorbed, due to electron impact only (taking } W = 30 \text{ eV)}$ .

This results in a total of *two double ionizations per 1620 eV photon absorbed* (one through K-shell photo-absorption and the other through electron impact). Taking this into account, we can deduce that the conversion factor of H<sub>2</sub>O<sup>2+</sup> to HO<sub>2</sub><sup>°</sup> drops to 50% ± 15%.

If we compare the superoxide production in our case with the one produced by particles of similar LET (e.g., 77 MeV A<sup>-1</sup> <sup>36</sup>S with a LET of 250 keV/μm or 70 MeV A<sup>-1</sup> <sup>40</sup>Ar with a LET of 290 keV/μm), we find very similar values of G(HO<sub>2</sub>) of 0.006 μmol/J.<sup>44,45</sup> However, for these ions, the G(H<sub>2</sub>O<sup>2+</sup>) (by ejection of two secondary electrons) is very significant, about 0.052 μmol/J (about 1 double ionization for 200 eV deposited in solution).<sup>23</sup> From these values, it can be estimated that for sulfur ions, the conversion factor from H<sub>2</sub>O<sup>2+</sup> to HO<sub>2</sub><sup>°</sup> is only of 10%. Thus, in these conditions, the reaction (3.3) seems much less efficient at producing superoxide than in soft X-rays tracks (more than 50% efficiency). With soft X-ray irradiation, the fact that an Auger emission occurs (with a time delay between the photoelectron and Auger electron, corresponding to the lifetime of O-K vacancy being 4.1 fs in water<sup>46</sup>) may reinforce the efficiency of the reaction (3.3), with respect to simultaneous double ionization occurring in the case of ions (see also section 3.2.5.2). Moreover, non-local relaxation mechanisms, namely, Intermolecular Coulombic Decay (ICD)<sup>47</sup> and Electron Transfer Mediated Decay (ETMD),<sup>48</sup> can compete with the local Auger decay and thereby decrease the H<sub>2</sub>O<sup>2+</sup> production. Due to their low contribution, at the moment that the Auger decay channel is open, these non-local decay pathways have not been considered until now.<sup>49</sup>

**Table 3.4:** G<sub>direct</sub>(HO<sub>2</sub><sup>°</sup>) production yield determined using WST-8 as a chemical probe, irradiated in different conditions. The measured production yield in the case of <sup>137</sup>Cs gamma source and 1620 eV synchrotron soft X-rays is given in the table along with the literature values of the yield in the case of high energy S ions and C ions. The yields are given in μmol/J.

<b>Irradiation source</b>	<b><sup>137</sup>Cs (LET = 0.4 keV/μm)<sup>26</sup></b>	<b>Synchrotron soft X-rays (1620eV, LET ~ 100 keV/μm)</b>	<b>S ions, (LET = 200 keV/μm)</b>	<b>C ions (LET ≤ 26 keV/μm)</b>

$G_{\text{direct}}(\text{HO}_2^\circ)$	$\leq 0.005$	0.0053 ( $\pm 0.0007$ )	0.005 <sup>50,51</sup>	$\leq 0.003$ <sup>23,25</sup>
( $\mu\text{mol/J}$ )	(present work)	(present work)		

### 3.2.5.2. Yields from indirect pathway

In addition to the soft X-ray experiments performed in the anoxic conditions (with SOD and catalase), the irradiation was also performed in the oxic condition (without SOD and Catalase, condition 1), which provides information on indirect HO<sub>2</sub><sup>•</sup> formation. The indirect HO<sub>2</sub><sup>•</sup> formation yield ( $G(\text{HO}_2^\circ)_{\text{indirect}}$ ) was found to be ~10 times that of the direct HO<sub>2</sub><sup>•</sup> formation yield, around 1600 eV. This facilitated an investigation of the indirect HO<sub>2</sub><sup>•</sup> production at lower photon flux and for a wider photon energy range. Hence, the evolution of indirect HO<sub>2</sub><sup>•</sup> yield (an indication for solvated electrons yield, see reaction 3.1) was investigated as a function of photon energy (350 eV to 1700 eV). The 400 eV-700 eV energy range was not studied because of the strong beam absorption in air and in the silicon nitride window and a very large contribution in the dose from higher order light in the synchrotron beam.

To determine the indirect HO<sub>2</sub> yield between 1100 eV to 1800 eV, the absorbance values were measured for three different flow rates (5  $\mu\text{l/min}$ , 10  $\mu\text{l/min}$ , 13  $\mu\text{l/min}$ ) and thus different dose values. The variation in the concentration of the probe calculated from the absorbance values (using Lambert Beer law) is shown as a function of dose in figure 3.23. It was indeed observed that this variation exhibits a linear response to the dose passing through the origin, indicating an efficient background correction. For each photon energy, the yields were then calculated (see table 3.2) for the three flow rates and averaged. At energies below 1 keV, the yield was measured only at a 5  $\mu\text{l/min}$  flow rate to maximize the dose. The reported yields below 1 keV, in figure 3.24, were measured only once.

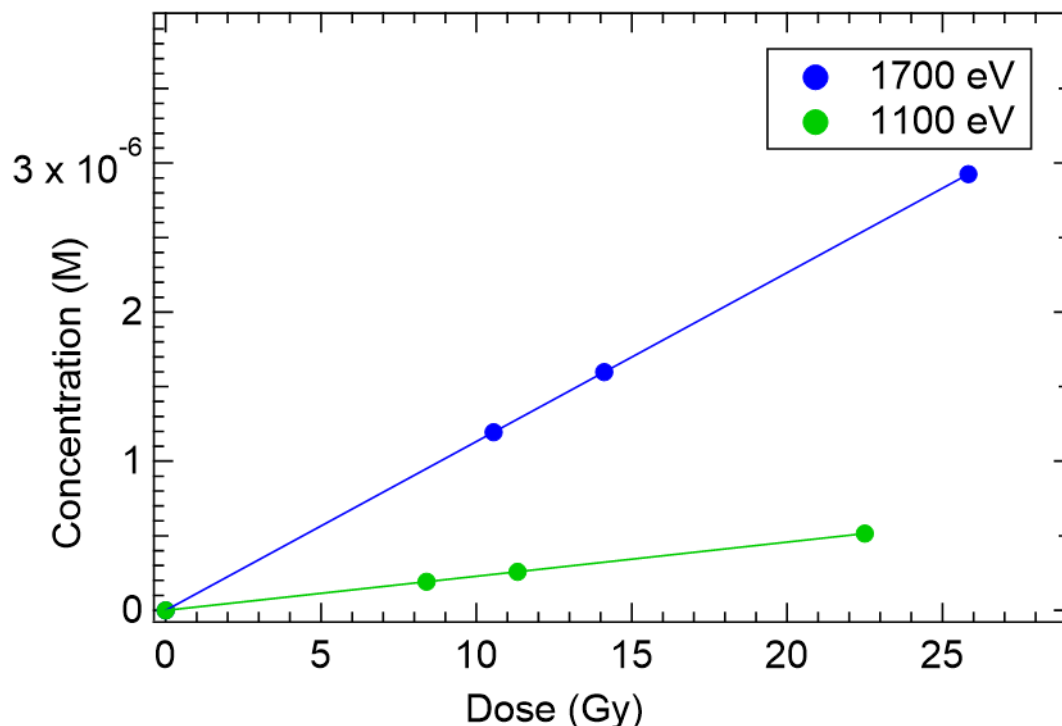


**Figure 3.23:** Variation in the concentration of the reduced probe (WST8 formazan, oxic conditions) as a function of dose, with 500  $\mu\text{m}$  monochromator slit size, at two different photon energies, namely, 1100 eV and 1700 eV.

The experimental indirect HO<sub>2</sub><sup>°</sup> yield as a function of energy is presented in figure 3.24, along with the Monte Carlo (MC) simulation (performed by Benoit Gervais) results for mono-energetic electrons. The MC results were taken from a previous work,<sup>31</sup> performed on a liquid water system containing 10 mM Benzoate. This work showed that the <sup>°</sup>OH yields had a minimum around 1 keV, owing to the increased ionization density in the nanometric tracks. The presence of benzoate (acting as a <sup>°</sup>OH scavenger) in the simulations can influence the indirect HO<sub>2</sub><sup>°</sup> yield, as <sup>°</sup>OH can react with it, (see reaction 1.21, Chapter 1), giving a higher indirect HO<sub>2</sub><sup>°</sup> yield compared to the experiments.

The first observation is the strong dependence of the measured indirect HO<sub>2</sub><sup>°</sup> yield with photon energy. The minimum in the experimental yield was measured to be almost zero at approximately 800 eV. In addition, there is a very steep decrease in the experimental yield around 1280 eV as the photon energy decreases.



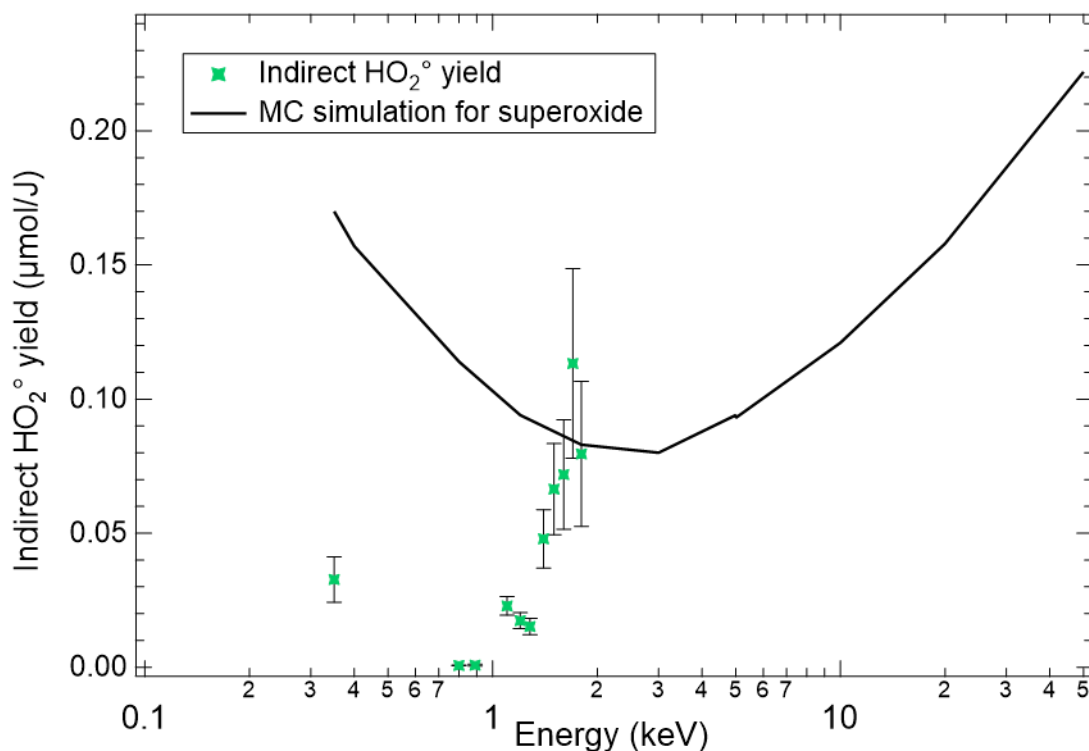


**Figure 3.24:** Evolution of the yield of indirect HO<sub>2</sub><sup>°</sup> (green symbols) as a function of photon energy and the MC simulation (black curve) results for superoxide.<sup>31</sup> The uncertainties on each energy are reported in the table 3.3. The yields below 1 keV were measured only once and those above 1 keV are an average of yield at 3 different flowrates (see text).

It is the photon energy range, where the photoelectron and Auger electron have the same energy and where the electron tracks are very compact.<sup>52</sup> Owing to the delayed emission of the Auger electron compared to the photoelectron, the probability that they interact directly with each other is quite low. However, there is a high probability that the Auger electron interacts with the highly ionized and compact tracks created by the photoelectron. This can result in an increase of the local ionization density and a decrease in radical yields. It would be interesting to adapt the Monte Carlo codes to test this hypothesis.

At 350 eV (below the O1s threshold, 535 eV), even if these effects are not expected to occur, the discussion on the yield remains difficult because of the large contribution of higher order light (see section 3.2.3.). This reflects the difficulties in the measurements of the yields at lower energies, due to higher order contamination and the large absorption of the beam in the air. This suggests that the experiment for low photon energy should be performed under vacuum conditions, to increase the dose (no absorption in air or the silicon nitride window of

the IRAD setup). Investigating low photon energies would allow a better understanding of low energy electron tracks.

### 3.3. Conclusion

The current work focuses on the effect of inner shell ionization on the water molecules, when irradiated with soft X-rays. In water, this resulted in double ionized water molecules that could dissociate (leading to oxygen atom) and undergo reactions in the dense tracks (leading to superoxide radical by reaction with °OH in the dense tracks). We, thereby, emphasize in this work that the production of superoxide radicals is as essential as the one of °OH radicals, in the dense ionization tracks. To measure the production yield of these superoxide radicals, a chemical detection system comprising a chemical probe (WST-8) and enzymes (catalase and SOD) was developed. The conditions of irradiation and concentrations, for the chemical system were optimized by rigorous experiments using the gamma source.

In this chapter, we also present the solution to the major challenges occurring when irradiating in the soft X-ray regime, i.e. their poor penetration and low radical yields. These solutions include the use of a microfluidic cell coupled to an in-line UV detection technique, allowing to measure the absorbance values down to 10<sup>-4</sup>. It was also shown that microfluidic cell alignment played a very important role in performing such experiments, which was facilitated by the development of new alignment device (SiPM) that allowed a fast and accurate alignment.

Thanks to the highly sensitive detection setup, the measurements of extremely low radical yields were possible. The yield of direct HO<sub>2</sub><sup>°</sup> was found to be 0.0053 (±0.0007) μmol/J at 1620 eV, using the synchrotron soft X-rays. It was found that the percentage of double ionization resulting in superoxide formation was much more pronounced for soft X-rays than for heavy ions. This suggested that a precise study on the mechanism underlying direct HO<sub>2</sub><sup>°</sup> production is required, for example using Ab-Initio Molecular Dynamics (AIMD) simulations. The yield of indirect HO<sub>2</sub><sup>°</sup> (0.072 μmol/J at 1600 eV), was found to be significantly larger than the yield of direct HO<sub>2</sub><sup>°</sup>, allowing its determination as a function of the photon energy. It showed an expected and strong dependence on the photon energy around 1280 eV that coincided with the maximum of the photo- and Auger electrons tracks overlap. Moreover, this study points out the necessity of performing the irradiations with the microfluidic cell under

vacuum for photon energies below 700 eV, to decrease absorption in air and in the extraction window of the IRAD set-up.

Electron-ionization tracks interactions in radiation chemistry is an old subject.<sup>53,54</sup> However it has gained a new attention due to the development of flash therapy, when track overlap is thought to be one possible origin of specific biological effect. Soft X-rays may also provide an interesting model of these effects.

## Reference

- (1) Chen, J.; Rogers, S. C.; Kavdia, M. Analysis of Kinetics of Dihydroethidium Fluorescence with Superoxide Using Xanthine Oxidase and Hypoxanthine Assay. *Ann Biomed Eng* **2013**, *41* (2), 327–337. <https://doi.org/10.1007/s10439-012-0653-x>.
- (2) Fridovich, I. Superoxide Radical and Superoxide Dismutases. *Annual Review of Biochemistry* **1995**, *64* (1), 97–112. <https://doi.org/10.1146/annurev.bi.64.070195.000525>.
- (3) Cheng, C.; Chen, L.; Chou, C.; Liang, J. Investigations of Riboflavin Photolysis via Coloured Light in the Nitro Blue Tetrazolium Assay for Superoxide Dismutase Activity. *Journal of Photochemistry and Photobiology B: Biology* **2015**, *148*, 262–267. <https://doi.org/10.1016/j.jphotobiol.2015.04.028>.
- (4) Ukeda, H.; Shimamura, T.; Tsubouchi, M.; Harada, Y.; Nakai, Y.; Sawamura, M. Spectrophotometric Assay of Superoxide Anion Formed in Maillard Reaction Based on Highly Water-Soluble Tetrazolium Salt. *Anal. Sci.* **2002**, *18* (10), 1151–1154. <https://doi.org/10.2116/analsci.18.1151>.
- (5) Chen, J.; Rogers, S. C.; Kavdia, M. Analysis of Kinetics of Dihydroethidium Fluorescence with Superoxide Using Xanthine Oxidase and Hypoxanthine Assay. *Ann Biomed Eng* **2013**, *41* (2), 327–337. <https://doi.org/10.1007/s10439-012-0653-x>.
- (6) Xu, C.; Liu, S.; Liu, Z.; Song, F.; Liu, S. Superoxide Generated by Pyrogallol Reduces Highly Water-Soluble Tetrazolium Salt to Produce a Soluble Formazan: A Simple Assay for Measuring Superoxide Anion Radical Scavenging Activities of Biological and Abiological Samples. *Analytica Chimica Acta* **2013**, *793*, 53–60. <https://doi.org/10.1016/j.aca.2013.07.027>.
- (7) Chamchoy, K.; Pakotiprapha, D.; Pumirat, P.; Leartsakulpanich, U.; Boonyuen, U. Application of WST-8 Based Colorimetric NAD(P)H Detection for Quantitative Dehydrogenase Assays. *BMC Biochemistry* **2019**, *20* (1), 4. <https://doi.org/10.1186/s12858-019-0108-1>.
- (8) Tominaga, H.; Ishiyama, M.; Ohseto, F.; Sasamoto, K.; Hamamoto, T.; Suzuki, K.; Watanabe, M. A Water-Soluble Tetrazolium Salt Useful for Colorimetric Cell Viability Assay. *Anal. Commun.* **1999**, *36* (2), 47–50. <https://doi.org/10.1039/A809656B>.
- (9) Ishiyama, M.; Miyazono, Y.; Sasamoto, K.; Ohkura, Y.; Ueno, K. A Highly Water-Soluble Disulfonated Tetrazolium Salt as a Chromogenic Indicator for NADH as Well as Cell Viability. *Talanta* **1997**, *44* (7), 1299–1305. [https://doi.org/10.1016/s0039-9140\(97\)00017-9](https://doi.org/10.1016/s0039-9140(97)00017-9).
- (10) Ishiyama, M.; Miyazono, Y.; Shiga, M.; Sasamoto, K.; Ohkura, Y.; Ueno, K. Benzothiazole-Containing Tetrazolium Salts That Produce Water-Soluble Formazan Dyes Absorbing at a Long Wavelength upon NADH Reduction. *ANAL. SCI.* **1996**, *12* (3), 515–519. <https://doi.org/10.2116/analsci.12.515>.
- (11) Ansenberger-Fricano, K.; Ganini, D. da S.; Mao, M.; Chatterjee, S.; Dallas, S.; Mason, R. P.; Stadler, K.; Santos, J. H.; Bonini, M. G. The Peroxidase Activity of Mitochondrial Superoxide Dismutase (MnSOD/SOD2). *Free Radic Biol Med* **2013**, *54*, 116–124. <https://doi.org/10.1016/j.freeradbiomed.2012.08.573>.
- (12) Ukeda, H.; Kawana, D.; Maeda, S.; Sawamura, M. Spectrophotometric Assay for Superoxide Dismutase Based on the Reduction of Highly Water-Soluble Tetrazolium Salts by Xanthine-

- Xanthine Oxidase. *Biosci Biotechnol Biochem* **1999**, *63* (3), 485–488.  
<https://doi.org/10.1271/bbb.63.485>.
- (13) McCord, J. M.; Fridovich, I. Superoxide Dismutase. An Enzymic Function for Erythrocyte (Hemocytin). *J. Biol. Chem.* **1969**, *244* (22), 6049–6055.
- (14) Schmitt, F.-J.; Renger, G.; Friedrich, T.; Kreslavskii, V.; Zharmukhamedov, S.; Los, D.; Kuznetsov, V.; Allakhverdiev, S. Reactive Oxygen Species: Re-Evaluation of Generation, Monitoring and Role in Stress-Signaling in Phototrophic Organisms. *Biochimica et biophysica acta* **2014**, *1837*. <https://doi.org/10.1016/j.bbabi.2014.02.005>.
- (15) Ogawa, K.; Kanematsu, S.; Asada, K. Generation of Superoxide Anion and Localization of CuZn-Superoxide Dismutase in the Vascular Tissue of Spinach Hypocotyls: Their Association with Lignification. *Plant and Cell Physiology* **1997**, *38* (10), 1118–1126.  
<https://doi.org/10.1093/oxfordjournals.pcp.a029096>.
- (16) Contente, M. L.; Marzuoli, I.; Iding, H.; Wetzl, D.; Puentener, K.; Hanlon, S. P.; Paradisi, F. Screening Methods for Enzyme-Mediated Alcohol Oxidation. *Sci Rep* **2022**, *12* (1), 3019.  
<https://doi.org/10.1038/s41598-022-07008-7>.
- (17) Feerman, D. E.; Winston, G. W.; Cederbaum, A. I. Ethanol Oxidation by Hydroxyl Radicals: Role of Iron Chelates, Superoxide, and Hydrogen Peroxide. *Alcoholism: Clinical and Experimental Research* **1985**, *9* (2), 95–102. <https://doi.org/10.1111/j.1530-0277.1985.tb05525.x>.
- (18) Vandewalle, P. L.; Petersen, N. O. Oxidation of Reduced Cytochrome c by Hydrogen Peroxide. *FEBS Letters* **1987**, *210* (2), 195–198. [https://doi.org/10.1016/0014-5793\(87\)81336-4](https://doi.org/10.1016/0014-5793(87)81336-4).
- (19) Dorfman, L. M. Reactivity of the Hydroxyl Radical in Aqueous Solutions.
- (20) Schultze, H.; Schulte-Frohlinde, D. OH Radical Induced Oxidation of Ethanol in Oxygenated Aqueous Solutions. Part 1.—Formation of Acetic Acid. *J. Chem. Soc., Faraday Trans. 1* **1975**, *71* (0), 1099–1105. <https://doi.org/10.1039/F19757101099>.
- (21) Watanabe, R.; Saito, K. Monte Carlo Simulation of Water Radiolysis in Oxygenated Condition for Monoenergetic Electrons from 100eV to 1MeV. *Radiation Physics and Chemistry* **2001**, *62* (2), 217–228. [https://doi.org/10.1016/S0969-806X\(01\)00195-5](https://doi.org/10.1016/S0969-806X(01)00195-5).
- (22) Tan, A. S.; Berridge, M. V. Superoxide Produced by Activated Neutrophils Efficiently Reduces the Tetrazolium Salt, WST-1 to Produce a Soluble Formazan: A Simple Colorimetric Assay for Measuring Respiratory Burst Activation and for Screening Anti-Inflammatory Agents. *Journal of Immunological Methods* **2000**, *238* (1), 59–68. [https://doi.org/10.1016/S0022-1759\(00\)00156-3](https://doi.org/10.1016/S0022-1759(00)00156-3).
- (23) Gervais, B.; Beuve, M.; Olivera, G. H.; Galassi, M. E. Numerical Simulation of Multiple Ionization and High LET Effects in Liquid Water Radiolysis. *Radiation Physics and Chemistry* **2006**, *75* (4), 493–513. <https://doi.org/10.1016/j.radphyschem.2005.09.015>.
- (24) Draganic, Z. D.; Draganic, I. Origin of Primary Hydrogen Peroxide Yield in the .Gamma. Radiolysis of Water. *J. Phys. Chem.* **1969**, *73* (8), 2571–2577.  
<https://doi.org/10.1021/j100842a019>.
- (25) LaVerne, J. A.; Schuler, R. H. Track Effects in the Radiolysis of Water: HO<sub>2</sub>· Production by 200–800 MeV Carbon Ions. *J. Phys. Chem.* **1992**, *96* (18), 7376–7378.  
<https://doi.org/10.1021/j100197a044>.

- (26) Alpen, E. L. Chapter 14 - High Linear Energy Transfer Radiation Effects. In *Radiation Biophysics (Second Edition)*; Alpen, E. L., Ed.; Academic Press: San Diego, 1998; pp 365–392. <https://doi.org/10.1016/B978-012053085-4/50016-8>.
- (27) Huart, L. Inner Shell Ionization Effects on Molecules of Biological Interest in an Aqueous Medium. phdthesis, Sorbonne Université, 2022. <https://tel.archives-ouvertes.fr/tel-03725615> (accessed 2022-09-02).
- (28) Henke, B. L.; Gullikson, E. M.; Davis, J. C. X-Ray Interactions: Photoabsorption, Scattering, Transmission, and Reflection at E = 50–30,000 eV, Z = 1–92. *Atomic Data and Nuclear Data Tables* **1993**, *54* (2), 181–342. <https://doi.org/10.1006/adnd.1993.1013>.
- (29) Huart, L.; Nicolas, C.; Hervé du Penhoat, M.-A.; Guigner, J.-M.; Gosse, C.; Palaudoux, J.; Lefrançois, S.; Mercere, P.; Dasilva, P.; Renault, J.-P.; Chevallard, C. A Microfluidic Dosimetry Cell to Irradiate Solutions with Poorly Penetrating Radiations: A Step towards Online Dosimetry for Synchrotron Beamlines. *J Synchrotron Rad* **2021**, *28* (3), 778–789. <https://doi.org/10.1107/S1600577521002691>.
- (30) Korde, R.; Cable, J. S.; Canfield, L. R. One Gigarad Passivating Nitrided Oxides for 100% Internal Quantum Efficiency Silicon Photodiodes. *IEEE Transactions on Nuclear Science* **1993**, *40* (6), 1655–1659. <https://doi.org/10.1109/23.273555>.
- (31) Huart, L.; Nicolas, C.; Kaddissy, J. A.; Guigner, J.-M.; Touati, A.; Politis, M.-F.; Mercere, P.; Gervais, B.; Renault, J.-P.; Hervé du Penhoat, M.-A. Soft X-Ray Radiation and Monte Carlo Simulations: Good Tools to Describe the Radiation Chemistry of Sub-keV Electrons. *J. Phys. Chem. A* **2020**, *124* (10), 1896–1902. <https://doi.org/10.1021/acs.jpca.9b10539>.
- (32) Yamaguchi, H.; Uchihori, Y.; Yasuda, N.; Takada, M.; Kitamura, H. Estimation of Yields of OH Radicals in Water Irradiated by Ionizing Radiation. *JRR* **2005**, *46* (3), 333–341. <https://doi.org/10.1269/jrr.46.333>.
- (33) Freyer, J. P.; Schillaci, M. E.; Raju, M. R. Measurement of the G-Value for 1.5 keV X-Rays. *International Journal of Radiation Biology* **1989**, *56* (6), 885–892. <https://doi.org/10.1080/09553008914552361>.
- (34) Lebl, R.; Cantillo, D.; Kappe, C. Continuous Generation, In-Line Quantification and Utilization of Nitrosyl Chloride in Photonitrosation Reactions. *Reaction Chemistry & Engineering* **2019**, *4*. <https://doi.org/10.1039/C8RE00323H>.
- (35) *CXRO X-Ray Interactions With Matter*. [https://henke.lbl.gov/optical\\_constants/](https://henke.lbl.gov/optical_constants/) (accessed 2023-05-19).
- (36) Tomanová, K.; Precek, M.; Múčka, V.; Vyšín, L.; Juha, L.; Čuba, V. At the Crossroad of Photochemistry and Radiation Chemistry: Formation of Hydroxyl Radicals in Diluted Aqueous Solutions Exposed to Ultraviolet Radiation. *Phys. Chem. Chem. Phys.* **2017**, *19* (43), 29402–29408. <https://doi.org/10.1039/C7CP05125E>.
- (37) Yeh, J. J.; Lindau, I. Atomic Subshell Photoionization Cross Sections and Asymmetry Parameters:  $1 \leq Z \leq 103$ . *Atomic Data and Nuclear Data Tables* **1985**, *32* (1), 1–155. [https://doi.org/10.1016/0092-640X\(85\)90016-6](https://doi.org/10.1016/0092-640X(85)90016-6).
- (38) Krause, M. O. Atomic Radiative and Radiationless Yields for K and L Shells. *Journal of Physical and Chemical Reference Data* **1979**, *8* (2), 307–327. <https://doi.org/10.1063/1.555594>.
- (39) Tavernelli, I.; Gageot, M. P.; Vuilleumier, R.; Stia, C.; Du Penhoat, M. A. H.; Politis, M. F. Time-Dependent Density Functional Theory Molecular Dynamics Simulations of Liquid Water

- Radiolysis. *ChemPhysChem* **2008**, *9* (14), 2099–2103.  
<https://doi.org/10.1002/cphc.200800177>.
- (40) Baldacchino, G.; Bouffard, S.; Balanzat, E.; Gardès-Albert, M.; Abedinzadeh, Z.; Jore, D.; Deycard, S.; Hickel, B. Direct Time-Resolved Measurement of Radical Species Formed in Water by Heavy Ions Irradiation. *Nuclear Instruments and Methods in Physics Research Section B: Beam Interactions with Materials and Atoms* **1998**, *146* (1), 528–532.  
[https://doi.org/10.1016/S0168-583X\(98\)00463-7](https://doi.org/10.1016/S0168-583X(98)00463-7).
- (41) Oubaziz, D.; Champion, C.; Aouchiche, H. Electron-Induced Double Ionization of Isolated Water Molecules. *Phys. Rev. A* **2013**, *88* (4), 042709.  
<https://doi.org/10.1103/PhysRevA.88.042709>.
- (42) Oubaziz, D.; Quinto, M. A.; Champion, C. H<sub>2</sub>O Double Ionization Induced by Electron Impact. *Phys. Rev. A* **2015**, *91* (2), 022703. <https://doi.org/10.1103/PhysRevA.91.022703>.
- (43) Tessaro, V. B.; Poignant, F.; Gervais, B.; Beuve, M.; Galassi, M. E. Theoretical Study of W-Values for Particle Impact on Water. *Nuclear Instruments and Methods in Physics Research Section B: Beam Interactions with Materials and Atoms* **2019**, *460*, 259–265.  
<https://doi.org/10.1016/j.nimb.2018.11.031>.
- (44) Baldacchino, G.; Deycard, S. Direct Observation of HO<sub>2</sub>/O<sub>2</sub><sup>-</sup> Free Radicals Generated in Water by a High-Linear Energy Transfer Pulsed Heavy-Ion Beam. *6*.
- (45) Gageot, M. P.; Vuilleumier, R.; Stia, C.; Galassi, M. E.; Rivarola, R.; Gervais, B.; Politis, M. F. A Multi-Scale Ab Initio Theoretical Study of the Production of Free Radicals in Swift Ion Tracks in Liquid Water. *Journal of Physics B: Atomic, Molecular and Optical Physics* **2007**, *40* (1), 1.  
<https://doi.org/10.1088/0953-4075/40/1/001>.
- (46) Sankari, R.; Ehara, M.; Nakatsuji, H.; Senba, Y.; Hosokawa, K.; Yoshida, H.; De Fanis, A.; Tamenori, Y.; Aksela, S.; Ueda, K. Vibrationally Resolved O 1s Photoelectron Spectrum of Water. *Chemical Physics Letters* **2003**, *380* (5–6), 647–653.  
<https://doi.org/10.1016/j.cplett.2003.08.108>.
- (47) Mucke, M.; Braune, M.; Barth, S.; Förstel, M.; Lischke, T.; Ulrich, V.; Arion, T.; Becker, U.; Bradshaw, A.; Hergenbahn, U. A Hitherto Unrecognized Source of Low-Energy Electrons in Water. *Nature Phys* **2010**, *6* (2), 143–146. <https://doi.org/10.1038/nphys1500>.
- (48) Zobeley, J.; Santra, R.; Cederbaum, L. S. Electronic Decay in Weakly Bound Heteroclusters: Energy Transfer versus Electron Transfer. *J. Chem. Phys.* **2001**, *115* (11), 5076–5088.  
<https://doi.org/10.1063/1.1395555>.
- (49) Gopakumar, G.; Muchová, E.; Unger, I.; Malerz, S.; Trinter, F.; Öhrwall, G.; Lipparini, F.; Mennucci, B.; Céolin, D.; Coleman, C.; Wilkinson, I.; Winter, B.; Slavíček, P.; Hergenbahn, U.; Björneholm, O. Probing Aqueous Ions with Non-Local Auger Relaxation. *Phys. Chem. Chem. Phys.* **2022**, *24* (15), 8661–8671. <https://doi.org/10.1039/D2CP00227B>.
- (50) Baldacchino, G.; Le Parc, D.; Hickel, B.; Gardès-Albert, M.; Abedinzadeh, Z.; Jore, D.; Deycard, S.; Bouffard, S.; Mouton, V.; Balanzat, E. Direct Observation of HO<sub>2</sub>/O<sub>2</sub><sup>-</sup> Free Radicals Generated in Water by a High-Linear Energy Transfer Pulsed Heavy-Ion Beam. *Radiat. Res.* **1998**, *149* (2), 128–133.
- (51) Gervais, B.; Beuve, M.; Olivera, G. H.; Galassi, M. E.; Rivarola, R. D. Production of HO<sub>2</sub> and O<sub>2</sub> by Multiple Ionization in Water Radiolysis by Swift Carbon Ions. *Chemical Physics Letters* **2005**, *410* (4–6), 330–334. <https://doi.org/10.1016/j.cplett.2005.05.057>.

- (52) Mullenax, C. A.; Goodhead, D. T. *Track Structure and the Quality Factor for Space Radiation Cancer Risk*; JSC-E-DAA-TN57173; 2018. <https://ntrs.nasa.gov/citations/20180006105> (accessed 2023-01-04).
- (53) Pimblott, S. M.; LaVerne, J. A.; Mozumder, A.; Green, N. J. B. Structure of Electron Tracks in Water. 1. Distribution of Energy Deposition Events. *J. Phys. Chem.* **1990**, *94* (1), 488–495. <https://doi.org/10.1021/j100364a084>.
- (54) Ponomarev, A. V.; Makarov, I. E.; Pikaev, A. K. Dynamics of Electron Tracks in Liquid Water. *High Energy Chemistry* **1992**, *25* (4), 260–265.





## CONTENTS CHAPTER 4

---

<b>Chapter 4: Modeling of HO<sub>2</sub> using Ab-initio approach</b> .....	<b>151</b>
<b>4.1. System of interest</b> .....	<b>152</b>
<b>4.2. Double ionization and early state dynamics of H<sub>2</sub>O<sup>2+</sup>: protocol A (TD DFT + CPMD approach)</b> .....	<b>154</b>
4.2.1. 30 fs Ehrenfest MD followed by CPMD .....	155
4.2.1.1. Analysis of double ionization of W32 .....	155
4.2.1.2. Analysis of double ionization at W28 .....	160
4.2.1.3. Analysis of double ionization at W42 .....	162
4.2.2. Protocol B: full CPMD and choice of a suitable pre-dissociated water molecule geometry .....	163
4.2.2.1. Using the TDDFT dynamics of W42 <sup>2+</sup> to generate a suitable pre-dissociated water molecule configuration.....	163
<b>4.3. Dynamics of pre-dissociated H<sub>2</sub>O<sup>2+</sup>: protocol B (CPMD approach)</b> .....	<b>167</b>
<b>4.4. Conclusion</b> .....	<b>174</b>
<b>References</b> .....	<b>175</b>

## Chapter 4: Dissociation of doubly ionized water

In this chapter, we present the theoretical counterpart for the experiments reported in chapter 3. In chapter 3, our hypothesis that the HO<sub>2</sub><sup>°</sup> produced via the interaction of an oxygen atom (a dissociation product of doubly ionized water molecules, H<sub>2</sub>O<sup>2+</sup>) with one of the OH radicals formed within nanometric distances in the photoelectron and Auger electron tracks, seems to be corroborated by our experimental findings. The aim of the theoretical study is to model this process (equation 4.1). The following color code is used: purple for the atoms constituting the dissociating doubly ionized water molecule, yellow for the OH radical and black for all the others atoms.



We model the dissociation of a doubly ionized water molecule in proximity to an HO<sup>°</sup> in liquid water, from the femtosecond to the picosecond time scale (physicochemical stage). This is modeled using a protocol combining (Ehrenfest TDDFT MD followed by a switch to CPMD (protocol A) and pure CPMD simulation (protocol B), described in section 2.5.2.3 of chapter 2. Firstly, we present the systems of study, followed by their preparation and equilibration. We then discuss the results obtained using the two protocols, wherein we demonstrate the mechanism of formation of the end products in the dense ionization tracks. We also emphasize on the effect of the hydroxyl radical in determining the fate of the end product.

### 4.1. System of interest

The importance of investigating the effects of radiation on pure water has been pointed out in the previous sections. In this section, we focus on the choice of the simulation systems to understand the formation mechanism of superoxide radicals in soft X-rays tracks, using computational approaches. To mimic the experiment described in chapter 3, the group first tried to model the time evolution of a system containing two ionized water molecules, H<sub>2</sub>O<sup>2+</sup> and H<sub>2</sub>O<sup>+</sup>, embedded in liquid water. Preliminary tests were thus performed using TDDFT MD to model the time evolution of such a system, but the total energy of the system was not conserved.

The dissociation of singly ionized water molecules has been well studied and shown to produce OH radicals in ionization tracks.<sup>1,2,3</sup> It was thus decided, to model the time evolution

of a doubly ionized water molecule and a neighboring OH radical, both surrounded by water molecules. In the simulation, the OH radical is therefore produced before the double ionization.

The two systems studied in this chapter are listed here (see also figure 4.1):

- a) OH radical + 63 H<sub>2</sub>O (Target system)
- b) 64 H<sub>2</sub>O (Control system)

These molecules are enclosed in a cubic box of size 12.43 Å, using periodic boundary conditions. Different water molecules are selected to create doubly ionized water molecule and study its dissociation.

In the target system, given the cell's dimensions, the doubly ionized water molecule and the OH radical will always be separated by less than approximately one nanometer. The dissociation mechanism is studied in detail by analyzing the trajectories of the TDDFT and CP or BO dynamics. As a control, to understand if OH radicals play a significant role in the formation of HO<sub>2</sub><sup>•</sup>, a similar system but without an OH radical was studied (control system).

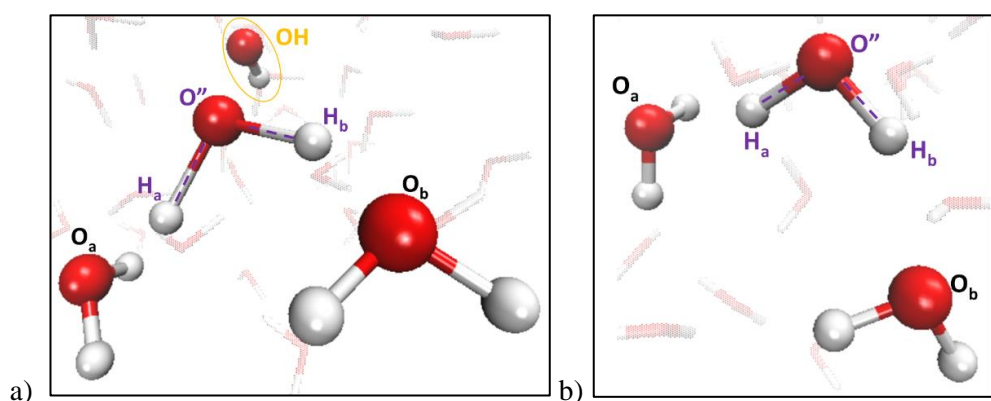


**Figure 4.1:** Systems of interest presented using a visualizing software, VMD.<sup>4</sup> a) Target system with an OH radical in liquid water; b) Control system, with only water. For clarity, the surrounding water molecules are kept translucent. The dissociating molecule is presenting with purple annotations, the hydroxyl radical is presented with yellow annotations and for all other molecules black annotations are used. O<sub>a</sub> and O<sub>b</sub> are the oxygen atoms of the water molecules hydrogen bonded to H<sub>a</sub> and H<sub>b</sub>, respectively.

The purple annotations used for the oxygen atom of the dissociating doubly ionized water molecule is O'', while its hydrogen atoms are denoted as H<sub>a</sub> and H<sub>b</sub> based on their respective

distances from the O'' atom. Specifically, Ha is the furthest hydrogen atom, while Hb is the closest hydrogen atom. The oxygen atoms of the water molecules that were hydrogen bonded to Ha and Hb are labeled Oa and Ob, respectively. The atoms of the initially present hydroxyl radical are labeled in yellow, with the subscript 'hydroxyl'. All other atoms in the simulation box are labeled in black.

#### 4.2. Double ionization and early state dynamics of $\text{H}_2\text{O}^{2+}$ : protocol A (TDDFT + CPMD approach)

In this section, we present the study of the target system ( $^{\circ}\text{OH} + 63 \text{H}_2\text{O}$ ) using protocol A. Protocol A involved, in its first step, the use of TDDFT MD (as explained section 2.5.2.3 of chapter 2) that allowed to simulate the dissociation dynamics of a doubly ionized water molecule,  $\text{H}_2\text{O}^{2+}$ , for 30 fs. The second step of the protocol involved the switch to CPMD, to follow the time evolution of the doubly ionized system for a longer timescale (approximately 1 ps).

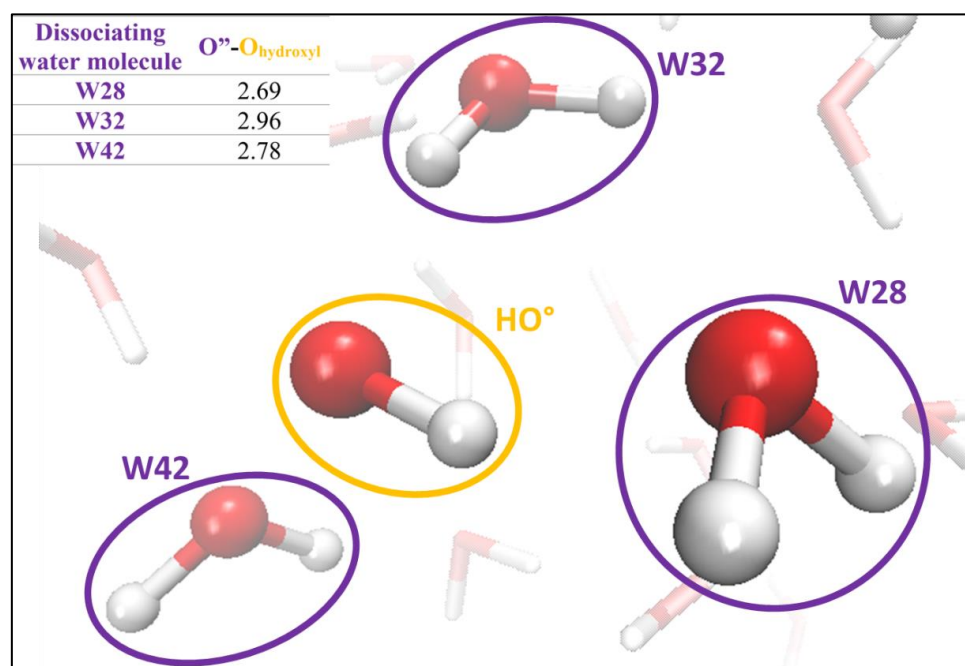


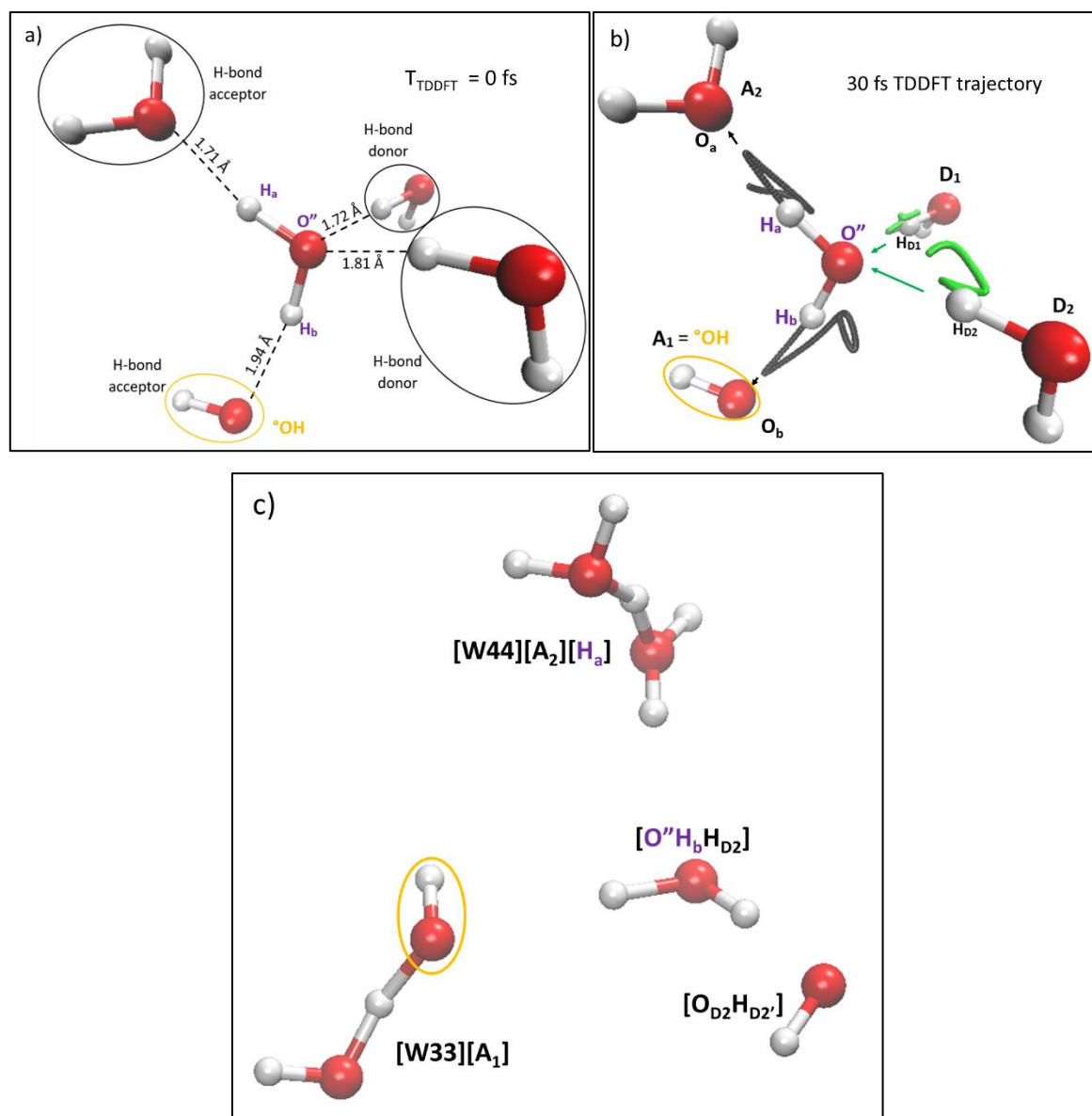
**Figure 4.2:** Water molecules selected (W28, W32 and W42) in the first hydration sphere of  $\text{HO}^{\circ}$ , in Geometry I, to perform the dissociation studies. The figure shows the distance (in Å) between the oxygen atoms of the dissociating doubly ionized water molecule and the hydroxyl radical, in the simulation box of size 12.43 Å.

To begin with, we chose Geometry I, which corresponds to the non-equilibrated OH geometry. The choice of starting with the geometry I was based on the fact that as per the experiments, the  $^{\circ}\text{OH}$  does not get enough time to relax in the ionization tracks. In this section, we will first analyze the three independent dynamics, that were initiated by removing two electrons from the 1b1 (outermost) MO of one of the water molecules present in the first hydration sphere of the  $\text{HO}^{\circ}$ , namely, W28, W32 and W42 (see figure 4.2). We then discuss the effect of the switch time (from TDDFT to CPMD) on the final products.

#### 4.2.1. 30 fs Ehrenfest MD followed by CPMD

##### 4.2.1.1. Analysis of double ionization of W32

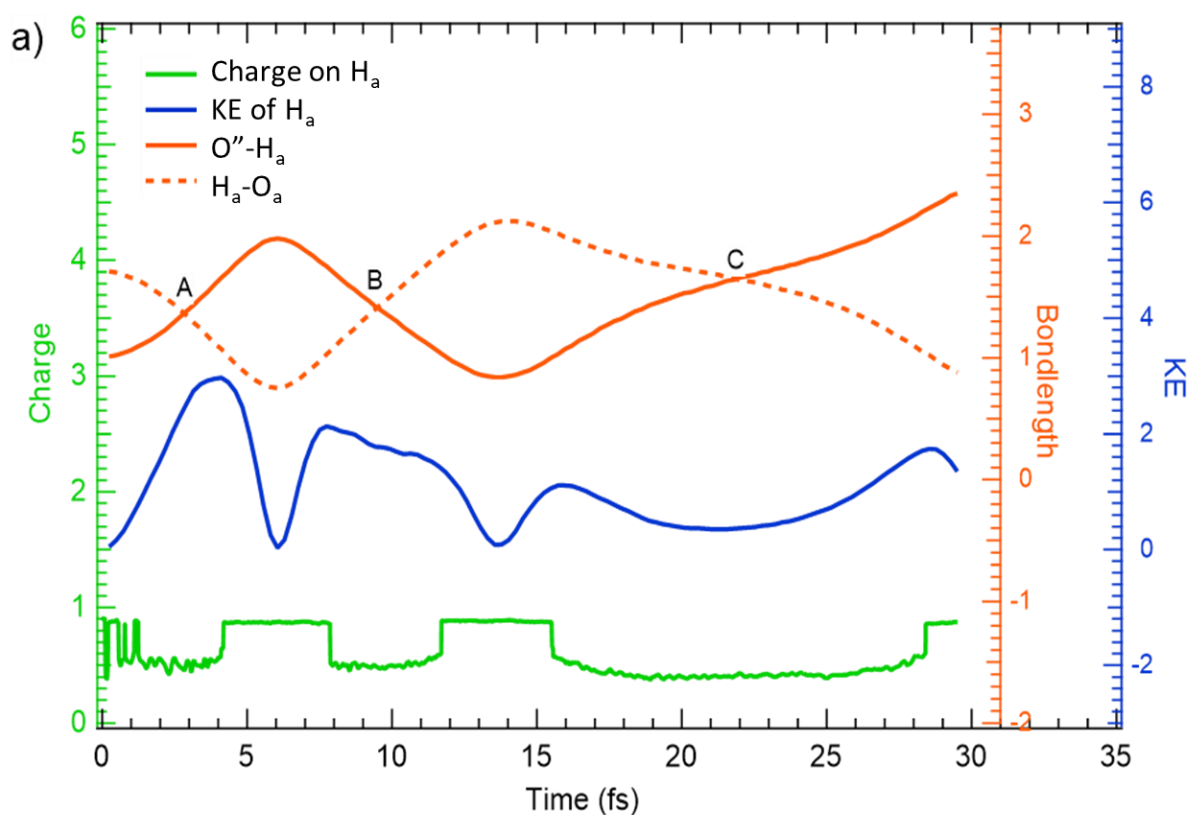
Figure 4.3. a illustrates the species present in the first hydration sphere of W32 at the onset of the TDDFT trajectory ( $T_{\text{TDDFT}} = 0$  fs). As seen in the figure, W32 has two hydrogen bond acceptors, among which the OH radical, and two hydrogen bond donors. Over the course of the 30 fs TDDFT trajectory, the dissociation of W32 was tracked and the path traced by the hydrogen atoms around the  $\text{O}''$  is shown in Figure 4.3. b.



**Figure 4.3:**  $W32^{2+}$  fragmentation dynamics: a)  $W32$  and its first hydration sphere at the onset of TDDFT trajectory, which was initiated by removing two electrons from the 1b1 MO of  $W32$ ; the donating groups are shown with symbol D and accepting groups are shown with symbol A. One of the accepting groups ( $A_1$ ) is the initial hydroxyl radical ( $^{\circ}OH$ ); b) the path (black and green lines) traced by the atoms ( $H_a$ ,  $H_b$ ,  $H_{D1}$ ,  $H_{D2}$ ) with considerable KE, during the 30 fs TDDFT trajectory, plotted with the initial geometry of oxygen (red spheres) and hydrogen (white spheres) atoms; c) Final species after 30 fs TDDFT analysis, involving two additional water molecules adjacent to the accepting groups. For clarity, the surrounding water molecules that do not interact during the analysis are not shown in the figure.

The trace shows that  $H_a$  and  $H_b$  hop between  $O''$  and their respective hydrogen bond acceptors ( $A_1$  and  $A_2$ ) and  $H_{D1}$  and  $H_{D2}$  hop between  $O''$  and their respective hydrogen bond donors ( $D_1$

and  $\mathbf{D}_2$ ). It should be noted that in this case, one of the acceptors ( $\mathbf{A}_1$ ) is the initially present hydroxyl radical. This hopping is also evident in the bond length analysis. For instance, the  $\mathbf{H}_a$  and  $\mathbf{H}_b$  bonds with  $\mathbf{O}''$  elongate, and break at approximately 3 fs, after which they collide on  $\mathbf{O}_a$  and  $\mathbf{O}_b$ , respectively (orange curve, figure 4.4). Points A, B and C, in the figure 4.4, correspond to the times when  $\mathbf{H}_a$  and  $\mathbf{H}_b$  are at the midpoint between the two oxygen atoms. At these points, the charge on  $\mathbf{H}_a$  and  $\mathbf{H}_b$  is 0.5 e. However, they attain a more positive charge (always less than e, around 0.87 e)<sup>9</sup> when they are bonded with either of the oxygen atoms (green curves, figure 4.4). When in proximity to the oxygen atom, computing the Bader charge becomes complicated (see section 2.5.2.4, chapter 2). It has been shown recently<sup>10</sup> that the process of delocalization of electrons in a liquid water, carries an excess energy and it take around 5 ps for the electrons to finally reach the ground state and localize.<sup>11</sup> Nevertheless, it is not straightforward to define if  $\mathbf{H}_a$  or  $\mathbf{H}_b$  behaves like a proton or a hydrogen atom, as the positive charge rapidly delocalizes. Since the code used to perform the simulations uses pseudopotentials to define these atoms, there can be some limitations with the polar H bonds (see section 2.5.2.4, chapter 2).<sup>12,13</sup>





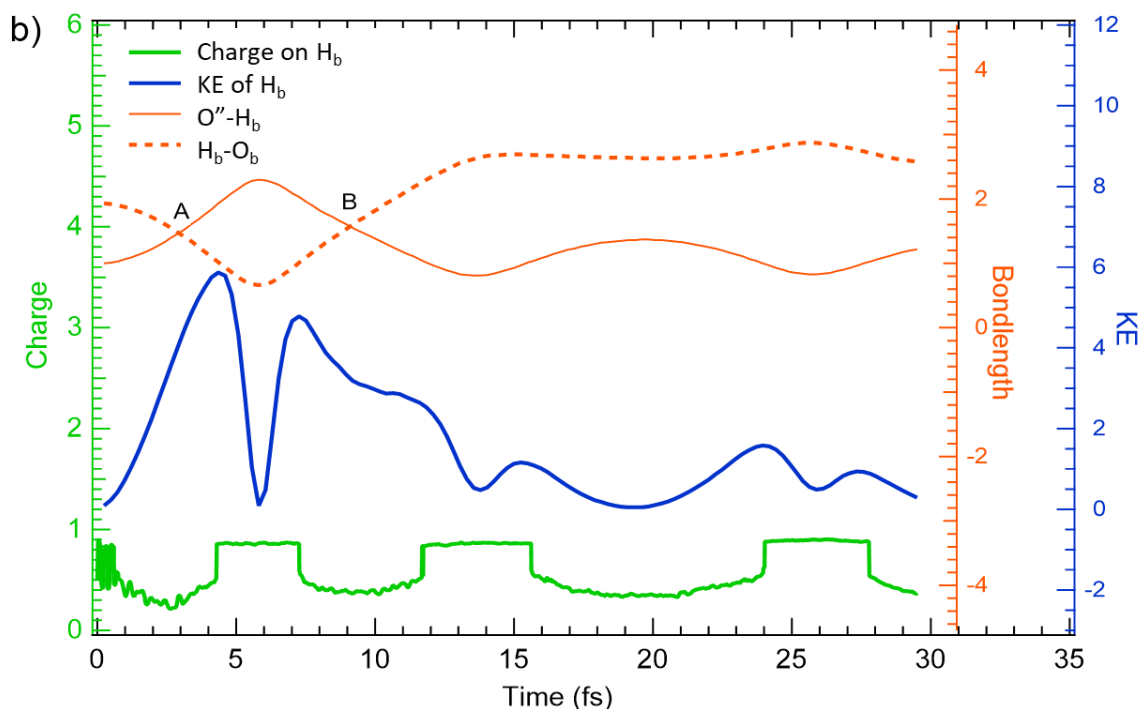


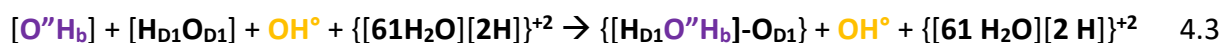
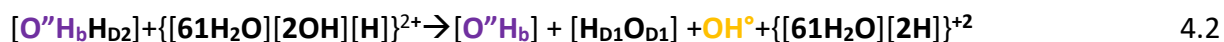
**Figure 4.4:** Analysis of  $W32^{2+}$ : Variation in the charge (in e) and KE (in eV) of a)  $H_a$  and b)  $H_b$  dissociating from their  $O''$  parent oxygen, and their respective distances with the neighboring oxygen atoms (in Angstrom).

The blue curve in figure 4.4 shows that  $H_a$  and  $H_b$  have very high KE (around 5.8 eV at 4.8 fs), resulting in a number of collisions with their neighboring molecules. Both  $H_a$  and  $H_b$  lose part of their KE on collision with the  $O_a$  and  $O_b$ , respectively (see Appendix II.II.). Additionally, when the  $H_{D1}$  and  $H_{D2}$  leave their parent oxygen, they start to gain some KE and lose a part of it as they collide with the  $O''$  (see Appendix II.II.). Thereby the chemistry triggered around the ionized molecule is somewhat of a ‘hot atom’ chemistry. By the end of the TDDFT trajectory, at 30 fs, the final species present in the simulation box are,  $[O''H_bH_{D2}]$ ,  $[O_{D2}H_{D2}]$ ,  $\{[W44][A_2][H_a]\}^+$ ,  $\{[W33][A_1]\}$  and  $[58 H_2O]^+$ . The square brackets represent a molecule and the curly brackets represent a complex.

To shift from TDDFT to CPMD, we selected in this case the configuration at 30 fs of the TDDFT analysis, as an input for the CPMD simulations, which corresponds to the time of 0 fs in CPMD analysis.

We observe the hopping of the  $H/H^+$  in the simulations box, with a +2 charge delocalized in the medium. The  $H_a$  starts to hops from 26 fs of CPMD trajectory and  $H_b$  starts the hopping a little later around 34 fs of CPMD trajectory. The  $H^+$  of  $D_1$  and  $D_2$  hop between their parent

oxygen and  $O''$ . Around 320 fs of the CPMD trajectory, the species present are  $[O''H_b]$ ,  $[H_{D1}O_{D1}]$  and  $OH^\circ$  in a simulation box with a delocalized +2 charge (see equation 4.2). At 420 fs, the two OH groups combine and result in a neutral complex (see equation 4.3 and figure 4.5 a) that looks like an oxywater, which is indeed an isomer of hydrogen peroxide.<sup>14</sup>



At 645 fs, we observe the abstraction of H atom from the neutral complex, by  $OH^\circ$ , resulting in the formation of  $HO_2^\circ$  (see equation 4.4 and figure 4.5) in the simulation box with a delocalized +2 charge.

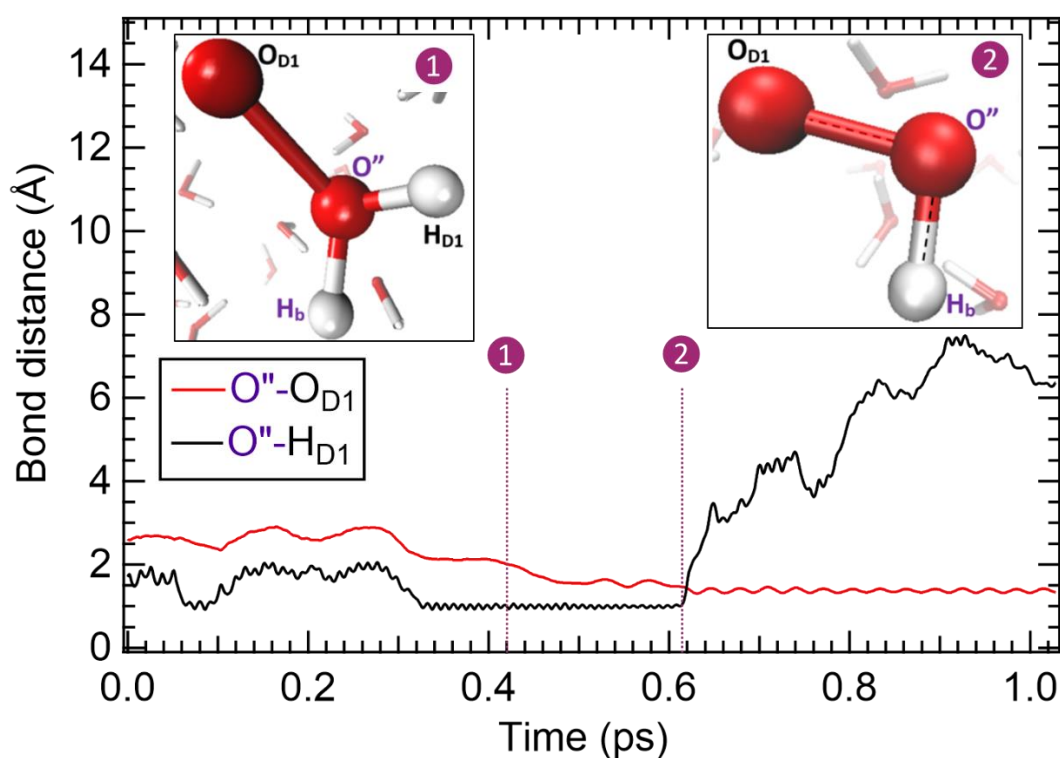


**Figure 4.5:** CPMD analysis of  $W32^{2+}$  after the switch from TDDFT: Formation of  $HO_2^\circ$  along the CPMD trajectory, evident from the variation in the bond lengths (in Angstrom).

From the analysis of the dynamics performed using  $W32$  as the dissociating doubly-ionized water molecule, we did observe the formation of  $HO_2^\circ$ . However, it was formed by the interaction of the OH from the dissociated water and one of the solvent water molecules (the

solvent water molecule acting as a H-bond donor,  $D_1$ ) and not via the pathway proposed earlier (see equation 4.1). A simplified mechanism for this formation can be given by the equation 4.5.



#### 4.2.1.2. Analysis of double ionization at W28

To gain more insights about this complex mechanism, involving fast moving H/H<sup>+</sup> with very high kinetic energy, we performed another simulation, by choosing a different starting water molecule to see the fate of the trajectory.

At the beginning of the TDDFT MD ( $t=0$ ), the first hydration shell of W28 comprised two H-bond acceptors and only one water molecule that acted as H-bond donor (unlike the case of W32). Note that the hydroxyl radical (OH) is in the first hydration sphere, even though it is not fulfilling the criteria of H bond defined (see section 2.5.2.4, chapter 2). Throughout the TDDFT trajectory,  $H_a$ ,  $H_b$  and  $H_{D1}$  hop around among the oxygen atoms of W28,  $A_1$ ,  $A_2$  and  $D_1$ . Similar to the case of W32, it is observed that atoms  $H_a$ ,  $H_b$  and  $H_{D1}$  are shortly neutral when they are not bound to the oxygen atoms, whereas, they carry a +1 charge when they enter the electronic cloud of the oxygen atom. This can be clearly seen from the figure 4.6, depicting the electron density and the trace of these hydrogen atoms, which were colored in green when they behave as protons (charge  $> 0.85e$ ) and in pink when they behave as hydrogen atoms (charge  $< 0.45e$ ). In either of the traces (pink or green trace) for charge, it was observed that the charge was never completely zero or 1.<sup>15</sup> As mentioned before, calculating the accurate Bader charge around the oxygen atom can be complicated. In addition, as reported for the isolated molecules simulation, the unphysical fractional charge are observed when the DFT methods are used.<sup>12</sup> Herein the +1 charge on hydrogen is not observed as such but is partial ( $> 0.83e$ ).<sup>12</sup> It should be noted that the  $\text{HO}^{\circ}$  did not participate in the entire 30 fs TDDFT trajectory, unlike in the case of W32. By the end of the TDDFT trajectory, the species present in the simulation box were  $\text{HO}^{\circ}$  and dissociated W28, with +2 charge delocalized in the simulation box.

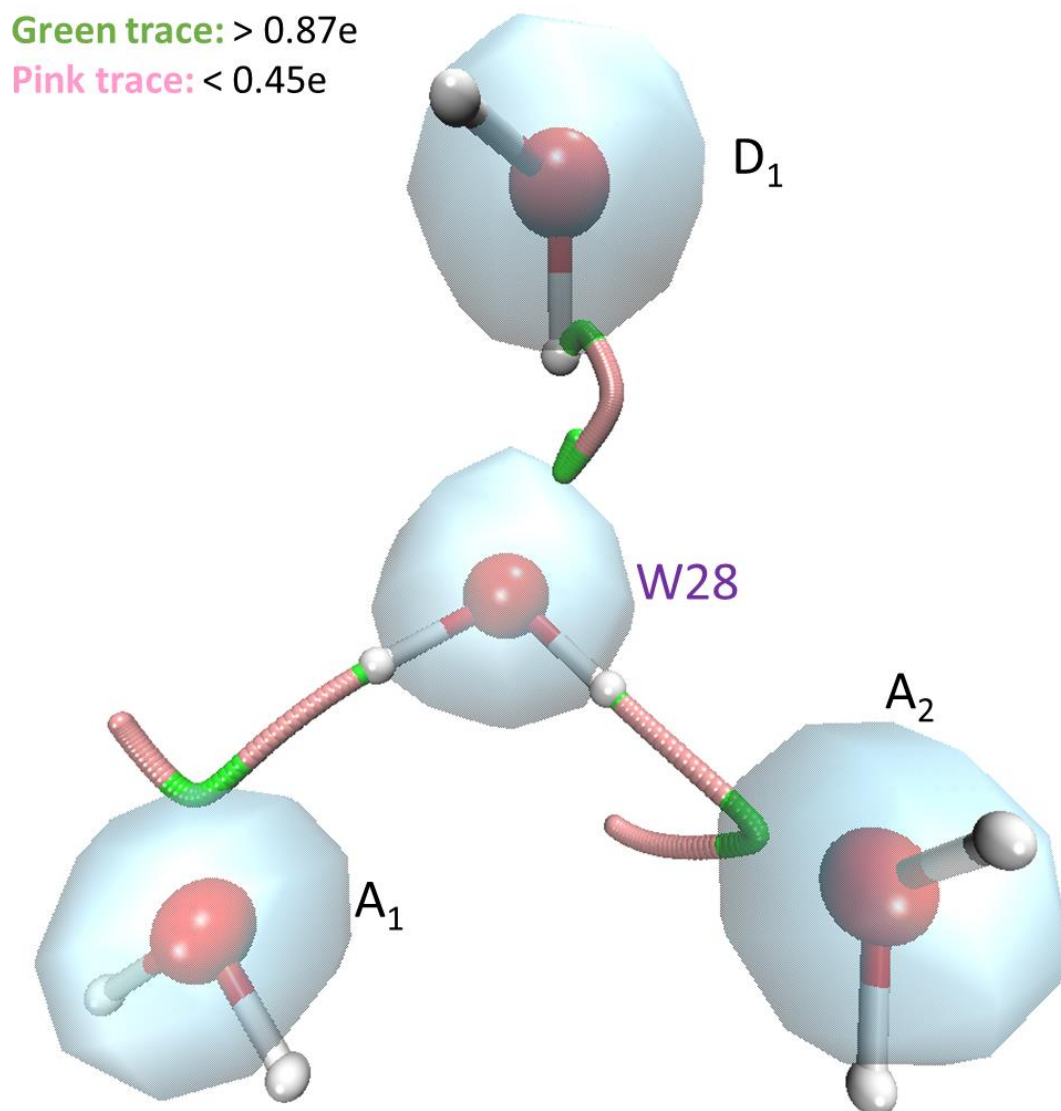


**Figure 4.6:** W28<sup>2+</sup> dynamics study of target system: The trajectory of H<sub>a</sub>, H<sub>b</sub> and H<sub>D1</sub>, hopping between different oxygen atoms. The hydroxyl radical (<sup>•</sup>OH) is present behind W28. For clarity, <sup>•</sup>OH and other solvent water molecules are not shown in the figure. The isovalue used for the density contour around the oxygen atoms is 0.5. The trace shows two regions, one where the atoms behave like protons (green trace), having a charge more than 0.85e in the vicinity of the oxygen atoms and the other where they behave like a hydrogen atom (pink trace), having a charge less than 0.45e.

The CPMD was performed on the geometry at the end of the 30 fs TDDFT. The hopping of H/H<sup>+</sup> was observed in the beginning of the CPMD trajectory, followed by the bonding of <sup>•</sup>O with H<sub>b</sub>, resulting in a hydroxyl radical at 70 fs. At 125 fs, the <sup>•</sup>O created a bond with the oxygen (O<sub>D1</sub>) of the donor water molecule, which simultaneously lost its H atom in the

surrounding, resulting in the formation of  $\text{H}_2\text{O}_2$ . The end products of the 1 ps CPMD trajectory are  $\text{H}_2\text{O}_2$ ,  $\text{HO}^\circ$  and two Zundel ion with a charge of around  $0.75e$  in liquid water.

During the one picosecond trajectory, we did not see the formation of  $\text{HO}_2^\circ$ .

#### 4.2.1.3. Analysis of double ionization at W42

Similar to the case of W28, the starting geometry of W42, in TDDFT, comprised two H-bond acceptors ( $\mathbf{A}_1$  and  $\mathbf{A}_2$ ) and one H-bond donor (W50 was the second H-bond donor prior to abstracting its H to form the initial hydroxyl radical). The hopping of H/ $\text{H}^+$  takes place in the medium, with the  $\mathbf{H}_a$ ,  $\mathbf{H}_b$  and  $\mathbf{H}_{D1}$  having very high kinetic energy, which fluctuates due the collisions that the atoms undergo during the TDDFT trajectory (see figure 4.7). The hydroxyl radical remained unreacted during the 30 fs TDDFT analysis. The species present at the end of the trajectory are three hydroxyl radicals with an excess of vibration energy in a simulation box with delocalized charge of + 2.

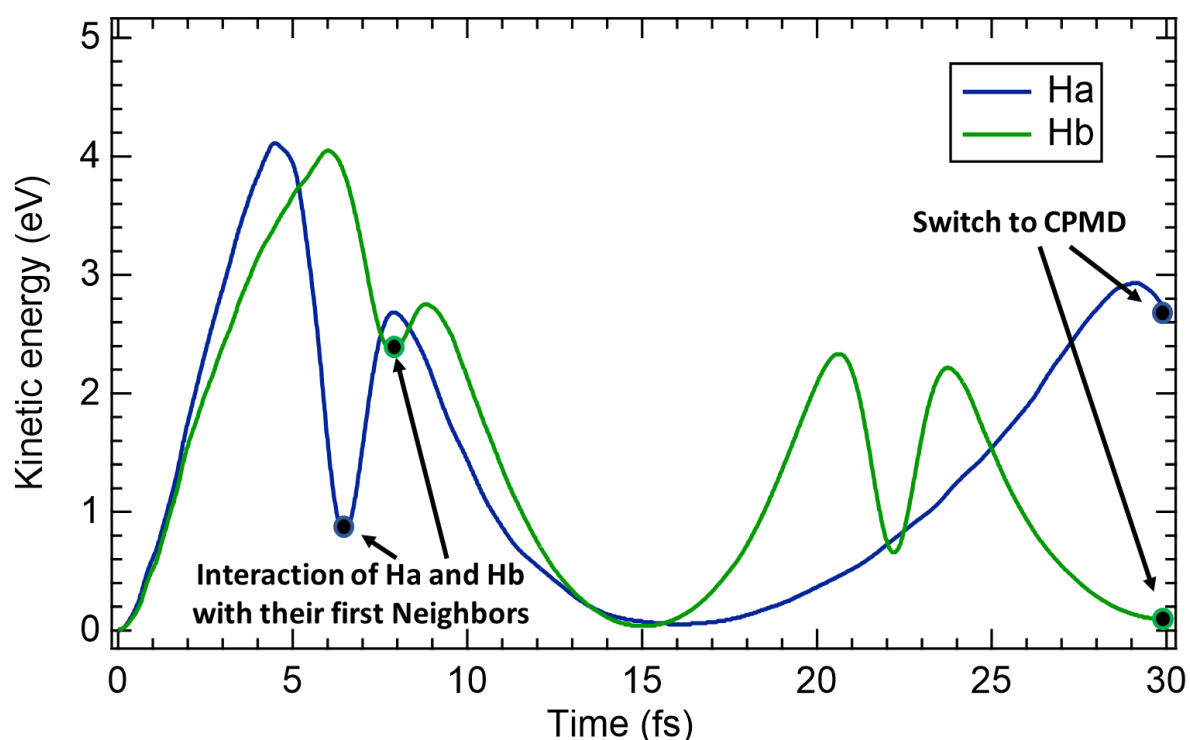


**Figure 4.7:** Variation in the KE of  $\text{H}_a$  and  $\text{H}_b$  along the 30 fs TDDFT trajectory, for W42.

The geometry obtained after 30 fs TDDFT was used to switch to CPMD. It was observed that the H/ $\text{H}^+$  transfers took place very rapidly, resulting in the following final species:  $\text{H}_2\text{O}_2$ , a zundel ion, a hydronium ion and  $^\circ\text{OH}$ , in liquid water. It should be noted at this point that  $\text{H}_2\text{O}_2$

formation has also been reported in the case of pure water dissociation study<sup>13</sup> and for the study of solvated deoxyribose ( $\text{H}_2\text{O}_2$  formed in 8 out of 24 cases in its first hydration sphere).<sup>14</sup>

In conclusion, in the case of the protocol A, the  $\text{HO}_2^\circ$  was formed only in one out of the three cases, when the W32 was doubly ionized and dissociated, for the target system. In this case, the hydroxyl radical participated in the reaction mechanism (as a H acceptor). However, in the case of W28 or W42, the hydroxyl radical did not participate in the reaction mechanism, be it in TDDFT or CPMD trajectory, behaving like pure water system (control system, shown in Appendix II.III.). This suggests that the orientation of the molecules with respect to the hydroxyl radical and the neighboring water molecules is an important factor in the deciding the fate of the final product at the picosecond timescale.

#### 4.2.2. Protocol B: full CPMD and choice of a suitable pre-dissociated water molecule geometry

The analysis presented in the previous section highlighted the need for further analysis to gain a better understanding of the mechanism. However, conducting these simulations (30 fs TDDFT + 1 ps CPMD) required a significant amount of time, so that performing additional analysis using this approach would be impractical due to computational and time constraints. To address this, we chose to utilize a computationally efficient (time inexpensive) protocol (Protocol B: CPMD, explained in section 2.5.2.3 of chapter 2). By opting for this protocol, we aimed to reduce the time investment, allowing for a larger number of dynamics to be explored.

However, performing the CPMD dynamics for a system where the double charge is initially localized on one water molecule is not feasible. Therefore, in order to utilize Protocol B, we employ the TDDFT approach from Protocol A to generate a pre-dissociated  $\text{H}_2\text{O}^{2+}$ . Subsequently, we can conduct multiple dynamics using protocol B, by replacing the parameters (OH bond length, HOH bond angle and velocities of the three atoms) of selected water molecules with those of the pre-dissociated water molecule.

#### 4.2.2.1. Using the TDDFT dynamics of $W42^{2+}$ to generate a suitable pre-dissociated water molecule configuration

Considering that the parameters obtained for the pre-dissociated water molecule will be used in all subsequent analyses performed using Protocol B, it is crucial to ensure that the pre-dissociated water molecule is adequately dissociated and minimally affected by neighboring water molecules. Any influence from the neighboring water molecules can hinder the replacement of the parameters for the other water molecules to be tested with those of the pre-dissociated water molecule.

Therefore, pre-dissociated geometries were specifically chosen at three times during the 30 fs of one of the TDDFT dynamics carried out in the previous section, i.e.  $W42^{2+}$ . These geometries were chosen just before the collision of  $H_a$  and  $H_b$  with their respective first neighboring water molecules, i.e. prior to 4.5 fs (see figure 4.7), to minimize the influence from neighboring water molecules. The selected switch times were 3 fs, 3.4 fs, and 3.8 fs. CPMD simulations were performed for around one picosecond using these switch geometries as starting points, followed by a thorough analysis to determine the appropriate configuration of the pre-dissociated water molecule (see table 4.1).

**Table 4.1:** Performing CPMD analysis with switch geometries at, a)  $T_{\text{TDDFT}} = 3$  fs; b)  $T_{\text{TDDFT}} = 3.4$  fs and c)  $T_{\text{TDDFT}} = 3.8$  fs along the 30 fs TDDFT trajectory. The initial parameters of the switch geometry are presented in the table, where the bond length of the dissociating molecule are shown in purple, the angle is shown in orange and the KE of  $H_a$  and  $H_b$  are shown in blue. The time of formation of superoxide is shown in red color. Some of the species present in the simulation box, at the end of the CPMD trajectory analysis is also shown. At the end of each case, the simulation box had localized +2 charge ( $H_3O^+$  or  $H_5O_2^+$ , having partial positive charge of around 0.8e).

Configuration at $T_{\text{CPMD}} = 0$ ps	Final configuration at $T_{\text{CPMD}}$ around 1 ps
<p>a) <math>T_{\text{TDDFT}} = 3.0</math> fs</p>	
<p>b) <math>T_{\text{TDDFT}} = 3.4</math> fs</p>	
<p>c) <math>T_{\text{TDDFT}} = 3.8</math> fs</p>	



As can be seen from the presented results, in table 4.1, the outcome of the simulation was influenced by the initial geometries. To gain insight into the reasons behind this dependence, the paths followed by the dissociating protons were traced during the CPMD trajectory for each starting geometry. Throughout the one picosecond analysis, these trajectories were found to be significantly different. The distinction between the trajectories could even be observed within the first few femtoseconds, as illustrated in Figure 4.8. This highlights the fact that slight changes in the orientation of the species relative to each other lead to variations in the final product. Additionally, when the switch is performed (from TDDFT to CPMD), a slight redistribution in the electronic cloud can occur when the optimization of the electronic structure is performed. However, the positions and the velocities of the atoms of solvent water molecules is unchanged. This suggests that at the different switch times, the atoms in the simulation box, especially the dissociating H/H<sup>+</sup> (**H<sub>a</sub>** and **H<sub>b</sub>**) do not feel the same potential that can result in a large impact on the trajectory of H/H<sup>+</sup>.

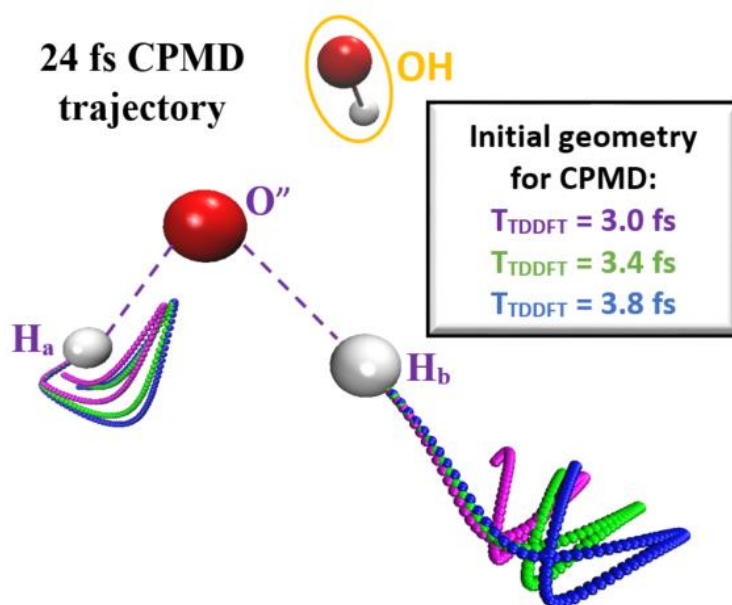


**Figure 4.8:** W42<sup>2+</sup> dynamics: Path traced by H<sub>a</sub> and H<sub>b</sub> during the CPMD trajectory. The atoms O'', H<sub>a</sub> and H<sub>b</sub> are represented as spheres and their positions correspond to the start of the CPMD trajectory. For simplicity, the trajectory is shown only for the first 24 fs and the neighboring water molecules are kept hidden.

As shown in the table 4.1, when using the geometry at the switch time of 3 fs, one of the dissociating OH bonds reformed and remained intact throughout the one picosecond CPMD

analysis. The resulting species at the end of the analysis, using the 3 fs switch geometry were three hydroxyl radicals and two hydronium ion with a positive charge delocalized in the simulation box, which did not seem relevant for our problem. Additionally, to avoid any influence of the parent oxygen ( $O''$ ) on the dissociating  $H/H^+$ , we preferred to be farther from the parent oxygen. Therefore, the 3 fs switch geometry was considered to be an insufficiently dissociated one.

When the geometries at switch times 3.4 fs and 3.8 fs were utilized, the final product was  $HO_2^\circ$ , along with two hydronium ions (not shown in the table for clarity). It is worth noting that in both cases, the formation of  $HO_2^\circ$  occurred through a one-step reaction between the oxygen atom of the dissociated water molecule and the hydroxyl radical, without any intermediate products. This corresponds to the expected pathway as shown in equation 4.1.

In order to avoid any influence of the neighboring water molecule's electronic cloud on the dissociating  $H_a$  and  $H_b$ , the geometry at 3.8 fs was not chosen for further analysis. The switch geometry at  $T_{TDDFT} = 3.4$  fs was therefore found to be suitable (the exact parameter of the switch geometry are,  $O''H_a = 1.52$  Å and  $O''H_b = 1.50$  Å and the bond angle,  $H_aO''H_b = 103.9^\circ$ , see figure 2.20 of chapter 2). Herein, the OH bond lengths are proven to have an irreversible dissociation in the liquid phase, ensuring that the water molecule is properly dissociated.<sup>15</sup>

### 4.3. Dynamics of pre-dissociated $H_2O^{2+}$ : protocol B (CPMD approach)

To begin with, we elaborate the dynamics of W32, to compare the results obtained with both the protocols.

In the non-equilibrated OH geometry (geometry I, figure 2.18 of Chapter 2), the parameters of the water molecule, W32, were replaced by that of the pre-dissociated W42 (from the switch geometry at  $T_{TDDFT} = 3.4$  fs). The double charge localized on the pre-dissociated water molecule in the ground state during the wavefunction optimization. This served as the starting point for the CPMD simulation (pre-dissociated doubly ionized water molecule in proximity to hydroxyl radical in liquid water), as shown in figure 4.9. The simulation was performed for one picosecond.

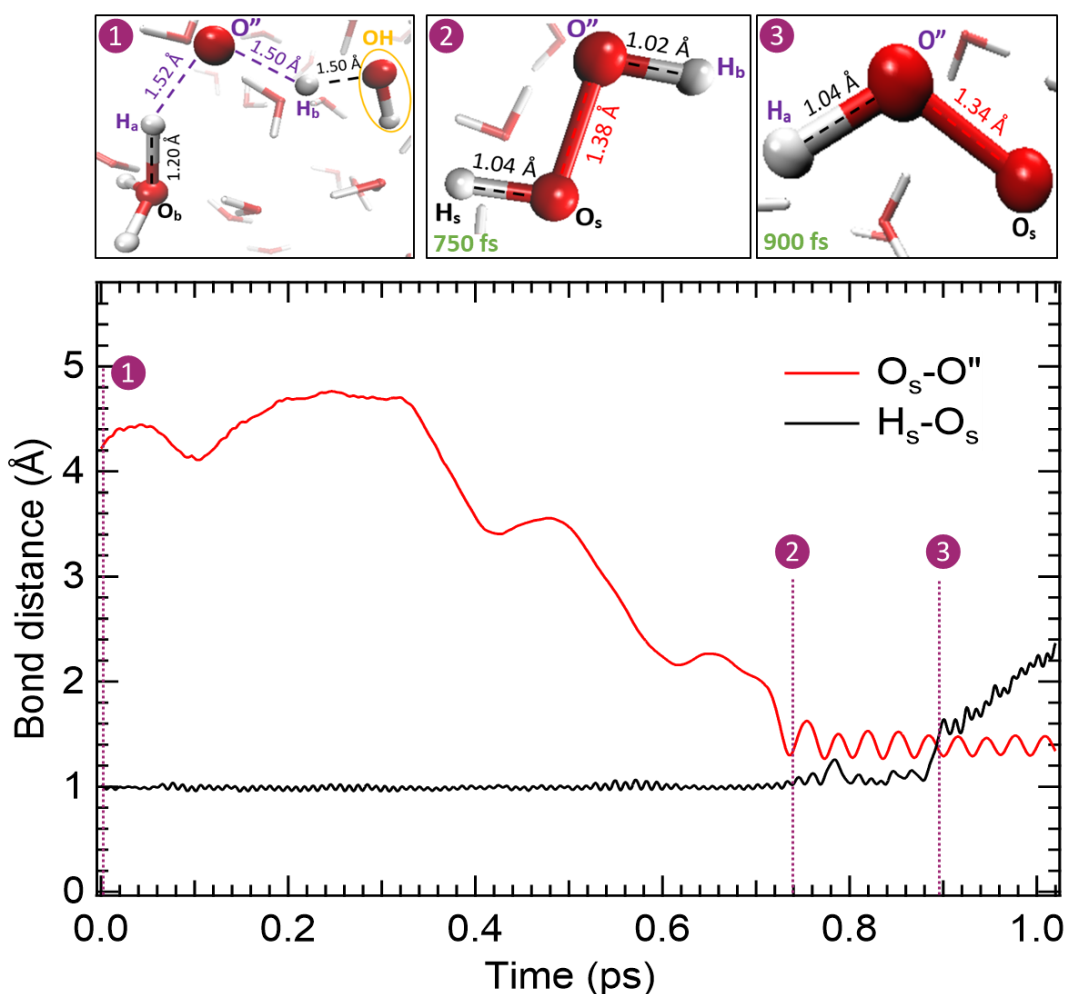
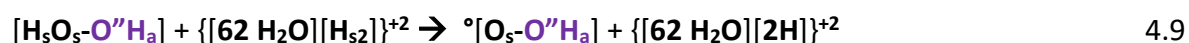
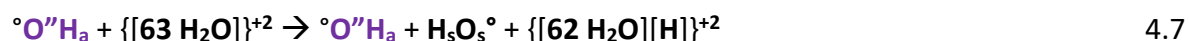
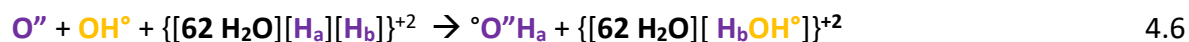


**Figure 4.9:** Protocol B applied to W32 in the non-equilibrated OH geometry: Initial geometry (①), intermediate product (②),  $\text{H}_2\text{O}_2$ , and the final product (③),  $\text{HO}_2$ . The time of formation of the species is indicated on the bottom left corner, in green, and is labeled in the graph of bond lengths ( $\text{\AA}$ ) variation as a function of time (ps) during the 1 ps trajectory. All the atoms apart from the dissociating water molecule and the  $^\circ\text{OH}$  are assigned the subscript 's' to denote that they belong to the solvent water molecules.

The mechanism of  $\text{HO}_2^\circ$  formation is explained in equations 4.6 to 4.9. At the start of the simulation,  $\text{O}''$  instantly accepts one of its hydrogen atoms ( $\text{H}_a$ ), at 8fs, resulting in hydroxyl radical ( $\text{H}_a\text{-O}''^\circ$ ) (see equation 4.6). The hydroxyl radical acts as a H-bond acceptor, forming a bond with  $\text{H}_b$ , resulting in a positively charged water molecule. Another positive charge is delocalized in the medium. One of the positively charged solvent water molecules abstracts a hydrogen atom from a neutral solvent water molecule, giving another hydroxyl radical ( $\text{H}_s\text{-O}_s^\circ$ ), see equation 4.7. The two hydroxyl radicals react to give the intermediate product,  $\text{H}_2\text{O}_2$ ,

by the formation of  $O_s-O''$  bond at 750 fs (red curve, figure 4.9 and equation 4.8). The  $H_2O_2$  lasts for a few femtoseconds, until at 880 fs one of the OH bond breaks (black curve, figure 4.9) as the  $H_s$  is abstracted by one of the positively charged water molecule, resulting in a  $HO_2^\circ$  species (see equation 4.9).



The simplified representation of the species involved in  $HO_2^\circ$  formation is given in equation 4.10.



It should be noted at this point that in both the protocol (A and B) for W32, the 'OH' of  $HO_2^\circ$  comes from the pre-dissociated water molecules (equation 4.5 and 4.10). The 'O' atom of  $HO_2^\circ$  comes from a solvent water molecule, see equation 4.10 (although different solvent water molecules). Additionally, the formation of  $HO_2^\circ$  in both the protocols occur via an intermediate formation ( $H_2O_2$  or its isomer, oxywater).

This difference can arise because of the fact that in protocol B, only the parameters of the W32 were replaced with those of the pre-dissociated water molecule and all other water molecules in the non-equilibrated OH geometry remain unchanged. However, in protocol A, the entire geometry evolves during the 3.4 fs TDDFT, which is not take into account in protocol B. This changes the orientation of the molecules with respect to each other and hence, the collisions of H/H<sup>+</sup> differ, resulting in different end products. This can be seen by the comparison of the trajectories of  $H_a$  and  $H_b$ , in both the protocols (figure 4.10).

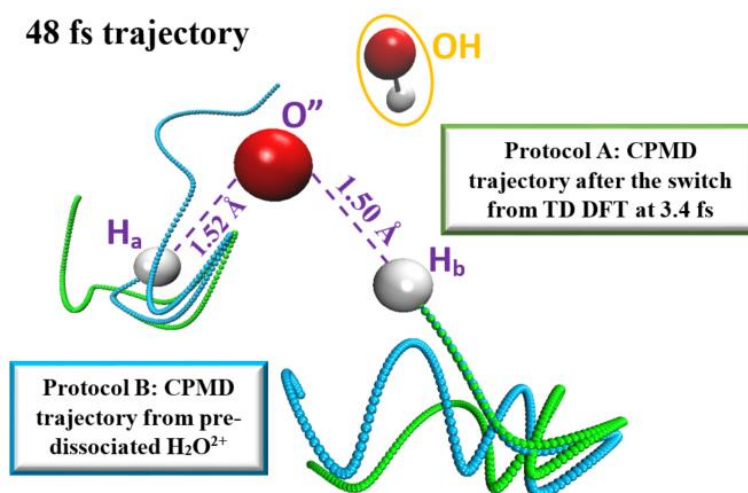


**Figure 4.10:** W42<sup>2+</sup> CPMD trajectory on the non-equilibrated OH geometry (geometry I) during the first 48 fs: Path traced by the H<sub>a</sub> and H<sub>b</sub> of the dissociating doubly ionized water molecule (W42) in the simulation box, using the protocol A and B. The bond lengths, O''H<sub>a</sub> = 1.52 Å and O''H<sub>b</sub> = 1.50 Å, labelled in the figure corresponds to the start of the CPMD trajectory. The white spheres represent H<sub>a</sub> and H<sub>b</sub> and red sphere represent the O'', at the start of the CPMD trajectory. For clarity, surrounding water molecules, present in the simulation box, are hidden.

These observations further imply that instead of discussing individual cases, a statistical analysis is more relevant to determining the interaction mechanism of the dissociation products of H<sub>2</sub>O<sup>2+</sup> with its surrounding hydroxyl radical and water molecules.

Therefore, we conducted a study using the protocol B, and replacing 7 different water molecules (labelled in figure 4.11) (one at a time) *with the parameters of pre-dissociated W42 from geometry at  $T_{TDFT} = 3.4$  fs*. This replacement was done on different starting geometries, non-equilibrated (GEOMETRY I), partially equilibrated (GEOMETRY II) and equilibrated (GEOMETRY III) °OH geometries (see figure 2.18 of Chapter 2), resulting in a total of 21 simulations. As mentioned in the computational method section, in 5 cases (W28, W32, W33, W35 and W42), the selected water molecules were in the first or second hydration sphere of the hydroxyl radical for all starting geometries. In two other cases (W0 and W4), the water molecule was further from the hydroxyl radical (see table 4.2), in order to understand the effect of hydroxyl radical in the mechanism, if any. The initial configurations for each of these dynamics, using protocol B, thus consisted in a pre-dissociated doubly ionized water molecule and an °OH radical in liquid water.

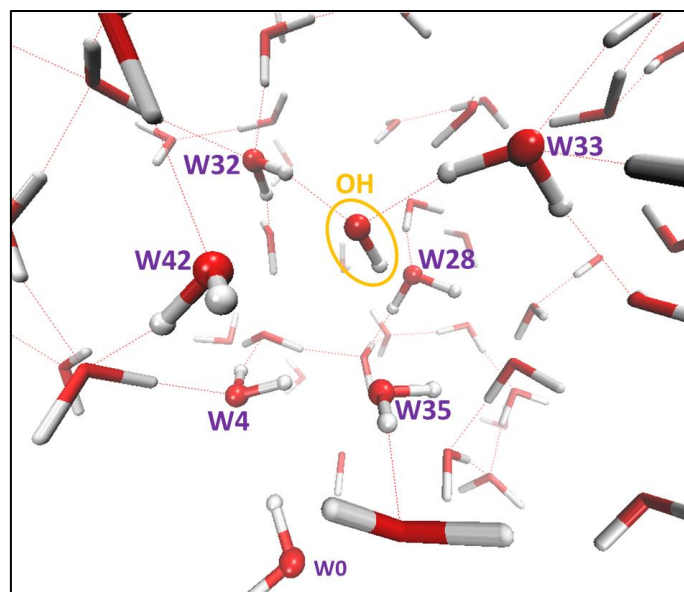


**Figure 4.11:** The seven water molecules, labeled in purple, selected to study the interaction of a pre-dissociated water molecule with its surrounding water molecules and a hydroxyl radical, labeled in yellow. Five of these water molecules are present in the first hydration sphere of the hydroxyl radical and the other two are far from the hydroxyl radical.

When the pre-dissociated water molecule was located at the two positions far from the hydroxyl radical (W0 and W4, as described in the two first rows table 4.2),  $\text{HO}_2^\circ$  formation was observed only in one of them. The other cases of W0 and W4, however, either resulted in the formation of a hydroxyl radical and a hydronium ion, with a charge delocalized (hot hole) in the simulation box, or hydrogen peroxide and two hydronium ions, in addition to the already existing OH. This is shown in table 4.3. This suggested that the distance between the pre-dissociating water molecule and the hydroxyl radical was one of the factors contributing in deciding the fate of the dynamics. If this distance was more than 4 Å, the hydroxyl radical could not participate in the mechanism. Similar end products were observed when the simulations were performed on the control system (explained in section 4.1), which has no hydroxyl radical at the onset of the simulations (see appendix II.III.). This further confirmed that a proximal  $^\circ\text{OH}$  plays an important role as a mediator to form  $\text{HO}_2^\circ$  in the picosecond time scale.

However, there are other cases where  $\text{HO}_2^\circ$  was not formed even if the initial O-O" distance was below 4 Å (see table 4.2), indicating that this distance is not the only factor impacting the superoxide formation mechanism.

**Table 4.2:** Distance between the oxygen atoms of the pre-dissociated water molecule and  $^{\circ}\text{OH}$ , at the start of the CPMD analysis. For each case studied, it is indicated whether the superoxide radical was formed or not and the time of its formation is also indicated in femtoseconds.

Oxygen of dissociated water ( $\text{O}^{\circ}$ )	1 ps CPMD analysis								
	Geometry I			Geometry II			Geometry III		
	Distance $\text{O}-\text{O}^{\circ}$	Superoxide formation		Distance $\text{O}-\text{O}^{\circ}$	Superoxide formation		Distance $\text{O}-\text{O}^{\circ}$	Superoxide formation	
		yes/no	time (fs)		yes/no	time (fs)		yes/no	time (fs)
W0	5.91	no	-	6.24	no	-	6.42	no	-
W4	4.00	yes	305	4.12	no	-	4.54	no	-
W28	2.69	yes	30	2.57	yes	927	3.04	no	-
W32	2.96	yes	900	2.83	yes	755	3.18	no	-
W33	2.81	no	-	2.86	yes	486	2.74	no	-
W35	2.81	yes	300	2.41	yes	700	2.53	yes	1000
W42	2.78	no	-	3.30	yes	100	3.13	no	-

The 15 dynamics (W28, W32, W33, W35 and W42, for Geometry I, II and III), where the pre-dissociated water molecule was in the first or the second hydration sphere of the  $\text{OH}^{\circ}$ , resulted in the formation of  $\text{HO}_2^{\circ}$  in 9 out of 15 cases. Amongst these cases, different mechanisms of  $\text{HO}_2^{\circ}$  formation were observed, like that shown in the case of protocol A in section 4.2. Some of these mechanisms involve a one-step process of  $\text{HO}_2^{\circ}$  formation (see equation 4.1), whereas in the other cases it's a two-step process. This two-step process involves  $\text{H}_2\text{O}_2$  or its isomer (oxywater) as an intermediate product (see equation 4.5 and 4.10). The other mechanisms are a direct one step reaction of a hydroxyl radical with an oxygen atom.

In the remaining 6 dynamics, even though the hydroxyl radical was initially close to the pre-dissociated molecule, its orientation with respect to the surrounding water molecules was different and hence, it could not participate in the reaction mechanism. In three cases out of 6, the oxygen atom formed after dissociation remained unreacted while its two protons hopped in the medium during the one picosecond trajectory. The three remaining cases, on the other hand, resulted in  $\text{H}_2\text{O}_2$  formation and a hydroxyl radical with the double charge delocalized in the simulation box (see table 4.3). These 6 dynamics belong to either non-equilibrated (two cases) or fully equilibrated  $^{\circ}\text{OH}$  geometry (four cases). In the case when the  $\text{OH}^{\circ}$  is partially equilibrated, all the dynamics having the dissociating water molecule in the first or second hydration sphere (W28, W32, W33, W35 and W42) resulted in the formation of  $\text{HO}_2^{\circ}$ . This could be probably because of the limited number of dynamics.

Statistically speaking,  $\text{HO}_2^\circ$  was a dominant product (9 out of 15 cases, 60%) in the dense ionization tracks upon the dissociation of  $\text{H}_2\text{O}^{2+}$ . The end products in all the dynamics are presented in table 4.3.

**Table 4.3:** The final species present at the end of one picosecond CPMD.  $\text{H}_3\text{O}^+$  in the table corresponds to the localized +1 charge (either hydronium ion or  $\text{H}_5\text{O}_2^+$ ) and  $\text{H}^+$  corresponds to the delocalized +1 charge. The color code (purple for pre-dissociated water molecules, yellow for the initial hydroxyl radical and black for solvent molecules) shows the atoms origin in the end products.

Species produced upon dissociation of $\text{H}_2\text{O}^{2+}$ , starting from dissociation parameters adapted from 3.4fs switch geometry of TDDFT	Oxygen of dissociated water ( $\text{O}^\circ$ )	Final species after 1ps CPMD simulation		
		Geometry I	Geometry II	Geometry III
	<b>W0</b>	<b>HO<sup>''</sup>-OH, OH</b> , 2 $\text{H}_3\text{O}^+$	<b>HO, HO<sup>''</sup></b> , 2 $\text{H}_3\text{O}^+$	<b>HO, HO<sup>''</sup></b> , 2 $\text{H}_3\text{O}^+$
	<b>W4</b>	<b>HO<sup>''</sup>-O</b> , 2 $\text{H}_3\text{O}^+$	<b>HO, HO<sup>''</sup></b> , 2 $\text{H}_3\text{O}^+$	<b>HO, HO<sup>''</sup></b> , 2 $\text{H}_3\text{O}^+$
	<b>W28</b>	<b>HO-O<sup>''</sup></b> , 2 $\text{H}_3\text{O}^+$	<b>HO-O</b> , 2 $\text{H}^+$	<b>HO, O<sup>''</sup></b> , 2 $\text{H}_3\text{O}^+$
	<b>W32</b>	<b>HO<sup>''</sup>-O</b> , 2 $\text{H}_3\text{O}^+$	<b>HO-O</b> , 2 $\text{H}_3\text{O}^+$	<b>OH-OH, <sup>''</sup>OH</b> , 2 $\text{H}_3\text{O}^+$
	<b>W33</b>	<b>O<sup>''</sup></b> , $\text{H}_3\text{O}^+$ , $\text{H}^+$ , OH	<b>HO-O<sup>''</sup></b> , $\text{H}_3\text{O}^+$ , $\text{H}^+$	<b>HO-OH, <sup>''</sup>OH</b> , 2 $\text{H}^+$
	<b>W35</b>	<b>HO<sup>''</sup>-O</b> , 2 $\text{H}_3\text{O}^+$	<b>HO<sup>''</sup>-O</b> , 2 $\text{H}^+$	<b>HO<sup>''</sup>-O</b> , $\text{H}_3\text{O}^+$ , $\text{H}^+$
	<b>W42</b>	<b>O<sup>''</sup></b> , $\text{H}_3\text{O}^+$ , $\text{H}^+$	<b>HO-O<sup>''</sup></b> , 2 $\text{H}^+$	<b>HO-<sup>''</sup>OH, OH</b> , 2 $\text{H}_3\text{O}^+$

It can also be noted from the table 4.2 and 4.3 (column of geometry I and II) that when the dynamics is performed using Geometry I (non-equilibrated  $^\circ\text{OH}$  geometry) or Geometry II (partially-equilibrated  $^\circ\text{OH}$  geometry) as the start geometry, the probability of  $\text{HO}_2^\circ$  formation is higher during the 1ps trajectory investigated. However, when the start geometry is Geometry III (fully-equilibrated  $^\circ\text{OH}$  geometry), statistically, there is no  $\text{HO}_2^\circ$  formation. These observations suggest that the probability of  $\text{HO}_2^\circ$  formation is higher when the  $^\circ\text{OH}$  doesn't get time to equilibrate in its surrounding.

The formation time of  $\text{HO}_2^\circ$  ranges from 30 fs to 1 ps (see table 4.2). The observed trend in the investigated dynamics, within the specified time frame of 1 ps, suggests that the dynamics involving the formation of  $\text{HO}_2^\circ$  through an intermediate product ( $\text{H}_2\text{O}_2$  or its isomer, oxywater) takes longer than the dynamics, where  $\text{HO}_2^\circ$  formation occurs without an intermediate product formation.

It can be seen from these fast changing dynamics of the system that the mechanism of  $\text{HO}_2^\circ$  formation is not straightforward and that it is due to the immediate reorganization of protons (as they are very energetic) and of positives charges (holes). These charge delocalize very



quickly, forming the hole equivalent of pre-solvated electron,<sup>16</sup> and can localize at different positions in the simulation box to form hydroxyl radicals. The delocalization of charge has shown to be favorable in the literature<sup>17</sup> for the system with +2 charge due to the strong Coulomb repulsions or due to the defects of DFT in approximations of the exchange terms.<sup>17</sup> As a result, the  $\text{HO}_2^\circ$  can be formed by many different combinations. Indeed, in addition to the expected pathway in chapter 3 (also shown in equation 4.1), where the 'OH' part of  $\text{HO}_2^\circ$  comes from the hydroxyl radical and the 'O' part of  $\text{HO}_2^\circ$  comes from dissociating  $\text{H}_2\text{O}^{2+}$ , the source of 'OH' and 'O' can be also traced to initially neutral solvent water molecules. A summary of the different species involved in the  $\text{HO}_2^\circ$  formation, in the 10 CPMD dynamics, is given the table 4.4.

**Table 4.4:** A summary of the species involved in the formation of superoxide radical, as an end product after 1 ps trajectories, using the protocol B.

		Source of OH in $\text{HO}_2$		
		$\text{OH}^\circ$	$\text{H}_2\text{O}^{2+}$	Solvent
Source of O in $\text{HO}_2$	$\text{OH}^\circ$		3	2
	$\text{H}_2\text{O}^{2+}$	2		1
	Solvent	0	2	

#### 4.4. Conclusion

The simulations revealed that the formation of superoxide species is dominant during the irradiation of water with soft X-rays, as indicated by the statistical results. This occurs through the well-known proton hopping mechanism. The hydroxyl radical plays a crucial role in the formation of  $\text{HO}_2^\circ$ , as it serves as a mediator, acting as a hydrogen bond donor or acceptor in all the mechanisms. In fact, the simulations conducted by the control system (without the hydroxyl radical) did not result in the formation of superoxide. Interestingly, it was observed that when the initial distance between the oxygen atom of the hydroxyl and dissociating  $\text{H}_2\text{O}^{2+}$  is greater than 4 Å,  $\text{HO}_2^\circ$  formation is not observed in the sub-picosecond time range. The formation of this species can occur through various mechanisms, where the hydroxyl radical, solvent, or the dissociating  $\text{H}_2\text{O}^{2+}$  can serve as sources for the OH and oxygen atom in  $\text{HO}_2^\circ$ . Thus, besides the source discussed in our previous experimental work,<sup>18</sup> it is now evident that

the hydroxyl radical and dissociating  $\text{H}_2\text{O}^{2+}$  are not the only sources for OH and oxygen in  $\text{HO}_2^\circ$ . Additionally, the results suggest that the formation of  $\text{HO}_2^\circ$  can occur through a one-step or two-step mechanism. Mechanisms involving solvent water molecules take longer for  $\text{HO}_2^\circ$  formation probably to the reorganization time of the protons in the solvent.

## References

- (1) Cobut, V.; Frongillo, Y.; Patau, J. P.; Goulet, T. MONTE CARLO SIMULATION OF FAST ELECTRON AND PROTON TRACKS IN LIQUID WATER—I. PHYSICAL AND PHYSICOCHEMICAL ASPECTS. *Monte Carlo simulation*.
- (2) Gervais, B.; Beuve, M.; Olivera, G. H.; Galassi, M. E. Numerical Simulation of Multiple Ionization and High LET Effects in Liquid Water Radiolysis. *Radiation Physics and Chemistry* **2006**, *75* (4), 493–513. <https://doi.org/10.1016/j.radphyschem.2005.09.015>.
- (3) Mozumder, A.; Magee, J. L. The Early Events of Radiation Chemistry. *International Journal for Radiation Physics and Chemistry* **1975**, *7* (2), 83–93. [https://doi.org/10.1016/0020-7055\(75\)90052-2](https://doi.org/10.1016/0020-7055(75)90052-2).
- (4) Humphrey, W.; Dalke, A.; Schulten, K. VMD: Visual Molecular Dynamics. *Journal of Molecular Graphics* **1996**, *14* (1), 33–38. [https://doi.org/10.1016/0263-7855\(96\)00018-5](https://doi.org/10.1016/0263-7855(96)00018-5).
- (5) Quaino, P.; Luque, N.; Soldano, G.; Nazmutdinov, R.; Santos, E.; Roman, T.; Lundin, A.; Gross, A.; Schmickler, W. Solvated Protons in Density Functional Theory—A Few Examples. *Electrochimica Acta* **2013**, *105*, 248–253. <https://doi.org/10.1016/j.electacta.2013.04.084>.
- (6) Ghalgaoui, A.; Fingerhut, B. P.; Reimann, K.; Elsaesser, T.; Woerner, M. Terahertz Polaron Oscillations of Electrons Solvated in Liquid Water. *Phys. Rev. Lett.* **2021**, *126* (9), 097401. <https://doi.org/10.1103/PhysRevLett.126.097401>.
- (7) *An Electron in Water*. Azimuth. <https://johncarlosbaez.wordpress.com/2015/12/30/an-electron-in-water/> (accessed 2023-05-30).
- (8) *4.2 About Bader's analysis*. [https://www.quantum-espresso.org/Doc/pp\\_user\\_guide/node7.html](https://www.quantum-espresso.org/Doc/pp_user_guide/node7.html) (accessed 2023-05-28).
- (9) *CCL:G: bader chargers*. <http://ccl.net/chemistry/resources/messages/2010/08/23.007-dir/index.html> (accessed 2023-05-28).
- (10) Meredith, C.; Hamilton, T. P.; Schaefer, H. F. I. Oxywater (Water Oxide): New Evidence for the Existence of a Structural Isomer of Hydrogen Peroxide. *J. Phys. Chem.* **1992**, *96* (23), 9250–9254. <https://doi.org/10.1021/j100202a034>.
- (11) Han, B.; Isborn, C. M.; Shi, L. Determining Partial Atomic Charges for Liquid Water: Assessing Electronic Structure and Charge Models. *J. Chem. Theory Comput.* **2021**, *17* (2), 889–901. <https://doi.org/10.1021/acs.jctc.0c01102>.
- (12) López-Tarifa, P.; Hervé Du Penhoat, M.-A.; Vuilleumier, R.; Gageot, M.-P.; Rothlisbergert, U.; Tavernelli, I.; Le Padellec, A.; Champeaux, J.-P.; Alcamí, M.; Moretto-Capelle, P.; Martín, F.; Politis, M.-F. Time-Dependent Density Functional Theory Molecular Dynamics Simulation of Doubly Charged Uracil in Gas Phase. *Open Physics* **2014**, *12* (2), 97–102. <https://doi.org/10.2478/s11534-014-0428-0>.
- (13) Tavernelli, I.; Gageot, M. P.; Vuilleumier, R.; Stia, C.; Du Penhoat, M. A. H.; Politis, M. F. Time-Dependent Density Functional Theory Molecular Dynamics Simulations of Liquid Water Radiolysis. *ChemPhysChem* **2008**, *9* (14), 2099–2103. <https://doi.org/10.1002/cphc.200800177>.
- (14) Hervé Du Penhoat, M. A.; Moraga, N. R.; Gageot, M. P.; Vuilleumier, R.; Tavernelli, I.; Politis, M. F. Proton Collision on Deoxyribose Originating from Doubly Ionized Water Molecule Dissociation. *Journal of Physical Chemistry A* **2018**, *122* (24), 5311–5320. <https://doi.org/10.1021/acs.jpca.8b04787>.
- (15) Gageot, M.-P.; Lopez-Tarifa, P.; Martin, F.; Alcamí, M.; Vuilleumier, R.; Tavernelli, I.; Hervé du Penhoat, M.-A.; Politis, M.-F. Theoretical Investigation of the Ultrafast Dissociation of Ionized Biomolecules Immersed in Water: Direct and Indirect Effects. *Mutation Research/Reviews in Mutation Research* **2010**, *704* (1), 45–53. <https://doi.org/10.1016/j.mrrev.2010.01.004>.
- (16) Lu, L.; Wildman, A.; Jenkins, A. J.; Young, L.; Clark, A. E.; Li, X. The “Hole” Story in Ionized Water from the Perspective of Ehrenfest Dynamics. *J. Phys. Chem. Lett.* **2020**, *11* (22), 9946–9951. <https://doi.org/10.1021/acs.jpcllett.0c02987>.
- (17) Gageot, M. P.; Vuilleumier, R.; Stia, C.; Galassi, M. E.; Rivarola, R.; Gervais, B.; Politis, M. F. A Multi-Scale Ab Initio Theoretical Study of the Production of Free Radicals in Swift Ion Tracks in Liquid Water. *Journal of Physics B: Atomic, Molecular and Optical Physics* **2007**, *40* (1), 1. <https://doi.org/10.1088/0953-4075/40/1/001>.
- (18) Rajpal, A.; Huart, L.; Nicolas, C.; Chevillard, C.; Guigner, J.-M.; Dasilva, P.; Mercere, P.; Gervais, B.; Hervé du Penhoat, M.-A.; Renault, J.-P. Superoxide Production under Soft X-Ray Irradiation of Liquid Water. *J. Phys. Chem. B* **2023**. <https://doi.org/10.1021/acs.jpcc.3c00932>.



## CONTENTS CHAPTER 5

---

<b>Chapter 5: Spectroscopic studies of biomolecules in aqueous environment...</b>	<b>178</b>
<b>5.1. Choice of the aqueous biomolecules.....</b>	<b>179</b>
<b>5.2. Understanding the effect of core ionizations .....</b>	<b>181</b>
<b>5.3. Valence band characterization.....</b>	<b>189</b>
<b>5.4. Identifying the involved orbitals: DOS calculations using AIMD .....</b>	<b>190</b>
<b>5.5. Enhancing specific electronic transitions: Resonant Auger study .....</b>	<b>196</b>
5.5.1. Enhancement at the Carbon edge.....	197
5.5.2. Enhancement at the Nitrogen edge .....	204
<b>5.6. Electronic structures of Gly and Gly-Gly .....</b>	<b>208</b>
<b>5.7. Conclusion .....</b>	<b>211</b>
<b>References.....</b>	<b>212</b>

## Chapter 5: Spectroscopic studies of biomolecules in aqueous environment

The previous chapters dealt with the interest of understanding the effects of synchrotron soft X-rays in causing inner shell ionization in liquid water that lead to the creation of a doubly ionized water molecule and two secondary electrons (a photoelectron and a Auger electron). It has been shown that the dissociation product of the doubly ionized water molecule can result in the formation of superoxide radicals as a result of interactions with its surrounding.

In this chapter, our objective is to explore the influence of the solvation on the electrons produced after ionization of aqueous biomolecules. To accomplish this, we adopt a multidisciplinary approach that combines various experimental and theoretical techniques. The first technique employed is X-ray photoelectron spectroscopy (XPS), performed using the liquid microjet set-up available at PLEIADES beamline, synchrotron SOLEIL. We began with investigating the core-electron XPS, which provided an understanding of the elemental composition, chemical environment, etc. Subsequently, we performed valence electron spectroscopy. Valence band studies provide information about the bonding orbitals and chemical reactivity, as these electrons are involved in the bond formations, and finally about the Highest Occupied Molecular Orbital (HOMO). Partial electron yields recorded around the C and N K-edges provide information about possible presence of electronic excitation resonances, between the core level and the Lowest Unoccupied Molecular Orbital (LUMO), below the ionization threshold. Then, we also present resonant studies that allowed to identify the involved molecular orbital (MO) of biomolecules in an aqueous environment in this core-excitation regime. The interpretations obtained using the resonant studies are supported by Density of States (DOS) calculations using AIMD simulations. Additionally, we employ UV-vis spectroscopy, both in solid and liquid phases, to elucidate the electronic structure of the biomolecules.

### 5.1. Choice of the aqueous biomolecules

Biomolecules are organic molecules that play a critical role in various biological processes such as metabolism, DNA replication, and cellular signaling.<sup>1</sup> They are embedded and perform their functions in an aqueous environment in living organisms. Therefore, studying their behavior

in their aqueous form becomes crucial to understand their physiological functions, interactions with other biomolecules, and responses to external stimuli.<sup>2</sup> For this purpose, we choose to investigate two biomolecules in an aqueous environment, Glycylglycine (Gly-Gly, the simplest peptide), and Glycine (Gly, the simplest amino acid) (structures shown in figure 5.1). Owing to their small size, both Gly and Gly-Gly serve as model systems to study amino acids and peptide bonds, respectively. Both the solutions had a pH of 7 and were used at a concentration of 1 M, with 50 mM salt (KCl), to avoid the charging of the jet.<sup>3</sup>

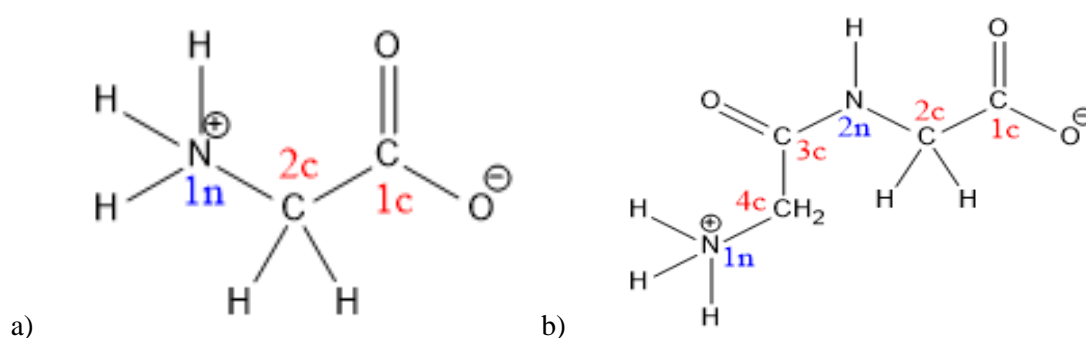


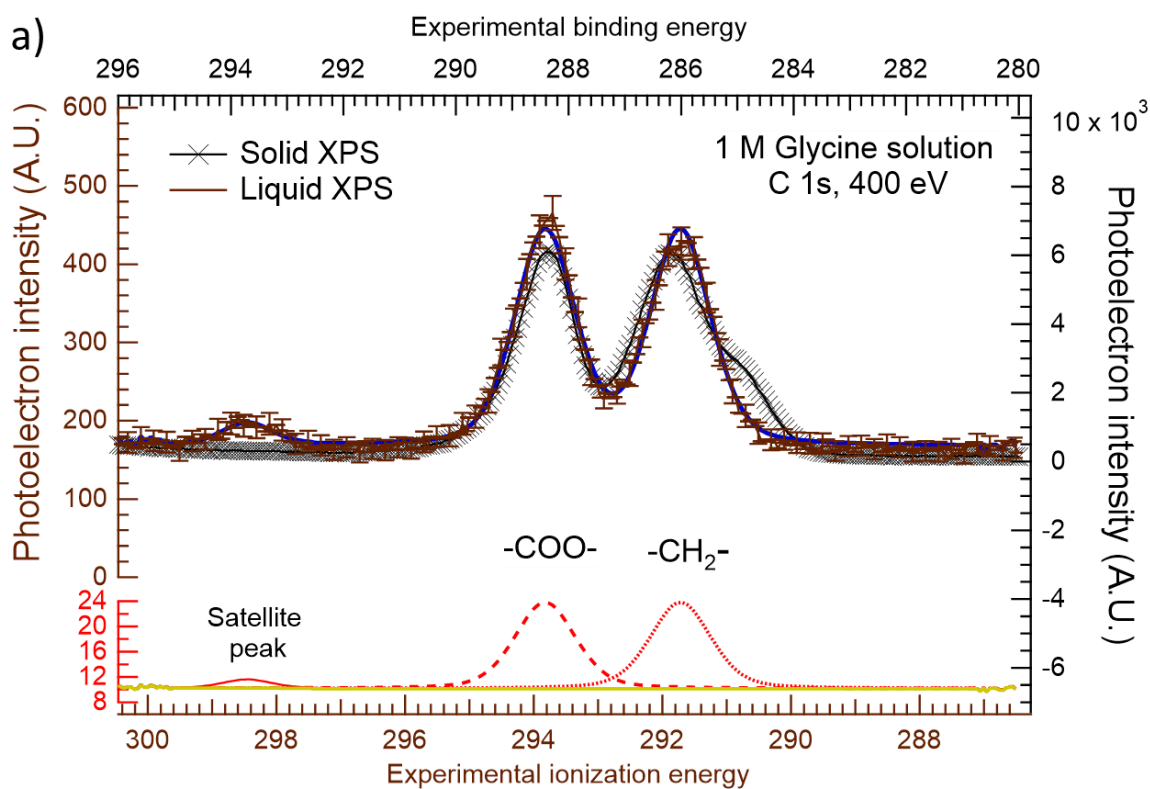
**Figure 5.1:** Chemical structure of a) Glycine and b) Glycylglycine, in their zwitterion forms. The nitrogen atoms are numbered in blue, starting from the N terminal and the carbon atoms are numbered in red, starting from the C terminal.

Gly and Gly-Gly exist in their neutral form in the gas phase whereas, they are present in their zwitterion form in the solid and aqueous phases.<sup>4,5</sup> They have been extensively studied in the gas phase, solid phase<sup>6,7</sup> (as mentioned in the section 1.4, Chapter 1) and in the liquid phase using highly penetrating radiations<sup>8</sup>, but liquid phase studies using soft X-rays are scarce.<sup>9,10,11,12</sup> In addition, owing to their small size, they are computationally less expensive, which allowed us to perform AIMD simulations.

We conducted an extensive photoemission spectroscopic analysis, to investigate the response of Gly and Gly-Gly aqueous solutions to soft X-rays (0.2-2 keV). Our aim was to understand the specific properties of peptide bonds. It is the most critical type of bond in biochemistry, and it is responsible for the protein's structural integrity and function.<sup>13</sup> We aimed to comprehend the impact of hydration on the peptide bond through comparative spectroscopic analyses of Gly and Gly-Gly, in both solid and aqueous phases.

## 5.2. Understanding the effect of core ionizations

We present here the results of liquid phase XPS of 1 M Gly and 1 M Gly-Gly solutions, measured using a liquid microjet. The carbon, nitrogen and oxygen core-level XPS spectra, for Gly and Gly-Gly, were recorded and their binding energies were calibrated as described in the section 2.4.5.4 of chapter 2. The C 1s and N 1s spectra, recorded in the liquid phase (at pH =7) and solid phase, are shown in the figures 5.2 and 5.3, respectively. The liquid phase XPS spectra are presented in ionization energy referenced with respect to the vacuum level of the analyzer, whereas the solid-state spectra are presented in binding energies referenced with respect to the gold Fermi level.





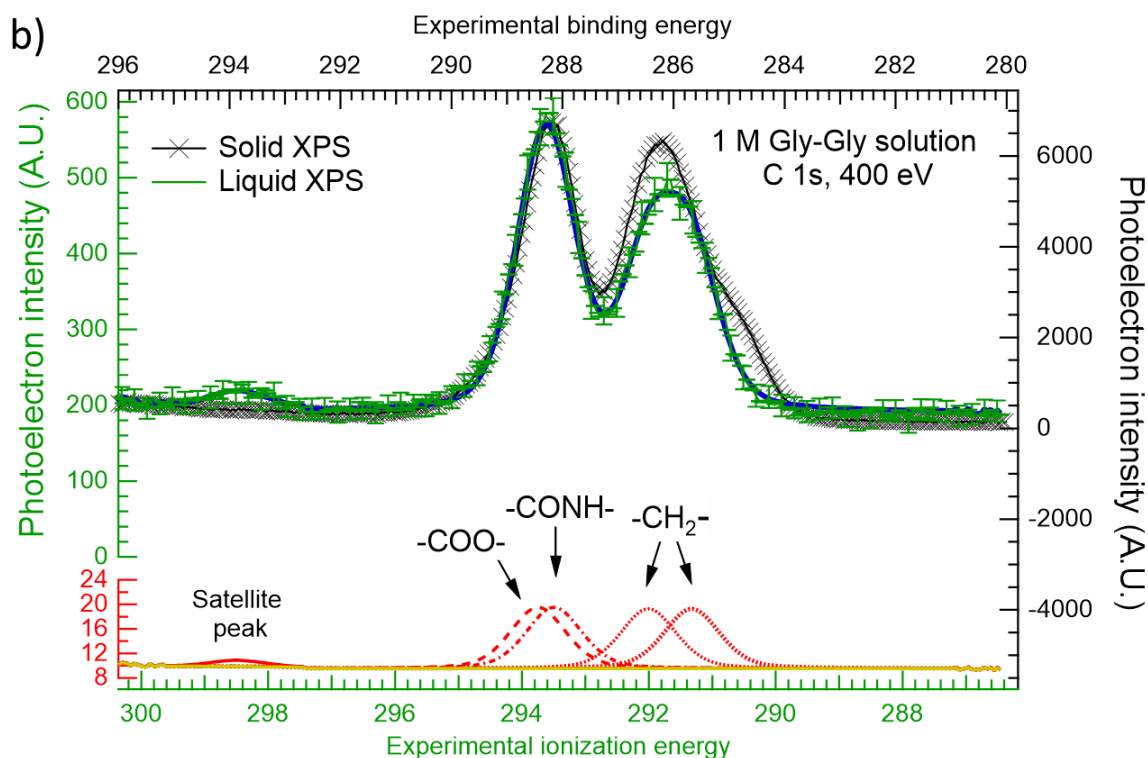


**Figure 5.2:** C1s XPS spectra recorded at 400 eV: Liquid-state XPS spectra of a) Gly (brown curve) and b) Gly-Gly (green curve) compared with their solid-state XPS spectra (black curves). The liquid-state (pass energy 50 eV) and solid-state XPS spectra (pass energy 20 eV) were recorded with a resolution of 0.32 eV and 0.35 eV, respectively. The peaks were fit using the line shape SGL(30) and the contribution from each spectral peak is shown (red, bottom scale) for the liquid-state spectra, with Tougaard background. The MC peak fit model simulation, a feature that is inbuilt in the CasaXPS, was used to check the quality of the fit. The peak fit model had negligible standard deviation for peak positions.

The fitting of the spectra was done with SGL line shape (see chapter 2, for conditions) with constrains on the area (as the chemical formula is known) and peak width for all the main peaks. These parameters were set to be equivalent for all the main peaks while the absolute value was flexible to adjust. For *solvated Gly* (brown curve, figure 5.2 a), the carbon 1s spectra had two major peaks, one peak originating from the carbon of hydrocarbon (labelled '2c' in figure 5.1 a) at 291.7 eV and the other from the terminal carboxylate carbon at 293.8 eV (labelled '1c' in figure 5.1 a). The peaks positions were compared with the data available in the literature for Gly (see table 5.1).<sup>11</sup> For *solvated Gly-Gly*, the two peaks in the carbon 1s spectra (green curve, figure 5.2 b) had a contribution from 4 carbons. Two hydrocarbon

carbons, labelled '2c' and '4c' in figure 5.1 b, contributed to the peak at lower ionization energy, with peaks position at 291.3 eV and 292 eV, respectively. The peak at high ionization energy was attributed to the carbon of the peptide bond (labelled '3c' in figure 5.1 b, at 293.5 eV) as well as the carbon of the carboxylate group (labelled '1c' in figure 5.1 b, at 293.8 eV). This attribution was based on the fact that the binding energy increases when the carbon atom is bonded to a more electronegative group. Also, similar peaks are reported for solid state Gly-Gly in the literature.<sup>6</sup> The solvated C 1s spectra for both the solutions showed an additional low intensity peaks around 298.5 eV, referred to as the satellite peak. These observed satellite peaks originated from what are known as shake-up processes (described in section 1.4.1.1 of chapter 1). The occurrence of such peaks is a common phenomenon in high-resolution core-electron spectra.<sup>14</sup> Since the shake-up process originates when an electronic transition occurs from an occupied to an unoccupied MO, the relative energy of the shake-up peak is either equivalent or higher than band gap (energy difference between the HOMO and LUMO).<sup>14</sup> We estimated it here, by the difference between the positions of the satellite peak and that of the main peak with the lowest experimental ionization energy. This difference was found to be 6.8 eV and 7.2 eV for Gly and Gly-Gly, respectively. This gave an upper bound for their band gaps in the aqueous state. Exact values ( $5.5 \pm 0.1$  eV for Gly and  $5.2 \pm 0.1$  eV for Gly-Gly) of the band gap were, however, calculated using the Tauc Plot in section 5.6. The intensity of the satellites was higher for Gly than for Gly-Gly.

The solid state C 1s spectra of both Gly and Gly-Gly displayed two prominent peaks each, similar to the peaks observed in their respective liquid state spectra (black curves, figure 5.2). However, in the solid state, a shoulder emerged on the peak centered at 291.6 eV, at a lower binding energy, resulting in a broadening of this peak. This corresponds probably to the adventitious carbon peak that came from handling of the powder sample.<sup>15, 21</sup> The solid state spectra of both Gly and Gly-Gly were found to be comparable to the reported data in the literature (see table 5.1).<sup>6</sup> The appearance of the adventitious carbon peak was prevented in liquid XPS spectra conducted under vacuum conditions, as the sample signal remained unaffected by atmospheric carbon species interference. Another striking feature present in the C1s spectra of the liquid and not of the solid phases was the satellite peak (described in section 1.4.1.1 of chapter 1).

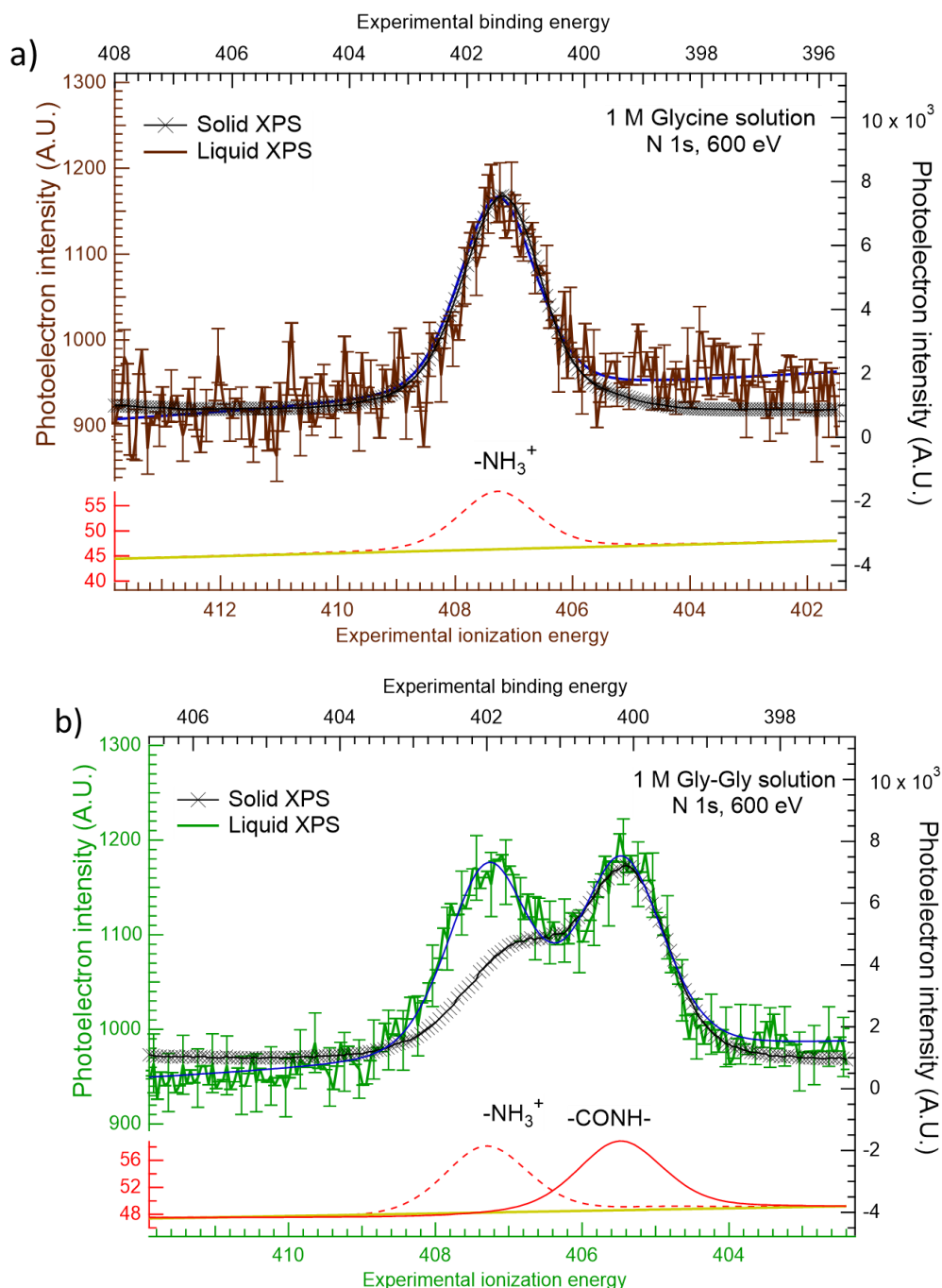


**Figure 5.3:** N1s XPS spectra recorded at 600 eV: Liquid-state XPS spectra of a) Gly (brown curve) and b) Gly-Gly (green curve) compared with their solid-state XPS spectra (black curve). The liquid-state (pass energy 50 eV) and solid-state XPS spectra (pass energy 20 eV) were recorded with a resolution of 0.32 eV and 0.35 eV, respectively. The peaks were fit using the line shape SGL(30) and the contribution from each spectral peak is shown (red, bottom scale) for the liquid-state spectra, with a linear background. The MC peak fit model simulation, a feature that is inbuilt in the CasaXPS, was used to check the quality of the fit. The peak fit model had negligible standard deviation for peak positions.

We propose that, since the kinetic energy of the photoelectrons in solid XPS was high (as we work with a 1486.6 eV X-ray source), it could possibly decrease the cross section of interaction between the photoelectron and the valence electron.<sup>16</sup>

For glycine, the separation in the positions of the two peaks was similar for the solid and liquid XPS C 1s spectra (2.1 eV in liquid and 2.2 eV in solid). This was also the case for Gly-Gly C 1s spectra (1.9 eV in liquid and in the solid is 2.0 eV).

The liquid phase N 1s spectra (at pH =7) for Gly and Gly-Gly are shown in figure 5.3. *Solvated Gly* had one peak located at 407.2 eV, that is attributed to the terminal nitrogen (labelled as '1n' in figure 5.1 a). The position of this peak is similar to the value reported earlier by Ottosson et al. (406.8 eV at pH 7), see table 5.1.<sup>11</sup> For *solvated Gly-Gly*, two main peaks were observed, which were set to have an identical width for the fit. The peak at higher ionization energy, 407.2 eV, was attributed to the terminal nitrogen,  $\text{NH}_3^+$ , (labelled '1n' in figure 5.1 b) and the other peak at 405.4 eV was attributed to the nitrogen participating in the peptide bond formation, CONH, (labelled '2n' in figure 5.1 b). Unlike the liquid phase C1s spectra, no shake-up peak was observed in the N1s spectra of Gly or Gly-Gly. This was probably due to the decrease in the cross section of the interaction (between the photoelectron and valence electrons) around the nitrogen edge.

In the solid phase N 1s spectra as well, Gly exhibited one peak, while Gly-Gly exhibited two peaks. However, the two peaks in solid state N1s spectra of Gly-Gly were not very well resolved. A similar spectrum is also reported in the literature,<sup>6</sup> even if the claim of the authors on the identical intensity of the two peaks seems over conclusive.<sup>6</sup> To obtain the best fit of the experimental spectrum, the width of the contribution at higher binding energy ( $\text{NH}_3^+$ , labelled '1n' in figure 5.1 b) should be higher than the other contribution (see appendix III.I). This could indicate that more than two components are present in the spectrum. It must be noted at this point that the difference between the position of the two nitrogen peaks, is not the same in the liquid (1.8 eV difference) and in the solid (1.4 eV difference) phase spectra, unlike that for the two carbon peaks. Also it seems that the solvation of the Gly-Gly has more effect on the core energy levels of nitrogen than the carbon ones (figure 5.2 b). A recent publication<sup>17</sup> shows indeed that the nitrogen core level seems to be more affected by the solvation.

The difference between the respective peak positions in liquid and solid phases provides an indirect method to estimate the work function of the solution ( $\Phi_{\text{indirect,Gly}}$ ,  $\Phi_{\text{indirect,Gly-Gly}}$ ) (see table 5.1).<sup>18, 19</sup> The average value of  $\Phi_{\text{indirect,Gly}}$  and  $\Phi_{\text{indirect,Gly-Gly}}$  was  $5.5 \pm 0.1$  eV and  $5.4 \pm 0.1$  eV, respectively.

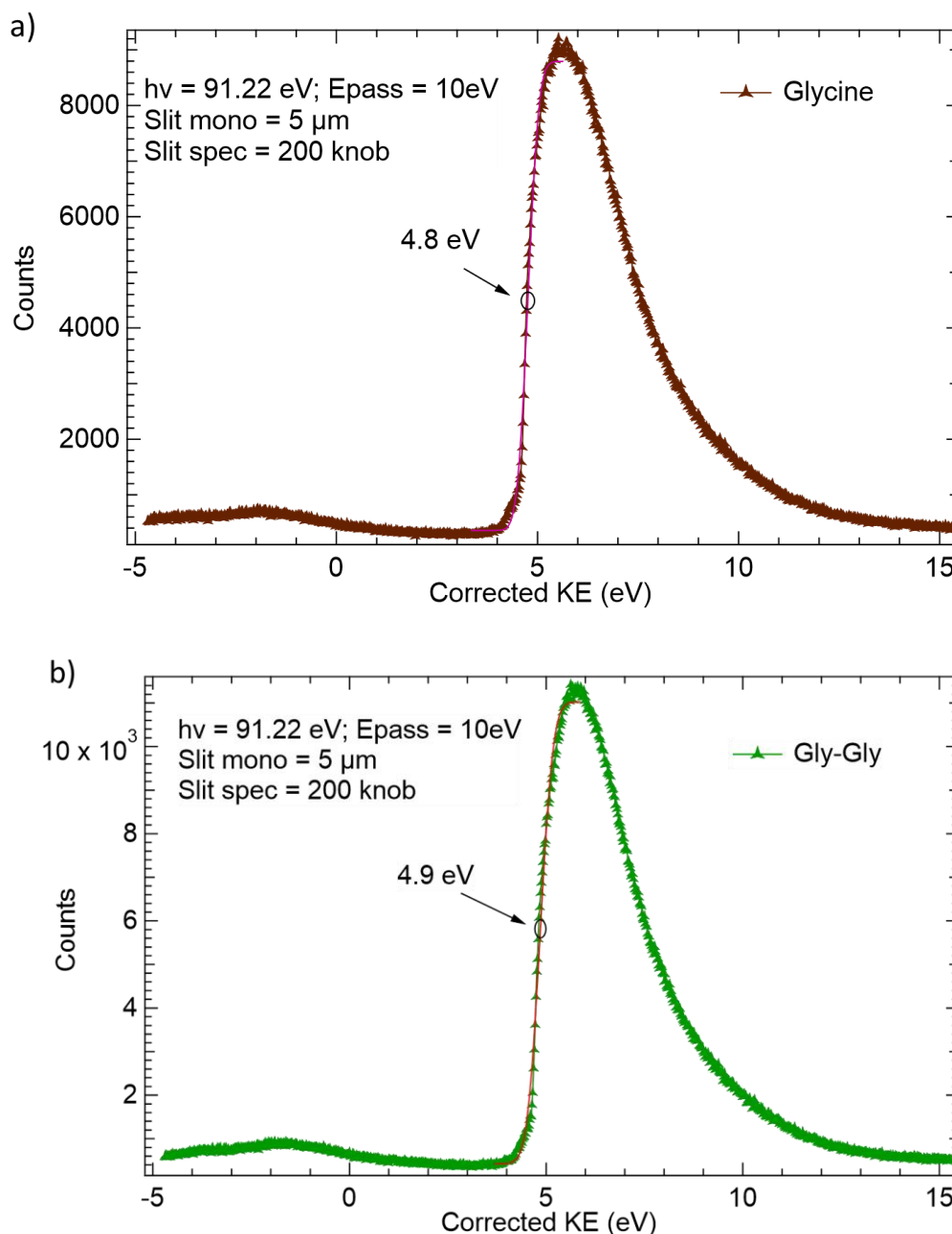


**Figure 5.4:** Secondary electron cut off spectra for a) 1 M Glycine (brown symbols) and b) 1 M Gly-Gly solutions (green symbols), at pH 7. The value of the work function obtained from the fitting function (red line) is shown in the figure. The value obtained is found to be comparable to that obtained using the peak differences between the solid and liquid (see text). The reported spectra were recorded at the bias of -50 V (subtracted on each figures).

The secondary electron cut off spectra (SECO) provided an alternative way to directly and precisely measure the work function of the solution ( $\Phi_{\text{direct,Gly}}$ ,  $\Phi_{\text{direct,Gly-Gly}}$ ). The SECO spectra for the reference 50 mM KCl solution (see section 2.4.5.4 of chapter 2) was used to calibrate the SECO spectra of aqueous Gly (see figure 5.4 a) and Gly-Gly (figure 5.4 b). The work function was determined using 'erf' fitting functions,<sup>20</sup> and was found to be  $4.8 \pm 0.1$  eV and  $4.9 \pm 0.1$  eV for Gly and Gly-Gly, respectively. These values are reported in the table 5.1.

In the case of the SECO measurement, the work function of the analyzer is considered via the calibration with KCl solution. However, in the case of indirect measurements small additional energy shifts could be introduced by surface potential effects at the analyzers level or even by some streaming potential linked to the jet flow through a glass capillary. The work function values obtained using the SECO spectra were used hereafter in this work.

**Table 5.1:** Summary of the peak positions in their solid and liquid XPS spectra (C 1s and N 1s spectra), for Gly and Gly-Gly. The literature values for the peaks position in the solid and liquid states are also presented. The difference in the respective peak position in solid and liquid phase spectra are reported as the work function ( $\Phi_{\text{indirect}}$ ). The work function obtained from the SECO spectra ( $\Phi_{\text{direct,Gly}}$ ,  $\Phi_{\text{direct,Gly-Gly}}$ ) is also reported.

System under investigation	Solid phase XPS				Liquid phase XPS			$\Phi_{\text{indirect}}$ (eV)
	Exp (Ref <sup>6</sup> ) (eV)	Exp (Ref <sup>21</sup> ) (eV)	Exp (Current work) (eV)	Peak width (current work)	Exp (Ref <sup>11</sup> ) (eV)	Exp (Current work) (eV)	Peak width (current work)	
<b>Glycine</b>	$\Phi_{\text{direct,Gly}}$ calculated from SECO spectra = 4.8 eV							
<b>C 1s (&gt;CH<sub>2</sub>)</b>	287.1	286.8	286.2	1.3	291.4	291.7	1.1	5.5
<b>C 1s (-COO<sup>-</sup>)</b>	289.3	288.7	288.4	1.3	293.6	293.8	1.1	5.4
<b>Satellite peak</b>	-	-	-	-	-	298.5	0.9	-
<b>Adventitious carbon</b>	286.0	285.0	285.0	1.3	-	-	-	-
<b>N 1s (-NH<sub>3</sub><sup>+</sup>)</b>	402.2	402.0	401.4	1.6	406.8	407.3	1.6	5.9
<b>Glycylglycine</b>	$\Phi_{\text{direct,Gly-Gly}}$ calculated from SECO spectra = 4.9 eV							
<b>C 1s (&gt;CH<sub>2</sub>)</b>	287.0	286.6	285.9	1.0	-	291.3	1.0	5.4
<b>C 1s (&gt;CH<sub>2</sub>)</b>	287.3	286.6	286.6	1.0	-	292.0	1.0	5.4
<b>C 1s (-CONH-)</b>	289	288.4	288.0	1.0	-	293.5	1.0	5.5
<b>C 1s (-COO<sup>-</sup>)</b>	289.3	288.4	288.6	1.0	-	293.8	1.0	5.2
<b>Satellite peak</b>	-	-	-	-	-	298.5	1.0	-
<b>Adventitious carbon</b>	286.0	285.0	285.0	1.3	-	-	-	-
<b>N 1s (-CONH-)</b>	400.7	400.4	399.9	1.3	-	405.5	1.3	5.6
<b>N 1s (-NH<sub>3</sub><sup>+</sup>)</b>	402.2		401.4	1.7	-	407.3	1.3	5.9

### 5.3. Valence band characterization

The lower band of the valence spectra of 1 M Gly and 1 M Gly-Gly were analyzed in comparison with the reference 50 mM KCl solution, see figure 5.5 a.

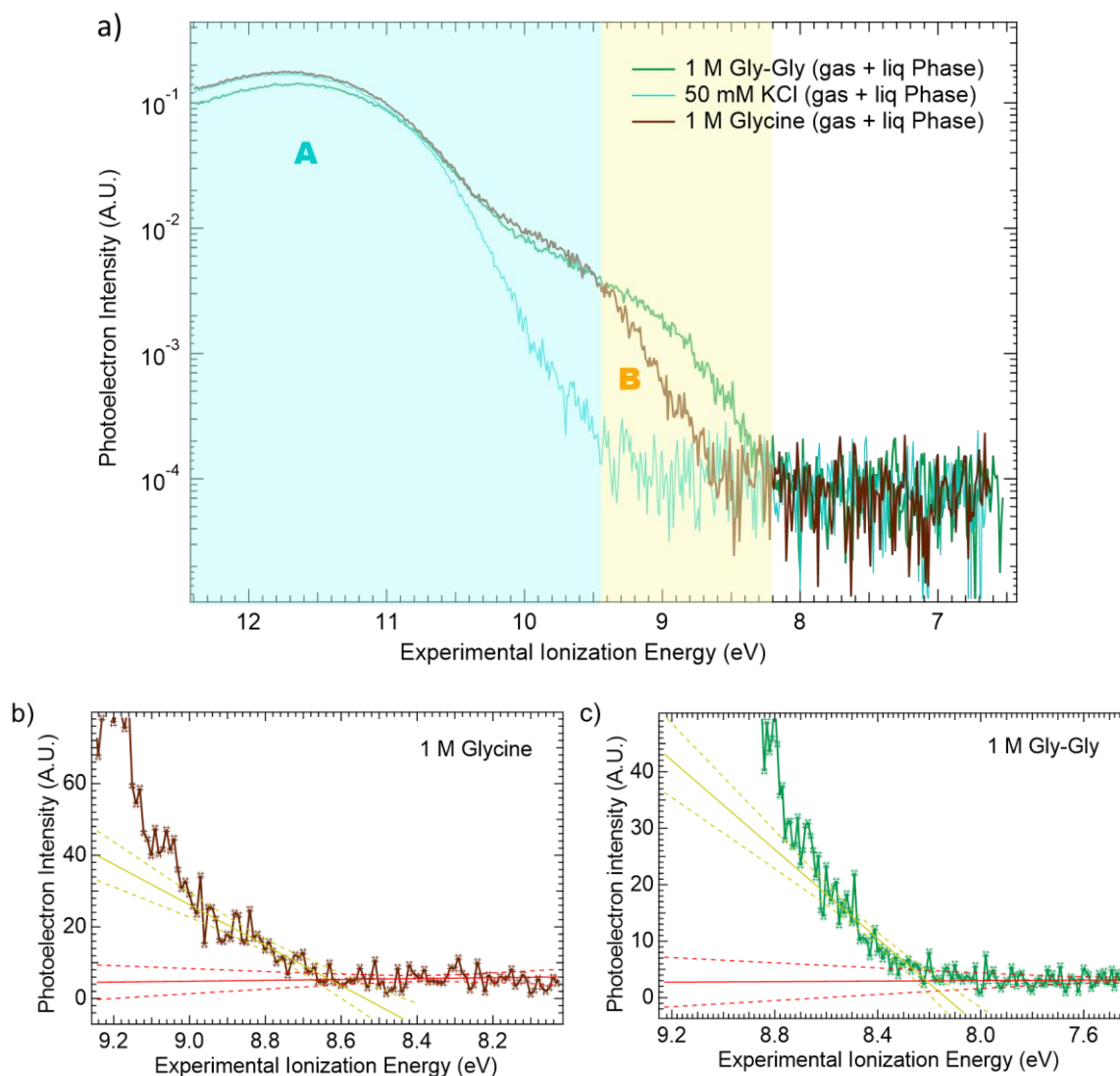


**Figure 5.5:** Liquid phase valence band spectra measured at 91.2 eV photon energy with a 10 eV pass energy for a) 50 mM KCl (blue), 1 M Gly (brown) and 1 M Gly-Gly (green), with the y-axis in logarithmic scale. The graph represents the intensity variation as a function of experimental ionization energy (eV) on the X-axis. The extrapolation of the slope of band 'B', b) for 1 M Gly and c) 1 M Gly-Gly, is represented with solid yellow line with 99% confidence bands shown in dotted yellow lines. The background of the curve is represented by solid red lines with 99% confidence bands shown in dotted red lines.



The figure 5.5 a clearly shows two bands, **A** and **B**, for aqueous Gly (brown curve) and Gly-Gly (green curve), whereas, only a single band (band **A**) is present in the valence spectra of KCl solution (blue curve). This indicates that the band **B** is specific to valence bands of Gly and Gly-Gly solutions. In addition, the band **A** centered at 11.63 eV can be attributed as the 1b<sub>1</sub> liquid water molecular band by comparison with the literature value for 1b<sub>1</sub> pure water (ranging from 11.16 eV to 11.67 eV).<sup>22,22</sup> The band **A** was observed at the same position (11.63 eV ± 0.10 eV) in all three curves, indicating that no chemical shift occurred in the 1b<sub>1</sub> band for either of the samples despite the high solutes concentration.

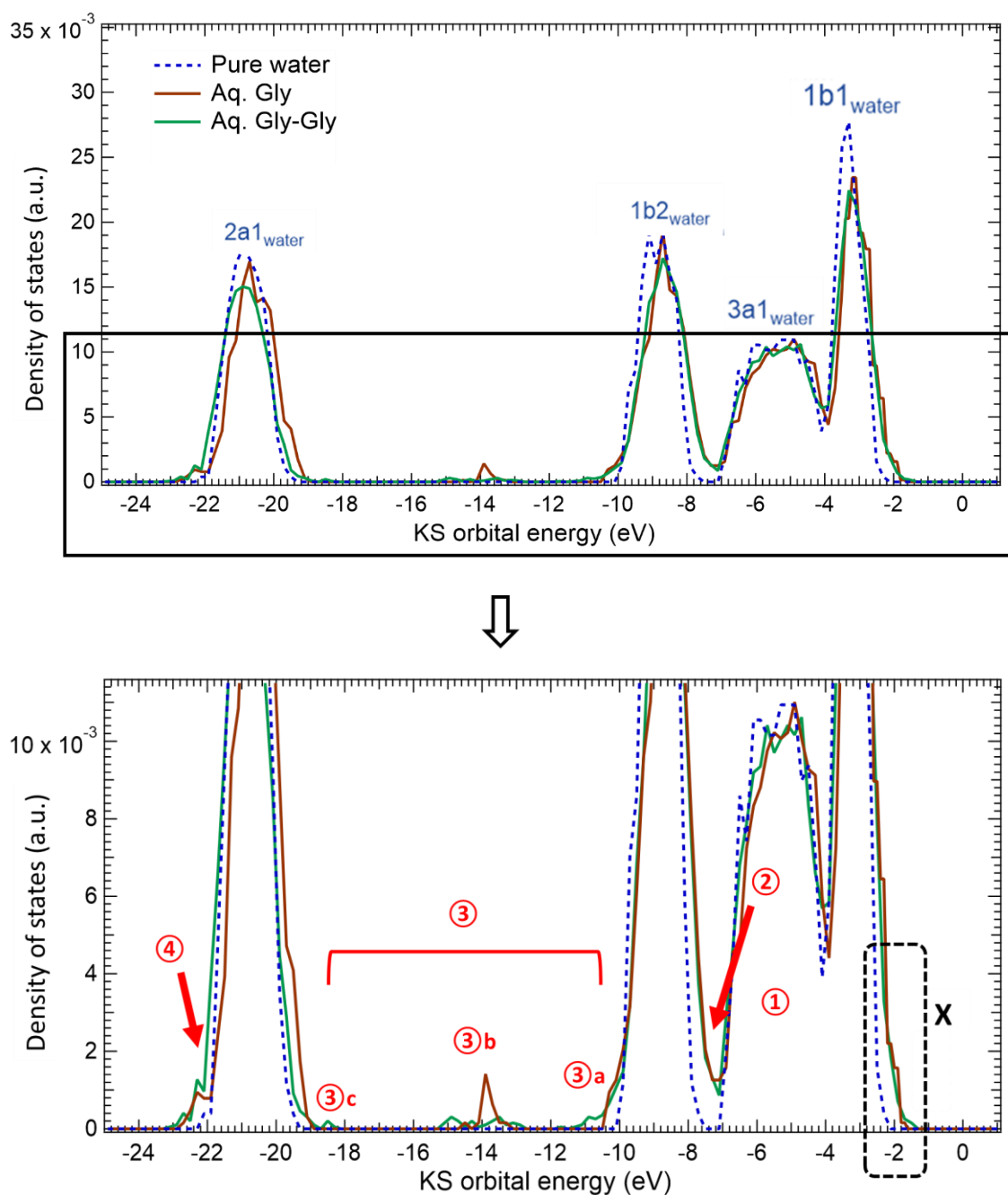
Figure 5.5 b and c allow determining the photon-ionization threshold of Gly (8.6 ± 0.2 eV) (comparable to the threshold value of 8.8 eV, in the vapor phase)<sup>23,24</sup> and Gly-Gly (8.2 ± 0.2 eV) in water, respectively. These values were obtained from the intersection point of the extrapolation of the slope (solid yellow line) and the background (solid red line). The energy of the highest occupied molecular orbital (HOMO) is given by the negative of the obtained ionization threshold values. This suggests that the HOMO of aqueous Glycine and Gly-Gly are -8.6 eV and -8.2 eV below the vacuum level, respectively.

#### 5.4. Identifying the involved orbitals: DOS calculations using AIMD

As demonstrated in the previous section, the XPS valence bands of the glycine and glycyglycine solutions overlap with those of liquid water above 9.5 eV. To have a better sight of them, it is important to calculate these solutions electronic density of states (DOS). This was done using AIMD simulations, as described in sections 2.4 and 2.5 of chapter 2.

A comparative study on the DOS, which provided insights into the occupancy of (valence) Kohn-Sham orbitals, was carried out. The DOS for pure water (dotted blue curve), aqueous Gly (solid brown curve) and aqueous Gly-Gly (solid green curve) are shown in figure 5.6 (top). It should be noted that the DOS was computed using the BLYP functional, which is known to result in shifts in the energy scale compared to the actual one-electron states energies.<sup>25,26</sup> The annotation for the different bands in the pure liquid water DOS curve (1b<sub>1water</sub>, 3a<sub>1water</sub>, 1b<sub>2water</sub> and 2a<sub>1water</sub>) and their respective energy shifts were determined by comparing to the experimental data reported in the literature (see appendix III.II).<sup>27,28</sup> It resulted in energy shifts of -8 eV (around the 1b<sub>1</sub> and 3a<sub>1</sub>), -8.4 eV (around 1b<sub>2</sub>) and 10 eV (around 2a<sub>1</sub>), partially due to the work function of the aqueous sample. This factor had to be taken into account when

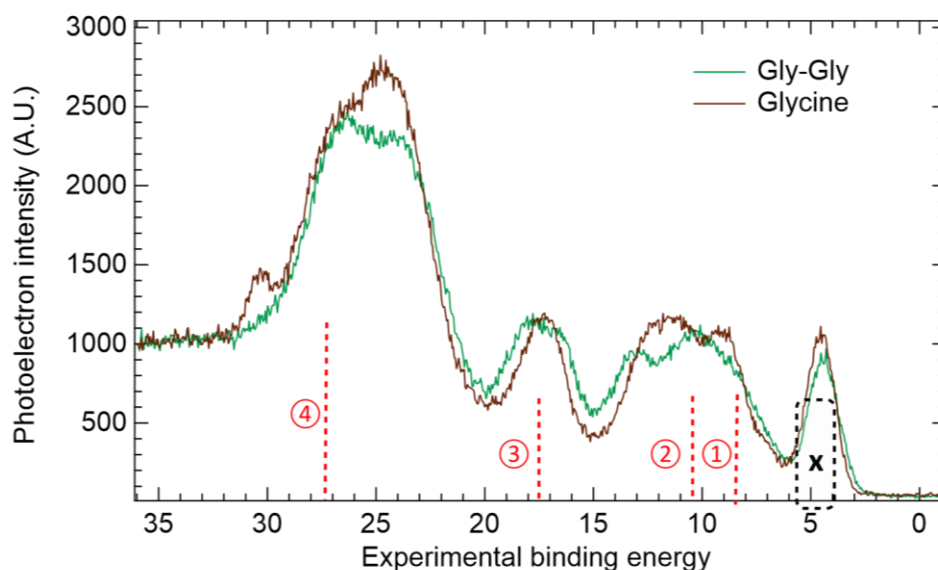
comparing the experimental RAS spectra (displayed in section 5.5) with the computed DOS curves.



**Figure 5.6:** Density of states calculation for a system of pure water (dotted blue curve), Gly-Gly in water (solid green curve) and Glycine in water (solid brown curve). The peaks of pure water system are labelled by comparison with the data present in the literature.<sup>27</sup> The computed DOS is normalized with respect to the number of electrons present in each system to have a reasonable Aq comparison. The magnified image of the DOS (bottom figure) shows low intensity peaks belonging to the MO of Gly and Gly-Gly.

From a first glance, the comparison of DOS curves for all the solutions indicates that the effect of adding the solute, Gly or Gly-Gly, appears to be fairly small. The shape and position of the four main bands remain almost the same, and are thereafter labelled  $1b_{1\text{water}}$ ,  $3a_{1\text{water}}$ ,  $1b_{2\text{water}}$  and  $2a_{1\text{water}}$  for all solutions. Since there is only one solute molecule in the simulation box that is surrounded by several water molecules (1 Gly in 43  $\text{H}_2\text{O}$  or 1 Gly-Gly in 123  $\text{H}_2\text{O}$ ), the fraction of the KS orbitals solely belonging to the solute is low. These orbitals can be observed in the magnified DOS curves, see figure 5.6 (bottom).

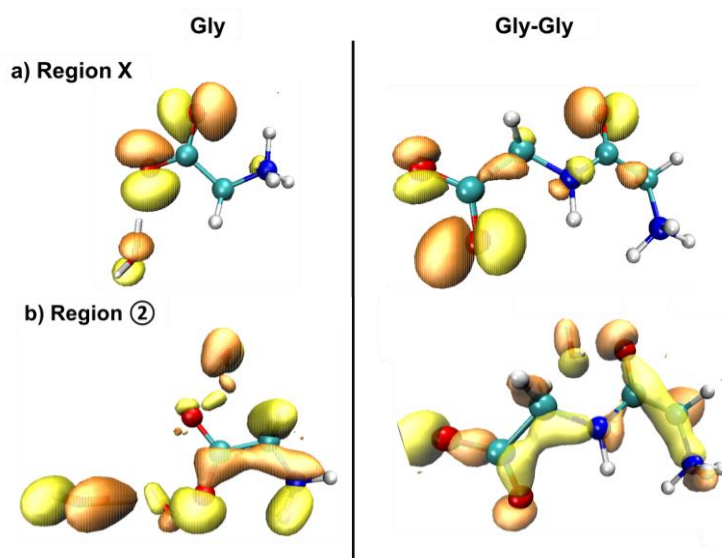
The regions of interest (labelled X, ①, ②, ③ and ④ in the figure 5.6 (bottom)), are presented in figures 5.7 and 5.8. These regions were looked at closely, as some characteristic differences were observed among the three DOS curves. The choice of these regions was supported by the solid-state valence spectra of Gly and Gly-Gly that covered all of these regions (after taking into account the work function) with significant peaks in the solid state valence spectra (see figure 5.7).



**Figure 5.7:** Solid state valence spectra of powdered Gly (brown curve) and powdered Gly-Gly (green curve). The spectra was recorded at the pass energy of 20 eV with a resolution of 0.35 eV. The binding energy is calibrated with respect to the gold Fermi level.

Region 'X' (just before the  $1b_{1\text{water}}$  band) shows some differences in the three DOS curves, indicating additional states. For aqueous Gly, these states had a contribution from the KS orbitals centered on the terminal carboxylic group of Gly along with some electron density distributed across the water molecules. However, for aqueous Gly-Gly, the electron density was concentrated on the Gly-Gly carboxylic group as sigma lone pair and some of it was

delocalized on the peptide bond (see figure 5.8 a). Region ① (around the  $3a_{1_{\text{water}}}$  band) was chosen as a reference domain and indeed it had contributions from orbitals localized majorly on the solvent water molecules (figure not shown). Region ② (between the  $3a_{1_{\text{water}}}$  and  $1b_{2_{\text{water}}}$  bands) had contributions from orbitals belonging majorly to the solute along with some of the water molecules that form H-bonds with the solute (see figure 5.8 b). In region ③ (between the  $1b_{2_{\text{water}}}$  and  $2a_{1_{\text{water}}}$  bands), the KS orbitals were plotted at three different points (labelled ③a, ③b and ③c). At point ③a, the electron density was delocalized over Gly-Gly. At ③c, the contribution to the orbitals was majorly from the peptide bond in Gly-Gly. At point ③b, the orbitals were delocalized all over Gly or Gly-Gly. There were no orbitals originating from water molecules in region ③. This can be seen in the figure 5.8 c. The analysis of the orbitals in region ④ (immediately after the  $2a_{1_{\text{water}}}$  band), for *solvated Gly*, showed that the orbitals belonged to the carboxylic group of Gly. On the other hand, for *solvated Gly-Gly*, the electron density was spread over the peptide bond (see figure 5.8 d).



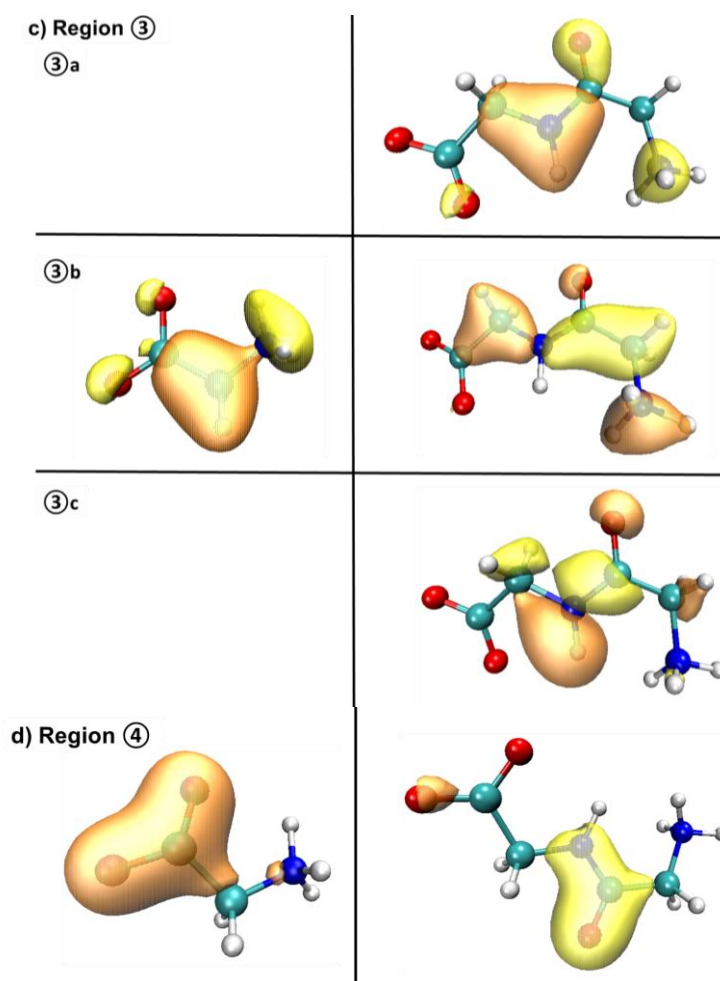


**Figure 5.8:** Kohn-Sham orbitals, computed at the regions of interest for a solute, Gly (left panel) and Gly-Gly (right panel), surrounded by water molecules in a simulation box (contour value: 0.05). For clarity, only a few water molecules around the solute are presented, only when they share a contribution in the electron density. The KS orbitals for the region ① are not shown as they majorly belonged to water.

It could be concluded that some KS orbitals present a pure solute origin (as in region ③ and ④) whereas others present a mixture of the solute and its first solvation sphere (as in region X, ① and ②).

The computed energies of the KS orbitals in these regions were compared with the literature MO energies of isolated zwitterionic Gly and zwitterionic Gly-Gly, obtained using Ab initio SCF calculations.<sup>29</sup> We identified the MO having contributions from the bonding and non-bonding pi-orbital of the peptide bond, delocalized sigma orbitals and the lone-pair orbital on the oxygen atom involved in the peptide bond, in the energies range of the marked regions (see

table 5.2). This comparison confirmed that the electron density in the aqueous samples (Gly and Gly-Gly) is more delocalized than in the isolated case.

**Table 5.2:** Summary of the distinct features observed in the DOS of aqueous zwitterionic Gly and Gly-Gly. Here,  $n$  denotes lone pair,  $\sigma$  denotes significantly delocalized sigma orbitals,  $\pi_n$  denotes pi non-bonding orbital and  $\pi_b$  denotes pi bonding orbital. The attribution to these regions is given by comparing the theoretical values with the literature SCF calculations for zwitterionic isolated Gly and Gly-Gly. The theoretical energy value (Theor. value) is the one computed from the AIMD simulation and these values can be compared to the experimental energy values by considering the respective energy shift factor (see text).

Region	Theor. value (eV)	Theor. value with energy shift (eV)	Assigned orbitals				
			Current work		Reference (Ab initio SCF calculations) <sup>29</sup>		
			Aq. Gly	Aq. Gly-Gly	Isolated Gly	Isolated Gly-Gly	
X	2.0	10.0	Carboxyl lone pair	Carboxyl lone pair + delocalized on peptide bond	$n$ (Carbonyl oxygen)	$n$ (Carbonyl oxygen)	
①	5.4	13.4	Delocalized across Water box	Delocalized across Water box	-	-	
②	7.2	15.2	Delocalized across solvation water and Gly	Delocalized across solvation water and Gly-Gly	$\pi_n$	$n$ (Carbonyl oxygen)	
③	③a	10.8	19.2	-	Delocalized across Gly-Gly	-	$\pi_{n,b}$ (peptide) and $\pi_b$ (COO-), $n$ (C=O of peptide)
	③b	14.0	22.4	Delocalized across Gly	Delocalized across Gly-Gly	$\pi_b$	
	③c	18.4	28.4	-	Peptide bond	-	
④	22.2	32.2	$\sigma$ (COO-)	$\sigma$ (Peptide bond)	$n$ (Carbonyl oxygen), $\sigma$	$\sigma$	

## 5.5. Enhancing specific electronic transitions: Resonant Auger study

In the previous section, various new electronic states were identified in aqueous Gly and Gly-Gly. To study these states, we performed Resonant Auger study. It allows, after a core-excitation, the selective probing of specific electronic states in a material.

The photon energy was tuned around the absorption edge of the atom (carbon or nitrogen) of interest, allowing a refined understanding of the influence of the environment on electronic structures.<sup>30</sup> As expected in such experiments, electron emission was enhanced at specific photon energies, because of the population of certain levels (molecular orbitals). Thus, it is also a method to follow the different de-excitations paths possible (see chapter 1 section 1.2.1.) following a core-excitation below the ionization threshold. In the following section, we present the 2D resonant Auger maps and the high-resolution Resonant Auger Spectra (RAS), only in liquid phase, to understand the element specific contribution to specific molecular orbitals.<sup>31</sup>

### 5.5.1. Enhancement at the Carbon edge

The 2D resonant maps shows the intensity of electron spectra recorded at different photon energies (286 eV to 295 eV with a step of 0.2 eV) as a function of electron kinetic energy (230 eV to 290 eV with step a 0.2 eV). The partial electron yield near the carbon edge (grey curve superimposed on the right side of the 2D map in figure 5.9 a, upper panel) was extracted from the map by summing over the kinetic energy window<sup>32</sup> and at each photon energy the total number of electrons detected. A broad peak around 288.8 eV was observed for *solvated Gly* (labelled as 'A' in figure 5.9 a, upper panel) due to resonance enhancement. This peak can be attributed to the  $C\ 1s^{-1}\pi^*(COO)$  transition, as reported in the literature for the *solid state* C K-edge spectra for Gly and the *DFT calculation* spectra of zwitterionic form of Gly absorbed onto substrates (see table 5.3).<sup>7,33,34</sup> Another distinct feature reported in these studies was a broad peak (with low intensity) spread from 290 eV to 291 eV, which is related to a  $C\ 1s^{-1}\sigma^*(C-NH_3^+)$ , i.e. atom '2c' in figure 5.1a) transition, see table 5.3. This feature is also observed in our case, for *solvated Gly*, however, it is shifted a little towards higher photon energy, 291.0 eV (labelled as 'B' in figure 5.9 a, upper panel). This could probably be an effect of solvation, resulting in electronic transitions changes, or due to the difficulty to normalize by the photon flux (see below).

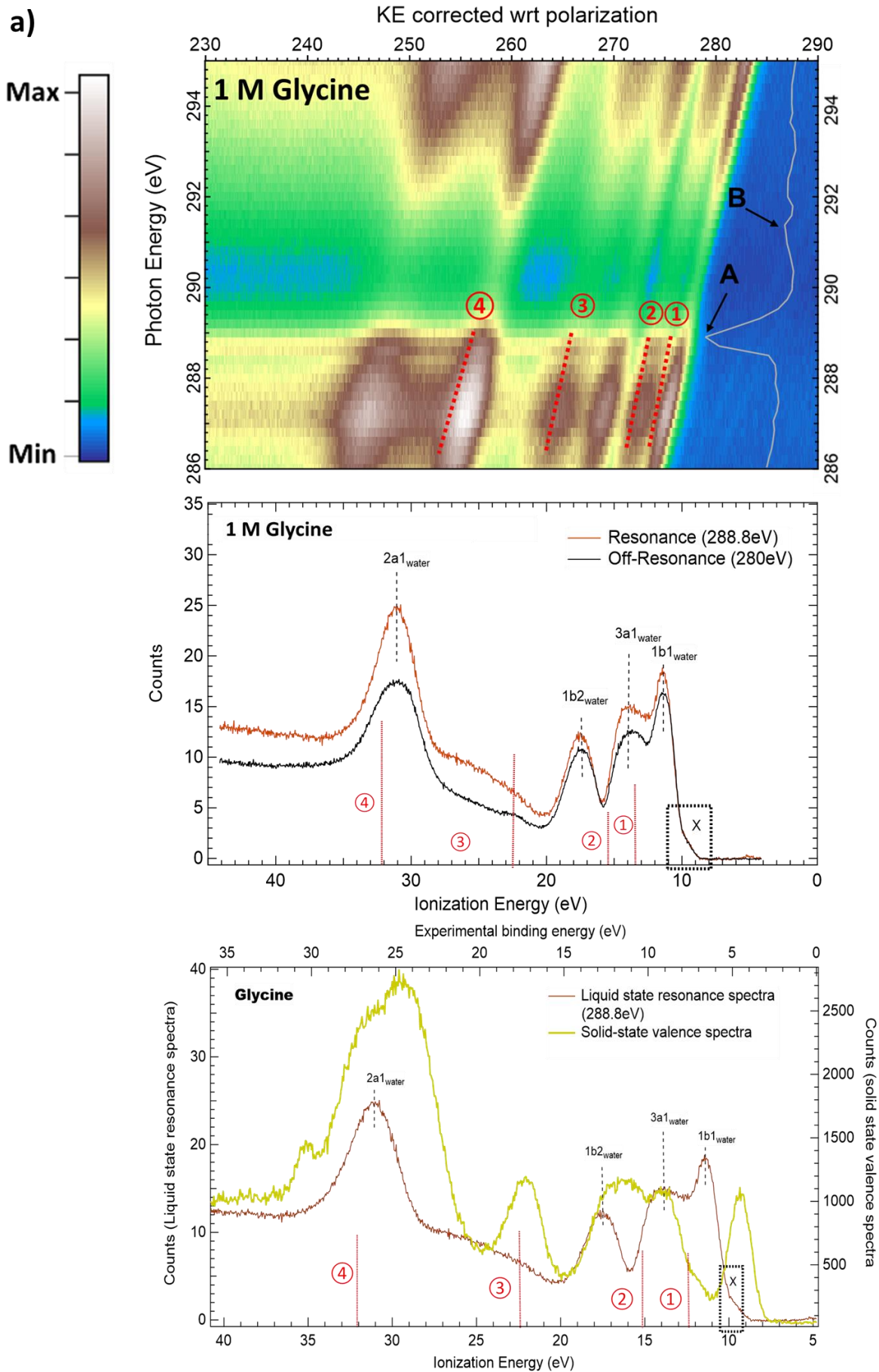
For *solvated Gly-Gly*, a similar 2D resonant map was recorded (see figure 5.9 b, upper panel). The partial electron yield near the carbon edge was extracted from the map (as explained for Gly) and is shown by a grey curve on the map (figure 5.9 b, upper panel), where a significant peak, at 288.3 eV, was observed due to the resonance enhancement. Upon comparison with the reported data for *solid state* Gly-Gly, this peak can be attributed to the carbon atom involved in the peptide bond (labelled '3c' in figure 5.1 b), with a  $C 1s^{-1}\pi^*(CONH)$  transition (see table 5.3).<sup>33,34</sup> This peak is also reported in the solid state C K-edge spectra of other amino acids with an amide group, like glutamine, indicating a signature of the peptide bond.<sup>33</sup>

It is important to note that the intensities of the partial electron yield spectra must be taken with caution. In this region of photon energies, due to carbon contamination of the different beamline optics and photodiodes, the measurement of an accurate photon flux is complex. Our methodology is detailed in section 2.4.5.4. of chapter 2.

**Table 5.3:** Summary of characteristic features observed in the partial electron yield NEXAFS-like spectrum, for 1 M Gly and 1 M Gly-Gly aqueous solutions, at the carbon K-edge. Reference data reported in the table is for Gly and Gly-Gly in solid state or using DFT calculations for their zwitterionic form.

	Carbon K-edge			
	Current work ( <i>solvated</i> )		Reference: <i>solid state</i> experiments and <i>zwitterionic</i> DFT calculations	
<b>1M Gly</b>	288.8 eV	$C1s^{-1}\pi^*$ (COO)	288.6 eV <sup>33</sup> 288.7 eV <sup>34</sup> 288.8 eV <sup>7</sup>	$\pi^*$ (COO)/(COOH) $\pi^*$ (COO) Glycine zwitterion carbonyl
	291.0 eV	$C1s^{-1}\sigma^*$ (C-NH <sub>3</sub> <sup>+</sup> )	290.3 eV to 291 eV <sup>33</sup> 290.1 <sup>7</sup>	$\sigma^*$ (C-NH <sub>3</sub> <sup>+</sup> ) Glycine zwitterions
<b>1M Gly-Gly</b>	288.3 eV	$C1s^{-1}\pi^*$ (-CONH-)	288.3 eV <sup>33,34</sup>	$\pi^*$ (-CONH-)





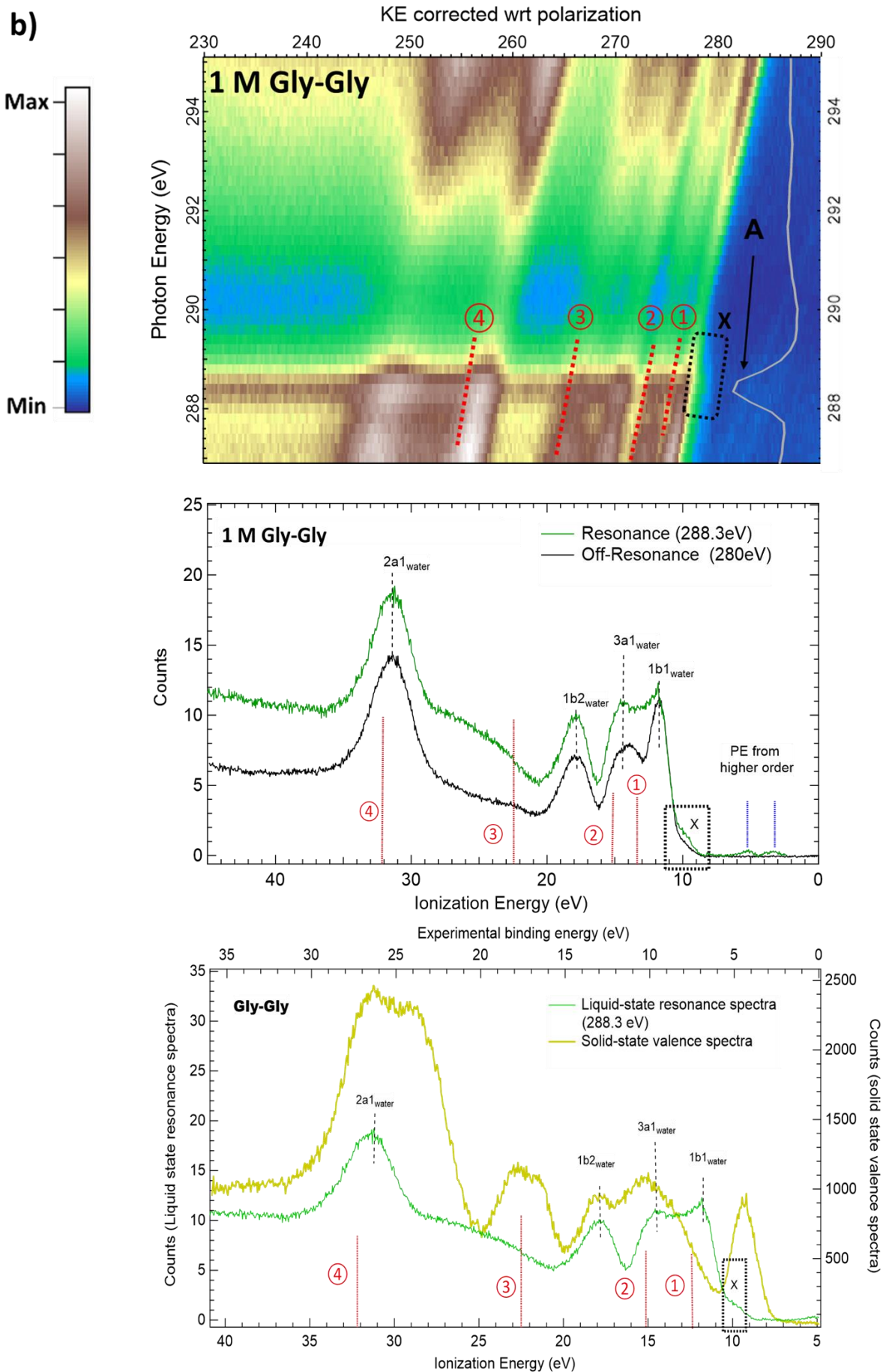


**Figure 5.9:** The resonant studies for a) Gly and b) Gly-Gly, at the carbon edge. For both a and b, the upper panel shows the 2D resonant absorption map along with partial electron yield NEXAFS-like spectrum, near the carbon edge. The middle panel shows the RAS spectra at the resonance and off-resonance (black curves). The lower panel shows the comparison between the solid-state valence spectrum (yellow curve) and the resonance spectra. The brown and green curves correspond to Gly and Gly-Gly, respectively. The maps were recorded at a bias of -50 V and the RAS spectra were recorded at a bias of -100 V, to eliminate the contribution from the gas phase around the cylindrical liquid jet. The vertical blue bars in the RAS spectra of Gly-Gly indicate photoelectrons generated by the higher order light. The red dotted bars correspond in maps and in spectra to specific regions detailed in the text. The binding energy values in solid-state spectra are referenced with respect to the Fermi level of gold. The energy scaling (x axis) factor in solid and liquid spectra corresponds to the work function of the sample (4.8 eV for Gly and 4.9 eV for Gly-Gly).

As a next step, to identify the specific molecular orbitals populated during de-excitation, a high-resolution RAS spectrum was recorded at the top of the resonance (288.8 eV for Gly and 288.3 eV for Gly-Gly) and at an energy significantly below the resonant peak, called off-resonance spectrum, at 280 eV (see figures 5.9 a and b, middle panel). In the RAS spectra, various regions are labelled according to the discussion in the previous section for DOS curves (X, ①, ②, ③ and ④).

For *solvate Gly-Gly*, a significant increase in the spectral peaks was observed along with the emergence of new features (see figure 5.9 b, middle panel). The lowest resonant band (labelled 'X') corresponds to the HOMO of the Gly-Gly, as in this region, only small overlap with the 1b<sub>1</sub> of water exists, it is mainly the ground electronic state of the Gly-Gly that is populated via participator Auger process. This feature corresponds to that discussed in the previous sections (see band B in figure 5.5 a and region X in figure 5.6). For the solvated Gly the same C1s<sup>-1</sup> π\* excitation does not give rise to an enhancement of the region 'X'. Either the geometry of the excited electronic state and the final state are different or it could also be due to same symmetry character of MOs between those two states (both π) that will decrease the transition probability. However, this doesn't seem to be the case for either of the solutions (Gly and Gly-Gly) as the X state has more sigma type symmetry (see appendix III.III).

The 1b1 state of water is almost insensitive to the resonant processes at this energy photon energy. Around the 3a1 state of water, region ①, the intensity increases, along with a difference in the shape. An increase in the intensity of the 1b2 state of water (region ②) is also observed. Since electronic states of Gly-Gly and water are overlapping in region ②, the interpretation is less trivial than at region X. As a 1s electron from carbon atom is excited, we could preferentially think of the involvement of Gly-Gly final electronic states in the modifications of region ① (as can be seen in figure 5.9, lower panel). However, it is not impossible at this stage to rule out completely an effect of two-center resonant photoionization,<sup>35,36</sup> i.e. resonant ICD, between the Gly-Gly and the water molecules. Even so, the DOS calculation seems to favour resonant ICD, as mainly in this region, a very low contribution of pure Gly-Gly is involved. Nevertheless, Gly-Gly still has some electronic states in this region as can be seen by its comparison with the solid state valence spectra (see figure 5.9 b, lower panel). This forbids us to conclude the de-excitation mechanism leading to this intensity enhancement.

The regions ① and ② for Gly have a different behaviour. Contrary to Gly-Gly, each electronic states of water (1b1, 3a1 and 1b2) seem to have an equivalent increase in intensity, perhaps with a slight distortion between the 1b1 and the 3a1 bands (less marked than for Gly-Gly). Either all the final states are equally populated via the resonant process, or it could be an artefact due to the photon flux normalization. However, like in the RAS spectra of Gly-Gly, the intensity dip between the water bands, 1b1 and 3a1, could be due to the presence of the electronic states of Gly that could resonate. This can be seen by comparing the resonance liquid state spectra with the solid state valence spectra of Gly (see figure 5.9 a, lower panel). The normalization with respect to the 1b1 band further confirmed that there exists a difference in the shape between the resonant and off-resonant spectra (see figure 5.10).

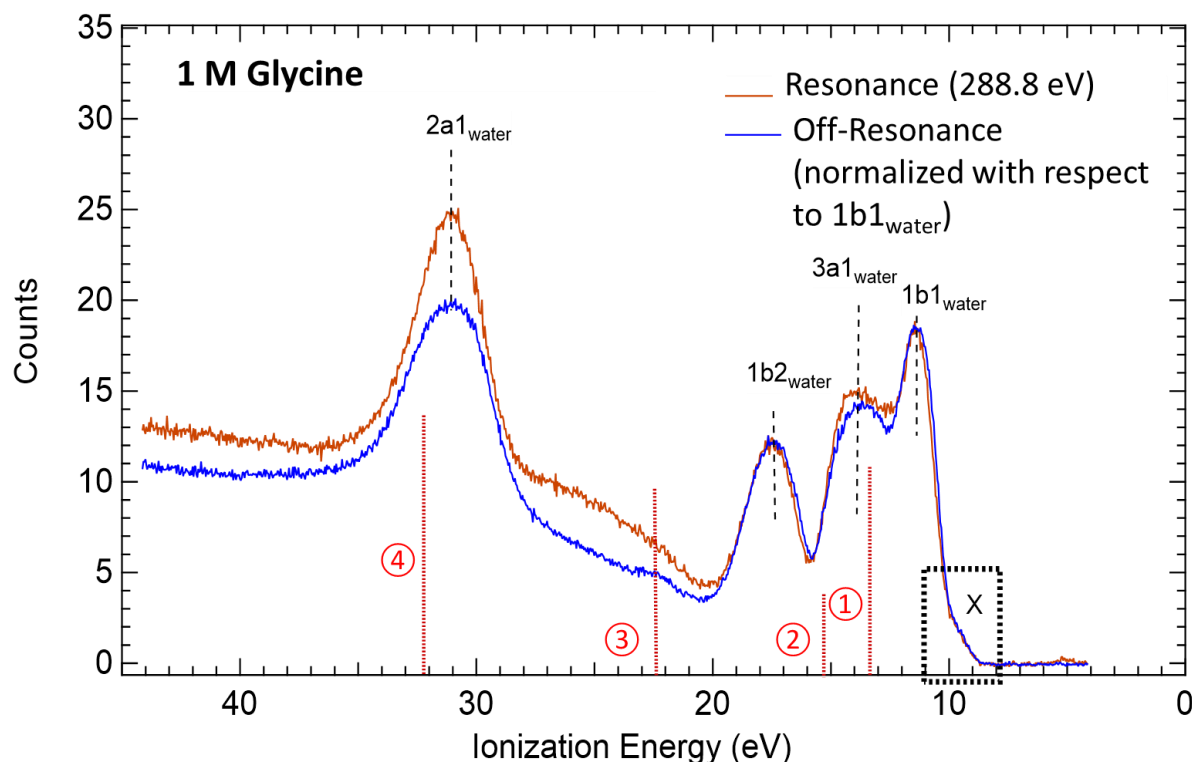


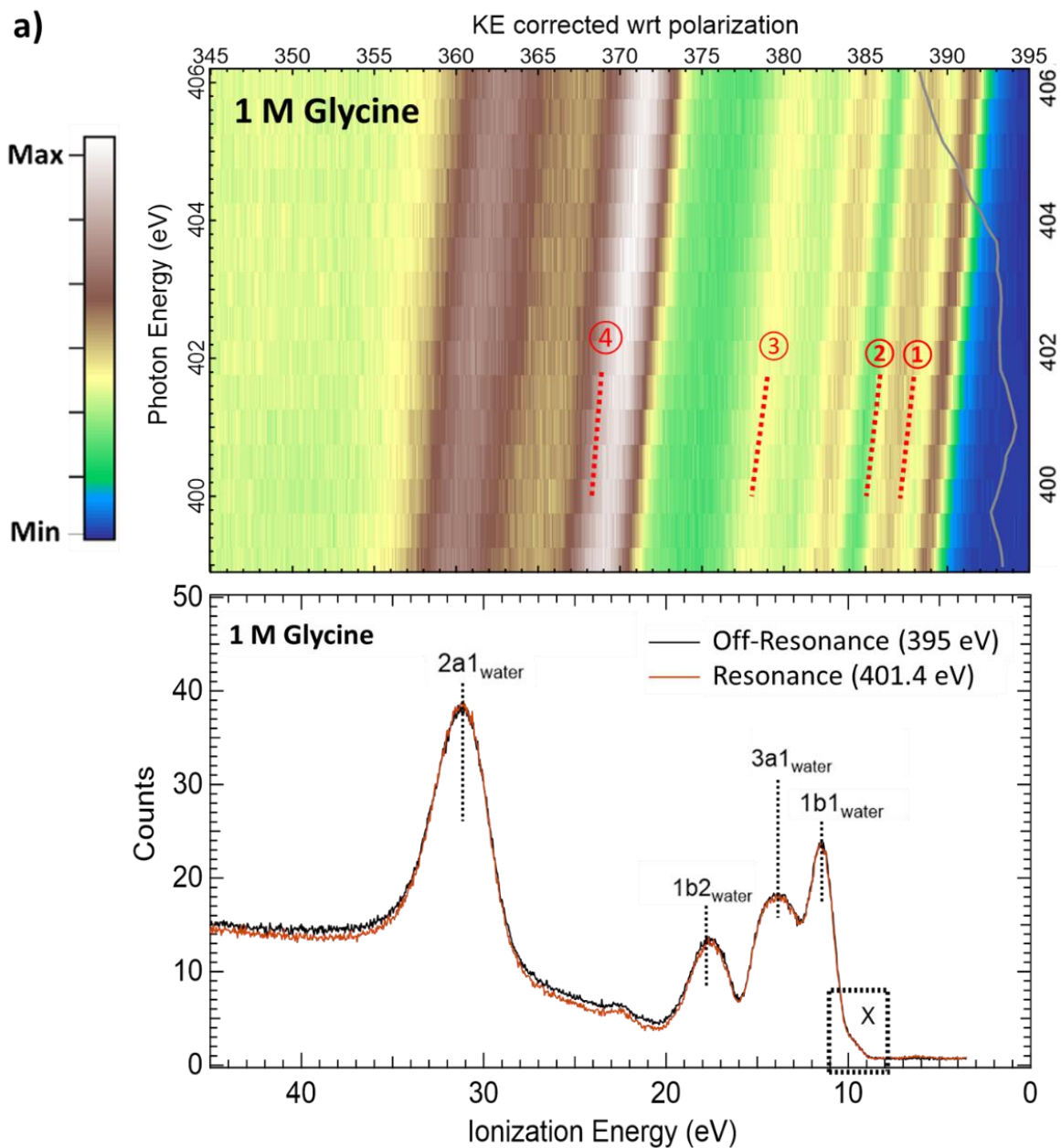
**Figure 5.10:** The RAS spectra of 1 M Gly at the resonance and off-resonance normalized with respect to the 1b1 state of water, to visualize the difference in the shape of the spectrum due to the resonance enhancement. The spectra were recorded at a bias of -100 V, to eliminate the contribution from the gas phase around the cylindrical liquid jet.

Region ③ (around 25 eV) and region ④ (at 32 eV) were also enhanced at the resonant energy for both Gly and Gly-Gly. On comparison with the DOS curve and the electron density distribution (see figure 5.6 and figure 5.8), these regions have a contribution from the MOs of the solute.

For *solvated Gly-Gly*, as it can be seen on the 2D map (figure 5.9 b, upper panel), a continuous horizontal thick line around 288.3 eV is suggesting an overall increase in intensity of photoelectron spectra, which was not very evident in *solvated Gly*. It is probably due to an increase of secondary electrons production due to the resonance processes involved in regions 'X' and above. Over this background, probably contributions of resonating spectators' states of the Gly-Gly are also present.

### 5.5.2. Enhancement at the Nitrogen edge

For *solvated Gly and Gly-Gly*, the 2D resonant absorption maps were also recorded, around the nitrogen edge, between 399 eV and 406 eV (steps of 0.2 eV), as a function of electron kinetic energy from 335 eV to 395 eV (steps of 0.2 eV). The partial electron yield NEXAFS-like spectrum had no resonant enhancement for Gly (grey curve in figure 5.11 a, upper panel), whereas weak resonant peaks centred at 399.6 eV (labelled 'A' in figure 5.11 b, upper panel) and 401.4 eV (labelled 'B' in figure 5.11 b, upper panel) for Gly-Gly are present. The peak **A** and **B** can be attributed to the chemical group imine ( $N 1s^{-1}\pi^*$  H-N-CH<sub>2</sub>) and peptide (O=C-N-H), respectively, upon comparison with the reported *DFT calculations*<sup>7</sup> (see table 5.4). These peaks appear due to the changes in the electronic structures around the nitrogen involved in the peptide bond, which explains their absence in Gly. The appearance of peak **B** is also reported using N K edge X-ray absorption spectra studies for *solid state* Gly-Gly and *liquid state* Gly-Gly (using the resonant inelastic scattering), where it was attributed to a  $N 1s^{-1}\pi^*$ <sub>peptide</sub> transition (see table 5.4).<sup>7,9,12</sup>



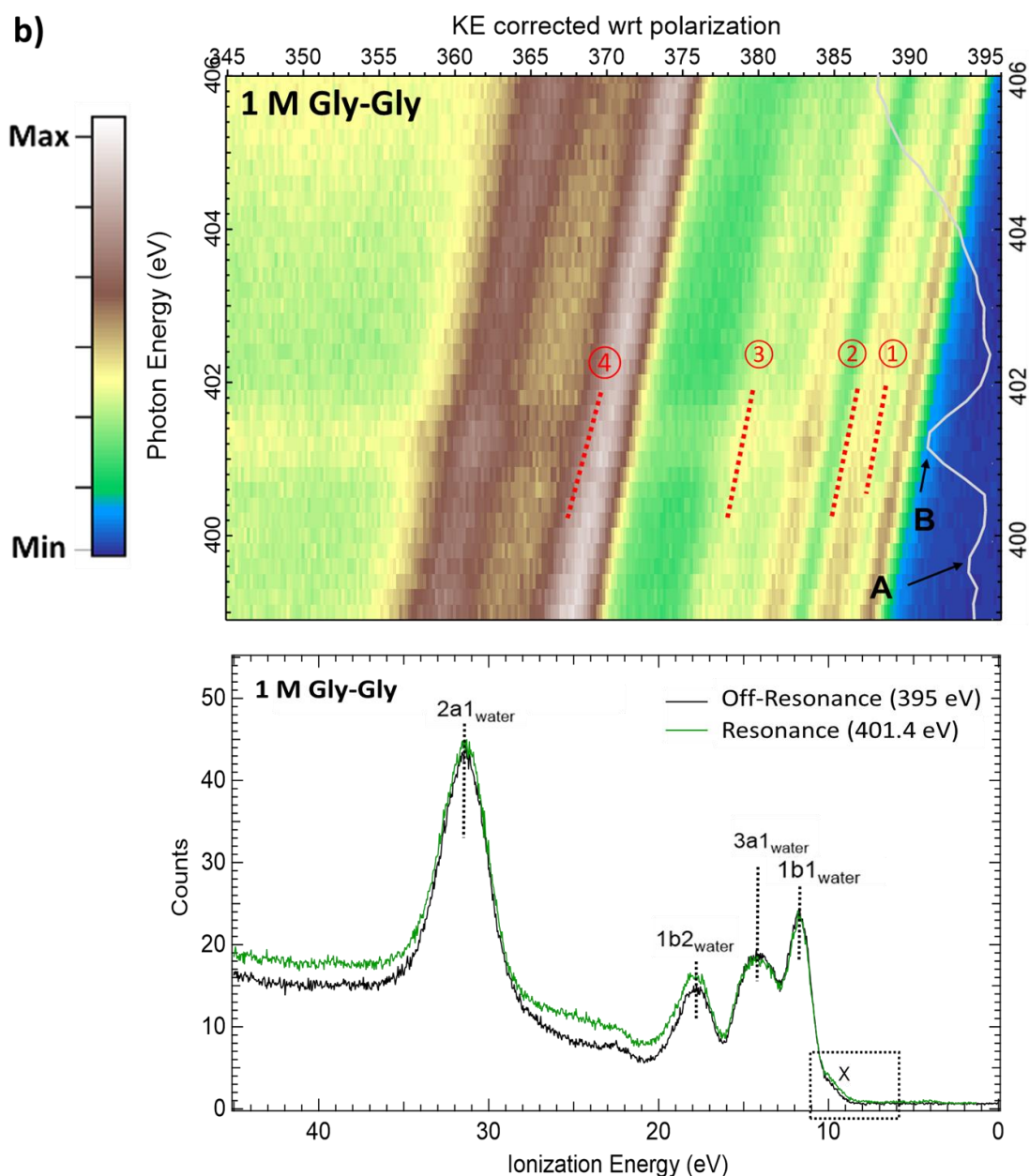


**Figure 5.11:** The resonant studies for a) Gly and b) Gly-Gly, at the nitrogen edge. For both a and b, the upper panel shows the 2D resonant absorption map along with partial electron yield NEXAFS-like spectrum, near the nitrogen edge. The lower panel shows the RAS spectra at the resonance energy and off-resonance (black curves). The Gly RAS spectra were recorded at the same resonance energy as Gly-Gly, as no resonance is observed in the 2D map of Gly. The brown and green curves correspond to Gly and Gly-Gly, respectively. The maps were recorded at a bias of -50 V and the RAS spectra were recorded at a bias of -100 V, to eliminate the contribution from the gas phase around the cylindrical liquid jet. It should be noted that the quality of normalization by the photon flux was much better than in the case of carbon, as the flux determination is more precise at the N edge.



Similar to the carbon edge study, high-resolution RAS spectrum were recorded at the top of the resonance (401.4 eV) as well as off resonance (395 eV) to identify the specific molecular orbitals populated during the resonant enhancement. The 2D maps did not show any resonance for Gly, however, in order to confirm this, the RAS map of *solvated Gly* (see figure 5.11 a, lower panel) was recorded at the energy where the Gly-Gly resonates and the energy below the resonance. The difference between the two spectra was negligible. The slight distortion of the signal between the two spectra, however, is due to the small remaining gas phase around the liquid jet. For *solvated Gly-Gly* (see figure 5.11 b, lower panel), an increase in the intensity of the 1b2 peak of water is visible, whereas the intensities of the lower energy states remain unchanged via the resonant process, excepted for a weak enhancement of the HOMO state. This could confirm the peptide character of the MO in the region X. Concerning the region ②, as the orbitals are delocalised between the waters molecules and the Gly-Gly, deciphering the causes of intensity increase is not trivial. Spectator Auger decays for the regions ③ and ④ could occur as probable de-excitation pathways in *solvated Gly-Gly* (see figure 5.11 b, lower panel). However, as these electronics states intensities are also affected by the increase of secondary background (see the faint horizontal line around 401.4 eV in the figure 5.11 b, upper panel) it is also difficult to conclude.

**Table 5.4:** Summary of characteristic features observed in the partial electron yield NEXAFS-like spectrum, for aqueous solutions of 1 M Gly-Gly, at the nitrogen K-edge. Reference data reported in the table is for Gly-Gly in solid state or using DFT calculations for its zwitterionic form. There is no characteristic feature observed for Gly.

	Nitrogen K-edge			
	Current work ( <i>solvated</i> )		Reference: <i>solid state</i> experiments and <i>zwitterionic DFT</i> calculations	
<b>1M Gly-Gly</b>	399.6 eV	C1s <sup>-1</sup> π* (H-N-CH <sub>2</sub> )	399.5 eV <sup>7</sup>	π* transition [imine (NHCH <sub>2</sub> )]
	401.4 eV	N1s <sup>-1</sup> π* (CONH-)	401.3 eV <sup>7</sup> 401.3 eV <sup>12,9</sup>	peptide (O=C-N-H) π* <sub>CONH</sub>

To summarize, resonant effects are more pronounced in the case of carbon excitation. In the case of carbon, the resonant Auger spectra display some enhancement in the intensity for the different valence water bands, in addition to some enhancements specific to the solute.

However, for region ①, the DOS seems to favor the resonant ICD de-excitation pathway, as the molecular orbitals are delocalized only on water.

The DOS calculation in region ② indicates the involvement of the molecular orbital from both water and the solute (Gly and Gly-Gly) for some electronic states. It suggests that in these cases the solute is not present as a “separate” entity but is strongly influenced by the surrounding water molecules, and it can therefore be considered as a supermolecule, where the electronic cloud around the solute rearranges itself as an effect of its surrounding. This effect can be further studied by measuring the band gap of the solute, with and without the solvent water molecules.

Additionally, for region ③ and ④, the de-excitation process favors the conventional participator Auger decay. However, in these regions, the effect of the presence of the secondary electron contribution complicates the interpretation.

### **5.6. Electronic structures of Gly and Gly-Gly**

Here, we present the energy diagram for both the samples (Gly and Gly-Gly) in the solid and liquid phase (figure 5.12 a and 5.12 b), highlighting their energy states and their fundamental properties.

The band gap (energy difference between HOMO and LUMO) of the sample depends on its atomic and electronic properties and is known to be affected by solvation.<sup>37</sup> The greater the interaction between the solvent and the solute, the greater is the effect on the band gap.

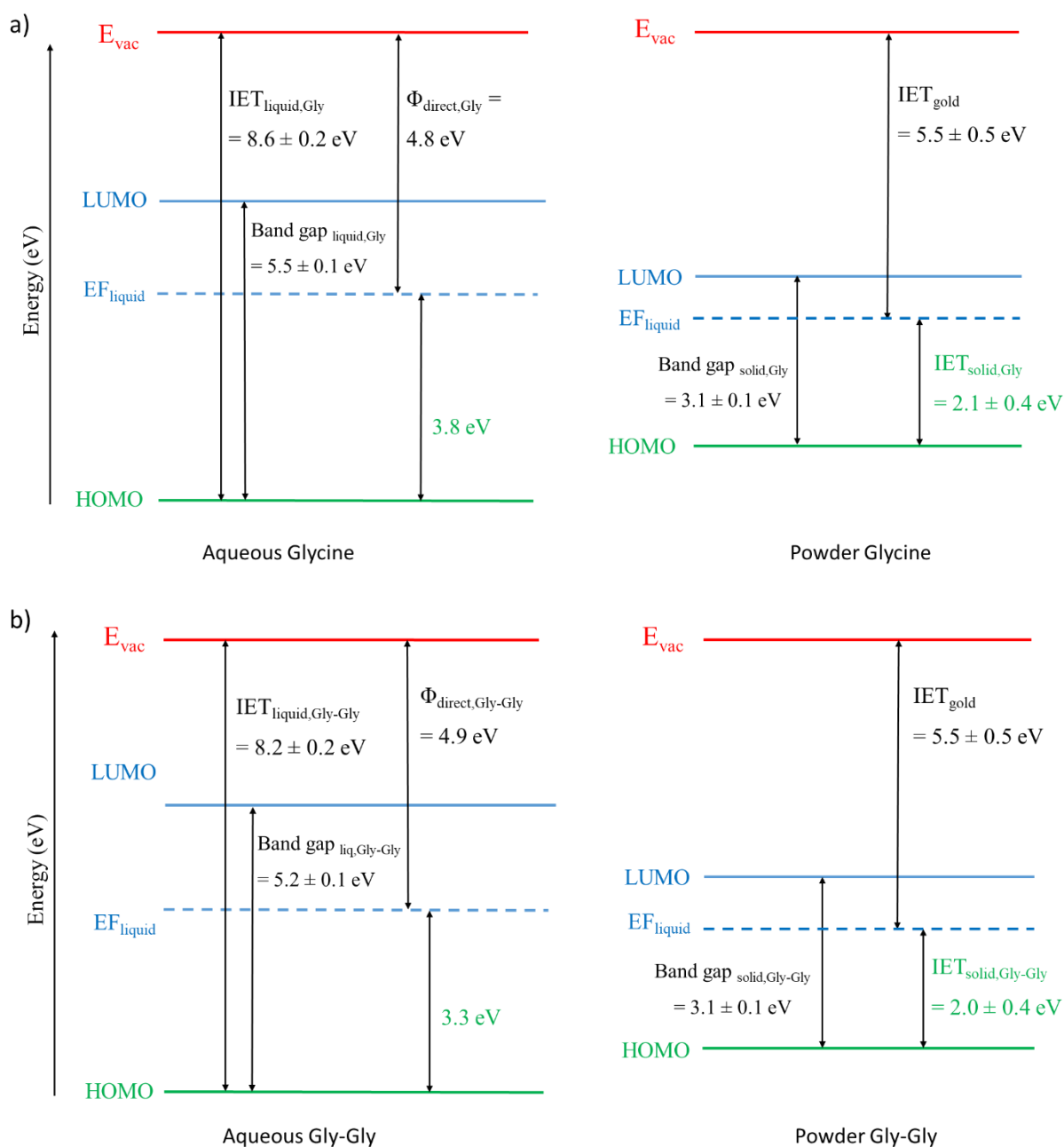


**Figure 5.12:** Schematic band structure of liquid phase (left) and solid phase (right) a) Gly and b) Gly-Gly. Both Gly and Gly-Gly behave as n type semiconductors, having electrons close to the LUMO (conduction band) and hence can be easily excited to LUMO.

The band gaps were measured using the Tauc plot, as explained in section 2.4.4.3 of chapter 2. For both Gly and Gly-Gly in the solid state, the band gap was found to be  $3.1 \pm 0.1 \text{ eV}$  (see figure 5.13 a and b). The samples are considered as semiconductors in their crystalline form. Literature studies indicate that the band gap of Gly crystal can vary to a large extent, depending upon the pressure and temperature conditions.<sup>38,39</sup>

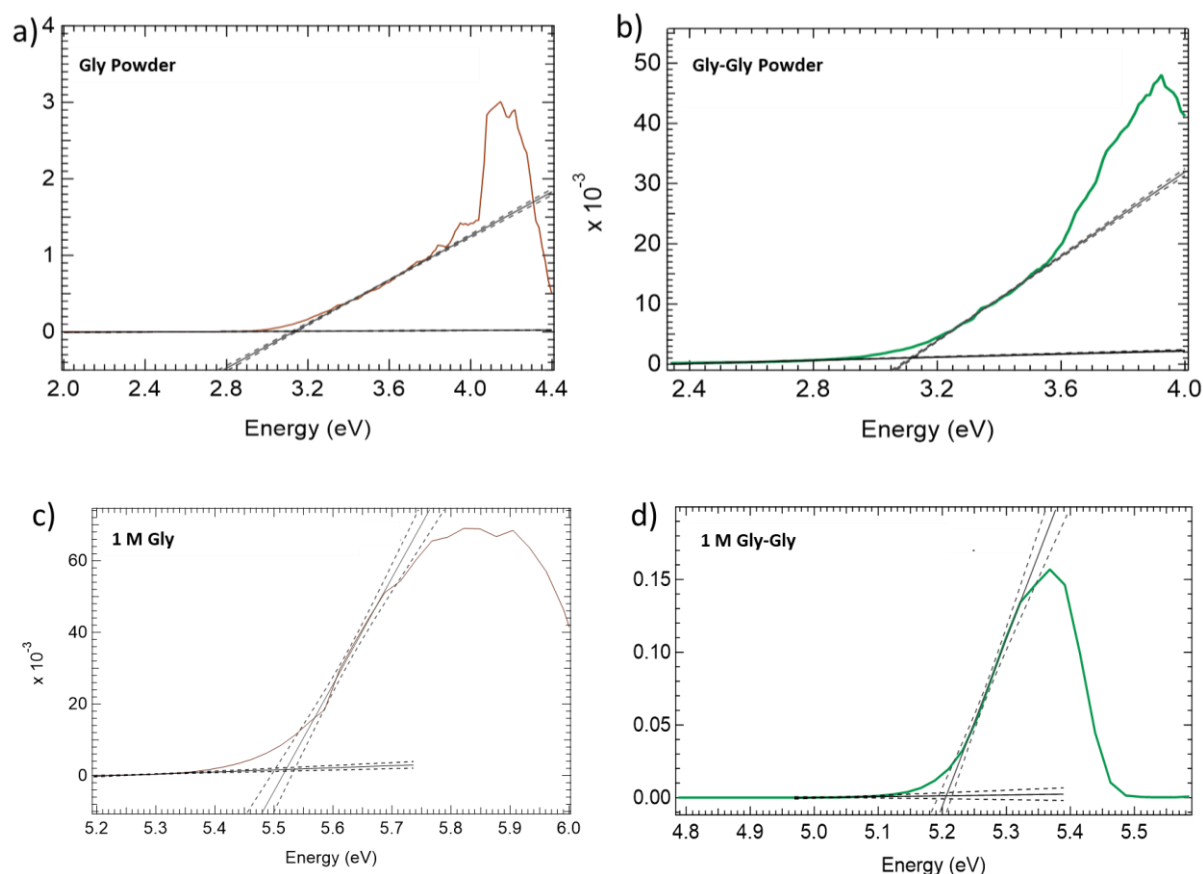


**Figure 5.13:** Band gap determination for Gly and Gly-Gly in solid state (powder) (a and b) and in liquid state (c and d), using tauc plot. Gly is represented with brown curves and Gly-Gly is represented with green curves. The band gap is determined by the extrapolation of the slope, (solid black line) with 99% confidence bands (dotted black lines). The background of the curve (horizontal solid black lines) is shown with 99% confidence bands (horizontal dotted black lines). The plotted graphs are an average of three measurements each.

Upon hydration of the powdered sample, the band gap increased. The resulting band gaps of aqueous Gly and Gly-Gly were  $5.5 \pm 0.1$  eV and  $5.2 \pm 0.1$  eV, respectively (see figure 5.13 c and d). Since the measured band gap is above 4 eV,<sup>40</sup> the sample properties changed to an insulator.<sup>37</sup> This is an intermediate value when compared to water (7.0 eV)<sup>41</sup> and our solid state samples (Gly and Gly-Gly). The change in the band gap upon hydration suggests a mixing of the orbitals. This interpretation is consistent with the previous results of RAS studies.

We must also mention that our observation can be of interest in the radiation chemistry field. Indeed, it should also be pointed out that if the decay via resonant ICD is plausible, (as was seen in our DOS calculations where the molecular orbitals was delocalized on the water molecules only), then in this case, the energy absorption by a solute (direct effect) can result

in solvent ionization (indirect effect). This pathway, however, is not evident in the resonance studies of the solutions.

### 5.7. Conclusion

The work presented an extensive spectroscopic study of the simplest amino acid (Gly) and the simplest dipeptide (Gly-Gly) using experimental as well as theoretical techniques. Experimentally, the liquid XPS spectra of Gly and Gly-Gly were recorded in liquid jet configuration. The solvation of the Gly-Gly seems to have more effect on the core energy levels of nitrogen than the carbon ones. The spectral peaks were shifted in energy, in comparison to the solid XPS spectra, for both samples. This shift was attributed to the work function of the aqueous sample, which was also measured using the SECO spectra. The work function was found to be  $(4.8 \pm 0.1 \text{ eV})$  and  $(4.9 \pm 0.2 \text{ eV})$  for Gly and Gly-Gly, respectively. The valence band spectra allowed to measure the photoionization threshold of solvated Gly ( $8.6 \pm 0.2 \text{ eV}$ ) and solvated Gly-Gly ( $8.2 \pm 0.2 \text{ eV}$ ). Using UV-vis spectroscopy, the band gaps of Gly and Gly-Gly were measured, in the liquid state as well as solid state. The Fermi level for the sample was close to the LUMO, behaving as n-type semiconductor. The band gap increased upon hydration, which tends to drift the electronic properties away from the semiconductor towards an insulator, for both solvated Gly and solvated Gly-Gly. This increase can be attributed to orbital mixing between the solvent water molecules and the solute (solid state sample). This interpretation was also supported by the results obtained using the resonance studies at the carbon and nitrogen K-edges. It was observed that the resonant variation at the carbon K-edge was more prominent than at the nitrogen K-edge.

Theoretically, the interpretation about the orbital mixing was supported by the DOS calculations using the AIMD simulation, where some of the Kohn-Sham orbitals of aqueous Gly and aqueous Gly-Gly had electron density contributions from both water and the solute. For the others, the electron density was either centered only around the solute (conventional participator/spectator Auger decays) or the solvent molecules (resonant ICD). Owing to the difference in the concentration of the solutes in the simulations and experiments (concentration is lower in simulations), it could underestimate the contribution of the DOS of the solutes, making difficult to segregate the different de-excitation pathways (resonant ICD involving water or conventional participator Auger decay) and thus the interpretation of the Auger spectra in general.

## References

- (1) Baltoumas, F. A.; Zafeiropoulou, S.; Karatzas, E.; Koutrouli, M.; Thanati, F.; Voutsadaki, K.; Gkonta, M.; Hotova, J.; Kasionis, I.; Hatzis, P.; Pavlopoulos, G. A. Biomolecule and Bioentity Interaction Databases in Systems Biology: A Comprehensive Review. *Biomolecules* **2021**, *11* (8), 1245. <https://doi.org/10.3390/biom11081245>.
- (2) Reisz, J. A.; Bansal, N.; Qian, J.; Zhao, W.; Furdui, C. M. Effects of Ionizing Radiation on Biological Molecules—Mechanisms of Damage and Emerging Methods of Detection. *Antioxid Redox Signal* **2014**, *21* (2), 260–292. <https://doi.org/10.1089/ars.2013.5489>.
- (3) Siegbahn, H. Electron Spectroscopy for Chemical Analysis of Liquids and Solutions. *J. Phys. Chem.* **1985**, *89* (6), 897–909. <https://doi.org/10.1021/j100252a005>.
- (4) Schwartz, C. P.; Saykally, R. J.; Prendergast, D. An Analysis of the NEXAFS Spectra of a Molecular Crystal:  $\alpha$ -Glycine. *The Journal of Chemical Physics* **2010**, *133* (4), 044507. <https://doi.org/10.1063/1.3462243>.
- (5) Plekan, O.; Feyer, V.; Richter, R.; Coreno, M.; de Simone, M.; Prince, K. C.; Carravetta, V. Investigation of the Amino Acids Glycine, Proline, and Methionine by Photoemission Spectroscopy. *J. Phys. Chem. A* **2007**, *111* (43), 10998–11005. <https://doi.org/10.1021/jp075384v>.
- (6) Chatterjee, A.; Zhao, L.; Zhang, L.; Pradhan, D.; Zhou, X.; Leung, K. T. Core-Level Electronic Structure of Solid-Phase Glycine, Glycyl-Glycine, Diglycyl-Glycine, and Polyglycine: X-Ray Photoemission Analysis and Hartree–Fock Calculations of Their Zwitterions. *J. Chem. Phys.* **2008**, *129* (10), 105104. <https://doi.org/10.1063/1.2976151>.
- (7) Wilks, R. G.; MacNaughton, J. B.; Kraatz, H.-B.; Regier, T.; Blyth, R. I. R.; Moewes, A. Comparative Theoretical and Experimental Study of the Radiation-Induced Decomposition of Glycine. *J. Phys. Chem. A* **2009**, *113* (18), 5360–5366. <https://doi.org/10.1021/jp900794v>.
- (8) Bolch, W. E.; Turner, J. E.; Yoshida, H.; Jacobson, K. B.; Hamm, R. N.; Crawford, O. H. Product Yields from Irradiated Glycylglycine in Oxygen-Free Solutions: Monte Carlo Simulations and Comparison with Experiments. *Radiat Environ Biophys* **1998**, *37* (3), 157–166. <https://doi.org/10.1007/s004110050111>.
- (9) Reinert, D. F.; Geurts, D. J. Eingereicht am: 18.08.2016 bei der Fakultät für Physik und Astronomie.
- (10) Gråsjö, J.; Andersson, E.; Forsberg, J.; Duda, L.; Henke, E.; Pokapanich, W.; Björneholm, O.; Andersson, J.; Pietzsch, A.; Hennies, F.; Rubensson, J.-E. Local Electronic Structure of Functional Groups in Glycine As Anion, Zwitterion, and Cation in Aqueous Solution. *J. Phys. Chem. B* **2009**, *113* (49), 16002–16006. <https://doi.org/10.1021/jp905998x>.
- (11) Ottosson, N.; Børve, K. J.; Spångberg, D.; Bergersen, H.; Sæthre, L. J.; Faubel, M.; Pokapanich, W.; Öhrwall, G.; Björneholm, O.; Winter, B. On the Origins of Core–Electron Chemical Shifts of Small Biomolecules in Aqueous Solution: Insights from Photoemission and Ab Initio Calculations of Glycineaq. *J. Am. Chem. Soc.* **2011**, *133* (9), 3120–3130. <https://doi.org/10.1021/ja110321q>.
- (12) Messer, B. M.; Cappa, C. D.; Smith, J. D.; Drisdell, W. S.; Schwartz, C. P.; Cohen, R. C.; Saykally, R. J. Local Hydration Environments of Amino Acids and Dipeptides Studied by X-Ray Spectroscopy of Liquid Microjets. *J. Phys. Chem. B* **2005**, *109* (46), 21640–21646. <https://doi.org/10.1021/jp053802v>.

- (13) Scoppola, E.; Sodo, A.; McLain, S. E.; Ricci, M. A.; Bruni, F. Water-Peptide Site-Specific Interactions: A Structural Study on the Hydration of Glutathione. *Biophys J* **2014**, *106* (8), 1701–1709. <https://doi.org/10.1016/j.bpj.2014.01.046>.
- (14) Capitán, M. J.; Álvarez, J.; Navio, C. Study of the Electronic Structure of Electron Accepting Cyano-Films: TCNQ versus TCNE. *Phys. Chem. Chem. Phys.* **2018**, *20* (15), 10450–10459. <https://doi.org/10.1039/C7CP07963J>.
- (15) Greczynski, G.; Hultman, L. X-Ray Photoelectron Spectroscopy: Towards Reliable Binding Energy Referencing. *Progress in Materials Science* **2020**, *107*, 100591. <https://doi.org/10.1016/j.pmatsci.2019.100591>.
- (16) Greczynski, G.; Hultman, L. A Step-by-Step Guide to Perform x-Ray Photoelectron Spectroscopy. *Journal of Applied Physics* **2022**, *132* (1), 011101. <https://doi.org/10.1063/5.0086359>.
- (17) Ponzi, A.; Rosa, M.; Kladnik, G.; Unger, I.; Ciavardini, A.; Di Nardi, L.; Viola, E.; Nicolas, C.; Došlić, N.; Goldoni, A.; Lanzilotto, V. Inequivalent Solvation Effects on the N 1s Levels of Self-Associated Melamine Molecules in Aqueous Solution. *J Phys Chem B* **2023**, *127* (13), 3016–3025. <https://doi.org/10.1021/acs.jpcc.3c00327>.
- (18) Olivieri, G.; Goel, A.; Kleibert, A.; Cvetko, D.; Brown, M. A. Quantitative Ionization Energies and Work Functions of Aqueous Solutions. *Phys. Chem. Chem. Phys.* **2016**, *18* (42), 29506–29515. <https://doi.org/10.1039/C6CP05682B>.
- (19) Renault, J.-P.; Huart, L.; Milosavljević, A. R.; Bozek, J. D.; Palaudoux, J.; Guigner, J.-M.; Marichal, L.; Leroy, J.; Wien, F.; Hervé Du Penhoat, M.-A.; Nicolas, C. Electronic Structure and Solvation Effects from Core and Valence Photoelectron Spectroscopy of Serum Albumin. *IJMS* **2022**, *23* (15), 8227. <https://doi.org/10.3390/ijms23158227>.
- (20) Pérez Ramírez, L.; Boucly, A.; Saudrais, F.; Bournel, F.; Gallet, J.-J.; Maisonhaute, E.; Milosavljević, A. R.; Nicolas, C.; Rochet, F. The Fermi Level as an Energy Reference in Liquid Jet X-Ray Photoelectron Spectroscopy Studies of Aqueous Solutions. *Phys. Chem. Chem. Phys.* **2021**, *23* (30), 16224–16233. <https://doi.org/10.1039/D1CP01511G>.
- (21) Clark, D. T.; Peeling, J.; Colling, L. An Experimental and Theoretical Investigation of the Core Level Spectra of a Series of Amino Acids, Dipeptides and Polypeptides. *Biochimica et Biophysica Acta (BBA) - Protein Structure* **1976**, *453* (2), 533–545. [https://doi.org/10.1016/0005-2795\(76\)90149-5](https://doi.org/10.1016/0005-2795(76)90149-5).
- (22) Thürmer, S.; Malerz, S.; Trinter, F.; Hergenhan, U.; Lee, C.; Neumark, D. M.; Meijer, G.; Winter, B.; Wilkinson, I. Accurate Vertical Ionization Energy and Work Function Determinations of Liquid Water and Aqueous Solutions. *Chem. Sci.* **2021**, *12* (31), 10558–10582. <https://doi.org/10.1039/D1SC01908B>.
- (23) Cannington, P. H.; Ham, N. S. He(I) and He(II) Photoelectron Spectra of Glycine and Related Molecules. *Journal of Electron Spectroscopy and Related Phenomena* **1983**, *32* (2), 139–151. [https://doi.org/10.1016/0368-2048\(83\)85092-0](https://doi.org/10.1016/0368-2048(83)85092-0).
- (24) Debies, T. P.; Rabalais, J. W. Electronic Structure of Amino Acids and Ureas. *Journal of Electron Spectroscopy and Related Phenomena* **1974**, *3* (4), 315–322. [https://doi.org/10.1016/0368-2048\(74\)80083-6](https://doi.org/10.1016/0368-2048(74)80083-6).
- (25) Ge, L.; Bernasconi, L.; Hunt, P. Linking Electronic and Molecular Structure: Insight into Aqueous Chloride Solvation. *Phys. Chem. Chem. Phys.* **2013**, *15* (31), 13169–13183. <https://doi.org/10.1039/C3CP50652E>.
- (26) Vyalikh, D. V.; Maslyuk, V. V.; Blüher, A.; Kade, A.; Kummer, K.; Dedkov, Yu. S.; Bredow, T.; Mertig, I.; Mertig, M.; Molodtsov, S. L. Charge Transport in Proteins Probed by

- Resonant Photoemission. *Phys. Rev. Lett.* **2009**, *102* (9), 098101.  
<https://doi.org/10.1103/PhysRevLett.102.098101>.
- (27) Yang, Y. Structural and Dynamical Properties of Water Adsorption on PtO<sub>2</sub> (001). *RSC Advances* **2018**, *8*, 15078–15086. <https://doi.org/10.1039/C8RA00952J>.
- (28) Winter, B.; Weber, R.; Widdra, W.; Dittmar, M.; Faubel, M.; Hertel, I. V. Full Valence Band Photoemission from Liquid Water Using EUV Synchrotron Radiation. *J. Phys. Chem. A* **2004**, *108* (14), 2625–2632. <https://doi.org/10.1021/jp030263q>.
- (29) Ryan, J. A.; Whitten, J. L. Self-Consistent Field Studies of Glycine and Glycylglycine. Simplest Example of a Peptide Bond. *J. Am. Chem. Soc.* **1972**, *94* (7), 2396–2400. <https://doi.org/10.1021/ja00762a033>.
- (30) Miteva, T.; Kryzhevoi, N. V.; Sisourat, N.; Nicolas, C.; Pokapanich, W.; Saisopa, T.; Songsiriritthigul, P.; Rattanachai, Y.; Dreuw, A.; Wenzel, J.; Palaudoux, J.; Öhrwall, G.; Püttner, R.; Cederbaum, L. S.; Rueff, J.-P.; Céolin, D. The All-Seeing Eye of Resonant Auger Electron Spectroscopy: A Study on Aqueous Solution Using Tender X-Rays. *J. Phys. Chem. Lett.* **2018**, *9* (15), 4457–4462. <https://doi.org/10.1021/acs.jpcclett.8b01783>.
- (31) Fogarty, R. M.; Palgrave, R. G.; Bourne, R. A.; Handrup, K.; Villar-Garcia, I. J.; Payne, D. J.; Hunt, P. A.; Lovelock, K. R. J. Electron Spectroscopy of Ionic Liquids: Experimental Identification of Atomic Orbital Contributions to Valence Electronic Structure. *Phys. Chem. Chem. Phys.* **2019**, *21* (35), 18893–18910. <https://doi.org/10.1039/C9CP02200G>.
- (32) Silly, M. G.; Charra, F.; Lux, F.; Lemercier, G.; Sirotti, F. The Electronic Properties of Mixed Valence Hydrated Europium Chloride Thin Film. *Phys. Chem. Chem. Phys.* **2015**, *17* (28), 18403–18412. <https://doi.org/10.1039/C5CP01256B>.
- (33) Zubavichus, Y.; Shaporenko, A.; Grunze, M.; Zharnikov, M. Innershell Absorption Spectroscopy of Amino Acids at All Relevant Absorption Edges. *J. Phys. Chem. A* **2005**, *109* (32), 6998–7000. <https://doi.org/10.1021/jp0535846>.
- (34) Zubavichus, Y.; Zharnikov, M.; Schaporenko, A.; Grunze, M. NEXAFS Study of Glycine and Glycine-Based Oligopeptides. *Journal of Electron Spectroscopy and Related Phenomena* **2004**, *134* (1), 25–33. <https://doi.org/10.1016/j.elspec.2003.09.006>.
- (35) Trinter, F.; Williams, J. B.; Weller, M.; Waitz, M.; Pitzer, M.; Voigtsberger, J.; Schober, C.; Kastirke, G.; Müller, C.; Gohl, C.; Burzynski, P.; Wiegandt, F.; Wallauer, R.; Kalinin, A.; Schmidt, L. Ph. H.; Schöffler, M. S.; Chiang, Y.-C.; Gokhberg, K.; Jahnke, T.; Dörner, R. Vibrationally Resolved Decay Width of Interatomic Coulombic Decay in HeNe. *Phys. Rev. Lett.* **2013**, *111* (23), 233004. <https://doi.org/10.1103/PhysRevLett.111.233004>.
- (36) Hans, A.; Schmidt, P.; Ozga, C.; Richter, C.; Otto, H.; Holzapfel, X.; Hartmann, G.; Ehresmann, A.; Hergenhan, U.; Knie, A. Efficient Fluorescence Quenching by Distant Production of a Free Electron. *J. Phys. Chem. Lett.* **2019**, *10* (5), 1078–1082. <https://doi.org/10.1021/acs.jpcclett.9b00124>.
- (37) Ain, Q. T.; Al-Modlej, A.; Alshammari, A.; Anjum, M. N. Effect of Solvents on Optical Band Gap of Silicon-Doped Graphene Oxide. *Mater. Res. Express* **2018**, *5* (3), 035017. <https://doi.org/10.1088/2053-1591/aab239>.
- (38) N, Nithya; R, Mahalakshmi; S, Sagadevan, Growth, Optical, Thermal and Electrical Properties of Nonlinear Optical  $\alpha$ -Glycine Single Crystal. *Sci. Res. Essays* **2015**, *10* (13), 421–429. <https://doi.org/10.5897/SRE2015.6267>.
- (39) Mei, A.; Luo, X. The Structural, Electronic and Optical Properties of  $\gamma$ -Glycine under Pressure: A First Principles Study. *RSC Adv.* **2019**, *9* (7), 3877–3883. <https://doi.org/10.1039/C8RA08547A>.



- (40) Paschotta, D. R. *band gap*. [https://www.rp-photonics.com/band\\_gap.html](https://www.rp-photonics.com/band_gap.html) (accessed 2023-06-09).
- (41) Grand, D.; Bernas, A.; Amouyal, E. Photoionization of Aqueous Indole: Conduction Band Edge and Energy Gap in Liquid Water. *Chemical Physics* **1979**, *44* (1), 73–79. [https://doi.org/10.1016/0301-0104\(79\)80064-6](https://doi.org/10.1016/0301-0104(79)80064-6).



**CONTENTS CHAPTER 6**

---

**Chapter 6: Conclusion and perspective.....216**

**6.1. Conclusion .....217**

**6.2. Perspective .....220**

**References.....231**

## Chapter 6: Conclusion and perspective

### 6.1. Conclusion

The interaction of light and matter has been studied widely over the years; however, a lot is still unknown, especially regarding the poorly penetrating densely ionizing radiations. Soft X-rays belong to this category, and because of their poor penetration, their studies have remained limited. Therefore, my PhD research aimed to partially bridge this gap in the existing knowledge of light-matter interaction. The research project was particularly focused on studying the interaction of soft X-rays with, one, pure water and two, solvated biomolecules. This study was performed using, both, experimental and theoretical studies. The experimental studies were conducted using synchrotron soft X-rays (SOLEIL synchrotron, France) and the theoretical studies were performed using *ab-initio* molecular dynamics simulations.

1. *The first objective of the thesis was to study the interaction of soft X-rays with water along with the following questions:*

▪ *What is the effect of inner-shell ionization on water molecules upon soft X-ray irradiation?*

The effect of inner-shell ionization on water molecules was investigated by irradiating aqueous solutions with synchrotron soft X-rays at the METROLOGIE Beamline (SOLEIL synchrotron). The beam was extracted in air using the IRAD setup.<sup>1</sup> Our observations were focused on the formation of superoxide as a putative product of doubly ionized water molecule ( $\text{H}_2\text{O}^{2+}$ ). Our results were in agreement with the proposition Jay Gérin and Ferradini, of the superoxide radical ( $\text{HO}_2^\bullet/\text{O}_2^\bullet$ ) as a dominant product of the dissociation of  $\text{H}_2\text{O}^{2+}$ . **We suggested also that the percentage of the doubly ionized water molecules giving superoxide radicals is much higher for soft X-rays (that behave like high LET<sup>2</sup> ionization radiation) than in the case of heavy ions**, an effect that we tried to understand using AIMD simulations.<sup>3</sup>

▪ *How to measure the extremely low production yield of superoxide radicals in the soft X-ray ionization tracks?*

To measure the yield of superoxide radicals ( $\text{pK}_a = 4.8$ ), a chemical detection system comprising a chemical probe (300  $\mu\text{M}$  WST8) and enzymes (0.62  $\mu\text{M}$  SOD and 0.62  $\mu\text{M}$

Catalase) was developed and optimized through rigorous experiments, using a reference gamma source. Thanks to the development of an automated **highly sensitive in-line detection technique**, i.e. a microfluidic cell coupled to an in-line UV detection cell, we were successful in addressing the challenges posed by the poor penetration of soft X-rays and low radical yields of soft X-rays. In addition to overcoming the poor penetration, the microfluidic cell allowed **an accurate real-time alignment of the cell thanks to the installation of a SiPM behind the cell**. The **in-line UV cell**, on the other hand, allowed us to measure **absorbance values down to  $10^{-4}$ , thanks to a real-time base line correction**. Thereby, we were able to detect and quantify the extremely low yields of superoxide species produced via the direct pathway ( $O + {}^{\circ}OH \rightarrow HO_2^{\circ}$ ) and indirect pathway ( $O_2 + e_{aq}^- \rightarrow O_2^{\cdot-}$ ) in the soft X-ray ionization tracks. The results also revealed that the **yield of superoxide via the direct pathway ( $0.0053 \pm 0.0007 \mu\text{mol/J}$ ) was significantly lower (8 times) than that via the indirect pathway ( $0.07 \pm 0.02 \mu\text{mol/J}$ ), at 1620 eV**. However, owing to the low photon flux, direct yield measurements were performed only at the photon energy (1620 eV) corresponding to the maximum flux. It would be very interesting to measure the direct yield of superoxide before and after the O-K edge. The perspective part, hereafter proposes strategies to this purpose. Taking advantage of the higher indirect superoxide yields (compared to direct superoxide yields), measurements were performed as a function of photon energy. Below 700 eV, the beam had contribution from higher order light (because the beamline's higher order rejection devices were not used in order to maximize the dose), which led to large uncertainties. **The indirect superoxide yields exhibited a strong dependence on the photon energy, particularly around 1280 eV, where the photo- and Auger electrons tracks overlap the most.**

- *What are the reaction pathways of doubly ionized water in soft X-ray tracks?*

AIMD simulations (shown in chapter 4) were performed to monitor the early stage dissociation of  $H_2O^{2+}$  in the proximity of  ${}^{\circ}OH$  and thereby to follow the reaction of the dissociation products with its surrounding for one picosecond. The results provided valuable insights on the formation of superoxide. It suggested that **the formation of  $HO_2^{\circ}$  was indeed quite complex as it occurred through a fast process, with hot atoms/ions involved. This formation was seen to occur via a one-step process or a two-step process** with the formation of intermediates ( $H_2O_2$  or its isomer, oxywater). **It was also pointed out that  ${}^{\circ}OH$  (and possibly its degree of**

**equilibration) played a crucial role in HO<sub>2</sub><sup>°</sup> formation**, reflecting that the equilibration state of °OH and its distribution in dense soft X-ray tracks controls the formation mechanism of HO<sub>2</sub><sup>°</sup>. It may explain the difference in superoxide production efficiency between soft X-ray and heavy ion irradiation.

It was shown also that °OH and O in the direct reaction pathway ( $O + °OH \rightarrow HO_2^\circ$ ) could originate from multiple sources (hydroxyl radical, solvent, and dissociating H<sub>2</sub>O<sup>2+</sup>). Owing to the different extent of the protons scrambling in the solvent, the formation time of HO<sub>2</sub><sup>°</sup> was seen to vary from 30 fs to 1 ps (the time at which the dynamics were stopped). The perspective part, hereafter proposes the use of time resolved experiments that could provide further information on the formation time of HO<sub>2</sub><sup>°</sup> and its potential intermediates.

2. The second objective of the thesis was to understand the interaction of soft X-rays with solvated biomolecules along with the following questions:

- *What is the interaction of soft X-rays with solvated biomolecules?*

The monitoring of these ultrafast processes, i.e. the direct interaction of the solutes with the soft X-ray photons, was possible using state-of-the-art liquid microjet X-ray photoelectron spectroscopy (XPS), at the PLEIADES beamline (SOLEIL synchrotron), along with complementary analysis using AIMD simulations. The biomolecule studied was a dipeptide, Glycylglycine (Gly-Gly), which is a model system to investigate the peptide bond that is present in all proteins. The amino acid, Glycine (Gly), was used as a reference system. The thesis focused on revealing the effects of solvation around the K-edge of nitrogen and carbon. These effects were observed by comparing the differences between the core-level spectra of the sample in the solid and the solvated phases. **It was concluded that the solvation of the Gly-Gly had more pronounced effects on the core energy levels of nitrogen than on those of carbon.** The valence spectra of solvated Gly-Gly and Gly had two bands in lower ionization energy range (7 eV to 12 eV), one of which overlapped with the 1b1 water band, at 11.63 eV, indicating that no chemical shift occurred in the 1b1 water band for either of the samples despite the high solutes concentration. The photon-ionization threshold of solvated Gly-Gly and Gly was found to be  $8.2 \pm 0.2$  eV and  $8.6 \pm 0.2$  eV, respectively. Further understanding on events occurring after the X-ray absorption, and the eventual fragmentation, were not

addressed using the liquid microjet XPS study. However, in the perspective part, we highlight the preliminary results of various experimental techniques and theoretical AIMD simulations performed to study the radiation-induced fragmentation.

- *How is the large amount of energy given to the biomolecules dissipated?*

Thanks to DOS calculations (using AIMD simulations) and resonance studies (RAS and NEXAFS), we were able to identify three different regions. In the first region, the electronic states were localized on the solute (conventional participator/spectator Auger decays). In the second region, the occupied states had contribution from both the solute and the solvent. In the third region, the electronic states were localized only on water (with a probability to lead to resonant ICD). **These results suggested that the solute was not present as a separate entity but was affected by its surrounding water molecules.** Nevertheless, it should be noted that the interpretation of the resonance effects in some regions could be difficult due to the secondary electron contribution and the overlapping electronic states from the water and the solute. The results of the resonance studies further indicated that the resonant variation at the carbon K-edge was more prominent than at the nitrogen K-edge. The band gap measurements (calculated using the Tauc plot) provided further **indication of orbital mixing of the solute and solvent** as the band gap value of the solvated Gly-Gly was found to be intermediate of pure water and the solid phase Gly-Gly. However, these analyses did not give a lot of information on the ultrafast structural re-organization. We propose the use of theoretical calculations, in the perspective part, to access this information.

Overall, the work presented in this PhD research demonstrated the significance of interdisciplinary approaches in addressing complex scientific questions. It emphasized on the importance of using advanced experimental and computational methods to gain a comprehensive understanding of chemical processes initiated by soft X-rays. The findings presented here contribute in expanding the existing knowledge in the field of radiation chemistry and hold the potential to impact diverse applications in medicine, biology, and materials science.

## 6.2. Perspective

1. *Our study of the interaction of soft X-rays with water raised new questions that we propose to address by the following strategies:*

- *Under vacuum experiments: how to measure yields at lower photon flux?*

The in-air soft X-ray irradiation experiments to measure the yield of direct  $\text{HO}_2^\circ$  were possible using the high sensitive in-line detection system. However, this yield was found to be very low and therefore, it hindered us from performing experiments at photon energies corresponding to lower photon flux. **We thereby propose to perform the measurements of such low yields by carrying out the soft X-ray irradiation experiments under vacuum, using the microfluidic cell**, as its compatibility for under vacuum irradiations has already been tested.<sup>2</sup> The advantage would be two-fold. First, the air gap between the exit window of the IRAD setup and the microfluidic cell window would be eliminated. Secondly, working under vacuum will eliminate the need of the exit window of the IRAD set-up. This would allow increasing the dose in the energy ranges, where the absorption of the X-ray beam in the air gap and the exit window is large.

- *XFEL time-resolved experiments: how to get information on the formation time scale of  $\text{HO}_2^\circ$ ?*

The ultrafast dissociation of  $\text{H}_2\text{O}^{2+}$  and its further recombination reactions was shown by AIMD to result in the formation of  $\text{HO}_2^\circ$ . **We propose experiments at the XFEL facility to directly look at these fast processes, and thereby obtain the structural evolution snapshots of  $\text{HO}_2^\circ$  formation with time.** In order to access these fast processes and to be confident that the yield of the target product is detectable, a source with high brilliance and ultrashort pulses is required.

A proposal to perform the experiment using the soft X-ray branch at the European XFEL, was submitted and crossed the first selection panel. Specifically, we proposed two types of experiments at the XFEL.

- Two color X-ray photoelectron spectroscopy:

The first strategy was to perform two color X-ray photoelectron spectroscopy (XPS) studies at the SQS instrument, provided a liquid jet could be adapted on the line (figure 6.1).



The first soft X-ray pulse will be used as the pump, to create the core ionization of water molecules. The second soft X-ray pulse will be used as a probe, with a delay of a few tens of fs. Its energy will be higher than the initial pump by a few tens of eV, then apparition of new electronic bands will be monitored according to the delay between the two light pulses.

Ideally, based upon the electronegativity of the species, the XPS peak for  $\text{HO}_2^\bullet$ ,  $\text{H}_2\text{O}_2$  or oxywater may appear both in the valence band and in the O K signal.

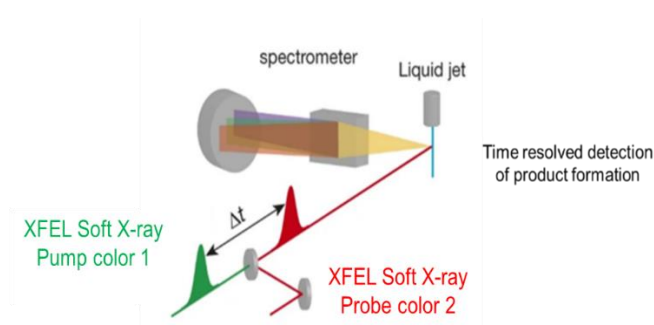


**Figure 6.1:** Time resolved detection of the product formation (figure adapted from Ph. Wernet et al. 2015.)

- Pump X-ray, probe UV-vis spectroscopy:

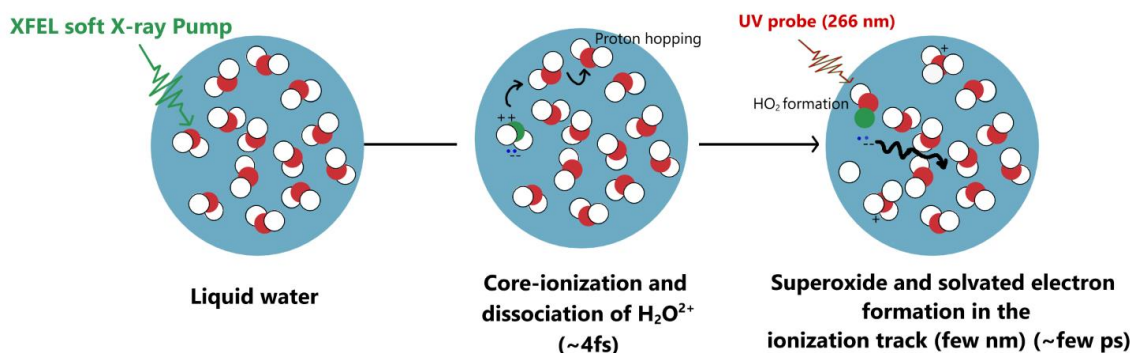


**Figure 6.2:** Core-ionization resulting in the superoxide formation and solvated electron tracks.

For longer time scale (up to nanoseconds), the spectroscopic studies can be performed at the SCS instrument, SASE3 branch. Here, we propose to utilize the XFEL soft X-rays as the pump, to create the core ionization of water molecules, and a synchronized time-delayed UV probe (266 nm, in the absorption band of superoxide), to monitor the process of recombination through a change in light transmission (see figure 6.2 and 6.3). Using the knowledge gained from our synchrotron measurements, we predict the optical density of superoxide to be

around 0.15 (Molar absorption coefficient of  $1940 \text{ M}^{-1}\text{cm}^{-1}$  @260 nm) for 30  $\mu\text{J}$  pulse focused at 20  $\mu\text{m}$ , on the liquid jet of 20  $\mu\text{m}$ .

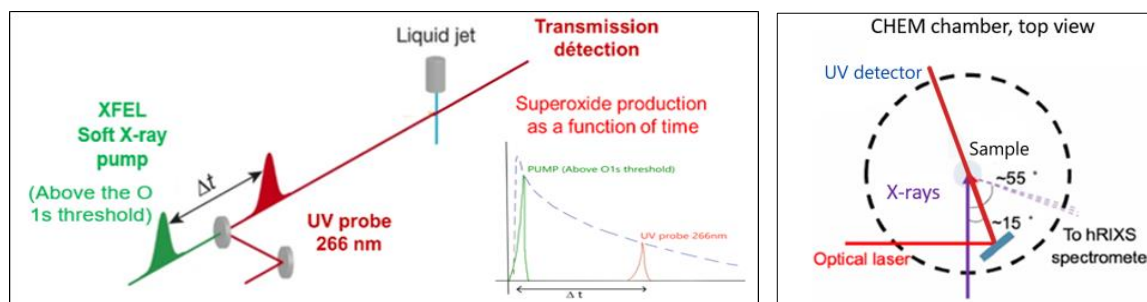


**Figure 6.3:** Monitoring the superoxide production as a function of time.

The expected observation window ranges from tens of fs (optical delay) to hundreds of ns (electronic delay) (*figure 6.3*). In order to detect this signal a fast photodiode (available at the beamline) will be used. In addition, we propose to also tune the optical probe at 800 nm (the laser fundamental) to probe the creation and dynamics of the solvated electron independently, in the ionization tracks (see *figure 6.2*), to obtain a complete picture of the system. This will enable us to understand the secondary electron track behavior<sup>4, 5, 8</sup> providing complementary information to understand the reaction following the X-ray irradiation.

2. *Our study of the interaction of soft X-rays with solvated biomolecules raised questions about the analysis of the radiation induced fragments and re-organization. We propose to address them by the following strategies:*

- *Near Ambient Pressure X-ray Photoelectron Spectroscopy (NAP-XPS):*

To further expand our study on the direct effects of soft X-ray irradiation and study the damage caused by radiation, we successfully performed some preliminary tests using the near ambient pressure XPS (NAP-XPS) technique. In these experiments, XPS spectra are recorded while the liquid sample is irradiated. From the first glance, the spectra, differ from those obtained using a liquid microjet. Moreover, the irradiation resulted in visible damage to the sample, as depicted in *Figure 6.4 a and b*. **We could thus perform the radiation damage studies using the NAP-XPS technique and attain information on damage caused to the solvated biomolecules by systematically recording the spectra over time and by developing a robust protocol for carrying out the experiments and recovering the sample after it.**

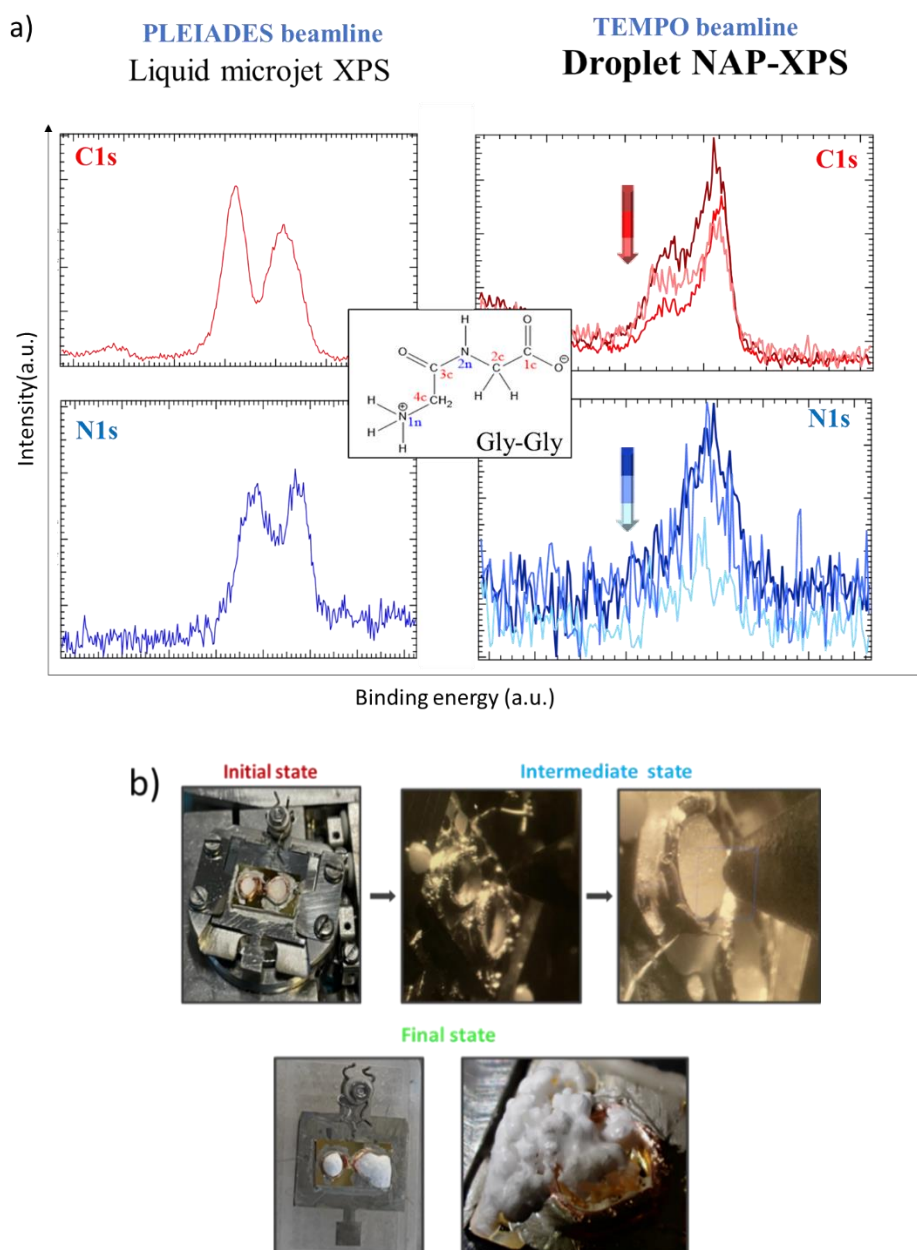


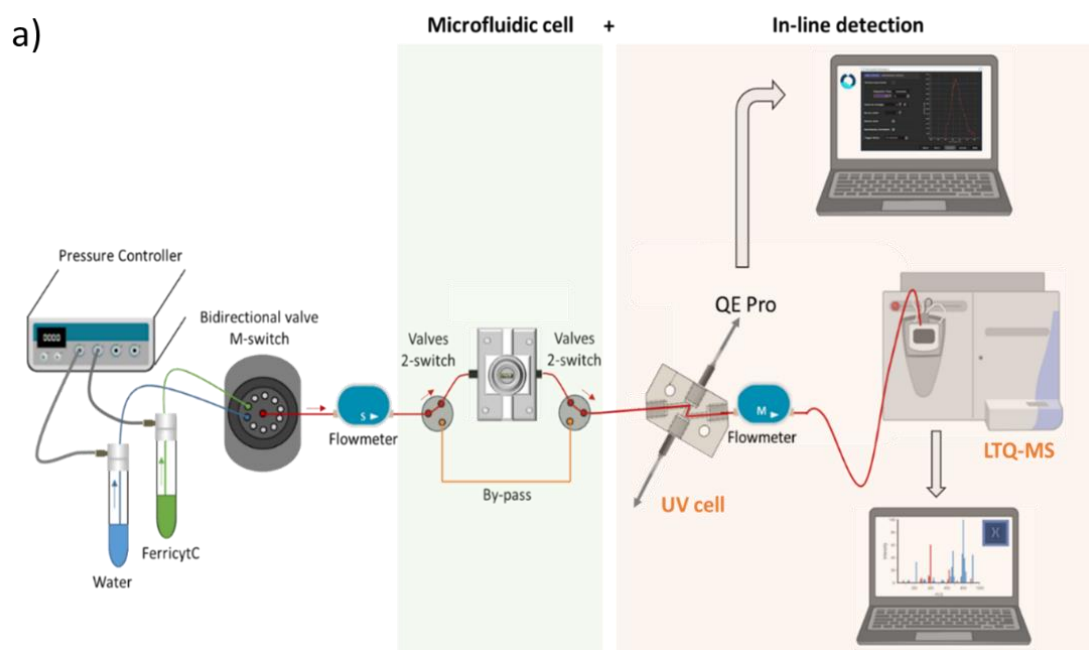
**Figure 6.4:** a) Comparison of the raw data of core-XPS of solvated Gly-Gly, recorded using NAP-XPS (obtained at TEMPO beamline, SOLEIL) (with the darkest color representing first acquisition, then the lightest ones representing the two next consecutive acquisitions. Each acquisition takes ~40 s) and liquid microjet XPS (obtained at PLIEADES beamline, SOLEIL). For liquid microjet, the sample was irradiated in a fine jet that renewed the sample and avoided damage. For NAP-XPS, the sample was irradiated in droplet form. b) The different stages of the Gly-Gly droplet formation during NAP-XPS analysis. The powder was first placed in a sample holder (initial state). A droplet formed at a temperature of 284 K and a pressure of 6 mbar (intermediate state), and XPS spectra were recorded. Finally, the droplet froze when the temperature went up and the sample could be recovered (final state) by stopping the vacuum.

- *Coupling the microfluidic cell with in-line detection of radiation products:*

Capitalizing on the advantages of the microfluidic setup and its capability to be coupled with an in-line detection system, which was developed during the thesis, we conducted additional experiments using promising additional in-line detection techniques listed below.

- *Coupling with Electrospray ionization mass spectrometry-MS:*

We were successful in coupling the microfluidic cell with both the in-line UV cell and an in-line mass spectrometer (see figure 6.5). Thanks to this coupling, it was possible to record the characteristic structural changes for the WST 8 probe after reaction with superoxide (see chapter 3) and in addition to get the information on the different irradiation products (fragments) formed by reaction with other radiolytic species. For Gly-Gly, various irradiation products<sup>6</sup> (succinic acid, aspartic acid and so on) have been reported in the literature that may be analyzed using the mass spectrometer used here.



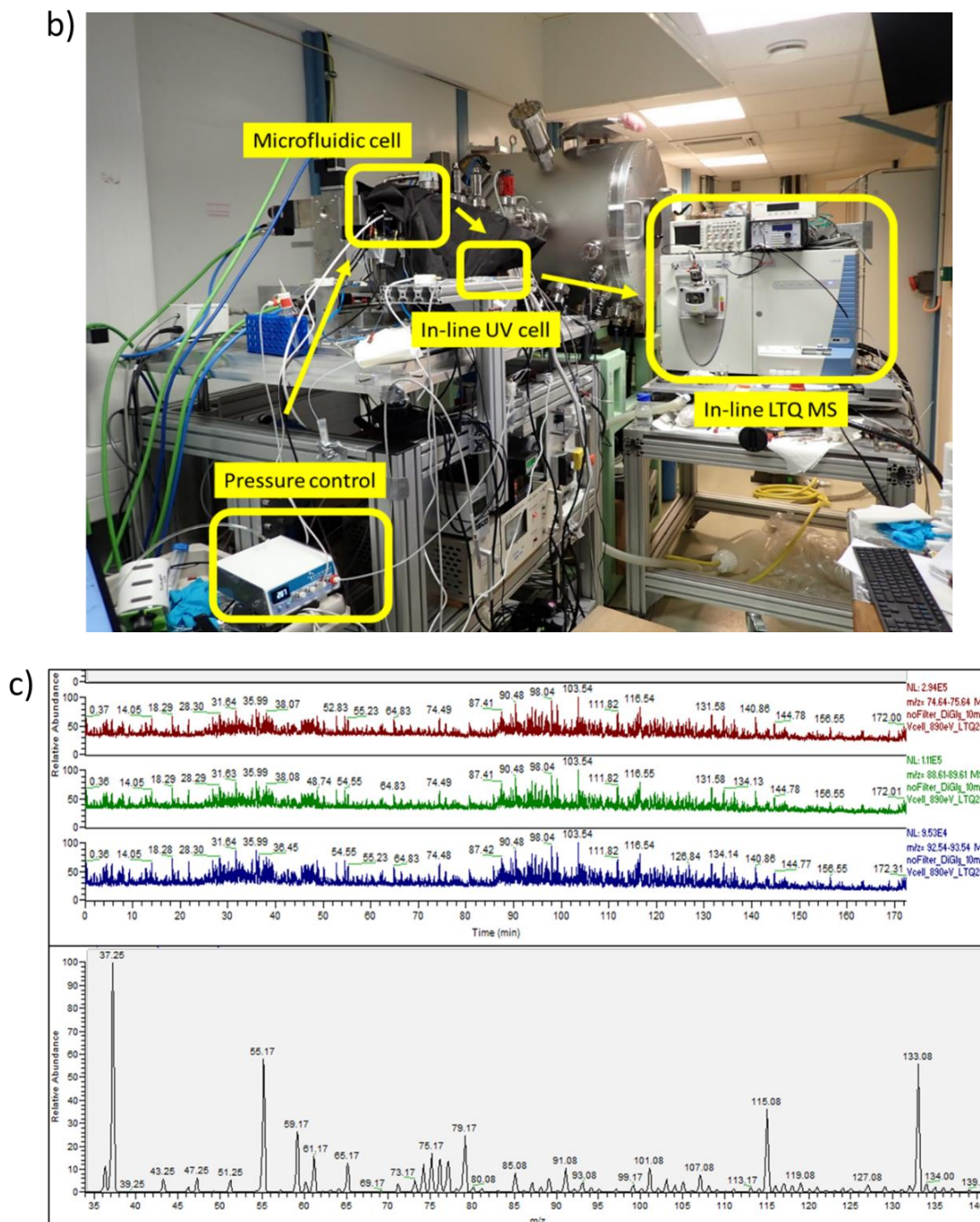
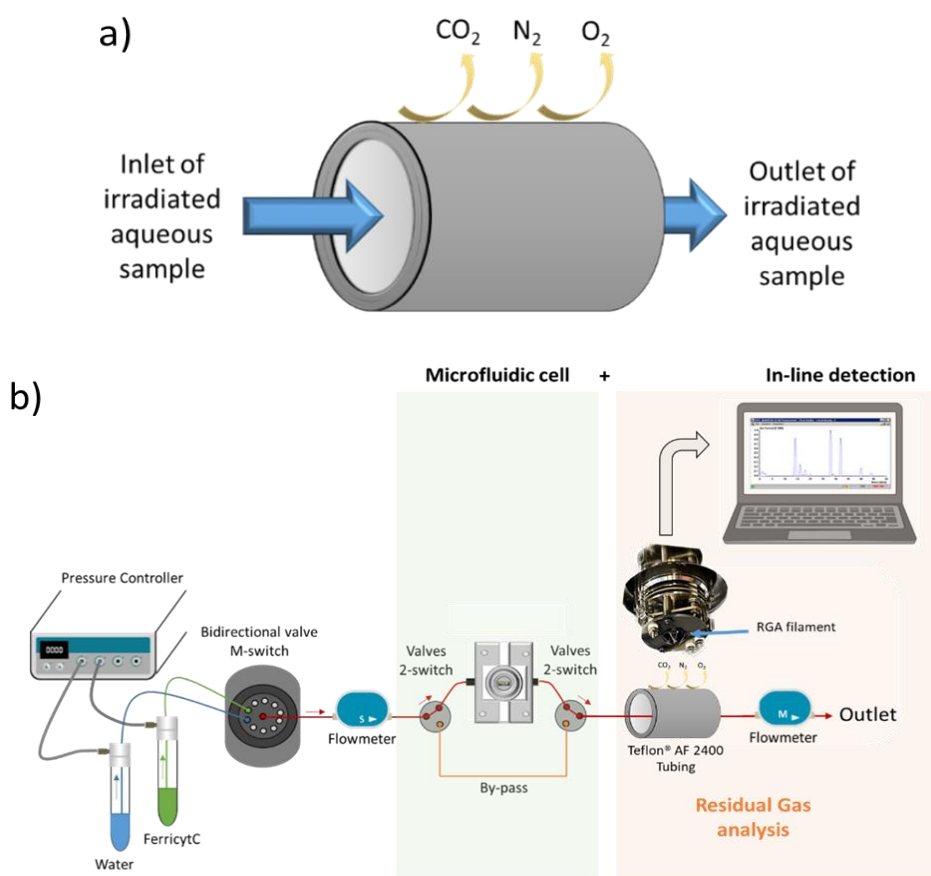


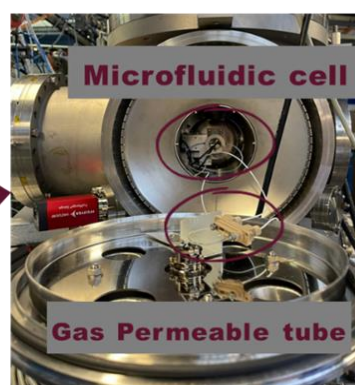
**Figure 6.5:** a) shows the schematic and b) shows the experimental image of the successful coupling of the microfluidic setup with the in-line UV cell and in-line mass spectrometer at the Metrologie beamline XUV branch, SOLEIL synchrotron, by extracting the beam in air, using the IRAD setup; c) shows the raw data obtained via the in-line mass analysis for 10 mM Gly-Gly. The entire mass spectra was recorded during the analysis and for each mass (black curve), it was possible to follow the evolution of different masses with time (red, green and blue curves).

○ *Coupling with Gas permeable tubing:*

The irradiation of solvated Gly-Gly was shown to result in some gaseous irradiation products including free ammonia and carbon dioxide.<sup>7,8</sup> This led to the development of an original in-line gas analysis scheme. It consists of the introduction of a gas permeable Teflon tube<sup>9</sup> (see figure 6.6 a) after the microfluidic cell, irradiated in vacuum, along with a residual gas analyzer to measure the gases released upon irradiation. The preliminary tests performed at PLEIADES beamline show its successful coupling with the microfluidic cell (see figure 6.6 b).



Experimental set-up to determine the gaseous radiolysis products



Microfluidic cell coupled with gas permeable teflon tube

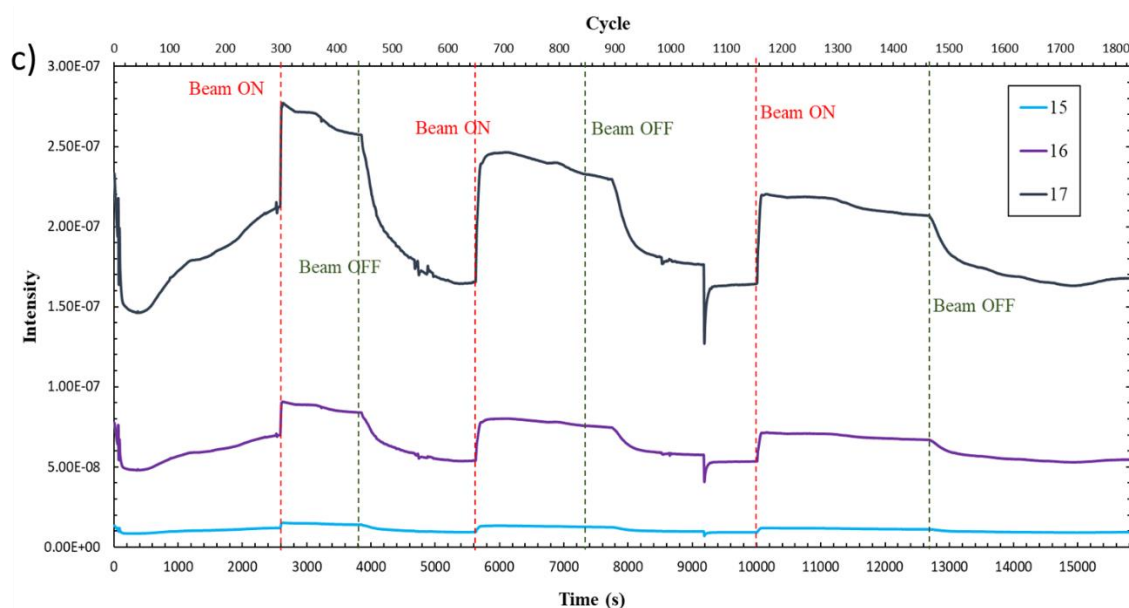


**Figure 6.6:** a) The schematic of the commercially available gas permeable Teflon tube, permeable to certain gases; b) The coupling of the microfluidic cell with the Teflon tube. The upper panel shows the schematic and the lower panel shows the experimental image of the coupled setup; c) Raw data, variation in the intensity of a particular mass as a function of time, obtained from in-line RGA analysis. The time at which the beam was turned off (no irradiation) and on (irradiation) is indicated by green and red vertical lines, respectively.

- *TDDFT of solvated biomolecules: first steps towards modeling the dissociation of molecules after C-K shell ionizations:*

We present the first steps (femtosecond time scale) to understand the dissociation of Gly-Gly, when the ionization occurs at the carbon edge (removal of two electrons from the molecular orbital localized on the C=O bond of the peptide). The carbon edge was preferred to the nitrogen edge owing the importance of the RAS phenomena observed in chapter 5. The 14.4 fs TDDFT dynamics of solvated doubly ionized Gly-Gly is presented in the figure 6.7.

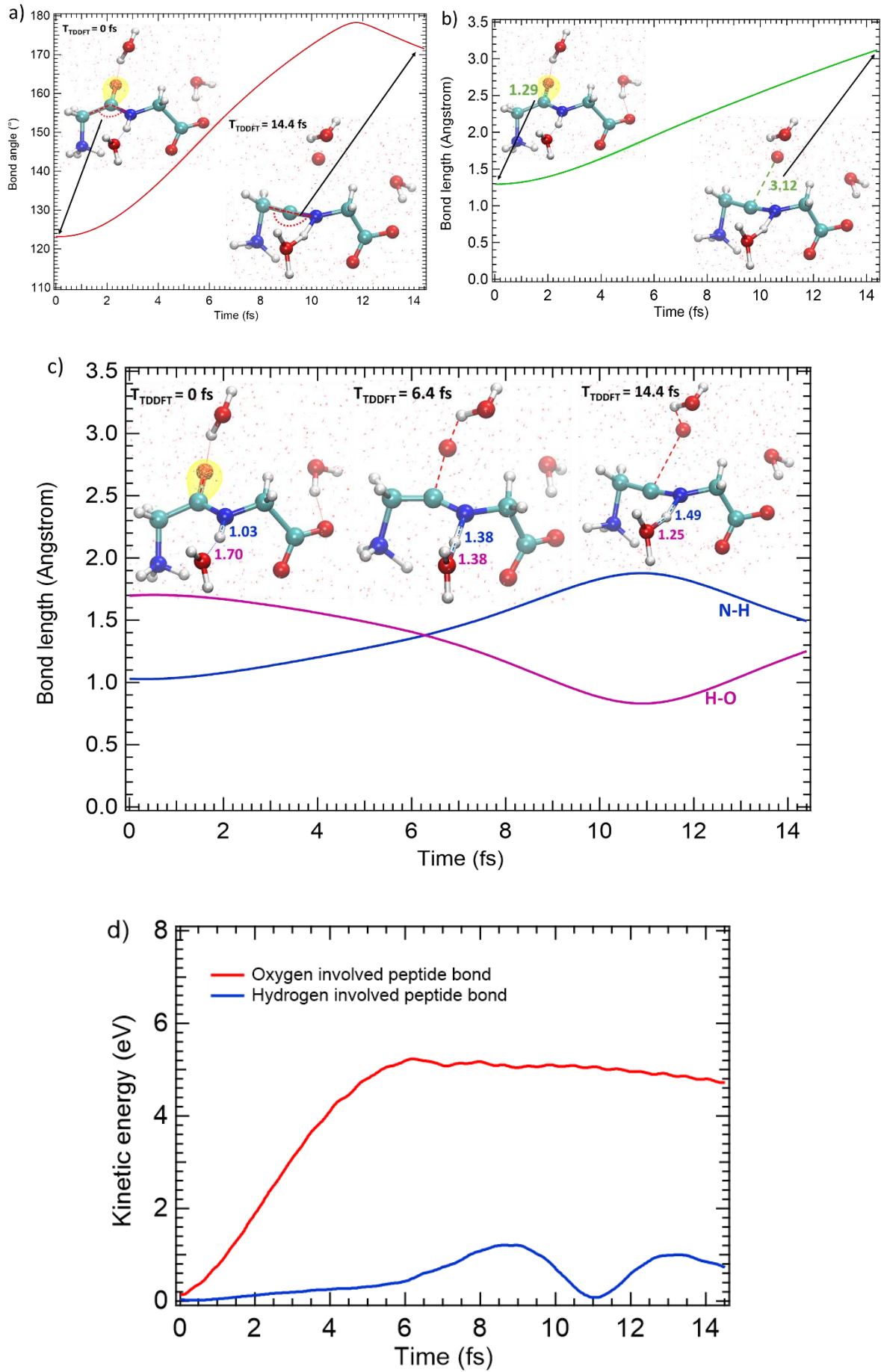




**Figure 6.7:** 14.4 fs TDDFT trajectory analysis of solvated Gly-Gly: Two electrons are removed from the molecular orbital localized on the C=O of the peptide bond at  $t = 0$ . a) The variation in the bond angle (centered on the carbon of the peptide bond); b) the variation in the C=O bond length involved in the peptide bond and c) the variation in the distance of the H atom involved in the peptide bond with its parent N and the oxygen atom of the neighboring water molecule. The configuration of the molecule is shown at the start of TDDFT, i.e. at  $T_{\text{TDDFT}} = 0$  fs, at  $T_{\text{TDDFT}} = 6.4$  fs and at  $T_{\text{TDDFT}} = 14.4$  fs. The water molecules that were hydrogen bonded at the start of the TDDFT analysis are shown, whereas all other solvent molecules are represented as dots; d) The time evolution of the kinetic energy of the oxygen and hydrogen atoms, involved in the peptide bond.

The structure of Gly-Gly cis is distorted during the TDDFT trajectory as the carbon atom involved in the peptide bond comes in the plane of the nitrogen atom of the peptide bond (see figure 6.7 a), where all the three atoms (C-C-N) make an angle of almost  $180^\circ$  at 12 fs. The oxygen atom of the peptide bond leaves the molecule completely within few femtoseconds (see figure 6.7 b), with a charge of  $-0.4 e$  and with a kinetic energy of 4.6 eV by the end of 14.4 fs TDDFT trajectory. The high kinetic energy of the oxygen atom shows evidence of hot chemistry, similar to that observed in case of the water +  $^\circ\text{OH}$  simulations. The H of the peptide bond starts to also leave its parent nitrogen with a kinetic energy of 1.2 eV, but bounces back, after interaction with a neighboring solvent water molecule, (see figure 6.7 c). The H is still partially bonded to the neighboring water and possesses a kinetic energy of 0.7 eV at 14.4 fs.

We will switch from the TDDFT simulation to CPMD to see if the oxygen can be an additional source of ROS, and study this dynamics for approximately 1 ps. However, it would be interesting to probe the effects of electron removal from other molecular orbitals but the TDDFT simulations are very demanding as it took around 6 months to perform the 14.4 fs trajectory shown in figure 6.7.

Therefore, simulations are currently under way on a smaller system, formamide, to understand specifically the effect of removing the electrons from different molecular orbitals around the O=C-N-H bond (see in appendix IV).

These three developments (in line analysis and TDDFT) will be pursued after the end of this thesis.

## Reference

- (1) Herve du Penhoat, M. A.; Fayard, B.; Abel, F.; Touati, A.; Gobert, F.; Despiney-Bailly, I.; Ricoul, M.; Sabatier, L.; Stevens, D. L.; Hill, M. A.; Goodhead, D. T.; Chetioui, A. Lethal Effect of Carbon K-Shell Photoionizations in Chinese Hamster V79 Cell Nuclei: Experimental Method and Theoretical Analysis. *Radiat Res* **1999**, *151* (6), 649–658.
- (2) Huart, L. Inner Shell Ionization Effects on Molecules of Biological Interest in an Aqueous Medium. PhD thesis, Sorbonne Université, 2022. <https://tel.archives-ouvertes.fr/tel-03725615> (accessed 2022-09-02).
- (3) Rajpal, A.; Huart, L.; Nicolas, C.; Chevillard, C.; Guigner, J.-M.; Dasilva, P.; Mercere, P.; Gervais, B.; Hervé du Penhoat, M.-A.; Renault, J.-P. Superoxide Production under Soft X-Ray Irradiation of Liquid Water. *J. Phys. Chem. B* **2023**, *127* (19), 4277–4285. <https://doi.org/10.1021/acs.jpcc.3c00932>.
- (4) Pimblott, S. M.; LaVerne, J. A. Diffusion-Kinetic Theories for LET Effects on the Radiolysis of Water. *J. Phys. Chem.* **1994**, *98* (24), 6136–6143. <https://doi.org/10.1021/j100075a016>.
- (5) Turner, J. E.; Magee, J. L.; Wright, H. A.; Chatterjee, A.; Hamm, R. N.; Ritchie, R. H. Physical and Chemical Development of Electron Tracks in Liquid Water. *Radiation Research* **1983**, *96* (3), 437–449. <https://doi.org/10.2307/3576111>.
- (6) Yoshida, H.; Turner, J. E.; Bolch, W. E.; Jacobson, K. B.; Garrison, W. M. Measurement of Products from X-Irradiated Glycylglycine in Oxygen-Free Aqueous Solutions. *Radiation Research* **1992**, *129* (3), 258–264. <https://doi.org/10.2307/3578024>.
- (7) Yoshida, H.; Bolch, W. E.; Jacobson, K. B.; Turner, J. E. Measurement of Free Ammonia Produced by X Irradiation of Glycylglycine in Aqueous Solution. *Radiation Research* **1990**, *121* (3), 257–261. <https://doi.org/10.2307/3577774>.
- (8) Bolch, W. E.; Turner, J. E.; Yoshida, H.; Jacobson, K. B.; Hamm, R. N.; Crawford, O. H. Product Yields from Irradiated Glycylglycine in Oxygen-Free Solutions: Monte Carlo Simulations and Comparison with Experiments. *Radiat Environ Biophys* **1998**, *37* (3), 157–166. <https://doi.org/10.1007/s004110050111>.
- (9) *Teflon AF2400 Gas Permeable Tube for degassing*. Biogeneral. <https://www.biogeneral.com/teflon-af/gas-permeable-tubing/> (accessed 2023-07-12).



## CONTENTS APPENDICES

---

Appendices .....	233
<b>Appendix I: Experimental approach for HO<sub>2</sub><sup>°</sup> detection .....</b>	<b>234</b>
I.I. Code for treatment of data obtained via in-line UV analysis .....	234
I.II. Dose-response curves .....	236
I.III. Hydrodynamic resistance .....	236
I.IV. Variation in SiPM signal as a function of flowrate .....	239
<b>Appendix II: Modeling of H<sub>2</sub>O<sup>2+</sup> using Ab-initio approach .....</b>	<b>240</b>
II.I. Python code to convert 'gro' files of Gromacs to readable format for CPMD package .....	240
II.II. Analysis of W32 <sup>2+</sup> during 30 fs TDDFT dynamics .....	246
II.III. Analysis of the control system (64 H <sub>2</sub> O) .....	248
II.IV. Additional tests for target system (°OH + 63 H <sub>2</sub> O) using protocol A .....	250
<b>Appendix III: Spectroscopic studies of biomolecules in aqueous .....</b>	<b>252</b>
III.I. Nitrogen 1s XPS spectra .....	252
III.II. Expected energy shifts in the theoretical DOS values .....	252
III.III. Symmetry of molecular orbitals of Gly and Gly-Gly .....	253
<b>Appendix IV: TDDFT of solvated formamide .....</b>	<b>254</b>
<b>Appendix V. List of conferences .....</b>	<b>259</b>
<b>Appendix VI. List of Publications .....</b>	<b>260</b>
<b>References .....</b>	<b>261</b>

## Appendix I: Experimental approach for HO<sub>2</sub><sup>o</sup> detection

### I.I. Code for treatment of data obtained via in-line UV analysis

*#Loading required packages*

```
import os
from os import listdir
from os.path import isfile, join
import matplotlib.pyplot as plt
import numpy as np
import pandas as pd
```

*#loading data from folder 'Data path'*

*#making a copy of raw data in folder 'Format path'*

*#Writing the output file after treatment in the folder 'Write path'*

```
DATA_PATH=r".\Data path\OD2"
FORMAT_PATH=r".\Format path\OD2"
WRITE_PATH=r".\Write path\OD2"
pathname = DATA_PATH
pathformat = FORMAT_PATH
fnamelist = [r"...._"]
```

*#list of the files present*

```
fnamelist = [f for f in listdir(pathname) if isfile(join(pathname,f))]
```

for fname in fnamelist :

```
    with open(os.path.join(pathname,fname)) as fin, open(os.path.join(pathformat,fname), 'w') as
fout:
```

*#In each file, the comma is replaced by a dot*

```
    for line in fin:
        fout.write(line.replace(',', '.'))
    print(fname)
```

*#While recording, each file is saved with a similar format to read them easily*

```
fname_format = r"WST8_oxic_OD2_QEP033341__{one:01}__{two:05}.txt"
```

*#the three parameter, 'a', 'b' and 'c', vary depending on the files present in the folder*

```
a=0
```

```
b=524
```

*#c is the last numbers of the first file minus 'a'*

```
c=(400-a)
fnamelist = [fname_format.format(un = i,deux = i+c) for i in range(a,b)]
#Creating empty list
evolution=[]
time=[]
i=0
#skipping first 14 rows, which is the header of Oceanoptics file
for fname in fnamelist :
    i=i+1
    data = np.loadtxt(os.path.join(pathformat,fname), skiprows = 14)
    data = data[data[:,0].argsort()]
#evolution list can be changed depending on the data treatment required
#Here the evolution list has the relative intensity
    y=data[362,1]/data[815,1]
    evolution.append(y)
    time.append(i*20)
#Plotting the evolution as a function of time
plt.plot(time,evolution, label='evolution at 460nm')
plt.xlabel(r"time (s)")
plt.ylabel(r"Delta intensity 460nm/800nm")
plt.legend()
plt.tight_layout()
plt.figure()
plt.show()
txt_to_write = [time, evolution]
#writing the file in text format
outfname = r"OD1_all.txt"
print(len(evolution))
print(len(time))
with open(os.path.join(WRITE_PATH,outfname), 'w') as fout:
    for i, j in zip(np.arange(0, 1028), np.arange(0, 1028)) :
        fout.write(str(time[i]) + "\t" + str(evolution[j]) + "\n")
```

### I.II. Dose-response curves

The dose response curves for three different conditions of the chemical detection system are shown in the figure A.1. These curves correspond to the irradiation using the gamma source with the dose rate of 5.5 Gy/min. The figure depicts that absorbance increases linearly as a function of dose delivered to the sample, indicating large amount of WST8 probe is reduced to its formazan product. Additionally, the absorbance is higher when the irradiation is carried out in oxic condition, when compared to the anoxic WST8 irradiation or anoxic irradiation with superoxide dismutase (SOD). These differences are discussed in detail in chapter 3.

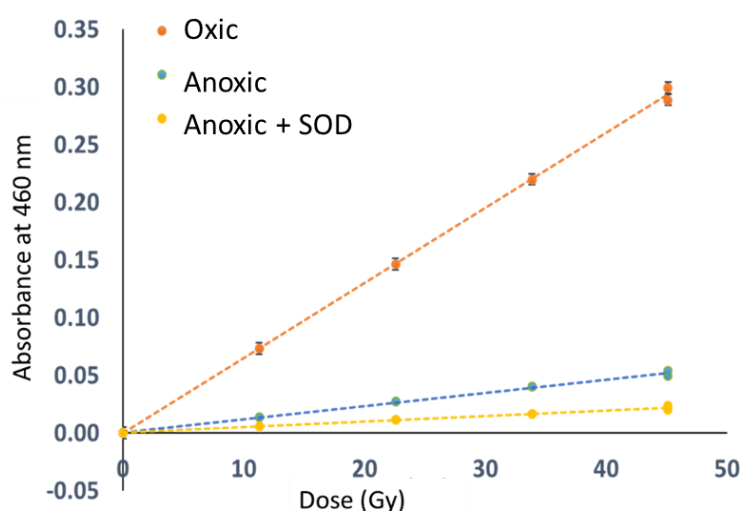


**Figure A.1:** The three dose response curves corresponding to oxic WST8 (orange curve), anoxic WST8 (blue curve) and anoxic WST8 with SOD (yellow curve). The concentration of WST8 and SOD is 300  $\mu\text{M}$  and 0.62  $\mu\text{M}$ , respectively.

### I.III. Hydrodynamic resistance

The modified cell design was used in the microfluidic set-up (explained in chapter 2). Along with the microfluidic cell, the different components present in this setup offer a resistance (or friction) to the flowing sample, referred to as the hydrodynamic resistance. It is therefore crucial to quantify this resistance to determine the flowrate of the sample. This is because the flowrate determines the time that the sample will remain exposed to the beam. If the flowrate is slow, the solution will spend more time in front of the beam and therefore the dose will increase. The resistance of the microfluidic channel can be calculated using equations A.1 and A.2, for cylindrical Teflon or PEEK tubing and for a rectangular channel in the microfluidic cell.<sup>1</sup>

$$R_h = \frac{8\mu L}{\pi r^4} \quad \text{A.1}$$

$$R_h = \frac{12\mu L}{[1-0.63(h/w)]wh^3} \quad \text{A.2}$$

Here,  $R_h$  is the hydrodynamic resistance experienced by the fluid of viscosity  $\mu$ , in the cylindrical tubing in the microfluidic channel with length  $L$  and radius  $r$ .  $w$  and  $h$  correspond to the depth and the length of the microfluidic cell. For each sample that was used during the irradiation experiment, the viscosity was determined using the Ostwald viscometer. These values were then used to determine the  $R_h$  for the different samples.

Thereafter, using the resistance measurements, the Poiseuille equation (equation A.3) was used to determine the flowrate of a given sample at different pressure. The calculated flowrate as a function of pressure is given by the black curve in figure A.2, for a 300  $\mu\text{M}$  WST8 solution flowing through the microfluidic channel.

$$\Delta P = R_h Q \quad \text{A.3}$$

We also recorded the flowrate of 300  $\mu\text{M}$  WST8 solution, using the flowmeter placed at the exit of the microfluidic cell, as a function of changing the inlet pressure (see blue curve in figure A.2). It was also observed that the resistance to the flowing sample increased over time. This increase in resistance is attributed to a contamination in the microfluidic channel, caused by the flowing sample. Consequently, after an exhaustive usage of the microfluidic cell, a higher pressure is now required to maintain the same flow rate (see figure A.2).

The bypass in the microfluidic set-up offers a low hydrodynamic resistance. This path is used for periodic cleaning of the microfluidic channel, after each sample irradiation.



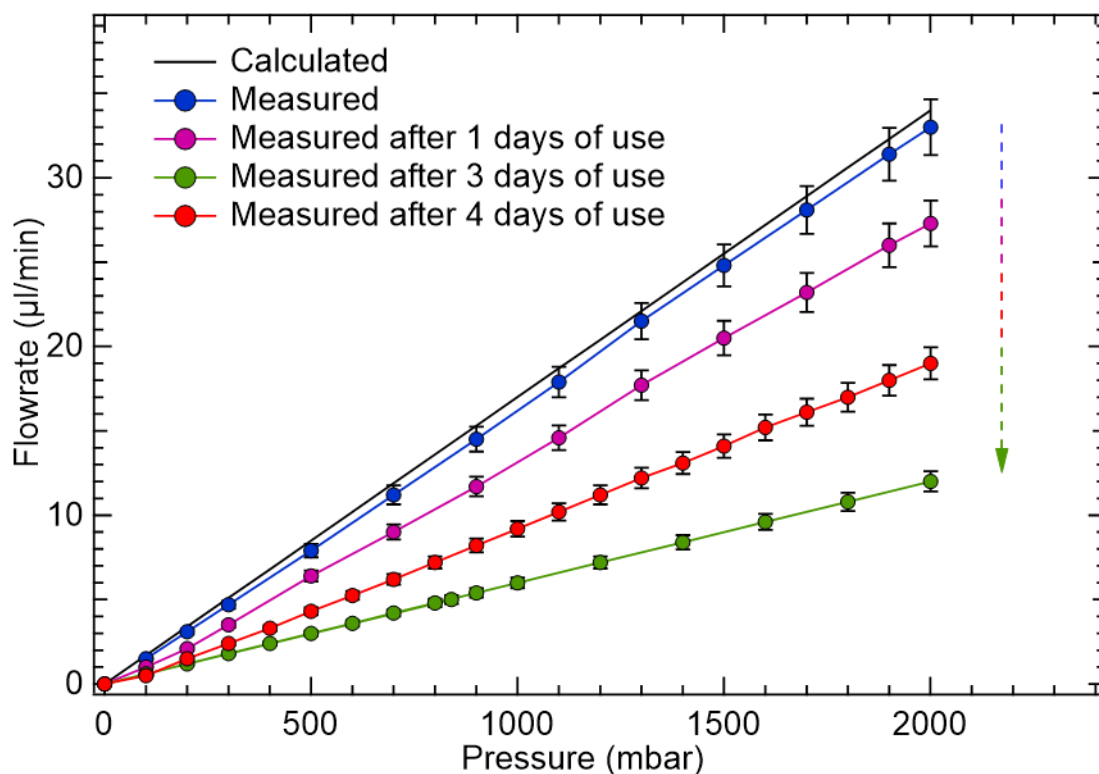


**Figure A.2:** The calculated and the measured flowrate of a 300 µm WST-8 solution flowing through the cell in the microfluidic channel, as a function of the applied pressure. The measured flowrate decreases, at a given pressure, as the time of use of the cell increases.

It is important to emphasize that the issue of contamination is more pronounced in the case of cytochrome C due to its tendency to aggregate. This aggregation poses a challenge for using the microfluidic setup for extended periods, and therefore, the use of Cyt C as a potential probe for superoxide was disregarded.

As the hydrodynamic resistance changes for each sample (depending upon its viscosity and density of the sample), the *flow units were calibrated for the sample*, to have an accurate flowrate measurement. To do so, at a given pressure, the flowrates recorded by the flow units were compared with the flowrates calculated by the estimated time (min) required for a given volume of sample (µL) to travel through the microfluidic channel. The ratio between the two flowrates, referred to as the feedback coefficient, is entered in the configuration panel of the A.i.O software, for each sample to correct for the discrepancy in the measured flowrates.

## I.IV. Variation in SiPM signal as a function of flowrate

Measuring the SiPM signal as a function of flowrate ( $Q$ ) can indirectly provide evidence for the bulging of the membranes, although it did not allow quantitative measurements because the response of the SiPM was not linear.

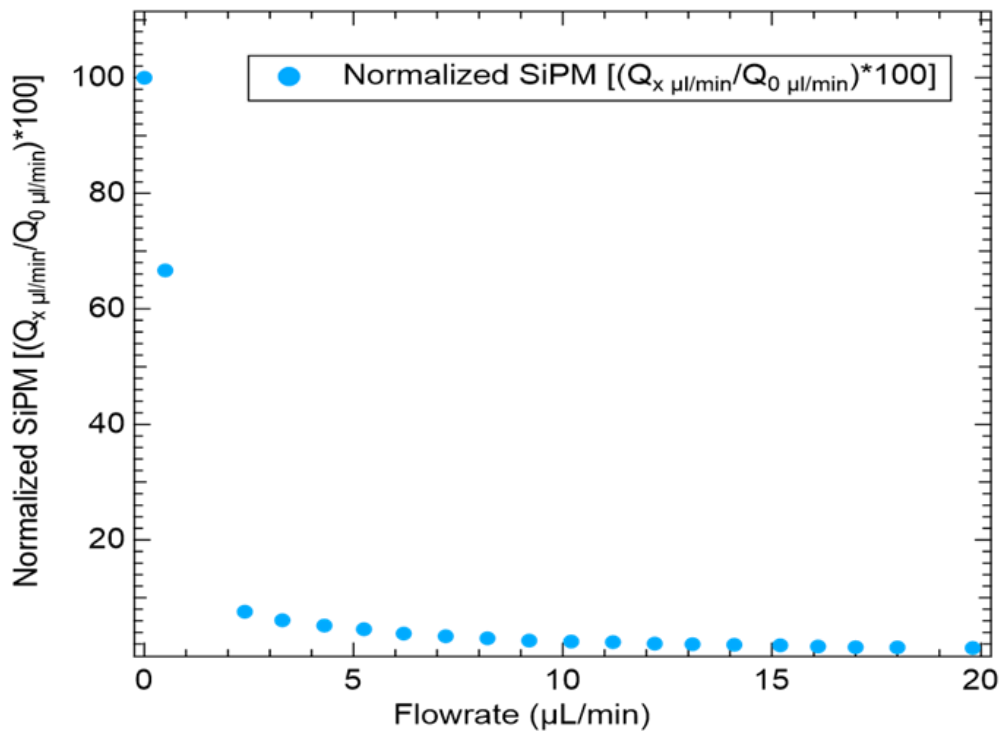


**Figure A.3:** Variation in the % SiPM signal as a function of the flowrate of the sample. The SiPM signal is normalized with respect to the SiPM signal of a static sample inside the microfluidic cell.

It is observed that as the flowrate increases (by increasing pressure), the SiPM signal decreases because the volume of the sample in front of the beam increases as a result of bulging of the membrane (see figure A.3), reaching its limit of detection.

## Appendix II: Modeling of $\text{H}_2\text{O}^{2+}$ using *Ab-initio* approach

II.I. Python code to convert 'gro' files of Gromacs to readable format for CPMD package

### Code A.1: 'gro' to geometry file with distance and velocity in atomic units.

```
#Loading the required packages
import os
import numpy
import pandas as pd
#This makes a list of all files with extension .gro
#in the same directory as the python programm. Now we have the specific .gro file we want
#This program can be run on multiple files simultaneously
a=213
files = [f for f in os.listdir() if os.path.isfile(f)]
print(files)
files_all = []
for f in files:
    temp = f.split('.')
    if(temp[1] == 'gro'):
        files_all.append(f)
for i in range(len(files_all)):
    df = pd.DataFrame(columns = ['Col_1', 'Col_2', 'Col_3', 'Col_4', 'Col_5', 'Col_6', 'Col_7', 'Col_8',
'Col_9'])
    #column_2 is the element name here
    F = open(files_all[i], 'r')
#opens files in order
    filename = files_all[i].split(".")
    count = -1
    flag = 0
    with open(files_all[i]) as F:
        Distance_conv=18.89726132885643067222711130708 # conversion from nm to au
        Velocity_conv= 4.5710289243323441597334125394034e-4 #conversion from nm/ps to au
        Box_size = 29.795878855047799933820653211213 # Box size from Angstrom to au
```

```

for line in F:
    count = count + 1
    if(count == 0):
        line1 = line
    if(count == 1):
        line2 = line
    if(count >= 2):
        temp = line.split()
        if(len(temp) == 9 and flag == 0):
'Col_5': temp[4], 'Col_6': temp[5]], ignore_index = True)
            df = df.append({'Col_1': temp[0], 'Col_2': temp[1], 'Col_3': temp[2], 'Col_4':
float(temp[3])*Distance_conv, 'Col_5': float(temp[4])*Distance_conv, 'Col_6':
float(temp[5])*Distance_conv, 'Col_7': float(temp[6])*Velocity_conv, 'Col_8':
float(temp[7])*Velocity_conv, 'Col_9': float(temp[8])*Velocity_conv}, ignore_index = True)
            elif(len(temp) == 3 and flag == 0):
                flag = 1
df = df.reset_index()
df.drop(columns = ['index'], inplace = True)
df.drop(columns = ['Col_1'], inplace = True)
#removes the column index, as inplace is true
#move all atoms
for i in range(a):
    df['Col_4'][i]=df['Col_4'][i]+(0.5*Box_size)
    df['Col_5'][i]=df['Col_5'][i]-(0.5*Box_size)
    df['Col_6'][i]=df['Col_6'][i]+(0.5*Box_size)
#move water molecule
for i in range(a):
    if df['Col_2'][i]=='OW':
        if df['Col_4'][i]<0:
            for j in range(3): df['Col_4'][i+j]=df['Col_4'][i+j]+Box_size
        elif df['Col_4'][i]>Box_size:
            for j in range(3): df['Col_4'][i+j]=df['Col_4'][i+j]-Box_size
    if df['Col_5'][i]<0:
        for j in range(3): df['Col_5'][i+j]=df['Col_5'][i+j]+Box_size
        elif df['Col_5'][i]>Box_size:

```

```

    for j in range(3): df['Col_5'][i+j]=df['Col_5'][i+j]-Box_size
if df['Col_6'][i]<0:
    for j in range(3): df['Col_6'][i+j]=df['Col_6'][i+j]+Box_size
elif df['Col_6'][i]>Box_size:
    for j in range(3): df['Col_6'][i+j]=df['Col_6'][i+j]-Box_size
#write in text file, in a way readable by CPMD package
with open(filename[0] + '_geometryfile.txt', 'w') as file:
    for i in range(a):
        if df['Col_2'][i]=='C'or df['Col_2'][i]=='CA':
            file.write(f"{df['Col_4'][i]: 20.12f} {df['Col_5'][i]: 20.12f} {df['Col_6'][i]: 20.12f}
{df['Col_7'][i]: 27.12f} {df['Col_8'][i]: 20.12f} {df['Col_9'][i]: 20.12f} \n")
        for i in range(a):
            if df['Col_2'][i]=='N':
                file.write(f"{df['Col_4'][i]: 20.12f} {df['Col_5'][i]: 20.12f} {df['Col_6'][i]: 20.12f} {df['Col_7'][i]:
27.12f} {df['Col_8'][i]: 20.12f} {df['Col_9'][i]: 20.12f} \n")
            for i in range(a):
                if df['Col_2'][i]=='O1'or df['Col_2'][i]=='O2' or df['Col_2'][i]=='O':
                    file.write(f"{df['Col_4'][i]: 20.12f} {df['Col_5'][i]: 20.12f} {df['Col_6'][i]: 20.12f} {df['Col_7'][i]:
27.12f} {df['Col_8'][i]: 20.12f} {df['Col_9'][i]: 20.12f} \n")
                for i in range(a):
                    if df['Col_2'][i]=='OW':
                        file.write(f"{df['Col_4'][i]: 20.12f} {df['Col_5'][i]: 20.12f} {df['Col_6'][i]: 20.12f} {df['Col_7'][i]:
27.12f} {df['Col_8'][i]: 20.12f} {df['Col_9'][i]: 20.12f} \n")
                    for i in range(a):
                        if df['Col_2'][i]=='H1'or df['Col_2'][i]=='H2' or df['Col_2'][i]=='H3' or df['Col_2'][i]=='HA1' or
df['Col_2'][i]=='HA2' or df['Col_2'][i]=='H':
                            file.write(f"{df['Col_4'][i]: 20.12f} {df['Col_5'][i]: 20.12f} {df['Col_6'][i]: 20.12f} {df['Col_7'][i]:
27.12f} {df['Col_8'][i]: 20.12f} {df['Col_9'][i]: 20.12f} \n")
                            for i in range(a):
                                if df['Col_2'][i]=='HW1' or df['Col_2'][i]=='HW2':
                                    file.write(f"{df['Col_4'][i]: 20.12f} {df['Col_5'][i]: 20.12f} {df['Col_6'][i]: 20.12f} {df['Col_7'][i]:
27.12f} {df['Col_8'][i]: 20.12f} {df['Col_9'][i]: 20.12f} \n")
#close the file after writing
file.close()
print('File created: {}'.format(filename[0] + '_geometryfile.txt'))

```

**Code A.2: 'gro' to input file with distance and velocity in atomic units.**

```
#Load required packages
import os
import numpy
import pandas as pd

#This makes a list of all files with extension .gro
#in the same directory as the python programm. Now we have the specific .gro file we want
#This program can be run on multiple files simultaneously
files = [f for f in os.listdir() if os.path.isfile(f)]
files_all = []
for f in files:
    temp = f.split('.')
    if(temp[1] == 'gro'):
        files_all.append(f)
for i in range(len(files_all)):

    df = pd.DataFrame(columns = ['Col_1', 'Col_2', 'Col_3', 'Col_4', 'Col_5', 'Col_6', 'Col_7', 'Col_8',
'Col_9'])
#opens files in order
    F = open(files_all[i], 'r')
    filename = files_all[i].split(".")
    count = -1
    flag = 0
    with open(files_all[i]) as F:
        Distance_conv=10 # Conversion nm to Angstrom
        Box_size = 15.7673 #Box size in Angstrom
        for line in F:
            count = count + 1
            if(count == 0):
                line1 = line
            if(count == 1):
                line2 = line
```

```

if(count >= 2):
    temp = line.split()
    if(len(temp) == 9 and flag == 0):
        df = df.append({'Col_1': temp[0], 'Col_2': temp[1], 'Col_3': temp[2], 'Col_4':
float(temp[3])*10, 'Col_5': float(temp[4])*10, 'Col_6': float(temp[5])*10, 'Col_7': temp[6], 'Col_8':
temp[7], 'Col_9': temp[8]}, ignore_index = True)
        elif(len(temp) == 3 and flag == 0):
            flag = 1

```

*#removes the column index, as inplace is true*

```

df = df.reset_index()
df.drop(columns = ['index'], inplace = True)
df.drop(columns = ['Col_1'], inplace = True)
#df.drop(columns = ['Col_2'], inplace = True)
df.drop(columns = ['Col_3'], inplace = True)
df.drop(columns = ['Col_7'], inplace = True)
df.drop(columns = ['Col_8'], inplace = True)
df.drop(columns = ['Col_9'], inplace = True)

```

*#move all atoms*

```

for i in range(386):
    df['Col_4'][i]=df['Col_4'][i]+(0.5*Box_size)
    df['Col_5'][i]=df['Col_5'][i]-(0.5*Box_size)
    df['Col_6'][i]=df['Col_6'][i]+(0.5*Box_size)

```

*#move water molecule*

```

for i in range(386):
    if df['Col_2'][i]=='OW':
        if df['Col_4'][i]<0:
            for j in range(3): df['Col_4'][i+j]=df['Col_4'][i+j]+Box_size
        elif df['Col_4'][i]>Box_size:
            for j in range(3): df['Col_4'][i+j]=df['Col_4'][i+j]-Box_size
        if df['Col_5'][i]<0:
            for j in range(3): df['Col_5'][i+j]=df['Col_5'][i+j]+Box_size
        elif df['Col_5'][i]>Box_size:
            for j in range(3): df['Col_5'][i+j]=df['Col_5'][i+j]-Box_size
        if df['Col_6'][i]<0:
            for j in range(3): df['Col_6'][i+j]=df['Col_6'][i+j]+Box_size

```

```

elif df['Col_6'][i]>Box_size:
    for j in range(3): df['Col_6'][i+j]=df['Col_6'][i+j]-Box_size
# write the input file, add specific keywords
with open(filename[0] + '_inpfile.inp', 'w') as file:
    file.write("*C_MT_BLYP KLEINMAN-BYLANDER")
    file.write("\n"+" LMAX=P"+" \n")
    file.write(" 4" + "\n")
    for i in range(386):
        if df['Col_2'][i]=='C'or df['Col_2'][i]=='CA':
            file.write(f"{df['Col_4'][i]: 20.12f} {df['Col_5'][i]: 20.12f} {df['Col_6'][i]: 20.12f} \n")
    file.write("*N_MT_BLYP KLEINMAN-BYLANDER")
    file.write("\n"+" LMAX=P"+" \n")
    file.write(" 2" + "\n")
    for i in range(386):
        if df['Col_2'][i]=='N':
            file.write(f"{df['Col_4'][i]: 20.12f} {df['Col_5'][i]: 20.12f} {df['Col_6'][i]: 20.12f} \n")
    file.write("*O_MT_BLYP KLEINMAN-BYLANDER")
    file.write("\n"+" LMAX=P"+" \n")
    file.write(" 126" + "\n")
    for i in range(386):
        if df['Col_2'][i]=='O1'or df['Col_2'][i]=='O2' or df['Col_2'][i]=='O':
            file.write(f"{df['Col_4'][i]: 20.12f} {df['Col_5'][i]: 20.12f} {df['Col_6'][i]: 20.12f} \n")
    for i in range(386):
        if df['Col_2'][i]=='OW':
            file.write(f"{df['Col_4'][i]: 20.12f} {df['Col_5'][i]: 20.12f} {df['Col_6'][i]: 20.12f} \n")
    file.write("*H_MT_BLYP")
    file.write("\n"+" LMAX=S"+" \n")
    file.write(" 254" + "\n")
    for i in range(386):
        if df['Col_2'][i]=='H1'or df['Col_2'][i]=='H2' or df['Col_2'][i]=='H3' or df['Col_2'][i]=='HA1' or
df['Col_2'][i]=='HA2' or df['Col_2'][i]=='H':
            file.write(f"{df['Col_4'][i]: 20.12f} {df['Col_5'][i]: 20.12f} {df['Col_6'][i]: 20.12f} \n")
    for i in range(386):
        if df['Col_2'][i]=='HW1' or df['Col_2'][i]=='HW2':
            file.write(f"{df['Col_4'][i]: 20.12f} {df['Col_5'][i]: 20.12f} {df['Col_6'][i]: 20.12f} \n")

```



```

#to_string() function is used to render a DataFrame to a console-friendly tabular output
#Converting data frame to string
# close the file after writing

```

```

file.write('&END')
file.close()
print('File created: {}'.format(filename[0] + '_infile' + '.inp'))

```

## II.II. Analysis of $W32^{2+}$ during 30 fs TDDFT dynamics

The Kinetic Energy (KE) analysis of the H/H+,  $H_a$  and  $H_b$ , of the dissociating water molecule,  $W32^{2+}$ , is shown in the figure A.4. They lose part of their KE on collision with the oxygen atoms of their neighboring water molecules that accept a H bond,  $O_a$  and  $O_b$ , respectively at 6 fs. (The initial and the final geometry during the  $W32^{2+}$  TDDFT dynamics is shown in chapter 4).

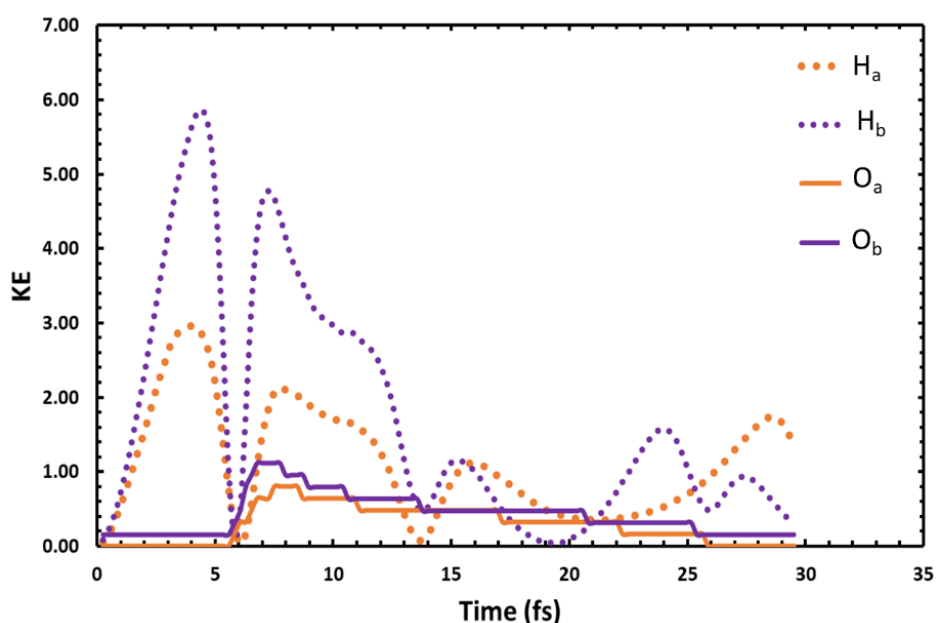


**Figure A.4:** The oxygen atoms ( $O_a$  and  $O_b$ ) gain KE after their collision with the  $H_a$  and  $H_b$ , at 6 fs, during 30 fs TDDFT dynamics of  $W32^{2+}$ .

The H/H+ of the H-bond donating water molecules around  $W32^{2+}$ ,  $H_{D1}$  and  $H_{D2}$ , leave their parent oxygen atom,  $O_{D1}$  and  $O_{D2}$ , respectively. In this process, they acquire some KE and then a part of it is lost, as they collide with the  $O''$ , see figure A.5. This represents the hot atoms chemistry, triggered around the ionized molecule.

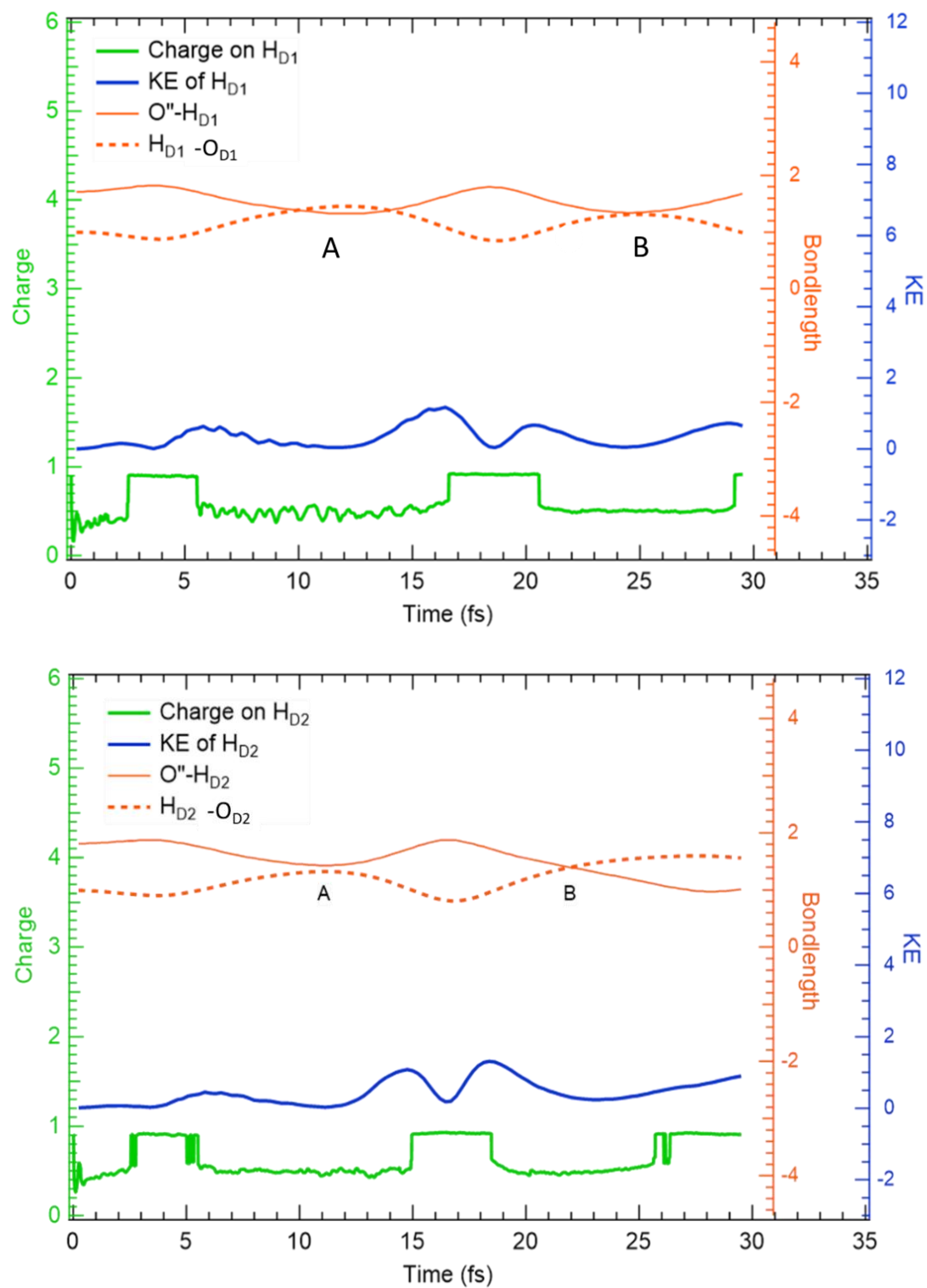


**Figure A.5:** Analysis of  $W32^{2+}$ : Variation in the charge and KE of  $H_{D1}$  (upper panel) and  $H_{D2}$  (lower panel) dissociating from their parent oxygen and  $O''$ .

### II.III. Analysis of the control system (64 H<sub>2</sub>O)

The control system used in this work was a simulation box having 64 H<sub>2</sub>O. The Box size effect is very small for 32 water molecules box and can be neglected for 64 water molecules. The former is commonly used for studying liquid water using first principle study.<sup>2</sup> The analysis of the control system, 64 H<sub>2</sub>O, was performed on the starting Geometry I (non-equilibrated °OH geometry), using both, LSD and no-LSD. The analysis resulted in the formation of H<sub>2</sub>O<sub>2</sub> in most of the cases, as suggested in the literature<sup>3</sup> or in the formation of OH radicals in liquid water, during the 1ps trajectory analysis.

**Table A.1:** Analysis of different dynamics of the control system using protocol B: Species present at the end of 1ps CPMD dynamics. The atoms originating from solvent water molecules are labelled in black, with a subscript 's', the atoms from the doubly ionized dissociation water molecule are labelled in purple. O\* is the oxygen atom of the doubly ionized dissociating water molecule.

System of study / Dissociating $H_2O^{2+}$		Final products after 1ps CPMD trajectory			
NO LSD	Charge 0	W35	W41	W42	W51
		W50	W32	W28	W33
LSD	Charge 0	W35	W41	W42	W51
		W50	W32	W28	W33
System of study / Dissociating $H_2O^{2+}$		Final products after 1ps CPMD trajectory			
NO LSD	Charge 0	W0	W4	W28	W32
		W33	W32	W28	W33
LSD	Charge 0	W0	W4	W28	W32
		W33	W32	W28	W33

II.IV. Additional tests for target system ( $^{\circ}\text{OH} + 63 \text{ H}_2\text{O}$ ) using protocol A

As shown in section 4.2 of chapter 4, the protocol A with the shorter switch was tested for  $\text{W42}^{2+}$ , and the switch geometry with the dissociation bond length of around  $1.5 \text{ \AA}$  was chosen as a suitable pre-dissociated switch geometry. This test was done for two additional dynamics,  $\text{W28}^{2+}$  and  $\text{W32}^{2+}$ . The  $\text{W28}^{2+}$  CPMD resulted in the formation of  $\text{H}_2\text{O}_2$  with a hydroxyl radical ( $\text{O}^{\bullet}\text{H}_b$ ) in its proximity, a Zundel ion and a hydronium ion in liquid water.  $\text{W32}^{2+}$ , on the other hand, resulted in the formation of  $\text{HO}_2^{\circ}$ , but by a three-step process.

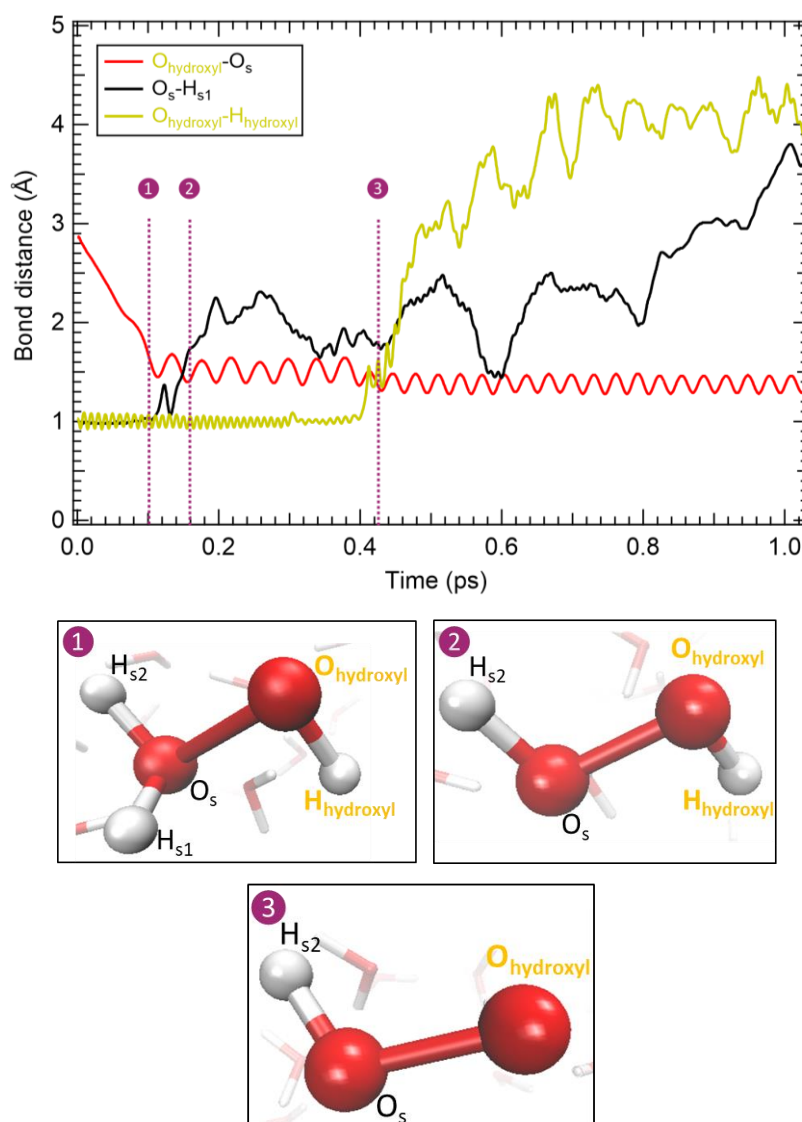
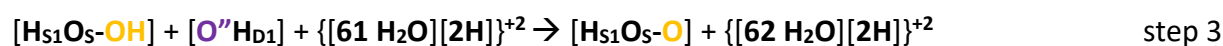
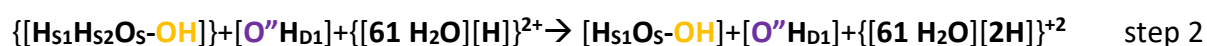


**Figure A.6:** CPMD analysis of  $\text{W32}^{2+}$ : Protocol A applied to  $\text{W32}$  in the non-equilibrated OH geometry, switched at shorter TDDFT switch time (3.3 fs): Complex (1),  $\text{H}_2\text{O}_2$  (2) and the final product,  $\text{HO}_2^{\circ}$  (3), formed along the 1 ps trajectory. The time of formation of the species is labeled in the graph of bond lengths ( $\text{\AA}$ ) variation as a function of time (ps) during the 1 ps trajectory.

The switch from TDDFT to CPMD corresponded to the (3.3fs) configuration, where  $\text{O}''\text{H}_a$  and  $\text{O}''\text{H}_b$  bonds were 1.53 Å and 1.43 Å respectively. At the start of the CPMD analysis, the  $\text{H}_a$  and  $\text{H}_b$  carry +1 charge, each, and bond to  $\text{A}_1$  and  $\text{A}_2$  ( $\text{HO}^\circ$ ), resulting in two positively charged species and simultaneously, one of the H-bond donor donates its  $\text{H}_{\text{D1}}$  to the  $\text{O}''$  resulting in an hydroxyl radical formation  $\text{O}''\text{H}_{\text{D1}}$ . The +2 charge is delocalized in the simulation box having solvent water,  $\text{HO}^\circ$  and  $\text{O}''\text{H}_{\text{D1}}$ .  $\text{HO}^\circ$  reacts with one of the solvent water molecules at 105 fs, when an O-O bond forms between them (see step 1 in the equations as well as in the figure A.6). One of the H from this complex hops to the adjacent water molecule, resulting in the formation of  $\text{H}_2\text{O}_2$  (step 2 in the equations as well as in figure A.6). It is followed by the abstraction of a hydrogen atom from  $\text{H}_2\text{O}_2$ , by a hydroxyl radical ( $\text{O}''\text{H}_{\text{D1}}$ ) in the simulation box (step 3 in the equations as well as in figure A.6), resulting in a superoxide radical.



The species present by the end of 1 ps of the CPMD simulation are the  $\text{HO}_2^\circ$ , a zundel ion (H+ shared between two water molecules) and a hydronium ion in liquid water.

## Appendix III: Spectroscopic studies of biomolecules in aqueous

### III.I. Nitrogen 1s XPS spectra

The solid state N1s spectra of Gly-Gly has two peaks that are not very well resolved (see chapter 5). The best fit, shown in figure A.7, of the experimental spectrum was obtained when the width of the contribution at higher binding energy (Nitrogen of the terminal group,  $\text{NH}_3^+$ ) was larger than the other contribution. This could indicate that more than two components are present in the spectrum.

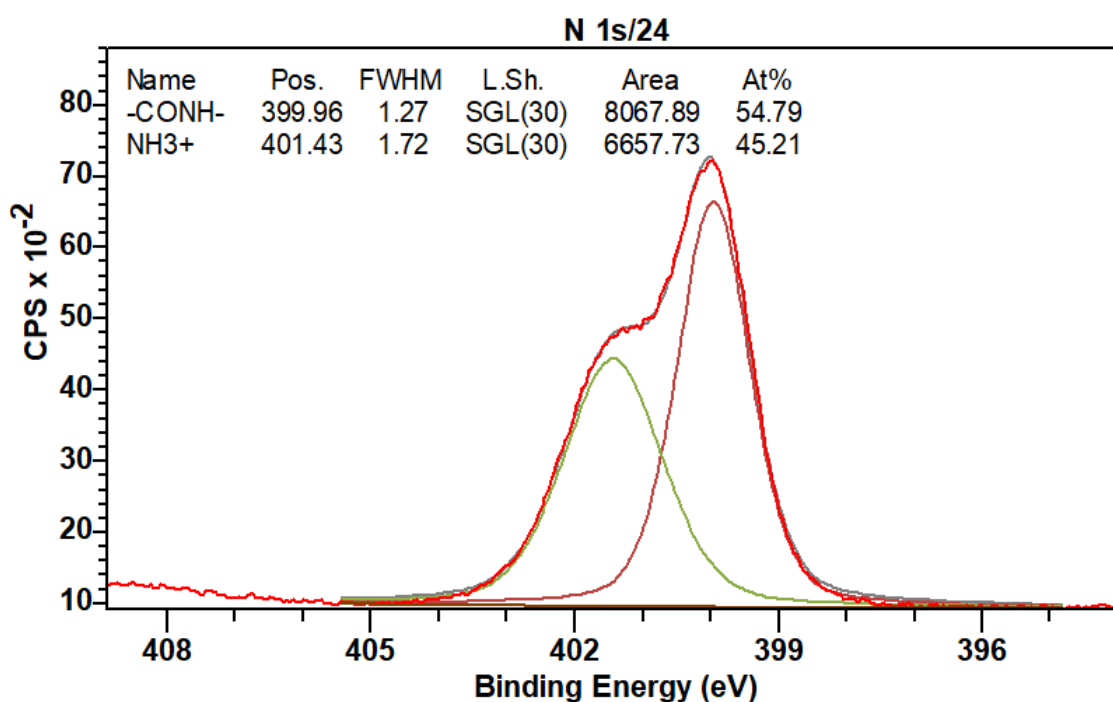


**Figure A.7:** The N 1s spectra of powder sample of Gly-Gly, recorded using laboratory XPS. The fit is performed on CasaXPS.

### III.II. Expected energy shifts in the theoretical DOS values

The theoretically obtained energy values via DOS calculations, for pure liquid water are shown in the table A.2. The different band of the pure liquid water,  $1b_{1\text{water}}$ ,  $3a_{1\text{water}}$ ,  $1b_{2\text{water}}$  and  $2a_{1\text{water}}$ , are also shown in the first column of the table. These values are compared with the experimental values of pure water, reported in the literature.<sup>4,5</sup> The difference between the theoretical and the experimental values is reported as the expected energy shift, in the last column of the table.

**Table A.2:** The expected shift of the theoretical values obtained from the comparison of the theoretical energy values from DOS calculations and the energy values from experimental water band present in the literature.

MOs of water	Theoretical value from DOS calculation	Experimental B.E. for liquid phase <sup>5</sup>	Expected energy shift
<b>1b1</b>	3.2	11.2	8.0
<b>3a1</b>	5.5	13.5	8.0
<b>1b2</b>	8.9	17.3	8.4
<b>2a1</b>	20.9	30.9	10.0

### III.III. Symmetry of molecular orbitals of Gly and Gly-Gly

The sigma type symmetry, i.e. the orbitals lying in the plane of the molecule,<sup>6</sup> at Region 'X' (just before the 1b1<sub>water</sub> band), for both the solutes (Gly and Gly-Gly), are shown in the figure A.8.

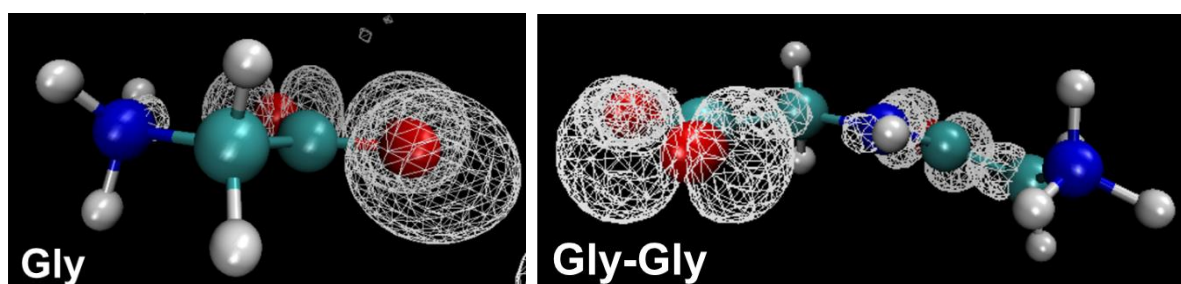


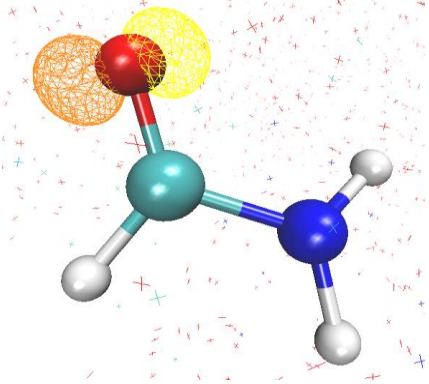
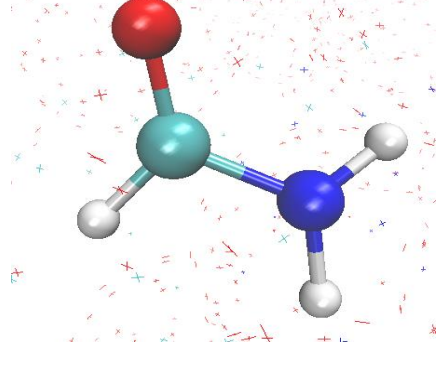
**Figure A.8:** The symmetry of MOs on Gly and Gly-Gly. The contour value used to plot the orbitals is 0.2. For clarity, the water molecules around the solutes are not shown in the figure.

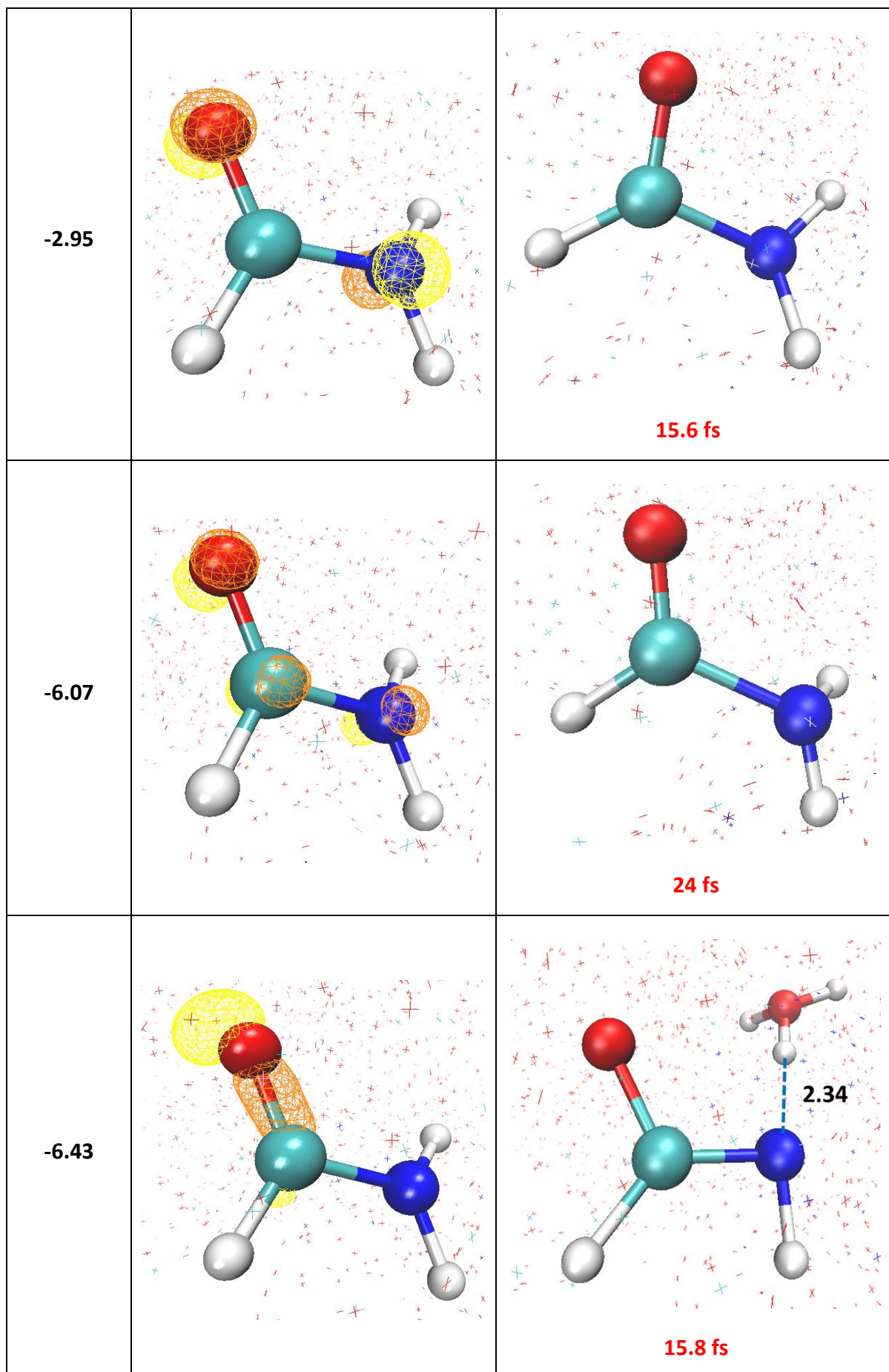


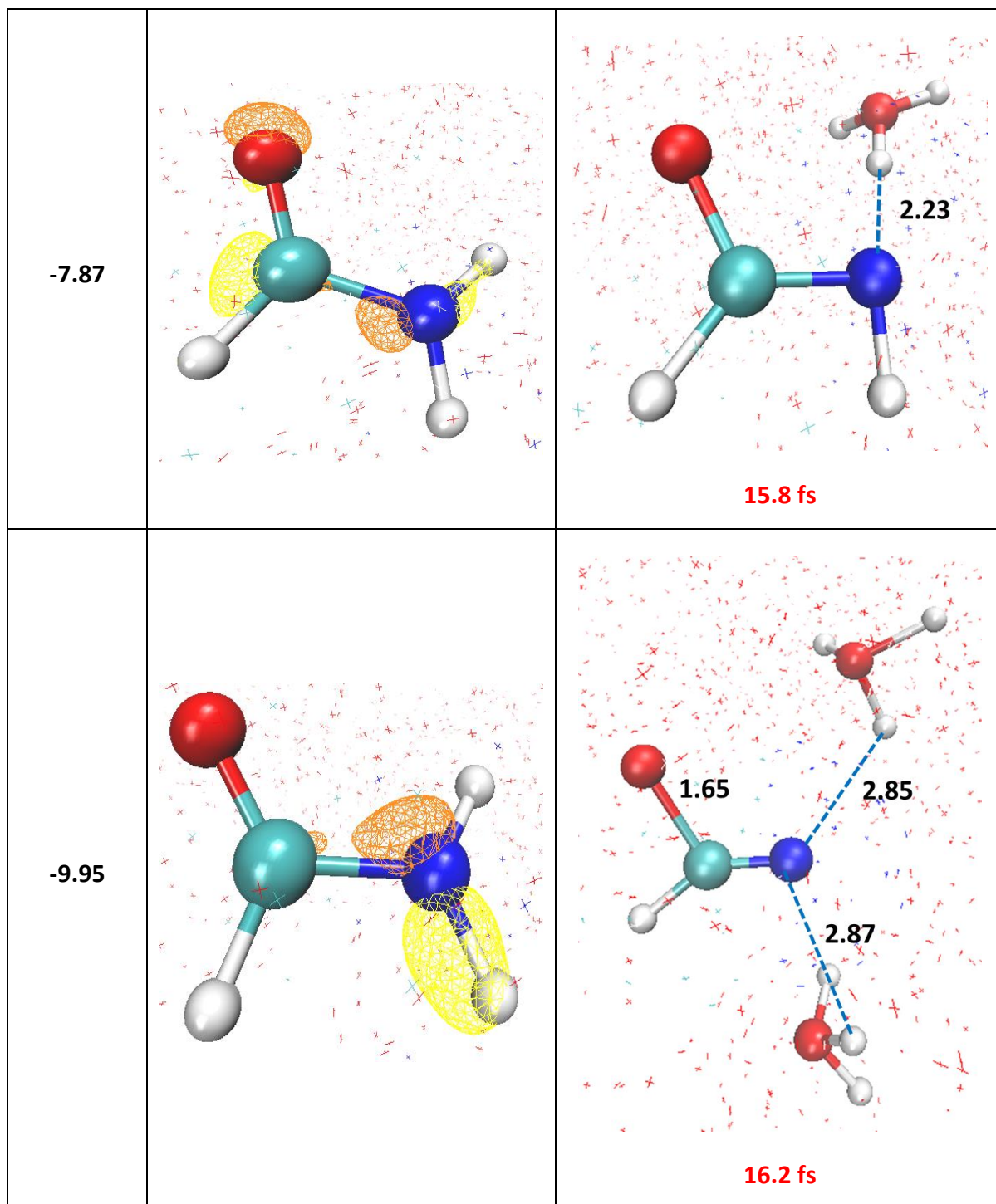
## Appendix IV: TDDFT of solvated formamide

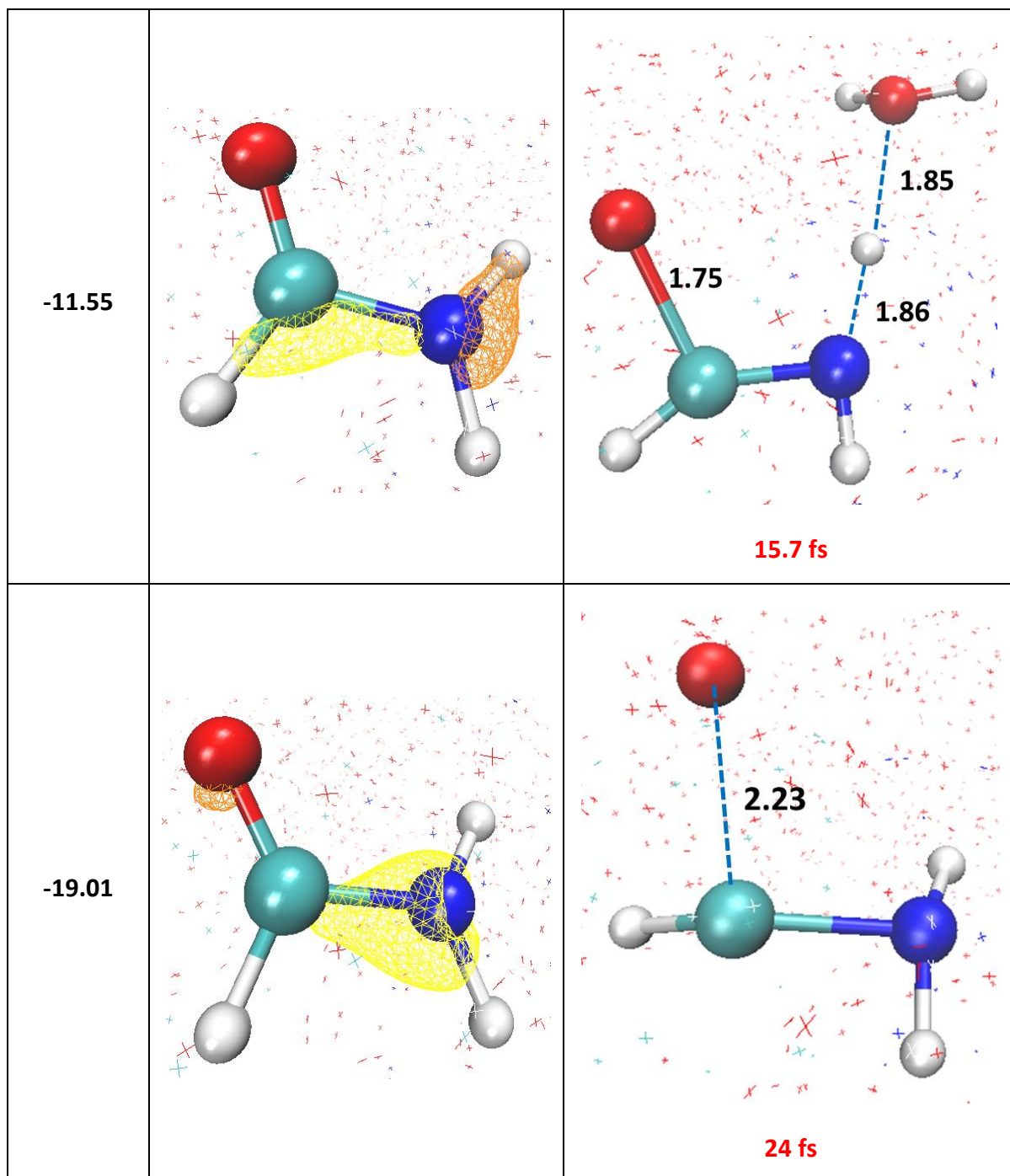
The first steps towards modeling the dissociation of solvated formamide are presented in the table below. Since formamide is a smaller system, when compared to Gly-Gly, large number of starting geometries (with electrons removed from different molecular orbitals, MOs) can be investigated. The first column of the table A.3 depicts the energy of the Wannier orbital from which the two electrons are removed. The second column depicts the Wannier orbital localized on different sites on the formamide molecule, with the contour value of 0.2. The last column shows the final geometry by the end of TDDFT dynamics (time up to which the TDDFT is performed, so far, is written in the table with red). For clarity, only a few water molecules around the solute are presented, when they are involved in the dissociation. All other solvent water molecules are presented as crosses. The TDDFT dynamics that show the bond breaking, among the ones presented in the table below, are being continued. At a certain point, the dynamics will be switched to CPMD, for analyzing the picosecond timescale.

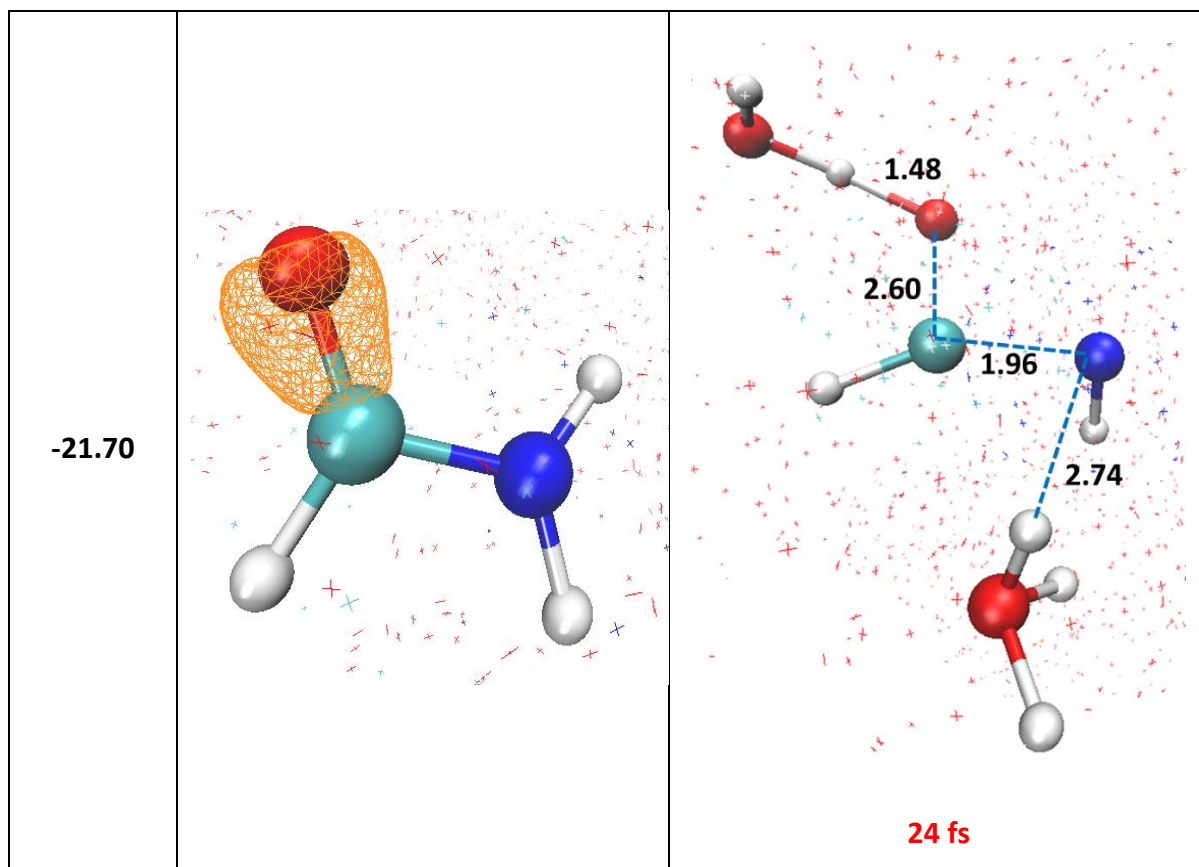
**Table A.3:** TDDFT analysis of formamide by removing two electrons for a specific Wannier MO: The start geometry of formamide, at  $T_{\text{TDDFT}} = 0$  fs and the geometry after few femtoseconds of TDDFT trajectory (marked with red in the table). The MOs are plotted with the contour value of 0.2. The bond lengths are denoted in black in Å and the formation time of the species is denoted in red in femtosecond.

Wannier MO (eV)	Start Geometry	End Geometry
-2.62		 <p style="text-align: center; color: red; font-weight: bold;">24 fs</p>









## Appendix V. List of conferences

The author underlined in the list below is the one who gave the presentation at the conference.

### Oral presentation:

- Rajpal, A.; Huart, L.; Nicolas, C.; Chevallard, C.; Dasilva, P.; Mercere, P.; Politis M.F.; Guigner, J.-M.; Hervé du Penhoat, M.-A.; Renault, J.-P., Detecting superoxide radical anions, resulting from core-shell ionization upon exposure to soft X-rays, *International Conference “Advanced Strategies for Radiotherapy”*, Orsay, France, November **2021**.  
**Prize: Best Oral Presentation by Young Investigator award**
- Rajpal, A.; Huart, L.; Nicolas, C.; Chevallard, C.; Dasilva, P.; Mercere, P.; Politis M.F.; Guigner, J.-M.; Hervé du Penhoat, M.-A.; Renault, J.-P., Detecting superoxide radical anions, resulting from core-shell ionization upon exposure to soft X-rays, *Miller Online Workshop on Radiation Chemistry organized by Miller Trust for Radiation Chemistry*, Online, February **2022**.
- Rajpal, A.; Huart, L.; Nicolas, C.; Chevallard, C.; Dasilva, P.; Mercere, P.; Politis M.F.; Guigner, J.-M.; Hervé du Penhoat, M.-A.; Renault, J.-P., Detecting superoxide radical anions, resulting from core-shell ionization upon exposure to soft X-rays, *3rd International Conference on Ionizing Processes (ICIP)*, Online, July **2022**
- Rajpal, A.; Huart, L.; Nicolas, C.; Chevallard, C.; Dasilva, P.; Mercere, P.; Politis M.F.; Guigner, J.-M.; Hervé du Penhoat, M.-A.; Renault, J.-P., Detecting superoxide radical anions, resulting from core-shell ionization upon exposure to soft X-rays, *2es Rencontres Rayonnement Radio-Chimie (R3C-2022)*, Nice, France, September **2022**

## Appendix VI. List of Publications

The first author is underlined in the list below.

### Published:

➤ **Superoxide Production under Soft X-ray Irradiation of Liquid Water**

Rajpal, A.; Huart, L.; Nicolas, C.; Chevillard, C.; Guigner, J.-M.; Dasilva, P.; Mercere, P.; Gervais, B.; Hervé du Penhoat, M.-A.; Renault, J.-P., *J. Phys. Chem. B* **2023**, 127, 4277–4285

➤ **Radiation-Responsive Benzothiazolines as Potential Cleavable Fluorogenic Linkers for Drug Delivery**

Tuo, W.; Renault, J.-P.; Rajpal, A.; Pin, S.; Le Gall, T.; Taran, F., *Chemistry – A European Journal* **2023**, 29, e202300358.

### To be submitted soon:

➤ **X-ray Photoelectron Spectroscopy of aqueous Glycylglycine using liquid micro-jet**

Rajpal, A.; Renault, J.-P.; Hervé du Penhoat, M.-A.; Milosavljević, A.R., Bozek, J.D., Robert, E.; Nicolas, C.

➤ **Superoxide production in the early stage dissociation of doubly ionized water in liquid water**

Rajpal, A.; Renault, J.-P.; Nicolas, C.; Politis M.F.; Hervé du Penhoat, M.-A.

➤ **Solutions properties can strongly affect soft X-ray induced radiation damage through photoelectron tracks**

Huart, L.; Rajpal, A.; Hervé du Penhoat, M.-A.; Chevillard, C.; Guigner, J.-M.; Palaudoux J.; Robert, E.; Dasilva, P.; Mercere, P.; Nicolas, C.; Renault, J.-P.

➤ **Investigation of the Fragmentation of Doubly-Ionized Deoxyribose: Role of the Liquid Water Environment**

Hervé du Penhoat, M.-A.; Souchaud A.; Rajpal A.; Vuilleumier R.; Gageot M.P.; Tavernelli I.; Fujii K.; Yokoya A.; Tendero S.D.; Politis M.F.

## References

- (1) Ainla, A. *The Multifunctional Pipette. A Microfluidic Technology for the Biosciences*; 2013.
- (2) Grossman, J. C.; Schwegler, E.; Draeger, E. W.; Gygi, F.; Galli, G. Towards an Assessment of the Accuracy of Density Functional Theory for First Principles Simulations of Water. *J. Chem. Phys.* **2003**, *120* (1), 300–311. <https://doi.org/10.1063/1.1630560>.
- (3) Tavernelli, I.; Gaigeot, M. P.; Vuilleumier, R.; Stia, C.; Du Penhoat, M. A. H.; Politis, M. F. Time-Dependent Density Functional Theory Molecular Dynamics Simulations of Liquid Water Radiolysis. *ChemPhysChem* **2008**, *9* (14), 2099–2103. <https://doi.org/10.1002/cphc.200800177>.
- (4) Yang, Y. Structural and Dynamical Properties of Water Adsorption on PtO<sub>2</sub> (001). *RSC Adv.* **2018**, *8*, 15078–15086. <https://doi.org/10.1039/C8RA00952J>.
- (5) Winter, B.; Weber, R.; Widdra, W.; Dittmar, M.; Faubel, M.; Hertel, I. V. Full Valence Band Photoemission from Liquid Water Using EUV Synchrotron Radiation. *J. Phys. Chem. A* **2004**, *108* (14), 2625–2632. <https://doi.org/10.1021/jp030263q>.
- (6) Chem2000\_exercise\_2.1\_sigma\_and\_pi\_symmetry.Pdf. [https://scholar.ulethbridge.ca/sites/default/files/susanfindlay/files/chem2000\\_exercise\\_2.1\\_sigma\\_and\\_pi\\_symmetry.pdf?m=1600442914](https://scholar.ulethbridge.ca/sites/default/files/susanfindlay/files/chem2000_exercise_2.1_sigma_and_pi_symmetry.pdf?m=1600442914) (accessed 2023-07-22).





## LIST OF FIGURES

List of Figures	Page no.
Figure 1.1: Classification of radiations based on their energy and type. The different interactions of the ionizing radiation with the matter are also shown.	3
Figure 1.2: The probability of different interaction processes of ionizing radiation with matter, as a function of incident photon energy and atomic number 'Z' of the target. The probability of the photoelectric effect, Compton scattering and pair production is denoted by $\tau$ , $\sigma$ and $\kappa$ . The two black curves denote the Z values and the photon energies, for which the probability of the neighboring effects is equal. The figure is taken from reference 8.	3
Figure 1.3: Interaction of ionizing radiation with living system, causing damage via either direct or indirect effects. Another type of damage (not shown here) to the biomolecules that occurs due to the transfer of the electrons and holes from the tightly bound solvation shell <sup>14</sup> is the quasi-direct effect. <sup>15,16</sup>	4
Figure 1.4: The absorption of the soft X-ray photons resulting in inner-shell ionization. The unstable system then stabilizes via either a radiative, resulting in 1 hole (1h), or non-radiative normal Auger decay, resulting in 2h. The preferable pathway depends on the atomic number (Z) of the target element.	6
Figure 1.5: Various non-radiative de-excitation pathways as a result of core-excitation of the atom. The well-known pathways include the participator and spectators Auger decay. Another decay pathway that can occur in the case of liquids is the electron delocalization. For each of the de-excitation pathways, the resulting final state is mentioned.	7
Figure 1.6: Non-local relaxation pathway after the core-hole creation: Inter-Coulombic Decay (ICD) in the left involving two molecules in the relaxation process. The relaxation using electron transfer mediated decay (ETMD) is shown in center and on the right, involving two and three different molecules during the decay, respectively.	8
Figure 1.7: Attenuation length of soft X-rays in water and protein, depicting the absorption K edge of the atoms. The water window is the region between the carbon and oxygen absorption K-edges. The attenuation length were calculated using CXRO <sup>42</sup> for water and for a protein with the composition H86C52N13O15S and density of 1.35 g/cm <sup>3</sup> . <sup>43,44</sup>	9
Figure 1.8: Interaction of photons with water: different stages involved in water radiolysis and photolysis based on the time scale of the events (adapted from Le Caër S., Water, 2011 <sup>65</sup> ), resulting in species responsible for indirect radiation damage. The knowledge of dissociation of the multiply ionized water molecule using soft X-rays is scarce.	12
Figure 1.9: IMFP of electrons in liquid water. The figure is taken from the reference [131], depicting the variation in the IMFP from the energy range of 10 eV to 10 keV, using calculations.	21
Figure 2.1: Side view of Gammacell® 3000 <sup>10</sup> . The samples can be placed in the canister for irradiation. Positions A, B and C (not to scale) in the canister refer to the three different heights at which the sample was placed for irradiation	48
Figure 2.2: Fricke Dosimetry-Variation in the dose (Gy) delivered to the Fricke solution (250 $\mu$ l) as a function of irradiation time (min), at a height of 9 cm (position B) in the canister	50
Figure 2.3: Schematic diagram of SOLEIL synchrotron, following a 7 step process to produce synchrotron radiation. <sup>16</sup>	52
Figure 2.4 : optical scheme of the X-UV branch of the METROLOGIE beamline (image adapted from <sup>17</sup> )	53
Figure 2.5: Schematic of the TEMPO beamline having two end station for UVH photoemission and NAP-XPS experiments.	54
Figure 2.6: Schematic of the PLEIADES beamline displaying the three branches for performing experiments with high resolution soft X-rays.	55
Figure 2.7: IRAD set-up installed at the front end of the METROLOGIE beamline, having a differential pumping system. It allows the extraction of beam under vacuum to air. The exit of the IRAD set-up is the 150 nm thick silicon nitride window, transparent to soft X-rays.	57
Figure 2.8: The installation of the microfluidic cell, YAG:Ce and the photodiode (placed at a known distance from each other) on the translation table, in the front of the exit window of the IRAD setup.	58

It should be noted that the distances shown in the figure are not with the sensitive surface of the devices but with the outer measurable surface of the device. The translation table allows the moment of the devices in front of the exit window along different axis, with a greater moment possible in Ts direction.	
Figure 2.9: a) Exploded view and b) assembled front view of the original microfluidic cell design with one Si <sub>3</sub> N <sub>4</sub> membrane on the front silicon chip. The two silicon chips are packed between two PDMS gaskets that prevent leakage of the flowing sample.	59
Figure 2.10: Microfluidic set-up comprising of various microfluidic devices that allow to control the flow of sample through the microfluidic cell. The figure shows the two paths that the liquid can flow through, the microfluidic cell and the bypass.	60
Figure 2.11: Experimental setup to measure interference patterns on the bulging membrane of the microfluidic cell using an optical interferometer (smartWLI, Germany) with a 20X objective. b) Pattern of the fringes when the sample is not flowing (left) and when it is flowing through the microfluidic cell (right).	62
Figure 2.12: Schematic representation of integrating sphere (image on the right) and the diffuse reflectance measurements (measurement light is irradiated at 0°, on the sample), on the left, used for measurement of the UV-vis spectra in reflectance. Images are taken from Shimadzu's website. <sup>29</sup>	64
Figure 2.13: Schematic of XPS setup with a hemispherical electron analyzer <sup>35</sup>	66
Figure 2.14: a) NAP-XPS end station; b) Sample holder; c) Sample analysis using NAP lens of 0.3 mm aperture set-up at TEMPO beamline, SOLEIL synchrotron.	69
Figure 2.15: Schematic diagram (left) and experimental image (right) of the liquid jet XPS set-up at PLEIADES beamline to perform high-resolution spectroscopy of liquid samples	70
Figure 2.16: Secondary electron cut off spectra for 50 mM KCl solution before calibration (blue curve) and after calibration (black curve). The value of the work function obtained (before calibration = x and after calibration = y) from the fitting function is shown in by red curve. The reported spectra were recorded at the bias of -50 V (subtracted on figure).	72
Figure 2.17: The plot of potential energy (E) vs the interatomic distance (R) between two covalently bonded atoms. The harmonic potential (red curve) is a good approximation for the exact potential between two covalently bonded atoms (blue curve) around its minimum, in the vicinity of the equilibrium inter-atomic distance. <sup>75</sup> It however does not allow the study of bond-breaking and bond-forming.	75
Figure 2.18: Preparation of starting geometries (I, II and III) of the target system, prior to double ionization. The first step corresponds to the removing of a hydrogen atom from a water molecule to have a hydroxyl radical in liquid water and it is followed by the equilibration step of 1 ps, using BO MD.	85
Figure 2.19: The scheme shows two protocols, A and B, used in our study to understand the dissociation of a doubly ionized water molecule in proximity of an OH radical in liquid water. The scheme presents the analysis of the target system. The water molecules selected in the first and the second hydration sphere of °OH, to perform dissociation studies, are labeled in purple. The two protocols are explained using one of the scenarios under investigation, i.e. W42 as the dissociating doubly ionized water molecule. The OH dissociation length, labelled in protocol A and B corresponds to that at 3.4 fs after the TDDFT trajectory.	89
Figure 2.20: The parameters of the pre-dissociated water molecule, W42, selected for protocol B.	89
Figure 2.21: The criteria used for defining the H-bond in the present work: The bond distance (r <sub>O-O</sub> ) between the oxygen atom of the accepting and donating water molecule is less than 3 Å and the angle β is less than 20°.	92
Figure 3.1: WST8 reducing to its formazan product.	105
Figure 3.2: Different pathways for the reduction of the chemical probe, WST-8, to the formazan product that gives a characteristic signal in UV at 460 nm.	106
Figure 3.3: The absorption spectrum, from 400 nm to 600 nm, at different irradiation conditions. The concentration of WST-8 was 300 μM and the concentration of SOD and catalase was 0.62 μM. The samples were irradiated at 45 Gy using the gamma source with the dose rate of 5.5 Gy/min. The dose response curve for each condition is given in the appendix.	108
Figure 3.4: Validation of the chemical system, when irradiated at 45 Gy, with the gamma source (5.5 Gy/min) in different conditions. The yields were calculated from the absorbance values at 460 nm recorded using the conventional UV-vis spectrophotometer (see figure 3.3 for complete absorption	109

spectra). The yields reported in the figure are an average of 5 data points and their standard deviation is plotted as error bars.	
Figure 3.5: Variation in absorbance of the probe, WST8, a) as a function of its concentration, ranging from 100 $\mu\text{M}$ to 500 $\mu\text{M}$ , irradiated at 100Gy; b) as a function of SOD concentration (from 0 $\mu\text{M}$ to 3.1 $\mu\text{M}$ ) with 300 $\mu\text{M}$ WST8 concentration @45Gy, when irradiated by a Cs-gamma source. The absorbance values plotted in the figure are an average of 5 data points and the error bars correspond to their standard deviation.	110
Figure 3.6: Average yield (of five data points per condition) of the reduced probe (300 $\mu\text{M}$ ) focusing on the two irradiation conditions which enable determining the direct $\text{HO}_2^\circ$ yield (among the six displayed in figure 3.3). The solutions were irradiated at 45 Gy, with a gamma source (5.5 Gy/min). The concentration of SOD and catalase were 500 times lower (0.62 $\mu\text{M}$ ). The error bars are standard deviation of the five data points for each condition.	112
Figure 3.7: a) Exploded view of the modified microfluidic cell design having two $\text{Si}_3\text{N}_4$ membranes b) back view of the assembled microfluidic cell, with a transparent square corresponding to the observation window, allowing the transmission of the beam	114
Figure 3.8: Installation of microfluidic cell and the alignment devices on the translation table of the IRAD setup (allowing the motion along different axis (Ts, Tx and Tz). The microfluidic cell is in the center with a scintillator (YAG:Ce) to its left and a photodiode with an aluminium mask to its right. Each device was also mounted on a one-direction manual translation device (along the TS-axis).	115
Figure 3.9: Beam shape visualized through the YAG crystal etched with the dimensions of the front silicon nitride membrane, captured using the CCD camera. The left and the right images was captured with the monochromator slit size of 200 $\mu\text{m}$ and 400 $\mu\text{m}$ , respectively.	116
Figure 3.10: a) Tx and b) Tz scans on the Ghost membranes: broken (green curves) and the intact (red curves) membranes taped on aluminum mask of the photodiode, at 1620eV with 500 $\mu\text{m}$ vertical slits and a Boron (0.4 $\mu\text{m}$ ) inline filter. The cell was translated horizontally (Tx), with a step of 0.05 mm and vertically (Tz) with a step of 0.1 mm, in front of the exit window of the IRAD set-up (in front of the synchrotron beam). The measurements are obtained with an air gap of 2 mm between the exit window of the IRAD setup and the aluminium mask of the photodiode.	117
Figure 3.11: SiPM installed behind the cell, allowing the detection of transmitted beam, thanks to the scintillator that converts X-rays to visible light. a) Exploded view of the modified cell with the SiPM behind; Photograph of b) the cell support back (left) and front (right) made of PEEK, to support the YAG:Ce (not visible), the microfluidic cell and SiPM; c) the entire assembly (microfluidic cell with the SiPM in the support) placed at a distance of 1 mm from the exit window of the IRAD setup on the METROLOGIE beamline at synchrotron SOLEIL, for in-air irradiations experiments.	120
Figure 3.12: Attenuation of the SR beam in water (5 $\mu\text{l}/\text{min}$ flow rate) resulting in a reduction of the SiPM signal (blue curve) when compared to the SiPM signal when the cell is filled with air (red curve). Both the signals are normalized with respect to the SiPM signal in air. The cell was translated horizontally, with steps of 0.05 mm in front of the exit window of the IRAD set-up (i.e. in front of the synchrotron beam). Both the curves were normalized with respect to the SiPM signal in air, so that the maximum of the red curve (channel filled with air) is 1.	121
Figure 3.13: variation in vertical width as a function of slit size of the beamline monochromator	122
Figure 3.14: Schematic diagram of the UV detection cell having a Z-geometry. The cell has a PEEK outer body and provides the connections for optical fibers and the fluidics. The optical path of the cell is 2.5 mm. The image is taken from SMA-Z drawing of FIALab.	123
Figure 3.15: Sensitive detection system: Coupled microfluidic setup with in-line UV detection cell. The cell is connected to the spectrometer (QE pro) and the light source using the optical fibres, allowing detection of extremely low radical yields.	124
Figure 3.16: Experimental raw data obtained using the in-line detection set-up, recording the beam on (30 mins) and beam off (30 mins) absorbance signal. Depicted absorbance trace was monitored at the desired wavelength (460 nm) of the reduced product.	126
Figure 3.17: Variation in the current of the photodiode by varying the photon energy, at 500 $\mu\text{m}$ slit size, with a B (0.4 $\mu\text{m}$ ) inline filter, 4.06 mm air gap between the exit window of the IRAD setup and the photodiode sensitive area, measured through the broken ghost membrane.	129
Figure 3.18: a) Pattern of the interference fringes when the sample is not flowing (left) and when it is flowing through the microfluidic cell (right) placed under the interferometer. b) 2D Image obtained from Interferometry representing the size of the membrane (1 mm x 0.3 mm) using a 10X objective	131

by placing the microfluidic cell directly under the interferometer, for a pressure applied of XX mbar. The color scale in the figure corresponds to the z axis of the 2D image.	
Figure 3.19: Deformation of the microfluidic cell's membranes, front and back, upon applying pressure for the sample to flow. Each reported values is an average of 3 data points, recorded at different times.	131
Figure 3.20: The decrease in the intensity of the beam when the distance between the microfluidic cell window and the exit window of the IRAD setup is increases. The minimum possible distance between the two is 1 mm, to avoid the breaking of the windows. The linear trend represents the absence of higher-order light at 1280 eV (blue curve) and the non-linear trend shows the contribution from higher-order light at 890 eV (red curve).	133
Figure 3.21: Experimental data obtained using the in-line detection set-up, after the data treatment (difference between the absorbance at 460 nm and that at 800 nm). The beam was periodically on and off. Absorbance were measured for a 300 $\mu$ M WST8 solution in anoxic condition, without SOD and without catalase, at 5 $\mu$ L/min corresponding to 32 Gy at 1620 eV	136
Figure 3.22: Yield of direct HO <sub>2</sub> <sup>o</sup> production resulting from the difference of the yield of the reduced probe in anoxic (condition 2) and anoxic+SOD+catalase (condition 4), using synchrotron 1620 eV soft X-ray.	137
Figure 3.23: Variation in the concentration of the reduced probe (WST8 formazan, oxic conditions) as a function of dose, with 500 $\mu$ m monochromator slit size, at two different photon energies, namely, 1100eV and 1700eV.	141
Figure 3.24: Evolution of the yield of indirect HO <sub>2</sub> <sup>o</sup> (green symbols) as a function of photon energy and the MC simulation (black curve) results for superoxide. <sup>31</sup> The uncertainties on each energy are reported in the table 3.3. The yields below 1 keV were measured only once and those above 1 keV are an average of yield at 3 different flowrates (see text).	142
Figure 4.1: Systems of interest presented using a visualizing software, VMD.4 a) Target system with an OH radical in liquid water; b) Control system, with only water. For clarity, the surrounding water molecules are kept translucent. The dissociating molecule is presenting with purple annotations, the hydroxyl radical is presented with yellow annotations and for all other molecules black annotations are used. Oa and Ob are the oxygen atoms of the water molecules hydrogen bonded to Ha and Hb, respectively.	153
Figure 4.2: Water molecules selected (W28, W32 and W42) in the first hydration sphere of HO <sup>o</sup> , in Geometry I, to perform the dissociation studies. The figure shows the distance (in Å) between the oxygen atoms of the dissociating doubly ionized water molecule and the hydroxyl radical, in the simulation box of size 12.43 Å.	154
Figure 4.3: W322+ fragmentation dynamics: a) W32 and its first hydration sphere at the onset of TDDFT trajectory, which was initiated by removing two electrons from the 1b1 MO of W32 and; the donating groups are shown with symbol D and accepting groups are shown with symbol A. One of the accepting groups (A1) is the initial hydroxyl radical ( <sup>o</sup> OH); b) the path (black and green lines) traced by the atoms (Ha, Hb, HD1, HD2) with considerable KE, during the 30 fs TDDFT trajectory, plotted with the initial geometry of oxygen (red spheres) and hydrogen (white spheres) atoms; c) Final species after 30 fs TDDFT analysis, involving two additional water molecules adjacent to the accepting groups. For clarity, the surrounding water molecules that do not interact during the analysis are not shown in the figure.	156
Figure 4.4: Analysis of W322+: Variation in the charge (in e) and KE (in eV) of a) Ha and b) Hb dissociating from their O" parent oxygen, and their respective distances with the neighboring oxygen atoms (in Angstrom).	158
Figure 4.5: CPMD analysis of W322+ after the switch from TDDFT: Formation of HO <sub>2</sub> <sup>o</sup> along the CPMD trajectory, evident from the variation in the bond lengths (in Angstrom).	159
Figure 4.6: W282+ dynamics study of target system: The trajectory of Ha, Hb and HD1, hoping between different oxygen atoms. The hydroxyl radical ( <sup>o</sup> OH) is present behind W28. For clarity, <sup>o</sup> OH and other solvent water molecules are not shown in the figure. The isovalue used for the density contour around the oxygen atoms is 0.5. The trace shows two regions, one where the atoms behave like protons (green trace), having a charge more than 0.85e in the vicinity of the oxygen atoms and the other where they behave like a hydrogen atom (pink trace), having a charge less than 0.45e.	161
Figure 4.7: Variation in the KE of Ha and Hb along the 30 fs TDDFT trajectory, for W42.	162
Figure 4.8: W422+ dynamics: Path traced by Ha and Hb during the CPMD trajectory. The atoms O",	166

<p>Ha and Hb are represented as spheres and their positions correspond to the start of the CPMD trajectory. For simplicity, the trajectory is shown only for the first 24 fs and the neighboring water molecules are kept hidden.</p>	
<p>Figure 4.9: Protocol B applied to W32 in the non-equilibrated OH geometry: Initial geometry (①), intermediate product (②), H<sub>2</sub>O<sub>2</sub>, and the final product (③), HO<sub>2</sub>. The time of formation of the species is indicated on the bottom left corner, in green, and is labeled in the graph of bond lengths (Å) variation as a function of time (ps) during the 1 ps trajectory. All the atoms apart from the dissociating water molecule and the °OH are assigned the subscript 's' to denote that they belong to the solvent water molecules.</p>	168
<p>Figure 4.10: W422+ CPMD trajectory on the non-equilibrated OH geometry (geometry I) during the first 48 fs: Path traced by the Ha and Hb of the dissociating doubly ionized water molecule (W42) in the simulation box, using the protocol A and B. The bond lengths, O"Ha = 1.52 Å and O"Hb = 1.50 Å, labelled in the figure corresponds to the start of the CPMD trajectory. The white spheres represent Ha and Hb and red sphere represent the O", at the start of the CPMD trajectory. For clarity, surrounding water molecules, present in the simulation box, are hidden.</p>	170
<p>Figure 4.11: The seven water molecules, labeled in purple, selected to study the interaction of a pre-dissociated water molecule with its surrounding water molecules and a hydroxyl radical, labeled in yellow. Five of these water molecules are present in the first hydration sphere of the hydroxyl radical and the other two are far from the hydroxyl radical.</p>	171
<p>Figure 5.1: Chemical structure of a) Glycine and b) Glycylglycine, in their zwitterion forms. The nitrogen atoms are numbered in blue, starting from the N terminal and the carbon atoms are numbered in red, starting from the C terminal.</p>	180
<p>Figure 5.2: C1s XPS spectra recorded at 400 eV: Liquid-state XPS spectra of a) Gly (brown curve) and b) Gly-Gly (green curve) compared with their solid-state XPS spectra (black curves). The liquid-state (pass energy 50 eV) and solid-state XPS spectra (pass energy 20 eV) were recorded with a resolution of 0.32 eV and 0.35 eV, respectively. The peaks were fit using the line shape SGL(30) and the contribution from each spectral peak is shown (red, bottom scale) for the liquid-state spectra, with Tougaard background. The MC peak fit model simulation, a feature that is inbuilt in the CasaXPS, was used to check the quality of the fit. The peak fit model had negligible standard deviation for peak positions.</p>	182
<p>Figure 5.3: N1s XPS spectra recorded at 600 eV: Liquid-state XPS spectra of a) Gly (brown curve) and b) Gly-Gly (green curve) compared with their solid-state XPS spectra (black curve). The liquid-state (pass energy 50 eV) and solid-state XPS spectra (pass energy 20 eV) were recorded with a resolution of 0.32 eV and 0.35 eV, respectively. The peaks were fit using the line shape SGL(30) and the contribution from each spectral peak is shown (red, bottom scale) for the liquid-state spectra, with a linear background. The MC peak fit model simulation, a feature that is inbuilt in the CasaXPS, was used to check the quality of the fit. The peak fit model had negligible standard deviation for peak positions.</p>	185
<p>Figure 5.4: Secondary electron cut off spectra for a) 1 M Glycine (brown symbols) and b) 1 M Gly-Gly solutions (green symbols), at pH 7. The value of the work function obtained from the fitting function (red line) is shown in the figure. The value obtained is found to be comparable to that obtained using the peak differences between the solid and liquid (see text). The reported spectra were recorded at the bias of -50 V (subtracted on each figures).</p>	187
<p>Figure 5.5: Liquid phase valence band spectra measured at 91.2 eV photon energy with a 10 eV pass energy for a) 50 mM KCl (blue), 1 M Gly (brown) and 1 M Gly-Gly (green), with the y-axis in logarithmic scale. The graph represents the intensity variation as a function of experimental ionization energy (eV) on the X-axis. The extrapolation of the slope of band 'B', b) for 1 M Gly and c) 1 M Gly-Gly, is represented with solid yellow line with 99% confidence bands shown in dotted yellow lines. The background of the curve is represented by solid red lines with 99% confidence bands shown in dotted red lines.</p>	190
<p>Figure 5.6: Density of states calculation for a system of pure water (dotted blue curve), Gly-Gly in water (solid green curve) and Glycine in water (solid brown curve). The peaks of pure water system are labelled by comparison with the data present in the literature.<sup>30</sup> The computed DOS is normalized with respect to the number of electrons present in each system to have a reasonable comparison. The magnified image of the DOS (bottom figure) shows low intensity peaks belonging to the MO of Gly and Gly-Gly.</p>	191

Figure 5.7: Solid state valence spectra of powdered Gly (brown curve) and powdered Gly-Gly (green curve). The spectra was recorded at the pass energy of 20 eV with a resolution of 0.35 eV. The binding energy is calibrated with respect to the gold Fermi level.	192
Figure 5.8: Kohn-Sham orbitals, computed at the regions of interest for a solute, Gly (left panel) and Gly-Gly (right panel), surrounded by water molecules in a simulation box (contour value: 0.05). For clarity, only a few water molecules around the solute are presented, only when they share a contribution in the electron density. The KS orbitals for the region ① are not shown as they majorly belonged to water.	194
Figure 5.9: The resonant studies for a) Gly and b) Gly-Gly, at the carbon edge. For both a and b, the upper panel shows the 2D resonant absorption map along with partial electron yield NEXAFS-like spectrum, near the carbon edge. The middle panel shows the RAS spectra at the resonance and off-resonance (black curves). The lower panel shows the comparison between the solid-state valence spectrum (yellow curve) and the resonance spectra. The brown and green curves correspond to Gly and Gly-Gly, respectively. The maps were recorded at a bias of -50 V and the RAS spectra were recorded at a bias of -100 V, to eliminate the contribution from the gas phase around the cylindrical liquid jet. The vertical blue bars in the RAS spectra of Gly-Gly indicate photoelectrons generated by the higher order light. The red dotted bars correspond in maps and in spectra to specific regions detailed in the text. The binding energy values in solid-state spectra are referenced with respect to the Fermi level of gold. The energy scaling (x axis) factor in solid and liquid spectra corresponds to the work function of the sample (4.8 eV for Gly and 4.9 eV for Gly-Gly).	201
Figure 5.10: The RAS spectra of 1 M Gly at the resonance and off-resonance normalized with respect to the 1b1 state of water, to visualize the difference in the shape of the spectrum due to the resonance enhancement. The spectra were recorded at a bias of -100 V, to eliminate the contribution from the gas phase around the cylindrical liquid jet.	203
Figure 5.11: The resonant studies for a) Gly and b) Gly-Gly, at the nitrogen edge. For both a and b, the upper panel shows the 2D resonant absorption map along with partial electron yield NEXAFS-like spectrum, near the nitrogen edge. The lower panel shows the RAS spectra at the resonance energy and off-resonance (black curves). The Gly RAS spectra were recorded at the same resonance energy as Gly-Gly, as no resonance is observed in the 2D map of Gly. The brown and green curves correspond to Gly and Gly-Gly, respectively. The maps were recorded at a bias of -50 V and the RAS spectra were recorded at a bias of -100 V, to eliminate the contribution from the gas phase around the cylindrical liquid jet. It should be noted that the quality of normalization by the photon flux was much better than in the case of carbon, as the flux determination is more precise at the N edge.	206
Figure 5.12: Schematic band structure of liquid phase (left) and solid phase (right) a) Gly and b) Gly-Gly. Both Gly and Gly-Gly behave as n type semiconductors, having electrons close to the LUMO (conduction band) and hence can be easily excited to LUMO.	209
Figure 5.13: Band gap determination for Gly and Gly-Gly in solid state (powder) (a and b) and in liquid state (c and d), using tauc plot. Gly is represented with brown curves and Gly-Gly is represented with green curves. The band gap is determined by the extrapolation of the slope, represented in solid black line, with 99% confidence bands shown in dotted black lines. The background of the curve, represented by horizontal solid black lines, with 99% confidence bands shown in horizontal dotted black lines. The plotted graphs are an average of three measurements each.	210
Figure 6.1: Time resolved detection of the product formation (figure adapted from Ph. Wernet et al. 2015.)	222
Figure 6.2: Core-ionization resulting in the superoxide formation and solvated electron tracks.	222
Figure 6.3: Monitoring the superoxide production as a function of time.	223
Figure 6.4: a) Comparison of the raw data of core-XPS of solvated Gly-Gly, recorded using NAP-XPS (obtained at TEMPO beamline, SOLEIL) (with the darkest color representing first acquisition, then the lightest ones representing the two next consecutive acquisitions. Each acquisition takes ~40 s) and liquid microjet XPS (obtained at PLIEADES beamline, SOLEIL). For liquid microjet, the sample was irradiated in a fine jet that renewed the sample and avoided damage. For NAP-XPS, the sample was irradiated in droplet form. b) The different stages of the Gly-Gly droplet formation during NAP-XPS analysis. The powder was first placed in a sample holder (initial state). A droplet formed at a temperature of 284 K and a pressure of 6 mbar (intermediate state), and XPS spectra were recorded. Finally, the droplet froze when the temperature went up and the sample could be recovered (final state) by stopping the vacuum.	224

<p>Figure 6.5: a) shows the schematic and b) shows the experimental image of the successful coupling of the microfluidic setup with the in-line UV cell and in-line mass spectrometer at the Metrologie beamline XUV branch, SOLEIL synchrotron, by extracting the beam in air, using the IRAD setup; c) shows the raw data obtained via the in-line mass analysis for 10 mM Gly-Gly. The entire mass spectra was recorded during the analysis and for each mass (black curve), it was possible to follow the evolution with time (red, green and blue curves).</p>	226
<p>Figure 6.6: a) The schematic of the commercially available gas permeable Teflon tube, permeable to certain gases; b) The coupling of the microfluidic cell with the Teflon tube. The upper panel shows the schematic and the lower panel shows the experimental image of the coupled setup; c) Raw data, variation in the intensity of a particular mass as a function of time, obtained from in-line RGA analysis. The time at which the beam was turned off (no irradiation) and on (irradiation) is by green and red vertical lines, respectively.</p>	228
<p>Figure 6.7: 14.4 fs TDDFT trajectory analysis of solvated Gly-Gly: Two electrons are removed from the molecular orbital localized on the C=O of the peptide bond at <math>t = 0</math>. a) The variation in the bond angle (centered on the carbon of the peptide bond); b) the variation in the C=O bond length involved in the peptide bond and c) the variation in the N-H bond length involved in the peptide bond and O-H bond length involving the oxygen atom of the neighboring water molecule. The configuration of the molecule is shown at the start of TDDFT, i.e. at TTDDFT = 0 fs, at TTDDFT = 6.4 fs and at TTDDFT = 14.4 fs. The water molecules that were hydrogen bonded at the start of the TDDFT analysis are shown, whereas all other solvent molecules are represented as dots; d) The time evolution of the kinetic energy of the oxygen and hydrogen atoms, involved in the peptide bond.</p>	230



## LIST OF TABLES

List of tables	Page no.
Table 2.1: List of chemicals used in the thesis, along with their specification, brand name and reference.	43
Table 2.2: List of devices/instruments used in the thesis, along with their specifications and supplier.	44
Table 2.3: Variation in dose rate inside the Gamma cell with respect to sample volume and position in the canister.	50
Table 2.4: List of systems studied in this work along with the simulation box size and available valence electrons in the system.	84
Table 2.5: Effective Wannier MO centered on W42. The other water molecules in the simulation box are hidden for clear visuals. The Wannier MO contours are represented with an iso-value of ( $\pm 0.06$ ), where the orange color denotes positive value and the yellow color denotes a negative value.	87
Table 2.6: Comparison of CPU time for the target system ( $\text{HO}^\circ + 63 \text{H}_2\text{O}$ ) using TDDFT MD (0.18 fs) and CPMD (120 fs).	92
Table 3.1: Different experimental conditions used to identify the contribution from different reaction pathways, for the reduction of the chemical probe, WST8. Different chemicals that were used are Superoxide Dismutase (SOD), Catalase, NaCl and Ethanol. (Tested using the Cs137 gamma source).	107
Table 3.2: Dose delivered (Gy) to the sample at different photon energies, as a function of flowrate	133
Table 3.3: Uncertainty in dose calculation as a function of photon energy, as detailed in reference <sup>29</sup> .	134
Table 4.1: Performing CPMD analysis with switch geometries at, a) $T_{\text{TDDFT}} = 3 \text{ fs}$ ; b) $T_{\text{TDDFT}} = 3.4 \text{ fs}$ and c) $T_{\text{TDDFT}} = 3.8 \text{ fs}$ along the 30 fs TDDFT trajectory. The initial parameters of the switch geometry are presented in the table, where the bond length of the dissociating molecule are shown in purple, the angle is shown in orange and the KE of $\text{H}_a$ and $\text{H}_b$ are shown in blue.	165
Table 4.2: Distance between the oxygen atoms of the pre-dissociated water molecule and hydroxyl radical, at the start of the CPMD analysis. For each case studied, it is indicated whether the superoxide radical was formed or not and the time of its formation is also indicated in femtoseconds.	172
Table 4.3: The final species present at the end of one picosecond CPMD. $\text{H}_3\text{O}^+$ in the table corresponds to the localized +1 charge (either hydronium ion or $\text{H}_5\text{O}_2^+$ ) and $\text{H}^+$ corresponds to the delocalized +1 charge. The color code (purple for pre-dissociated water molecules, yellow for the initial hydroxyl radical and black for solvent molecules) shows the atoms origin in the end products.	173
Table 4.4: A summary of the species involved in the formation of superoxide radical, as an end product after 1 ps trajectories, using the protocol B	174
Table 5.1: Summary of the peak positions in their solid and liquid XPS spectra (C 1s and N 1s spectra), for Gly and Gly-Gly. The literature values for the peaks position in the solid and liquid states are also presented. The difference in the respective peak position in solid and liquid phase spectra are reported as the work function ( $\Phi_{\text{indirect}}$ ). The work function obtained from the SECO spectra ( $\Phi_{\text{direct,Gly}}$ , $\Phi_{\text{direct,Gly-Gly}}$ ) is also reported.	188
Table 5.2: Summary of the distinct features observed in the DOS of aqueous zwitterionic Gly and Gly-Gly. Here, n denotes lone pair, $\sigma$ denotes significantly delocalized sigma orbitals, $\pi_n$ denotes pi non-bonding orbital and $\pi_b$ denotes pi bonding orbital. The attribution to these regions is given by comparing the theoretical values with the literature SCF calculations for zwitterionic isolated Gly and Gly-Gly. The theoretical energy value (Theor. value) is the one computed from the AIMD simulation and these values can be compared to the experimental energy values by considering the respective energy shift factor (see text).	195
Table 5.3: Summary of characteristic features observed in the partial electron yield NEXAFS-like spectrum, for 1 M Gly and 1 M Gly-Gly aqueous solutions, at the carbon K-edge. Reference data reported in the table is for Gly and Gly-Gly in solid state or using DFT calculations for their zwitterionic form.	198
Table 5.4: Summary of characteristic features observed in the partial electron yield NEXAFS-like spectrum, for aqueous solutions of 1 M Gly-Gly, at the nitrogen K-edge. Reference data reported in the table is for Gly-Gly in solid state or using DFT calculations for its zwitterionic form. There is no characteristic feature observed for Gly.	207

## LIST OF ABBREVIATIONS

<b>Abbreviations</b>	<b>Meaning</b>
<b>SR</b>	Synchrotron Radiation
<b>ROS</b>	Reactive Oxygen Species
<b>XPS</b>	X-ray Photoelectron Spectroscopy
<b>NAP-XPS</b>	Near Ambient Pressure X-ray Photoelectron Spectroscopy
<b>ICD</b>	Intermolecular Coulombic Decay
<b>ETMD</b>	Electron Transfer Mediated Decay
<b>XFEL</b>	X-ray Free Electron Laser
<b>XAS</b>	X-ray Absorption Spectroscopy
<b>AES</b>	Auger Electron Spectroscopy
<b>XES</b>	X-ray Emission Spectroscopy
<b>PE</b>	Photo-electron
<b>BE</b>	Binding Energy
<b>FWHM</b>	Full Width at Half Maximum
<b>NEXAFS</b>	Near Edge X-ray Absorption Fine Structure
<b>PEY</b>	Partial Electron Yield
<b>IMFP</b>	Inelastic Mean Free Path
<b>NBT</b>	Nitroblue Tetrazolium
<b>WST</b>	Water Soluble Tetrazole
<b>SOD</b>	Superoxide Dismutase
<b>PDMS</b>	PolyDiMethylSiloxane
<b>MO</b>	Molecular Orbital
<b>HOMO</b>	Highest Occupied Molecular Orbital
<b>LUMO</b>	Lowest Unoccupied Molecular Orbital
<b>OD</b>	Optical Density
<b>SECO</b>	Secondary electron cut off spectra
<b>AIMD</b>	Ab Initio Molecular Dynamics
<b>LET</b>	Linear Energy Transfer
<b>MC</b>	Monte Carlo
<b>CPMD</b>	Car-Parinello Molecular Dynamics
<b>TDDFT</b>	Time-Dependent Density Functional Theory
<b>NEXAFS</b>	Near Edge X-ray Absorption Fine Structure
<b>AIMD</b>	Ab Initio Molecular Dynamics
<b>BOMD</b>	Born-Oppenheimer Molecular Dynamics
<b>CPMD</b>	Car-Parrinello Molecular Dynamics
<b>DFT</b>	Density Functional Theory
<b>KMC</b>	Kinetic Monte Carlo
<b>MC</b>	Monte Carlo
<b>MD</b>	Molecular Dynamics
<b>MO</b>	Molecular Orbital
<b>PES</b>	Potential Energy Surface

<b>SCF</b>	Self-Consistent Field
<b>TDDFT</b>	Time-Dependent Density Functional Theory
<b>TISE</b>	Time Independent Schrodinger equation
<b>TDSE</b>	Time Dependent Schrodinger equation
<b>DOS</b>	Density of States
<b>NPT</b>	Number of Particles, Volume and Temperature
<b>NVT</b>	Number of Particles, Pressure and Temperature
<i><b>Universal Constants</b></i>	
<b>E</b>	Charge of an electron
<b>m<sub>e</sub></b>	Mass of an electron
<b>h</b>	Planck's constant

## Résumé étendu en français

---

Au cours du siècle dernier, les scientifiques ont essayé de comprendre l'interaction des photons avec la matière. Cela a conduit à une bonne connaissance des différentes gammes d'énergie des photons, y compris la lumière ultraviolette (UV), qui entraîne principalement des événements d'excitation, et les radiations électromagnétiques très pénétrantes (rayons X durs ou rayons gamma) qui produisent des traces d'ionisation éparses.

Cependant, beaucoup de choses demeurent inconnues, en particulier en ce qui concerne les radiations peu pénétrantes et densément ionisantes, comme les rayons X mous (0,2 keV - 2 keV, entre les UV et les rayons X durs). Mes travaux de recherche doctorale visent à combler partiellement cette lacune dans les connaissances actuelles sur l'interaction lumière-matière. Mon projet de recherche est particulièrement axé sur l'étude de l'interaction des rayons X mous avec, d'une part, de l'eau pure et, d'autre part, des dipeptides solvatés. Cette étude est réalisée à l'aide de méthodes expérimentales et théoriques.

Les études expérimentales ont été menées à l'aide du rayonnement synchrotron X mou (synchrotron SOLEIL, France) sur trois lignes de lumière différentes, à savoir METROLOGIE, PLEIADES et TEMPO. Sur la ligne de faisceau METROLOGIE, des expériences d'irradiation d'échantillons d'eau liquide (à l'aide d'une cellule microfluidique) ont été réalisées ; tandis que, sur les lignes de faisceau PLEIADES et TEMPO, des études spectroscopiques ( spectroscopie de photoélectrons X soit sur un micro-jet liquide, soit sur une goutte ) ont permis d'étudier l'interaction des rayons X mous avec le dipeptide solvaté.

Des calculs théoriques sont effectués à l'aide de simulations de dynamique moléculaire ab-initio, sur les supercalculateur Occigen (CINES), Jean-Zay (IDRIS) et MeSU (Sorbonne Université) en France.

**Les résultats de ma thèse de doctorat sont les suivants :**

1. Le premier objectif était d'étudier les effets indirects des rayons X mous, c'est-à-dire leur interaction avec l'eau pure, car l'eau joue un rôle crucial en radiobiologie. L'accent a été mis sur l'étude de la formation d'une espèce radicale ( $\text{HO}_2^\circ$ ), qui proviendrait de la réaction du produit de dissociation d'une molécule d'eau doublement ionisée (produite après effet Auger,

à l'échelle de temps de la femtoseconde) avec son environnement, dans les traces d'ionisation denses. Outre la faible pénétration des rayons X mous, les rendements radicalaires dans cette gamme d'énergie sont extrêmement faibles. Pour surmonter ces limitations, une technique de détection de pointe ultra-sensible a été développée, et consiste en une cellule microfluidique couplée à une cellule de détection UV en ligne. Ces expériences ont été réalisées sur la ligne de faisceau de métrologie du synchrotron SOLEIL. Le rendement de  $\text{HO}_2^\circ$ , produit via la réaction  $\text{O} + \text{OH} \rightarrow \text{HO}_2^\circ$  (voie directe), est égale à  $0,0053 \pm 0.0007 \mu\text{mol/J}$  à 1620 eV, proche de celui des ions lourds de haut TEL (200 keV/ $\mu\text{m}$ ). Le rendement de  $\text{HO}_2^\circ$  par la voie indirecte (essentiellement par réaction des électrons aqueux avec l'oxygène moléculaire dissout) présente un minimum vers 800 eV et une augmentation abrupte vers 1300 eV. Des simulations AIMD sont également présentées pour comprendre le mécanisme de formation de  $\text{HO}_2^\circ$  au sein des traces d'ionisation denses générées par les X mous. Pour cela, l'évolution dynamique du système ( $\text{H}_2\text{O}^{2+}$  proche d'un radical hydroxyle, immergés dans l'eau liquide), de l'échelle de temps de la femto à picoseconde, est modélisée en utilisant de simulations de dynamique moléculaire TD-DFT (Time-Dependent Density Functional Theory), suivie par des simulations de type Car-Parrinello ou Born-Oppenheimer, à l'aide du code CPMD.

2. Le deuxième objectif de la thèse était de comprendre les effets directs des rayons X mous, c'est-à-dire leur interaction initiale avec les biomolécules solvatées. L'échelle de temps des effets directs est différente de celle des effets indirects, les premiers étant plus rapides. Pour étudier ces effets ultrarapides, des expériences ont été réalisées sur des biomolécules solvatées, à savoir un l'acide aminé (Glycine) et un dipeptide (Glycylglycine), afin d'étudier la liaison peptidique, en utilisant des techniques de spectroscopie de rayons X mous (XPS et XAS). Ces expériences sont possibles grâce à l'installation d'un micro-jet liquide sous vide sur la ligne PLEIADES du synchrotron SOLEIL. Les propriétés électroniques des biomolécules et la manière dont ces propriétés sont affectées par la solvatation ont été étudiées. Les résultats suggèrent que le soluté ne peut pas être considéré comme une entité distincte, mais que ses propriétés électroniques sont affectées par les molécules d'eau environnantes. L'effet de la solvatation de la glycylglycine est plus prononcé sur les niveaux de cœur de l'azote, que du carbone. Une contrepartie théorique, c'est-à-dire des simulations AIMD pour déterminer les différents états électroniques (Kohn-Sham) d'une biomolécule (glycine et glycylglycine) immergée dans l'eau liquide, permet d'interpréter les études de résonance des biomolécules solvatées.

